

**Seismic stratigraphy and structural analysis of shallow seabed in  
the southern Arkona Basin, Baltic Sea – delineating seismic  
attributes for resolving geological complexity and predicting  
geotechnical cone resistance**

Dissertation

Zur Erlangung des Doktorgrades der Naturwissenschaften  
am Fachbereich Geowissenschaften  
der Universität Bremen

vorgelegt von

**Opeyemi Ogunleye**

Bremen, Dezember 2023

## **Gutachter:**

Prof. Dr. Volkhard Spiess

Prof. Katrine Juul Andresen

## **Datum des Promotionskolloquiums:**

06.02.2024

# Versicherung an Eides Statt / Affirmation in lieu of an oath

**gem. § 5 Abs. 5 der Promotionsordnung vom 28.04.2021 /  
according to § 5 (5) of the Doctoral Degree Rules and Regulations of 28 April, 2021**

Ich / I, Opeyemi Ogunleye (Wohnort: Bremen)

versichere an Eides Statt durch meine Unterschrift, dass ich die vorliegende Dissertation selbständig und ohne fremde Hilfe angefertigt und alle Stellen, die ich wörtlich dem Sinne nach aus Veröffentlichungen entnommen habe, als solche kenntlich gemacht habe, mich auch keiner anderen als der angegebenen Literatur oder sonstiger Hilfsmittel bedient habe und die zu Prüfungszwecken beigelegte elektronische Version (PDF) der Dissertation mit der abgegebenen gedruckten Version identisch ist. / With my signature I affirm in lieu of an oath that I prepared the submitted dissertation independently and without illicit assistance from third parties, that I appropriately referenced any text or content from other sources, that I used only literature and resources listed in the dissertation, and that the electronic (PDF) and printed versions of the dissertation are identical.

Ich versichere an Eides Statt, dass ich die vorgenannten Angaben nach bestem Wissen und Gewissen gemacht habe und dass die Angaben der Wahrheit entsprechen und ich nichts verschwiegen habe. / I affirm in lieu of an oath that the information provided herein to the best of my knowledge is true and complete.

Die Strafbarkeit einer falschen eidesstattlichen Versicherung ist mir bekannt, namentlich die Strafandrohung gemäß § 156 StGB bis zu drei Jahren Freiheitsstrafe oder Geldstrafe bei vorsätzlicher Begehung der Tat bzw. gemäß § 161 Abs. 1 StGB bis zu einem Jahr Freiheitsstrafe oder Geldstrafe bei fahrlässiger Begehung. / I am aware that a false affidavit is a criminal offence which is punishable by law in accordance with § 156 of the German Criminal Code (StGB) with up to three years imprisonment or a fine in case of intention, or in accordance with § 161 (1) of the German Criminal Code with up to one year imprisonment or a fine in case of negligence.

Bremen, 05.12.2023

---

Ort / Place, Datum / Date

# Contents

List of figures .....	vi
List of tables.....	xv
Preface.....	xvii
<b>Thesis abstract .....</b>	<b>1</b>
<b>Zusammenfassung.....</b>	<b>4</b>
<b>Chapter 1 .....</b>	<b>7</b>
<b>Introduction.....</b>	<b>7</b>
1.1 Motivation and objectives .....	7
1.2 State-of-the-art: integration of geological, geophysical and geotechnical data .....	15
1.2.1 Stratigraphic and structural seismic techniques.....	15
1.2.1.1 Qualitative seismic interpretation integrated with lithologic description and CPT data .....	16
1.2.1.2 Quantitative seismic technique.....	18
1.2.2 Borehole velocity log interpretation .....	19
1.2.3 Cone penetration test (CPT) profiles - interpretation and prediction of geotechnical data.....	20
1.3 Regional geological setting.....	22
1.4 Thesis outline and declaration of co-author contributions .....	25
<b>Chapter 2 .....</b>	<b>31</b>
<b>Data and methods .....</b>	<b>31</b>
2.1 Data.....	31
2.2 Methods.....	32
2.2.1 Data acquisition.....	33
2.2.1.1 3D MCS data acquisition .....	33
2.2.1.2 2D MCS data acquisition .....	34
2.2.2 MCS data processing.....	35
2.2.2.1 3D MCS data processing in Claritas .....	37
2.2.2.1.1 3D seismic pre-processing.....	37
2.2.2.1.2 3D pre-stack seismic processing .....	38

2.2.2.1.2.1 Surface-related multiple elimination (SRME).....	38
2.2.2.1.2.2 Velocity analysis and spherical divergence correction.....	39
2.2.2.1.2.3 Second velocity analysis - normal move-out and static corrections.....	39
2.2.2.1.3 3D stacking and post-stack processing .....	41
2.2.2.2 2D MCS data processing in Claritas .....	42
2.2.2.3 2D MCS data processing in VISTA .....	43
<b>Chapter 3 .....</b>	<b>45</b>
<b>Seismic stratigraphy and structural analysis of shallow seabed in the southern Arkona Basin.....</b>	<b>45</b>
<b>Abstract .....</b>	<b>45</b>
3.1 Introduction.....	46
3.2 Geological setting .....	47
3.3 Material and methods .....	48
3.3.1 Material.....	48
3.3.2 Methods.....	49
3.3.2.1 2D and 3D MCS data processing.....	49
3.3.2.2 Seismic data interpretation .....	50
3.4 Results.....	52
3.4.1 Regional seismic units .....	52
3.4.1.1 Seismic Unit 1 (SU1) .....	52
3.4.1.2 Seismic Unit 2 (SU2) .....	54
3.4.1.3 Seismic Unit 3 (SU3) .....	54
3.4.1.4 Seismic Unit 4 (SU4) .....	55
3.4.2 South central area: detailed 3D stratigraphic and structural description.....	55
3.4.2.1 Vertical stacking pattern and lineaments .....	55
3.4.2.2 Time structure and thickness maps .....	55
3.4.2.3 Facies and structures observed on horizontal seismic sections .....	59
3.4.2.4 RMS amplitude maps .....	61
3.4.3 2D stratigraphic and structural description in adjoining areas.....	61
3.4.3.1 Southeastern to western profile.....	61
3.4.3.2 Northwestern to southcentral profile .....	64
3.4.3.3 Central to northern profile.....	64
3.5 Discussion .....	65

3.5.1	Architecture of the shallow Cretaceous to Holocene succession .....	65
3.5.2	Pleistocene ice flow during tunnel valley formation in the Arkona Basin - sedimentation and reworking of glaciogenic valley fills .....	69
3.5.3	Weichselian glaciation - local ice flow direction, sediment deposition and buried glacial landforms.....	71
3.5.4	Post-glacial sedimentation .....	73
3.5.5	Late Cretaceous to Pleistocene structural deformation of bedrock chalk and unchanneled Pleistocene till unit – the influence of varying tectonic and glacial processes .....	74
3.5.6	Conceptual model for the Late Cretaceous to Holocene evolution of shallow seabed in the 3D MCS area.....	77
3.5.7	Significance of seismic stratigraphy for facies prediction and sediment correlation .....	77
3.6	Conclusions.....	78
3.7	Acknowledgements.....	81
<b>Chapter 4</b>	.....	<b>82</b>
<b>Statistical boundary conditions of subsoil physical properties in the Arkona Basin - delineating potential seismic attributes for predicting near-surface geotechnical parameters.....</b>		<b>82</b>
<b>Abstract</b>	.....	<b>82</b>
4.1	Introduction.....	83
4.2	Geological setting .....	85
4.3	Material and methods .....	86
4.3.1	Material.....	86
4.3.2	Methods.....	86
4.3.2.1	CPT data interpretation integrated with seismic facies .....	86
4.3.2.2	Derivation of physical properties from downhole velocity logs.....	87
4.3.2.3	Statistical analysis of small strain physical properties of geological units and their comparison with measured cone resistance.....	88
4.4	Results.....	88
4.4.1	Correlation of a vertical seismic section with borehole sediment descriptions and CPT profiles .....	90
4.4.2	Spatial variation of seismic facies in relation to the CPT behavior of subsoil units .....	90
4.4.3	Summary statistics and vertical profiles of the small strain physical properties of near-surface geological formations .....	94

4.4.3.1	Histograms and quantitative measures of the derived physical parameters.....	94
4.4.3.2	Vertical profiles of Poisson’s ratio and small strain shear modulus across seismo-stratigraphic units .....	94
4.4.4	Plots of the median physical and CPT properties of subsoil units.....	95
4.5	Discussion .....	97
4.5.1	Relationship between seismic and CPT data - its implication for CPT data prediction.....	97
4.5.2	Interface-related seismic attributes: guides for CPT data prediction.....	98
4.5.3	Statistical boundary conditions of small strain physical properties of geological units - their evaluation and usefulness for seismic inversion.....	99
4.5.4	Predicting cone resistance from acoustic impedance.....	101
4.6	Conclusions.....	101
4.7	Acknowledgements.....	102
<b>Chapter 5</b>	<b>.....</b>	<b>104</b>
	<b>Post-stack acoustic impedance as a reliable indicator of variation in lithologic and geotechnical properties in the southern Arkona Basin - assessment of two near-surface impedance inversion approaches using stationary wavelets....</b>	<b>104</b>
	<b>Abstract .....</b>	<b>104</b>
5.1	Introduction.....	105
5.2	Geological setting .....	107
5.3	Material and methods .....	107
5.3.1	Dataset .....	107
5.3.2	Post-stack impedance inversion.....	108
5.3.2.1	Impedance inversion with velocity-guided background trend (velocity-guided approach) .....	108
5.3.2.2	Impedance inversion with layer cake low-frequency model (band-limited approach).....	109
5.4	Results.....	111
5.4.1	Lithology-related anomalies on the absolute acoustic impedance sections derived from an inversion of full stacks using the velocity-guided approach....	111
5.4.2	Post-stack absolute acoustic impedance predicted with the band-limited approach - its comparison with the product of velocity-guided inversion .....	116
5.4.3	Correlation of the measured cone resistance and sleeve friction with the predicted absolute acoustic impedance - velocity-guided and band-limited inversion approaches.....	117

5.5	Discussion .....	119
5.5.1	Resolving stratigraphic and structural complexity in the near-surface sedimentary record of the southern Arkona Basin - significance of the correlation between absolute acoustic impedance and lithologic ground truth.....	119
5.5.2	Qualitative consideration of the potential of acoustic impedance as an attribute for predicting CPT data .....	122
5.5.3	Assessment of the approaches for post-stack acoustic impedance prediction – quantitative relationship between the predicted impedance and CPT data	123
5.6	Conclusions.....	126
5.7	Acknowledgements.....	127
<b>Chapter 6</b>	.....	<b>129</b>
<b>Conclusions and outlook</b>	.....	<b>129</b>
6.1	Seismic stratigraphy and structural analysis of shallow seabed in the southern Arkona Basin .....	130
6.2	Statistical boundary conditions of subsoil physical properties and the potential seismic attributes for predicting near-surface geotechnical parameters .....	133
6.3	Post-stack acoustic impedance as a reliable indicator of variation in lithologic and geotechnical properties - assessment of two near-surface impedance inversion approaches using stationary wavelets .....	134
6.4	Outlook .....	136
<b>Acknowledgements</b>	.....	<b>138</b>
<b>References</b>	.....	<b>140</b>
<b>Appendix</b>	.....	<b>151</b>
A1	DGG 2023 – 83 Jahrestagung der Deutschen Geophysikalischen Gesellschaft.....	151
A2	American Geophysical Union—AGU23 meeting, San Francisco, CA and Online Everywhere.....	152

## List of figures

- Fig. 1.1: Trend in the development of offshore wind power in the EU between 1991 and 2008. Notice the growth in cumulative installed capacity over the years examined (adapted from Bilgili et al., 2011) ..... 7
- Fig. 1.2: Sedimentary evidences of Saalian and Weichselian glaciations in the southeastern margin of Arkona Basin based on different Pleistocene glacial till units penetrated in well cores. Saalian Warthe till was only found within channels in the area. Middle Weichselian tills belonging to an unknown glacier advance and the Warnow advance have been preserved locally. Pomeranian till is limited to the southeastern part of the area shown, while the till of the Mecklenburg advance can be found in all boreholes (Obst et al., 2017)..... 10
- Fig. 1.3: Result of inverting a single-channel boomer data (a) to yield acoustic impedance (b) in Walney I windfarm site. Notice the similarity in stratigraphic and structural details contained in the seismic amplitude and impedance sections, and the varying intra-unit property values in the latter section (modified from Vardy et al., 2018) ..... 11
- Fig. 1.4: Transverse section through CPT locations depicting correlation between lithofacies, their CPT profile characteristics, and seismic facies in Dogger Bank, North Sea. Major changes in the CPT logs correspond to significant changes in seismic attributes of formations (Emery et al., 2019) ..... 12
- Fig. 1.5: Fundamental processes of a genetic algorithm for carrying out post-stack acoustic impedance inversion as shown by Vardy et al. (2015). The algorithm begins with random generation of initial impedance models. .... 14
- Fig. 1.6: Basic terminology for a cone penetrometer (Robertson and Cabal, 2014). 20
- Fig. 1.7: Example of CPTu data. ( $q_t$  = corrected total cone resistance;  $f_s$  = sleeve friction;  $u$  = pore pressure; 1 tsf  $\sim$  0.1 MPa; 14.5 psi = 100 kPa; 1 ft = 0.3048 m) (adapted from Robertson and Cabal, 2014) ..... 21
- Fig. 1.8: SBTn chart proposed by Robertson (1990) and modified by Robertson (2009) for interpreting soil type from CPT data.  $Q_{tn}$  = normalized cone resistance;  $F_r$  = normalized friction ratio;  $I_c$  = soil behavior type index (adapted from Robertson, 2016) ..... 21

- Fig. 1.9: Comparing blindly predicted and measured total tip resistance at location CPT29 in a deep-water site. The predicted tip resistance was derived from acoustic impedance (adapted from Chen et al., 2021) ..... 22
- Fig. 1.10: Overview map of the study area (red outline in inset) in the southern Arkona Basin displaying the bathymetry and main pre-Quaternary faults of the Tornquist Zone (fault lines were adapted from Obst et al., 2017). EMODnet Bathymetry Consortium (2020) is the source of the water depth shown. Map coordinates are based on UTM 33N..... 23
- Fig. 1.11: Seismo-stratigraphic units in the Bornholm Basin (modified from Tóth et al., 2014)..... 24
- Fig. 2.1: An overview map of the southern Arkona Basin showing the coverage of 3D and 2D seismic reflection data and the sites with sediment descriptions, velocity logs and Cone Penetration Test (CPT) data used in this research. 17 sites in the central, northern, northwestern, western, southcentral and southeastern areas are represented with orange, red, black, brown, white and lilac points, respectively. The sites are named as follows: the number shown in the figure followed by BH/CPT (where CPT data are available); 16 of the sites have sediment descriptions; only Sites 1, 14 and 16 BH have no CPT data (i.e. their names are 1, 14 and 16 BH, without CPT). Velocity logs are available only at Sites 1 BH and 2, 3, 4, 6 and 11 BH/CPT. The faults shown belong to the Tornquist Zone (Obst et al., 2017). EMODnet Bathymetry Consortium (2020) is the source of the water depth; geographic coordinates are based on UTM 33N..... 31
- Fig. 2.2: 3D MCS data acquisition configuration. Active streamer sections are represented as jointed horizontal bars with alternating purple and black segments. Offset ranges from 31 to 89 m. .... 33
- Fig. 2.3: Geometry of the 96-channel streamer used for acquiring 2D MCS data along AL446-GeoB14, AL464-GeoB15 and AL566-GeoB21 profiles in this study. The spacing in red represents the length of connectors between active sections of the streamer..... 34
- Fig. 2.4: 2D and 3D MCS data processing sequence used in this study (static correction was not applied to Profile AL464-GeoB15-053)..... 36
- Fig. 2.5: Constant velocity stacks (1480 m/s) along Inline 16 in the 3D MCS data before (a) and after (b) SRME. Notice the suppression of multiples in the circled region. TWT

= Two-Way Travel-time (vertical exaggeration was calculated based on a velocity of 2000 m/s)..... 38

Fig. 2.6: Gather of CDP 2270538 in the 3D MCS cube before (a) and after (b) static correction using smoothed seafloor picks. The gather in '2.6a' has been corrected for NMO. Notice the improvement in event flattening within the circled region after static correction. TWT = Two-Way Travel-time..... 40

Fig. 2.7: Stacked MCS data along Inline 18 within the 3D seismic cube before (a) and after (b) 2.5D finite-difference time migration. In the circled regions, notice the significant reduction in the diffracted energy after migration. TWT = Two-Way Travel-time (vertical exaggeration was calculated based on a velocity of 2000 m/s)..... 41

Fig. 2.8: Full stack of 2D seismic Profile AL402-GeoB12-167 before (a) and after (b) multiple suppression by predictive deconvolution method. Notice the reduction of multiple energy in the circled region. TWT = Two-Way Travel-time (vertical exaggeration was calculated based on a velocity of 2000 m/s)..... 42

Fig. 3.1: Bathymetric map of the study area (red outline in inset) in the southern Arkona Basin showing the coverage of 3D and 2D seismic reflection data as well as boreholes available in this research. Boreholes in the central, northern, northwestern, western, southcentral and southeastern areas are displayed, and their locations are shown as orange, red, black, brown, white and lilac dots, respectively. The format of borehole names is the number of the borehole shown in the figure followed by BH/CPT (where borehole and Cone Penetration Test (CPT) data are available), except for Holes 1, 14 and 16 which have no CPT data (i.e. 1, 14 and 16 BH). Velocity logs are available at Sites 1 BH and 2, 3, 4, 6 and 11 BH/CPT alone. Main pre-Quaternary faults of the Tornquist Zone are indicated (e.g. Schluter et al., 1997). Water depth is based on the EMODnet Digital Bathymetry (DTM 2020) provided online by EMODnet Bathymetry Consortium (2020). Map coordinates are based on UTM 33N in this study..... 46

Fig. 3.2: 2D seismic Profile AL464-GeoB15-053 (see fig. 3.1 for location): (a) un-interpreted seismic section of the profile tied with lithologic logs from 13 BH/CPT, 14 BH and 15 BH/CPT; (b) regional stratigraphy and structure interpreted on the seismic section shown in '3.2a'. SU1 reflectors (Cretaceous bedrock) have been displaced along lineaments (faults) and bent (folded). Notice the major lineaments interpreted as relatively shallow and basement faults, the latter category being the Nordadler faults (see text for details). D1-4 are Depressions 1 to 4 in fig. 3.3. These and other channels shown in '3.2b' contain either subparallel or chaotic seismic reflectors (glaciogenic sediments) which are different in character from the surrounding SU1. TWT = Two-Way Travel-time; SU = Seismic Unit (vertical exaggeration was calculated based on a velocity of 2000 m/s) ..... 51

Fig. 3.3: Inline 90 in the 3D MCS cube acquired in the southcentral part of the study area (see fig. 3.4b for location): (a) un-interpreted seismic section of the inline tied with lithologic log from Hole 13 BH/CPT; (b) sketch of seismo-stratigraphic and structural framework interpreted along '3.3a'. Notice the lineaments of fault and bending of reflectors in SU1 (bedrock chalk). Four depressions (D1-4) have been incised into SU1. The double-ended red and green arrows together with the dotted red line delineate the interval within which the RMS amplitude map in fig. 3.8a was extracted. TWT = Two-Way Travel-time; SU = Seismic Unit (vertical exaggeration was calculated based on a velocity of 2000 m/s) ..... 53

Fig. 3.4: Time structure maps derived from the 3D seismic cube (see fig. 3.1 for location): (a) an internal Cretaceous horizon dissected by normal faults in the vicinity of D1 and deformed into an anticline. Notice the converging orientations of Depressions 1-3; (b) the base of the laterally extensive SU3 (unchannelized till-dominated glaciogenic sediments). The black arrow indicates the local ice flow direction of a Weichselian glacier in the study area; (c) the top of SU3. D = Depression; TWT = Two-Way Travel-time; SU = Seismic Unit. .... 56

Fig. 3.5: Isochore maps based on the 3D MCS data: (a) the true vertical thickness of SU2 sediments filling D1-4 (Quaternary glacial valleys; see fig. 3.3 for a vertical section cutting across the depressions). These depressions appear to interconnect in the southern part of the area and beyond; (b) the true vertical thickness map of SU4 (post-glacial) sediments. D = Depression (time-depth conversion was carried out with stacking velocity values of 2100 and 1475 m/s for SU2 and SU4, respectively, which were deduced during seismic data processing). .... 57

Fig. 3.6: Time slices through SU1 and SU2 in the 3D MCS data: (a) time slice at 0.097 s TWT and its description. Red outline delineates NW-SE trending Depression 1 (valley) filled with high-amplitude packages (SU2). Stippled and bold orange outlines are the respective spatial limits of Depressions 2 and 3. Facies boundaries of valley fills are shown as stippled blue and lilac lines; (b) interpreted version of '3.6a' showing the spatial distribution of sedimentary facies and structures; (c) section of the time slice at 0.080 s TWT displaying a meandering section of Depression 4 (purple outline) oriented NE-SW. TWT = Two-Way Travel-time; SU= Seismic Unit. .... 58

Fig. 3.7: Time slice at 0.064 s TWT in the 3D seismic cube: (a) un-interpreted version of the time slice; (b) distribution of sedimentary facies of SU1, SU2 and SU3 as interpreted on the time slice. Notice the NW-SE and NE-SW trending amplitude structures defined by seismic events in SU3. TWT = Two-Way Travel-time; SU = Seismic Unit. .... 59

Fig. 3.8: RMS amplitude maps generated for SU1 to SU3 in the southcentral part of the study area: (a) an integrated map showing the amplitude characteristics of SU1 (Cretaceous chalk) and depression-filling SU2. Bold black and green lines delineate the flanks of Depressions 1 and 4, respectively; stippled black and purple lines are the respective limits of Depressions 2 and 3. The depressions are surrounded by SU1. The time windows within which RMS amplitudes of SU1 and SU2 were calculated are shown in fig. 3.3b; (b) un-interpreted RMS amplitude map generated from the top to base of SU3 (unchannelized glaciogenic unit) in the area; (c) interpreted RMS amplitude map of '3.8b'. Notice the polygonal features of a patterned ground in an ancient permafrost terrain. SU = Seismic Unit; amp. = amplitude ..... 60

Fig. 3.9: 2D seismic Profile AL402-GeoB12-167 (see fig. 3.1 for location): (a) un-interpreted version of the seismic section tied with lithologic logs from boreholes 7 and 12 BH/CPT; (b) seismo-stratigraphic succession and structural features interpreted on '3.9a'. SU1a-c represent three subunits of the bedrock chalk. Two generations of depressions (Pleistocene tunnel valleys) which cut into SU1 are shown. TWT = Two-Way Travel-time; SU = Seismic Unit (vertical exaggeration was calculated with a velocity of 2000 m/s)..... 62

Fig. 3.10: 2D MCS Profile AL566-GeoB21-130 (see fig. 3.1 for location): (a) un-interpreted version of the seismic section tied with lithologic logs from boreholes 1 BH, 2 BH/CPT and 3 BH/CPT in the northern part of the study area; (b) sketch of the stratigraphic framework interpreted from '3.10a'. Notice a major depression belonging to an undifferentiated generation of tunnel valley, which contains an interbedded lens of coarse-grained sediments as part of its infill. A relatively minor depression interpreted as a glaciofluvial channel was incised into SU3. TWT = Two-Way Travel-time; SU = Seismic Unit (vertical exaggeration was calculated based on a velocity of 2000 m/s)..... 63

Fig. 3.11: Model of the Late Cretaceous to Holocene geological evolution in the 3D MCS coverage area. Green and blue arrows indicate ice advance and retreat, respectively, in Pleistocene. (a) folding of the bedrock chalk during a Late Cretaceous inversion; (b) Tertiary crustal extension formed normal faults in the chalk; (c) subglacial meltwater erosion of the bedrock during Pleistocene glacier advancement(s) formed tunnel valleys in the area. (d-e) one to two episode(s) of till-dominated sedimentation filled the valleys, with multiple events of deposition being separated by a period of erosion of pre-existing valley fills; (f) retreat of valley-filling glacier was probably associated with deposition of sediments; (g) advancing Weichselian glacier(s) removed part of the pre-existing glaciogenic sediments and produced subglacial s-forms across the top of Cretaceous chalk and Pleistocene valley fills. Subsequent deposition of glacial debris led to formation of the laterally extensive Weichselian till unit; (h) after the last glacial retreat, NW-SE trending ridges and relict permafrost structures have been left on and within the Weichselian till unit, respectively; (i)

sedimentation in the area culminated in the deposition of post-glacial silt and/or clay.  
 ..... 76

Fig. 4.1: Map of the Arkona Basin showing the study area (red outline in inset), coverage of 3D and 2D seismic reflection data, and sites with sediment descriptions, velocity logs and CPT data. The sites in the central, northern, northwestern, western, southcentral and southeastern areas are shown as orange, red, black, brown, white and lilac dots, respectively. The format of site names is the number shown in the figure followed by BH/CPT (where CPT data are available); only Sites 1, 14 and 16 have no CPT data (i.e. their names are 1, 14 and 16 BH). Only 10 BH/CPT has no sediment description. Velocity logs are available only at 6 sites, namely: 1 BH and 2, 3, 4, 6 and 11 BH/CPT. The pre-Quaternary faults shown belong to the Tornquist Zone (Obst et al., 2017). The bathymetry is based on EMODnet Bathymetry Consortium (2020). Map coordinates are based on UTM 33N (adapted from chapter 3). ..... 84

Fig. 4.2: Correlation of 2D seismic Profile AL402-GeoB12-167 with lithologic logs and CPT profiles: (a) interpreted seismic section of the profile showing the stratigraphic and structural framework of the shallow Cretaceous to Holocene succession in the study area (see fig. 4.1 for location; modified from chapter 3). The profile is tied with lithologic logs from two sites, namely: 7 and 12 BH/CPT; (b) zoomed seismic section (blue outline in '4.2a') showing the correlation of variations in measured cone resistance ( $q_c$ ) and friction ratio ( $R_f$ ) at 7 BH/CPT with changes in seismic subfacies within the post-glacial interval; (c) close-up section (green rectangle in '4.2a') showing the correlation of changes in measured cone resistance and sleeve friction ( $f_s$ ) at 12 BH/CPT with variations in seismic facies from the post-glacial interval through the unchannelized till to the depression (valley) fill. TWT = Two-Way Travel-time; SU = Seismic Unit; CPT = Cone Penetration Test (vertical exaggeration was calculated based on a velocity of 2000 m/s) ..... 89

Fig. 4.3: Normalized soil behavior type plots for Seismic Unit 1 (SU1) at different parts of the study area using the Robertson (1990) chart. The geotechnical plots for SU1 in the southeastern, southcentral and western areas are color-coded on the chart. Corresponding seismic facies of the uppermost chalk subunit (SU1c) penetrated at Sites 13 and 15 BH/CPT are shown, described and bounded with corresponding colored outlines. .... 91

Fig. 4.4: Normalized soil behavior type plots for Seismic Unit 3 (SU3) at Sites 2, 5, 11 and 15 BH/CPT on the Robertson (1990) chart. Corresponding seismic facies of the unchannelized till unit (SU3) penetrated at these sites are shown, described and bounded with corresponding colored outlines. .... 91

Fig. 4.5: Histograms of Primary (P) and Shear (S) impedances of geological formations showing the range, 95% confidence interval of grand mean (C.I. of  $\mu_{\bar{x}}$ ) and median value. (a) and (d) are for the chalk, (b) and (e) for the valley fill, and (c) and (f) for the unchannelized till in our study..... 92

Fig. 4.6: Vertical profiles of Poisson's ratio (black) and small strain shear modulus (red) correlated per seismic unit across Sites 1 BH (north) and 2, 6 and 11 BH/CPT (located in the northern, northwestern and central parts of the study area, respectively). SU = Seismic Unit; SU1 = Cretaceous chalk; SU2 = valley fill; SU3 = unchannelized till; SU3lgr = sediments in glaciofluvial channel; SU4 = post-glacial sediments. .... 95

Fig. 4.7: Plots of the physical properties and measured cone resistance across Seismic Units 1 to 4 (SU1-4) based on their median values: (a) step plots of the median  $G_o$  and  $Z_p$  as well as the measured median  $q_c$ ; (b) cross plot of the measured median  $q_c$  versus the median  $Z_p$ ; (c) cross plot of the measured versus predicted median  $q_c$ .  $G_o$  = small strain shear modulus;  $Z_p$  = primary impedance;  $q_c$  = cone resistance; SU1 = Cretaceous chalk; SU2 = till-dominated valley fill; SU3 = unchannelized till; SU4 = post-glacial sediments..... 96

Fig. 5.1: Map of the study area (red outline in inset) in the southern Arkona Basin showing the 2D seismic reflection profiles that were inverted in this study and sites with sediment descriptions, velocity logs and Cone Penetration Test (CPT) data. The sites are shown as dots (black dots represent sites located on the inverted seismic profiles; red dot indicates an additional site utilized in both chapters 3 and 4). The name of each site is the number shown in the figure (numbers follow the order introduced in chapter 3) followed by BH/CPT at the locations with CPT data; Site 1 has no CPT data, so its name is 1 BH. 1 BH and 2, 3, 4, 6 and 11 BH/CPT have velocity logs which were utilized in chapter 4 for estimating median physical properties of geological units. Pre-Quaternary faults of the Tornquist Zone are depicted (Obst et al., 2016). EMODnet Bathymetry Consortium (2020) is the basis of the water depth values. Map coordinates are in UTM 33N (modified from chapter 3). .... 106

Fig. 5.2: Work flow of the band-limited acoustic impedance inversion approach in which a band-limited impedance result is merged with a layer cake low-frequency model ..... 110

Fig. 5.3: 2D seismic Profile AL402-GeoB12-167 tied to the lithologic logs at Sites 7 and 12 BH/CPT (see fig. 5.1 for location): (a) interpreted seismic amplitude section showing the major near-surface seismic units and their lithologic characterization in our study area based on the work presented in chapter 3; (b) un-interpreted absolute acoustic impedance section of the profile generated with the velocity-guided inversion approach; (c) interpreted version of the impedance section in '5.3b' which has been

correlated with sediment descriptions. Notice how impedance anomalies indicate the lateral extent and vertical stacking of stratigraphic units. Two Pleistocene valleys are depicted as cutting into the Cretaceous chalk. Stippled red lines delineate a lenticular zone with relatively low impedance values in a valley fill. TWT = Two-Way Travel-time; SU = Seismic Unit (vertical exaggeration was calculated based on a velocity of 2000 m/s) ..... 112

Fig. 5.4: 2D seismic Profile AL402-GeoB12-168 tied to the lithologic logs at Sites 6 and 11 BH/CPT (see fig. 5.1 for location): (a) un-interpreted seismic amplitude section along the profile; (b) un-interpreted absolute acoustic impedance section generated from '5.4a' with the velocity-guided inversion approach; (c) interpreted version of the impedance section in '5.4b' showing the spatial distribution of lithologic units, an intra-till property boundary, and the structural features of geological intervals. TWT = Two-Way Travel-time; SU = Seismic Unit (vertical exaggeration was calculated based on a velocity of 2000 m/s)..... 113

Fig. 5.5: 2D seismic Profile AL402-GeoB12-167 tied to the lithologic log at Site 12 BH/CPT: (a) seismic amplitude section of the profile showing the horizons independently picked along the same unit boundaries that were interpreted in chapter 3. These horizons formed the stratigraphic framework of an initial low-frequency impedance model employed in the band-limited approach; (b) un-interpreted absolute impedance section of the profile generated with the band-limited inversion approach. It corresponds to a part of fig. 5.3; (c) interpreted version of '5.5b' correlated with sediment descriptions. The stippled red line is the top of the high-impedance interval within the uppermost subunit filling Valley 1. This high-impedance zone is characterized by anomalous lithologic and geotechnical properties within the valley. Notice how impedance anomalies show the detailed spatial distribution of lithologic units, thereby allowing improvements on the initial horizon interpretation shown in '5.5a'. Artifacts occur as vertical stripes on this impedance section. TWT = Two-Way Travel-time; SU = Seismic Unit (vertical exaggeration was calculated based on a velocity of 2000 m/s)..... 115

Fig. 5.6: Raw data plot of the CPT measurements of sleeve friction and cone resistance and the impedance inversion results at Site 12 BH/CPT. Seismic Units SU4, SU3 and SU2 are shown with blue, purple and light brown backgrounds, respectively. Please note that the band-limited impedance is shifted upward by 1.07 m (the rationale for this decision is given in fig. 5.9). ..... 117

Fig. 5.7: Cross plots of measured cone resistance and predicted impedance at Site 12 BH/CPT with a correlation coefficient of 0.27 for the velocity-guided results and 0.82 for the band-limited results. The color code of the seismic units follows the code in fig. 5.6. .... 118

Fig. 5.8: Cross plots of measured sleeve friction and predicted impedance at Site 12 BH/CPT with a correlation coefficient of 0.40 for the velocity-guided results and 0.90 for the band-limited results. The color code of the seismic units follows the code in fig. 5.6. .... 118

Fig. 5.9: Correlation coefficient of measured cone resistance and predicted impedance as a function of constant depth shift at Site 12 BH/CPT. .... 119

## List of tables

Table 1.1: Possible geological interpretation from reflector parameters in a seismic unit (modified from Mitchum et al., 1977) .....	16
Table 1.2: Case study of lithologic interpretation of seismic attributes in an area that overlaps with our working area in the Arkona Basin. The table shows major seismic units marked by reflectors and their corresponding lithologic record along the southeastern margin of the Arkona Basin (Obst et al., 2017).....	17
Table 1.3: Regional seismo-stratigraphic scheme for the study area as presented by Hübscher et al. (2019). BCU, base Cretaceous unconformity; BCG, base Chalk Group; BCA, base Campanian; BLM, base lower Maastrichtian; ILM, internal lower Maastrichtian; IUM, base internal upper Maastrichtian; BPU, base Pliocene unconformity. ....	24
Table 2.1: Summary of sites with sediment descriptions, primary and shear wave velocity (P-S) logs, and CPT data in this study. Green- and orange-filled fields indicate that sediment descriptions or measurement types are available and unavailable, respectively.....	32
Table 3.1: Representative seismic units and their geological interpretation corroborated with sediment descriptions in boreholes, published stratigraphy of the southern Baltic Sea and its coastal region, and glaciotectonic concepts (e.g. Mathys et al., 2005; Kenzler et al., 2010; Gehrman et al., 2017). ....	52
Table 4.1: Summary statistics of the small strain physical properties of each seismo-stratigraphic unit and its subunits (the error in estimated density relative to the measured value at Site 2 BH/CPT: -9.4% in SU3 and SU2; +0.5% in SU1).....	93
Table 4.2: Summary statistics of the measured large strain geotechnical properties of each seismo-stratigraphic unit and its subunits.....	93
Table 5.1: Impedance inversion parameters for the genetic algorithm and merging of band-limited impedance with a low-frequency model .....	110
Table 5.2: Measured and predicted statistical estimates of acoustic impedance for each seismic unit. The ground truth (measured) values are based on a compilation of velocity logs as shown in chapter 4, while the velocity-guided and band-limited values	

are based on the impedance predicted in each seismic unit along the entire section of Profile AL402-GeoB12-167. The velocity-guided and band-limited values for each seismic unit are calculated by summing the products of mean impedance and sample size at each trace location and dividing this sum by the total number of samples for all the locations. The unit of the statistical measures is (m/s)\*(g/cc). The estimated mean values are grand means. Min. = Minimum Value; Max. = Maximum Value; SU = Seismic Unit..... 116

## Preface

This work was submitted to the Department of Geosciences, University of Bremen, for the degree of Doktor der Naturwissenschaften (Dr.rer.nat.). The research was carried out as part of a larger project called SynCore, which was funded by the Federal Ministry for Economic Affairs and Climate Action, Germany. In addition to the University of Bremen, other members of SynCore's consortium were: Fraunhofer Institute for Wind Energy Systems (IWES), Fraunhofer Institute for Industrial Mathematics (ITWM), Geotechnik und Dynamik Consult GmbH, and RWE Renewables.

The study took place at the University of Bremen in the Marine Technology and Environmental Research group under the supervision of Prof. Dr. Volkhard Spiess. Prof. Katrine Juul Andresen is the second reviewer of this thesis. The work contained herein formed the basis of abstracts submitted and accepted for poster presentations at two conferences in Germany and the United States of America (see Appendix for the abstracts).

The MARUM graduate school GLOMAR sponsored my research placement at the Norwegian Geotechnical Institute (NGI) in Oslo from April to June, 2023. In the course of my research, important scientific collaborations were forged with members of staff of Fraunhofer IWES (Natasha Morales and Taisiya Pein) and NGI (Guillaume Sauvin and Maarten Vanneste) for my manuscripts. NGI used its computing resources to invert 5 seismic profiles for this work. Other co-authors for my research manuscripts include Dr. Hanno Keil and Nikolas Römer-Stange, who are part of our research group.

This dissertation has been written in a cumulative form comprising of 3 standalone research manuscripts that will be submitted for publication in international peer-reviewed journals. The first chapter in the dissertation shows the motivation and objectives as well as the context of this research. The following chapter discusses the material and methods utilized. My 3 research manuscripts constitute the next 3 chapters. Finally, the sixth chapter brings out the conclusions reached in this study and the outlook for future work.

Opeyemi Ogunleye  
Bremen, December 2023

## Thesis abstract

The German Baltic Sea, including the Arkona Basin, has become a target for windfarm development. This calls for more studies on combining high-quality seismic data with geological and geotechnical soil properties as well as borehole geophysical data in the Arkona Basin. However, the geological setting of the basin is complex, and thus ground models need to be accurate. In addition to the inevitable disturbance of the seabed during drilling operations, which is a source of inaccuracy in measurements, Cone Penetration Test (CPT) data and sediment cores are limited to 1D domain and upper few 10s of meters below the seafloor. Consequently, there is a need to cost-effectively use extant geophysical and geotechnical data for predicting CPT parameters between and beyond drilled points.

Thus, this research focuses on the southern Arkona Basin and aims to: (1) establish the stratigraphic and structural framework of shallow geological formations in the area using qualitative and quantitative seismic attributes, and also reveal the Late Cretaceous to Holocene evolution in the area; (2) evaluate the prediction of CPT data from ultra-high-resolution seismic reflection data in the study area, and show the interface-related and layer-based seismic attributes that can be used for such predictions; (3) establish the statistical boundary conditions of small strain physical properties of geological formations, and show how they can be used in seismic inversion; and (4) assess two impedance inversion approaches using stationary wavelets within the near-surface interval in the study area. The comprehensive database consists of 7 km<sup>2</sup> of 3D ultra-high-resolution seismic data, 133 km 2D ultra-high-resolution seismic profiles, and sediment descriptions from 16 out of 17 available boreholes. In addition, 6 downhole logs of Primary (P) and Shear (S) wave velocity, and CPT data at 14 locations are available.

The study presents the seismic units and their lithologic characterization in the area, and also reveals the stratigraphic and structural architecture of the shallow sub-seafloor. Following the Late Cretaceous inversion that folded the Cretaceous interval, two regimes of Tertiary extension formed normal faults in the chalk, and Quaternary glaciotectonic processes further deformed the bedrock. The glaciogenic geological units deposited in the Pleistocene were partly eroded and deformed by glacial processes, with tunnel valleys, sculptured s-forms, ridges, permafrost structures and late-stage glaciofluvial channel(s) being left as glacial imprints and buried landforms

in the southern Arkona Basin. An erosional s-form, observed in the sedimentary record and imaged by the 3D seismic data, indicates a northeast to southwest local Weichselian ice flow direction. A conceptual model for the evolutionary changes in the area from the Late Cretaceous to Holocene is shown herein.

Moreover, this study shows that there is a qualitative correlation between spatial changes in interface-related seismic attributes and variations in normalized Soil Behavior Type (SBT<sub>n</sub>). Variations in acoustic impedance equally correspond to changes in lithology and CPT measurements. Based on ground truths, relatively precise physical property values have been derived for the Cretaceous chalk, till-dominated valley fill and unchannelized till as well as the soft post-glacial sediment cover, and these values correlate with seismic facies, structural deformation and geotechnical parameters.

Furthermore, the research indicates that absolute acoustic impedance sections tied with borehole sediment descriptions exhibit the vertical stacking, lateral extent and structural configuration of lithologic units as well as lines of weakness representing fissures in glacially influenced terrains - our study area being an example. Additionally, the research shows that absolute acoustic impedance reveals intra-unit lithologic changes and the associated property boundary that are not clearly observable on seismic amplitude sections. At a CPT site in our study, acoustic impedance values predicted by a seismic inversion approach vary simultaneously with measured cone resistance and sleeve friction across lithologic boundaries. The impedance values highly correlate with the CPT parameters in quantitative terms. The two seismic inversion approaches used in this research are based on stationary wavelets, and they produce meaningful absolute acoustic impedance anomalies which correlate with ground truths.

The stratigraphic and structural architecture revealed from interface-related seismic attributes in this study are important for ground modeling purposes in the southern Arkona Basin. The outcomes of the study indicate the importance of 3D seismic data for accurate subsurface modeling, and the significance of seismic stratigraphy and geological evolution for facies prediction and sediment correlation. A quantitative seismic tool that can be used to further resolve geological complexity in a glacially influenced terrain has been revealed. Moreover, the study significantly contributes to the emerging topic of CPT data prediction from ultra-high-resolution seismic data by

showing that acoustic impedance is a layer-based seismic attribute that can be used for such CPT data predictions. However, the prediction should be guided by composite interface-related seismic attributes consisting of trace envelope, instantaneous frequency and lateral continuity of reflectors. Besides, the summary statistical estimates established as boundary conditions in this research can serve as the basis of generating initial low-frequency model in a seismic inversion scheme where there are no borehole geophysical data on the seismic profile of interest in the southern Arkona Basin. Finally, assessing the two impedance inversion approaches used in this study reveals some factors that might impact the impedance values predicted with genetic algorithms.

## Zusammenfassung

Der Ausbau von Windkraftanlagen wird in der deutschen Ostsee und insbesondere im Arkonabecken vorangetrieben. Daher sind weitere Studien zur Kombination hochwertiger seismischer Daten mit geologischen und geotechnischen Bodeneigenschaften sowie geophysikalischen Bohrlochdaten im Arkonabecken erforderlich. Die geologische Situation des Beckens sind jedoch komplex und so müssen die Untergrundmodelle genau sein. Zusätzlich zu den unvermeidlichen Störungen des Meeresbodens während der Bohrungen, die eine Quelle für ungenaue Messungen sind, beschränken sich die Daten von Drucksondierungen (im Englischen: cone penetration tests: CPT) und Sedimentkernen auf den eindimensionale Informationen in die oberen Zehner Metern unter dem Meeresboden. Daher besteht die Notwendigkeit, vorhandene geophysikalische und geotechnische Daten kosteneffizient für die Vorhersage von CPT-Parametern zwischen und über die gebohrten Punkte hinaus zu nutzen.

Daher konzentriert sich diese Forschungsarbeit auf das südliche Arkona-Becken und hat folgende Ziele: (1) die stratigraphischen und strukturellen Rahmenbedingungen der oberflächennahen geologischen Formationen in diesem Gebiet mit Hilfe qualitativer und quantitativer seismischer Attribute festzulegen und die Entwicklung von der späten Kreide bis zum Holozän in diesem Gebiet aufzuzeigen; (2) die Vorhersage von CPT-Daten aus ultra-hochauflösenden seismischen Reflexionsdaten im Untersuchungsgebiet zu bewerten und die damit verbundenen grenzflächenbezogenen und schichtbasierten seismischen Attribute aufzuzeigen, die für derartige Vorhersagen genutzt werden können; (3) die statistischen Randbedingungen der physikalischen Eigenschaften bei geringen Dehnungsraten der geologischen Formationen festzulegen und aufzuzeigen, wie sie bei der seismischen Inversion verwendet werden können; und (4) zwei Impedanzinversionsansätze unter Verwendung stationärer Wavelets im oberflächennahen Intervall des Untersuchungsgebiets zu bewerten. Die umfassende Datenbank besteht aus einem 3D-ultrahochauflösenden seismischen Datensatz von 7 km<sup>2</sup>, 133 km 2D-ultrahochauflösenden seismischen Profilen und Sedimentbeschreibungen von 16 der 17 verfügbaren Bohrlöcher. Darüber hinaus sind 6 Bohrlochprotokolle der Primär- (P) und Scherwellengeschwindigkeit (S) sowie CPT-Daten an 14 Standorten verfügbar.

In der ersten Arbeit werden die seismischen Einheiten und ihre lithologische Charakterisierung in diesem Gebiet vorgestellt und die stratigraphische und strukturelle Architektur des flachen Unterwasserbodens aufgezeigt. Nach der spätkreidezeitlichen Inversion, die das Kreide-Intervall faltete, zwei Phasen von tertiäre Extension Abschiebungen in der Kreide-Einheit bildeten. Glaziale Prozesse im Quartär deformierten das Grundgestein weiter. Die im Pleistozän abgelagerten glazialen geologischen Einheiten wurden teilweise durch glaziale Prozesse erodiert und verformt. Tunnel-Täler, skulptierte S-Formen, Grate, Permafroststrukturen und spätstadielle glazifluviale Kanäle blieben als glaziale Abdrücke und begrabenene Landformen im südlichen Arkona-Becken zurück. Ein erosive S-Form, die im sedimentären Archiv durch die 3D-Seismikdaten abgebildet wurde, deutet auf eine Nordost-Südwestliche lokale Eisflussrichtung während der Weichsel hin. Ein konzeptionelles Modell für die evolutionären Veränderungen in diesem Gebiet von der späten Kreidezeit bis zum Holozän wird hierin dargestellt.

Darüber hinaus zeigt diese Forschung, dass es eine qualitative Korrelation zwischen räumlichen Veränderungen von grenzflächenbezogenen seismischen Attributen und Variationen im normalisierten Soil Behavior Type (SBT<sub>n</sub>) gibt. Variationen in der akustischen Impedanz entsprechen Veränderungen in der Lithologie und CPT-Messungen. Auf der Grundlage von direkten Messungen wurden relativ genaue physikalische Eigenschaften der Kreidegestein, der von Geschiebelehm dominierten Talfüllungen und der nicht-kanalisierten Geschiebelehme sowie der weichen postglaziale Sedimente abgeleitet. Diese physikalischen Eigenschaftswerte korrelieren mit seismischen Fazies, struktureller Verformung und geotechnischen Parametern.

Darüber hinaus weist die Forschung darauf hin, dass Absolutwerte der akustischen Impedanz, in Verbindung mit Beschreibungen von Bohrlochsedimenten, die vertikale Stapelung, laterale Ausdehnung und strukturelle Konfiguration von lithologischen Einheiten sowie Linien der Schwäche, die Spalten in glazial beeinflussten Gebieten repräsentieren - unser Untersuchungsgebiet ist ein Beispiel dafür. Zusätzlich zeigt die Forschung, dass absolute akustische Impedanz intraeinheitliche lithologische Veränderungen und die zugehörige Eigenschaftsgrenze offenbart, die auf seismischen Amplitudensektionen nicht deutlich erkennbar sind. An einer CPT-Stelle in unserer Studie variieren die von einem seismischen Inversionsansatz vorhergesagten akustischen Impedanzwerte gleichzeitig mit gemessenen

Kegelwiderstands- und Hülsenreibungsdaten über lithologische Grenzen hinweg. Die Impedanzwerte korrelieren quantitativ stark mit den CPT-Parametern. Die beiden in dieser Forschung verwendeten seismischen Inversionsansätze basieren auf stationären Wavelets und erzeugen sinnvolle absolute akustische Impedanzanomalien, die mit direkten Messungen korrelieren.

Die in dieser Studie aufgedeckte stratigraphische und strukturelle Architektur, die auf grenzflächenbezogenen seismischen Attributen basiert, ist von Bedeutung für Modellierungszwecke im südlichen Arkona-Becken. Die Ergebnisse der Studie weisen auf die Wichtigkeit von 3D-Seismikdaten für eine präzise Untergrundmodellierung hin sowie auf die Bedeutung der seismischen Stratigraphie und geologischen Entwicklung für die Vorhersage von Fazies und die Korrelation von Sedimenten. Ein quantitatives seismisches Werkzeug, das dazu verwendet werden kann, die geologische Komplexität in einem glazial beeinflussten Gelände weiter aufzulösen, wurde aufgezeigt. Darüber hinaus trägt die Studie erheblich zum aufkommenden Thema der CPT-Datenprädiktion aus ultra-hochauflösenden seismischen Daten bei, indem sie zeigt, dass die akustische Impedanz ein schichtbasiertes seismisches Attribut ist, das für solche CPT-Datenprädiktionen verwendet werden kann. Allerdings sollte die Vorhersage durch zusammengesetzte, grenzflächenbezogene seismische Attribute, bestehend aus Spurenumschließung, Momentanfrequenz und lateraler Kontinuität von Reflektoren, geleitet werden. Darüber hinaus können die im Rahmen dieser Forschung festgelegten Zusammenfassungen statistischer Schätzungen als Grundlage dienen, um ein anfängliches Modell mit niedriger Frequenz in einem seismischen Inversionsansatz zu generieren, wenn auf dem interessierenden seismischen Profil im südlichen Arkona-Becken keine geophysikalischen Bohrlochdaten vorhanden sind. Abschließend zeigt die Bewertung der beiden Impedanzinversionsansätze, die in dieser Studie verwendet wurden, einige Faktoren auf, die die mit genetischen Algorithmen vorhergesagten Impedanzwerte beeinflussen könnten.

# Chapter 1

## Introduction

### 1.1 Motivation and objectives

Conditions at sea/ocean offer a huge source of wind energy to be harnessed for generating electricity. Offshore winds tend to flow at higher speeds than onshore winds, thereby making offshore turbines generate more electricity (Bilgili et al., 2011). As the renewable energy industry is experiencing increased activities in its offshore wind energy sector in Europe as shown by the growth in cumulative installed capacity of offshore wind farms (fig. 1.1), site investigation campaigns are now shifting into more complex geological settings and deeper water (Vardy et al., 2018).

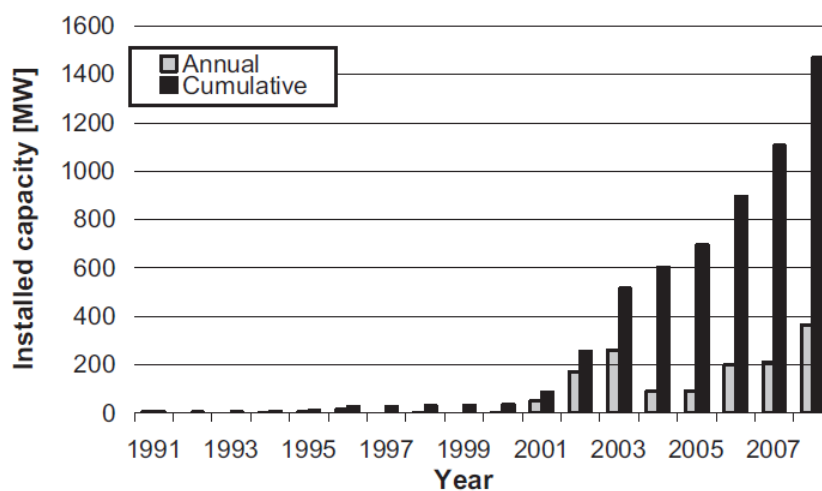


**Fig. 1.1: Trend in the development of offshore wind power in the EU between 1991 and 2008. Notice the growth in cumulative installed capacity over the years examined (adapted from Bilgili et al., 2011)**

Traditionally, offshore site investigations for foundation purposes involve stratigraphic correlation of sediment cores, downhole velocity logs and cone penetration test (CPT) data to seismic facies. In the early phase of such investigations, it is imperative to use geophysical surveys to gain a full understanding of spatial variability of geological structures (faults, fissures, folds, unconformities, etc.) and sediment properties. In a later phase of site investigation, geotechnical surveys are carried out in order to determine the engineering properties of target soils. Data from geotechnical surveys are integrated with the results of geophysical survey to obtain an improved geological model (e.g. Sauvin et al., 2018).

However, a contemporaneous increase in financial costs on the global economic scene accompanies recent expansion and growth in offshore windfarm construction and investments. This dictates the need for a cost-effective way to characterize the subsurface in great detail and simultaneously reduce risks during different phases of offshore site investigation. Therefore, an in-depth understanding of geological complexity in the shallow seabed has become a necessity for ground modeling (Emery et al., 2019).

Furthermore, geotechnical ground truth data consisting of CPT measurements and sediment cores are limited to upper few 10s of meters into the subsurface (e.g. Coughlan et al., 2017). The accuracy of downhole CPT measurements is affected by inevitable disturbance of seabed soil during drilling operations (Lu et al., 2020). The 1D nature of CPT data and sediment cores means that dependable and accurate geotechnical information would also be needed in areas between and beyond drilled points to account for differences between ground investigation and infrastructure locations caused by micro-siting. Consequently, there is an urgent need for an integrated approach of site investigation that would not only fill these gaps but also allow full use of extant geophysical and geotechnical data.

Global trends in the investigation of shallow subsurface has shown the potential of using high-resolution seismic reflection techniques to image sub-seafloor geology for early-phase and later-phase applications in offshore site investigations. These techniques involve the use of qualitative (e.g. amplitude, reflector continuity, configuration, frequency, etc) and quantitative (e.g. acoustic impedance, density, etc) seismic attributes to characterize the subsurface in detail, unravelling not only its geological architecture, structure and history, but also the spatial variability of its lithologic properties (e.g. Obst et al., 2017; Vardy et al., 2018; Prins and Andresen, 2021; Wenau et al., 2022). Based on the possibility of acquiring seismic reflection data in continuous 2D and 3D configurations, one of the quantitative seismic attributes - acoustic impedance - has been portrayed as having the potential to serve as a predictor of geotechnical data not only at depths beyond the uppermost 10s of meters (i.e. beyond the reach of conventional CPT profiling and coring in site investigations), but also in inter- and extra-borehole locations. Different seismic inversion techniques are being used to transform seismic waveforms connected with reflection coefficients at interfaces to unit-related attributes such as acoustic impedance and density (Avseth et al., 2005). Some seismic inversion approaches geared towards generating acoustic

impedance are applied to full stacks of seismic reflection data, and they are termed post-stack impedance inversion approaches.

This current doctoral project forms an integral part of a parent project called SynCore, the overarching objective of which is to make seismic inversion and related methods practically usable for site investigation in offshore wind energy industry, giving stakeholders an optimal knowledge of offshore ground conditions and maximum flexibility in the planning process. SynCore focuses on the North and Baltic Seas, and its specific goals are to:

- (1) Further develop and extend seismic acquisition and processing methods for seismic inversion
- (2) Integrate and calibrate geotechnical data
- (3) Develop an integrated and comprehensive geostatistical model of the subsurface in the offshore planning area, with the ability to generate synthetic design profiles.
- (4) Apply stochastic methods in foundation design, considering the scattering properties of the design models predicted from the spatial subsurface model.

Since Arkona Basin - a part of the southern Baltic Sea - is receiving increased attention in the offshore wind energy industry in Europe, this doctoral research focuses on the shallow seabed or near-surface interval in the southern section of the basin as a case study for glacially influenced terrains. The primary scientific objectives of this specific research in the southern Arkona Basin are to:

- (1) Investigate the stratigraphic and structural features of the Cretaceous to Holocene succession using qualitative and quantitative seismic attributes (Chapters 3 and 5)

We seek to establish the detailed geological framework and history of shallow seabed in the southern Arkona Basin primarily using 2D and 3D ultra-high-resolution seismic reflection data. Aside from the Late Cretaceous inversion which folded bedrock chalk, Tertiary extensional event faulted existing sedimentary strata in the southern Baltic Sea (Al Hseinat and Hübscher, 2017). Therefore, this current work aims to use seismic amplitude sections to investigate and characterize the regimes and products of this extensional event in the southern Arkona Basin.

On the basis of analog single-channel seismic reflection data in the Arkona Basin, Flodén et al. (1997) reported three generations of glacial valleys incised into the Cretaceous bedrock during Quaternary glaciations. In this thesis, we use conventional ultra-high-resolution multi-channel seismic reflection data to investigate the formation

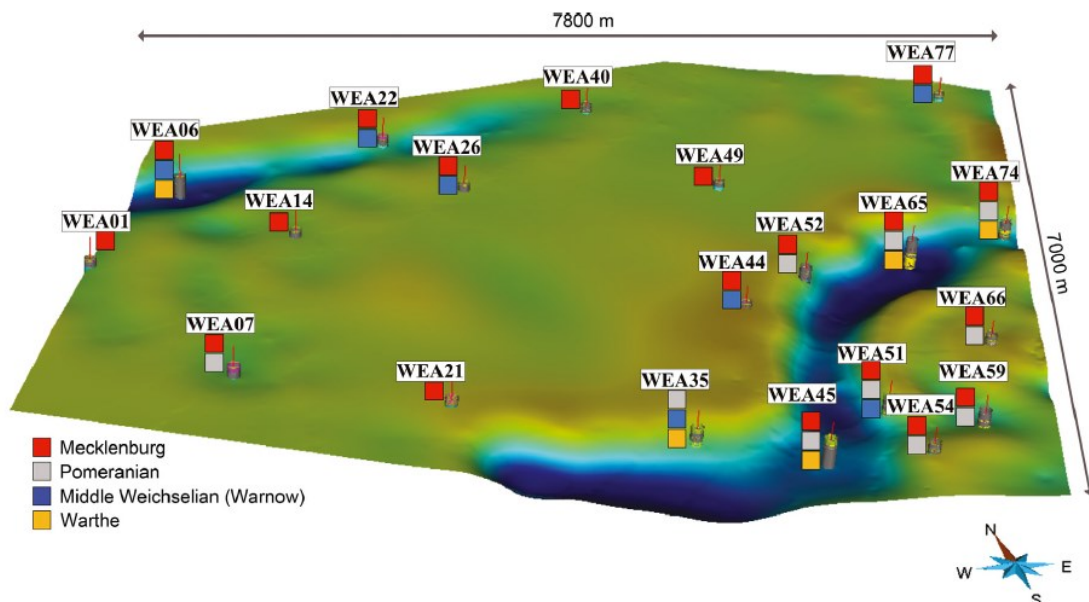


**Fig. 1.2: Sedimentary evidences of Saalian and Weichselian glaciations in the southeastern margin of Arkona Basin based on different Pleistocene glacial till units penetrated in well cores. Saalian Warthe till was only found within channels in the area. Middle Weichselian tills belonging to an unknown glacier advance and the Warnow advance have been preserved locally. Pomeranian till is limited to the southeastern part of the area shown, while the till of the Mecklenburg advance can be found in all boreholes (Obst et al., 2017)**

mechanism, number of generations and sedimentary infills of these valleys. Since Saalian and Weichselian glaciations have been recorded along the southeastern margin of the Arkona Basin in an area which overlaps with the working area of this thesis (e.g. fig. 1.2; Obst et al., 2017), this current study searches for and examines buried erosional structures and topographic landforms as well as possible permafrost features left as imprints by Pleistocene glacier(s). The approach includes using 3D seismic data to decipher a probable local ice flow direction during the Weichselian glacier advance.

Past authors have documented land evidences of glaciotectonic deformation of Cretaceous chalk and glaciogenic sediments in the coastal regions of the Baltic Sea including the Jasmund Peninsula (e.g. Gehrman et al., 2017; Gehrman and Harding, 2018). Around a neighbouring Kossau valley in the Bay of Kiel, Al Hseinat and Hübscher (2014) also reported glaciotectonic folding of Tertiary sediments during the Quaternary. Consequently, this current research uses seismic-based evidences to understand the structural impacts of Quaternary glacial deformation on the Cretaceous

chalk and glacially deposited sediments in the southern Arkona Basin, thereby contributing to a regional understanding of the glaciotectonic phenomenon.

Thus, given the complexity of geological processes that have affected this terrain, it is important to build a novel conceptual model that summarizes the Late Cretaceous to Holocene evolution in the part of the study area covered by 3D seismic data. Besides, for the purpose of building ground models, we aim to bring to the fore the roles of seismic stratigraphy and depositional history in facies prediction and sediment correlation in the southern Arkona Basin.

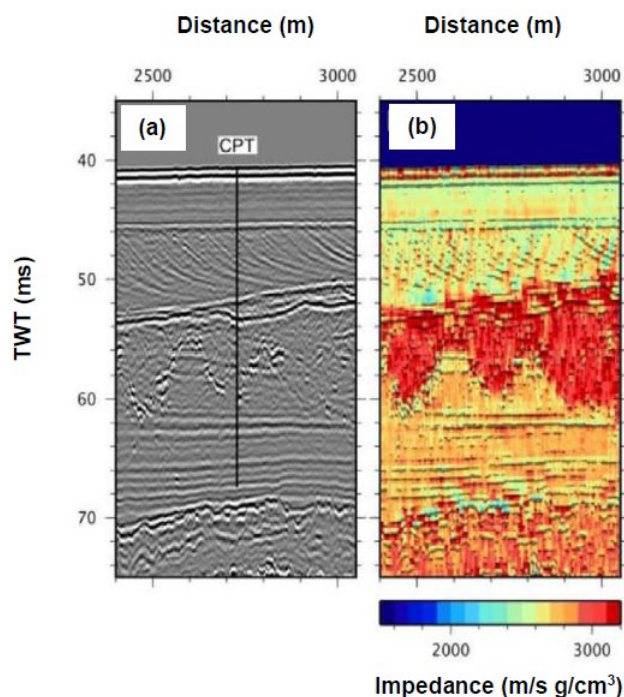


**Fig. 1.3: Result of inverting a single-channel boomer data (a) to yield acoustic impedance (b) in Walney I windfarm site. Notice the similarity in stratigraphic and structural details contained in the seismic amplitude and impedance sections, and the varying intra-unit property values in the latter section (modified from Vardy et al., 2018)**

Furthermore, Vardy et al. (2018) inverted a section of single-channel boomer data from the Walney I windfarm site in the Eastern Irish Sea. The resultant acoustic impedance section showed impedance values that varied within each stratigraphic unit, with the structural configuration of the units been well-defined on the impedance section (fig. 1.3). Thus, it is imperative for us to invert our multi-channel seismic data to yield a quantitative layer-based elastic attribute - absolute acoustic impedance - of geological units. This attribute would help to further resolve stratigraphic and structural

complexity and delineate heterogeneity that might not be clearly evident on seismic amplitude sections in our study area. Performing seismic inversion could demonstrate the use of absolute acoustic impedance as a reliable indicator of lithologic variations in a glacially influenced terrain.

- (2) Assess geotechnical data prediction from seismic reflection data and delineate interface- and layer-related seismic attributes for the prediction (Chapters 4 and 5)

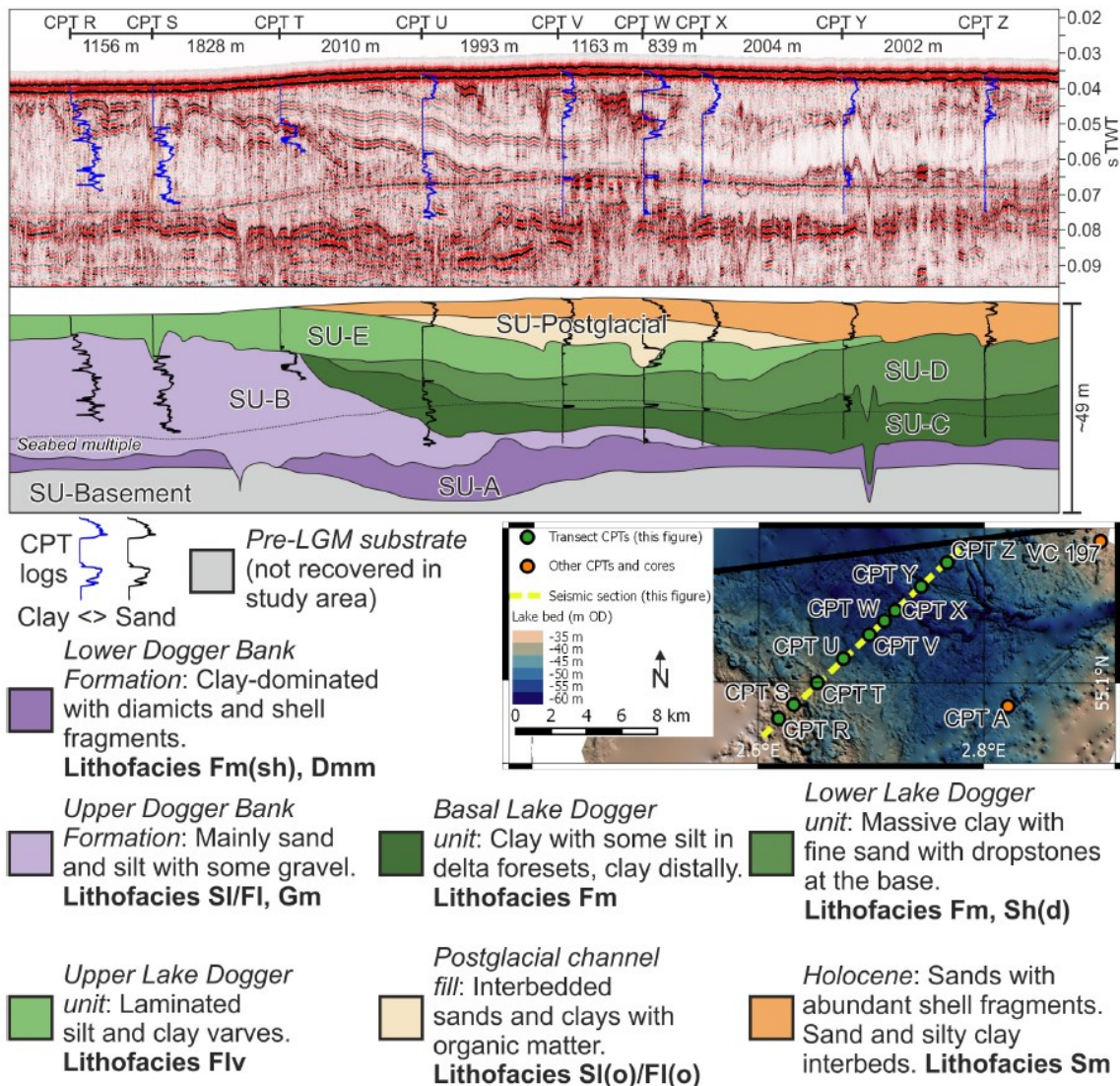


**Fig. 1.4:** Transverse section through CPT locations depicting correlation between lithofacies, their CPT profile characteristics, and seismic facies in Dogger Bank, North Sea. Major changes in the CPT logs correspond to significant changes in seismic attributes of formations (Emery et al., 2019)

Integration of geophysical and geotechnical data with geological interpretation has been carried out at different places and scales across the globe (e.g. Prins and Andresen, 2021), particularly in areas (e.g. North Sea) with a long history of offshore site investigations. Sauvin et al. (2018) reported an integrated study which entailed tying CPT tip resistance to multi-channel seismic reflection data (vertical and horizontal resolution of 2 and 4 m) at Borssele site in the Southern Bight (North Sea). Besides, the paleogeographic evolution of southeastern Dogger Bank (North Sea) has been examined using seismic reflection data (maximum vertical resolution of 1-3 m)

integrated with CPT logs and sediment cores (Emery et al., 2019). In the data published for the aforementioned studies, major changes in the seismic character of geological units correspond to drastic variations in the CPT measurements, which might indicate that there is a relationship between seismic attributes and CPT data in the North Sea (e.g. fig. 1.4). However, the southern Arkona Basin (Baltic Sea) has only received significant interest from offshore wind energy industry recently, and this could account for the paucity of publications that have addressed the relationship between CPT data and ultra-high-resolution seismic data in the area. Since the trend of development in the offshore wind energy industry is to predict CPT data from seismic reflection data (e.g. through the machine learning approach of Sauvin et al., 2019), it is imperative to integrate available geological, geophysical and geotechnical data - similar to those used in the North Sea - in the southern Arkona Basin to answer the following pertinent scientific questions which hitherto have not been sufficiently addressed in publications in the region: (1) Do CPT profile changes correspond to variations in physical property and seismic attribute shown on ultra-high-resolution seismic reflection data (vertical resolution 1-1.5 m) in the southern Arkona Basin? (2) If yes to '1,' how does seismic facies imaged on the ultra-high-resolution seismic data vary spatially in relation to normalized Soil Behavior Type within seismo-stratigraphic units? (3) Partly based on the answer to '2,' which interface-related and layer-based seismic attributes can be used for predicting CPT profiles from seismic data in the southern Arkona Basin and how can they be used? (4) Based on the answer to '3,' is there a statistical correlation between acoustic attribute(s) and CPT parameters, and what factor(s) should be considered for reliable prediction of geotechnical data from seismic data? One or more attribute(s) might be established as an indicator of geotechnical variations.

(3) Establish and evaluate statistical boundary conditions of small strain physical properties of geological units – their implication for initial model building during seismic inversion (Chapter 4)

Traditionally, in the oil and gas industry where seismic inversion has been intensely used, initial models are generated by extrapolating inversion parameters observed from boreholes along the interfaces picked on seismic section (Sun et al., 2022). However, Vardy et al. (2015) recently published a basic flow chart for inverting very-high-resolution seismic reflection data for acoustic impedance using a genetic algorithm (fig. 1.5). The work flow begins by randomly generating starting impedance

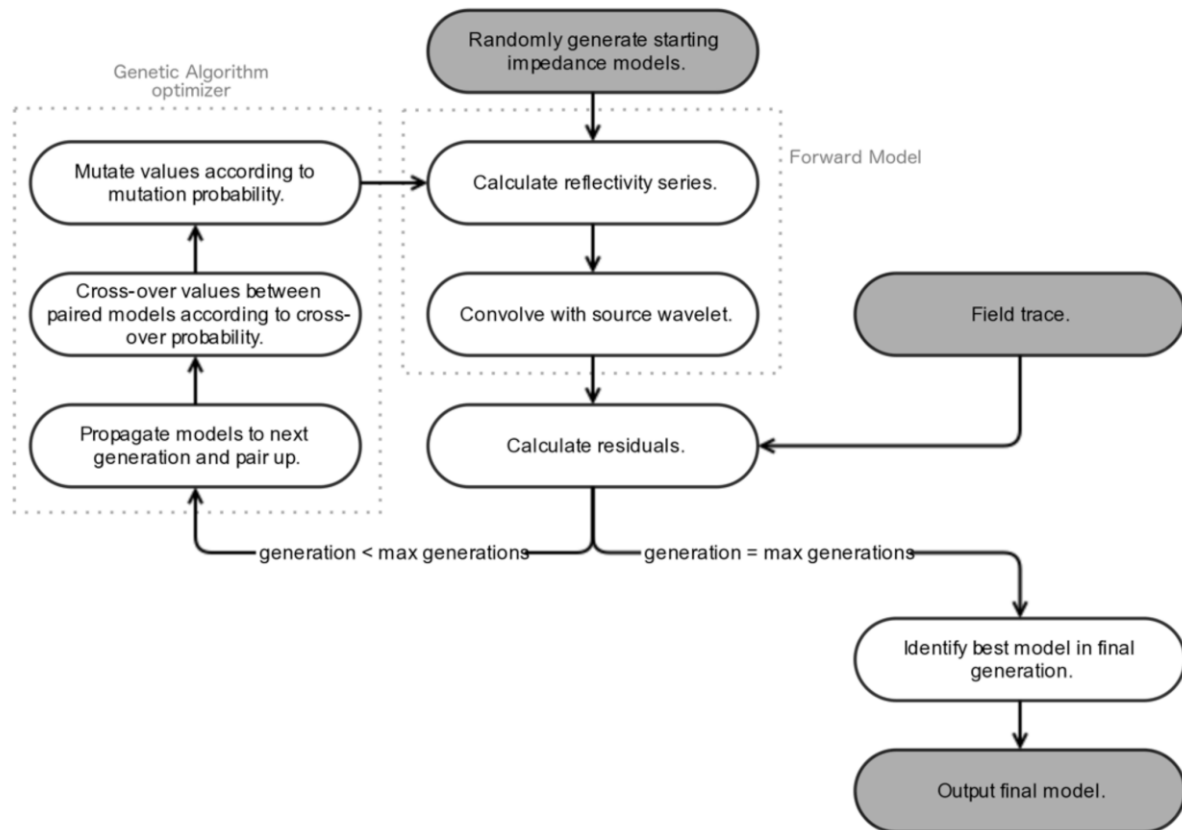


**Fig. 1.5: Fundamental processes of a genetic algorithm for carrying out post-stack acoustic impedance inversion as shown by Vardy et al. (2015). The algorithm begins with random generation of initial impedance models.**

models. However, since small strain physical properties (e.g. Poisson's ratio, small strain shear and Young's moduli, and acoustic impedance) characterize subsurface geological units, and they can be quantified from downhole velocity logs, it would be useful to investigate the use of summarized statistical estimates of these physical properties (not their random values) as initial model constraints in acoustic impedance inversion of ultra-high-resolution seismic data in the southern Arkona Basin. This might be appropriate in a scenario where no acoustic borehole measurements are available on the seismic profile of interest. In this thesis, it would mean determining the statistical estimates of physical properties for previously defined seismic units and sub-units based on a compilation of velocity logs in the southern Arkona Basin, evaluating the estimates from a geological interpretation perspective, and proposing how to use them in absolute acoustic impedance inversion.

#### (4) Assess two near-surface impedance inversion approaches using stationary wavelets (Chapter 5)

Prior to this thesis, research on seismic inversion in the southern Baltic Sea has not been sufficiently published in journals. This thesis would be one of the first studies to

show near-surface impedance inversion of ultra-high-resolution seismic data in the southern Arkona Basin. Herein, two approaches of post-stack acoustic impedance inversion using stationary wavelets would be implemented and evaluated. The two approaches would utilize the seismic inversion method proposed by Vardy (2015). One of these approaches would use the minimum and maximum values of acoustic impedance estimated from velocity logs to determine an initially random set of impedance models. However, following a concept previously proposed in this thesis, the other inversion scheme would incorporate an initial low-frequency model deduced from the combination of seismic horizons and median values of impedance estimated for each seismic unit from velocity logs. The efficacy of this latter approach would be tested where there are no acoustic borehole measurements on a seismic profile. Therefore, the two acoustic impedance inversion approaches would be compared based on their products and the following questions would be considered in this part of the thesis: (1) What differences exist between the predicted impedance sections produced by the two different approaches? (2) What could be the reason(s) for the possible differences? (3) How can these approaches be improved in future work?

## **1.2 State-of-the-art: integration of geological, geophysical and geotechnical data**

### **1.2.1 Stratigraphic and structural seismic techniques**

Derivatives of a seismic measurement are termed attributes. The fundamental attributes in seismic data include time, amplitude and frequency. Generally, time-derived attributes indicate structural configuration of geological formations, whereas attributes derived from amplitude provide information about stratigraphy, lithological properties and fluid content (Brown, 2004). Frequency-derived attributes might also be related to stratigraphy and lithological properties; for instance anomalously high instantaneous frequency has been correlated with high sand content in some depositional settings.

Amplitude is perhaps the most widely used fundamental seismic attribute. During acquisition of seismic data, amplitude is mostly affected by the following factors: (1) spherical divergence due to geometrical spreading of seismic energy; (2) laterally discontinuous high impedance body that reduces the amount of energy reaching the underlying strata; (3) tuning effect in areas of geological thinning (for instance, around

angular unconformities and stratigraphic pinch-outs); and (4) angle of incidence, the effects of which depends on combined rock and pore-fluid properties (Henry, 2004).

Seismic processing steps may also significantly affect the amplitudes observed in seismic data. These steps include: (1) migration of seismic reflection amplitudes to their proper subsurface positions; (2) stacking or summation of traces within a common depth point (CDP) gather after normal move-out (NMO) correction; (3) velocity analysis, the product of which affects the alignment of amplitudes during NMO correction prior to stacking; and (4) deconvolution - a step that requires a minimum phase wavelet to achieve stable results (Henry, 2004).

### 1.2.1.1 Qualitative seismic interpretation integrated with lithologic description and CPT data

A seismic amplitude section shows interface-related seismic attributes of geological strata. Its qualitative interpretation involves dividing it into mappable packages of seismic reflectors, the specific parameters (e.g. configuration and external shape, continuity, amplitude, frequency and interval velocity) of which differ from those of contiguous packages. Each of these mappable packages is termed a seismic unit. Its characteristic reflector parameters allow for an interpretation of depositional environment, energy of the depositing medium, and possible lithofacies of the corresponding geological strata (Mitchum et al. 1977). The possible geological interpretations that can be made from reflector parameters of a seismic unit are shown

**Table 1.1: Possible geological interpretation from reflector parameters in a seismic unit (modified from Mitchum et al., 1977)**

Reflector parameter	Geological interpretation
<b>Configuration</b>	<ul style="list-style-type: none"> <li>• Bedding patterns</li> <li>• Depositional properties</li> <li>• Erosion and paleo-topography</li> <li>• Fluid contacts</li> </ul>
<b>Continuity</b>	<ul style="list-style-type: none"> <li>• Lateral continuity of strata</li> <li>• Depositional processes</li> </ul>
<b>Amplitude</b>	<ul style="list-style-type: none"> <li>• Velocity and density contrasts of individual interfaces</li> <li>• Bed spacing</li> <li>• Bed thickness</li> </ul>
<b>Frequency</b>	<ul style="list-style-type: none"> <li>• Bed thickness</li> <li>• Fluid content</li> </ul>
<b>Interval velocity</b>	<ul style="list-style-type: none"> <li>• Lithofacies estimations</li> <li>• Porosity estimations</li> <li>• Fluid content</li> </ul>

in table 1.1. A case study demonstrating the relationship between seismic attributes and lithofacies in a glacially influenced area is the work of Obst et al. (2017) who related features of seismic units with their corresponding lithology along the southeastern margin of the Arkona Basin (table 1.2).

**Table 1.2: Case study of lithologic interpretation of seismic attributes in an area that overlaps with our working area in the Arkona Basin. The table shows major seismic units marked by reflectors and their corresponding lithologic record along the southeastern margin of the Arkona Basin (Obst et al., 2017)**

Seismic unit	Seismic features	Lithology	Main/minor reflector
A (thinning towards E)	Very low amplitude and virtually no internal reflections	Holocene mud	Sea floor = top sediments
B3	High to medium amplitude, diffuse to chaotic pattern	Till of the Mecklenburg advance (qw3)	Top of qw3 till or sea floor (if unit A is missing)
B2 (only in the SE)	Medium to low amplitude, chaotic pattern	Till of the Pomeranian advance (qw2)	<i>Within till sequence = top of qw2 till</i>
B1 (in channels)	Medium to high amplitude, chaotic and sometimes parallel patterns	Till of the Warthe advance (qs2) and glacialfluvial sediments and remnants of Mid-Weichselian advances (qw* and qw0)	<i>Within till sequence, top of qs2 till (or base of qw2 till)</i>
C2	Low to medium amplitude with parallel reflectors	Upper Maastrichtian cherty limestone	Top Cretaceous and base of cherty limestone
C1	Low to medium amplitude, sometimes parallel reflectors	Lower and upper Maastrichtian chalk	Top Cretaceous

Establishing sequences of geological strata is an integral part of qualitative seismic interpretation. This involves defining major stratigraphic units composed of relatively conformable succession of genetically related strata, which are bounded by unconformities or their correlative conformities (Mitchum, 1977). Depositional sequences can then be subdivided into smaller seismic units. Such qualitative interpretation of seismic data frequently includes not only a description of seismic facies but also structural mapping of horizons using the two-way travel-time (TWT) of seismic events as well as extraction of post-stack seismic attributes (e.g. root mean square amplitude, instantaneous frequency, coherency etc.). Time slices in 3D seismic data and time/depth structure maps derived from picking horizons help to visualize spatial variability of seismic facies and structural features. Correlation of available lithologic logs and CPT profiles to seismic facies provides detailed information about sedimentary and geotechnical properties of seismic units. This requires time-depth functions that will tie seismic amplitude data (usually in time domain) to lithologic logs and CPT measurements (in depth domain). Thus, to understand the subsurface framework and geological processes documented in an area, seismic facies succession and thickness variation within depositional sequences as well as structural configuration and termination of reflectors and lineaments as observed on seismic sections and resultant maps are integrated and interpreted.

### 1.2.1.2 Quantitative seismic technique

Seismic inversion is the prediction/derivation of quantitative information about the nature of subsurface from seismic data based on the amplitude, phase, move-out, and frequency content of recorded reflections. This usually involves an iteration in which a synthetic seismic dataset is generated from a model of the subsurface and updated based on the differences between the real and synthetic data (Tarantola, 1984). Seismic inversion as a composite quantitative technique includes analysis of Amplitude Variation with Offset, impedance inversions, and Full Waveform Inversion, among others.

Acoustic impedance inversion refer to the generation of impedance parameter from seismic waveform. This could be done either on a full stack (post-stack inversion) or partial stacks (pre-stack inversion). Post-stack seismic inversion methods can be model-based inversion, band-limited inversion, colored inversion and sparse spike inversion methods. We would use band-limited inversion to illustrate the concept of post-stack acoustic impedance inversion in this chapter.

Acoustic impedance ( $Z$ ) of a layer is the product of the medium's density ( $\rho$ ) and velocity ( $v$ ). If it is known, then an estimate of earth's reflectivity ( $r$ ) at normal incidence can be written as:

$$r_j = \frac{Z_{j+1} - Z_j}{Z_{j+1} + Z_j} \quad \text{equation 1.1}$$

$Z_j$  is the acoustic impedance of  $j^{\text{th}}$  layer and  $r_j$  is seismic reflectivity at the interface between  $j^{\text{th}}$  and  $(j + 1)^{\text{th}}$  layers. It can be shown that for multiple layers (starting with the first layer), the expression in equation 1.1 can be re-written as:

$$\ln\left(\frac{Z_{j+1}}{Z_j}\right) = \left(\sum_{k=1}^j \ln\left(\frac{1+r_k}{1-r_k}\right)\right) \approx (2 \sum_{k=1}^j r_k) \quad \text{equation 1.2}$$

For small values of  $r$ , equation 1.2 becomes:

$$Z_{j+1} = Z_1 \exp(2 \sum_{k=1}^j r_k) \quad \text{equation 1.3}$$

Modeling the seismic trace as scaled reflectivity,  $S_k = \frac{2r_k}{\gamma}$ , then equation 1.3 is transformed to:

$$Z_{j+1} = Z_1 \exp(\gamma \sum_{k=1}^j S_k) \quad \text{equation 1.4}$$

Band-limited impedance method employs equation 1.4 for the post-stack inversion of seismic trace (Waters, 1987; Ferguson and Margrave, 1996). To derive a broadband frequency spectrum of inverted results, a low-frequency model is incorporated into an inversion scheme. Usually in the oil and gas industry, the low-frequency model is built by lateral interpolation and extrapolation of geophysical property estimated from well logs at borehole locations in a manner that is guided by seismic horizons.

Evidently, acoustic impedance is a quantitative layer property (e.g. fig. 1.3). Derived from low-frequency seismic reflection data in the oil industry, its variation allows an easy interpretation of stratigraphy. With such seismic data, it is possible to link acoustic impedance to sediment properties including porosity. Consequently, it is imperative to examine whether acoustic impedance generated from ultra-high-resolution multi-channel seismic reflection data has similar potentials in the southern Arkona Basin, a terrain that has been influenced by Quaternary glaciers.

### **1.2.2 Borehole velocity log interpretation**

Caliper, natural gamma and velocity logs are routinely acquired in boreholes as geophysical data. While a caliper log is mostly used to derive information on borehole conditions and diameter, gamma ray logs are lithologic logs that respond to the natural radioactivity of geological intervals and can thus be useful for discriminating between radioactive (clay-bearing) sediments and less radioactive (sand-bearing) sediments. Generally, the higher the clay content of sediments, the higher their level of radioactivity and gamma ray readings. Thus, lithologic boundaries can be defined based on gamma ray logs.

Commonly, velocity logs consisting of primary and shear wave measurements (P-S logs) are records of the velocity of sediments acquired downhole with P-S Suspension Loggers. During data acquisition, it is a common practice to fire an energy source contained in the suspension logger when the tool is at a survey depth. The time that the energy arrives at the near and far detectors in the tool is recorded and used to calculate the P- and S-wave velocities. The velocities and the ratio between them indicate rock strength, and together with density they can be used to derive shear, bulk and Young's moduli (e.g. Robertson, 2009), impedance and Poisson's ratio.

### 1.2.3 Cone penetration test (CPT) profiles - interpretation and prediction of geotechnical data

A cone penetrometer is a tool that consists of a cone on the end of a series of rods and is pushed into the ground at a constant rate during geotechnical investigations to provide near-continuous measurements which indicate soil properties. The tool measures resistance to the penetration of the cone and of a surface sleeve. The fundamental terminology for a cone penetrometer is shown in fig. 1.6.

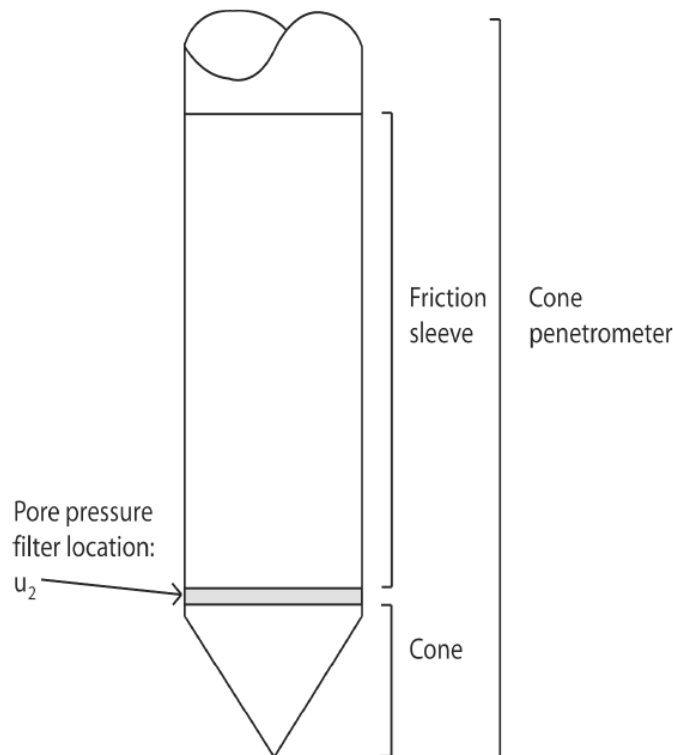


**Fig. 1.6: Basic terminology for a cone penetrometer (Robertson and Cabal, 2014)**

Today, most CPT equipment provide digital CPT results and include pore-pressure measurements (i.e. CPTu systems). Thus, CPTu data combine cone resistance ( $q_c$ ), sleeve friction ( $f_s$ ) and penetration pore pressure commonly measured behind the cone ( $u_2$ ) (Robertson, 2009). There is a need to correct cone resistance  $q_c$  to the corrected total cone resistance,  $q_t$ . However, in coarse-grained soils (i.e. sands),  $q_c$  is large relative to the water pressure, and hence  $q_t \sim q_c$ . Nevertheless, the correction is always needed in very soft fine-grained soil. An example of a CPTu profile is presented in fig. 1.7.

Soil stratigraphy and type can be determined from CPT data. This involves the use of charts that link cone parameters to soil type. A chart widely used for determining soil behavior, which works in most soils, is the normalized soil behavior type (SBTn) chart

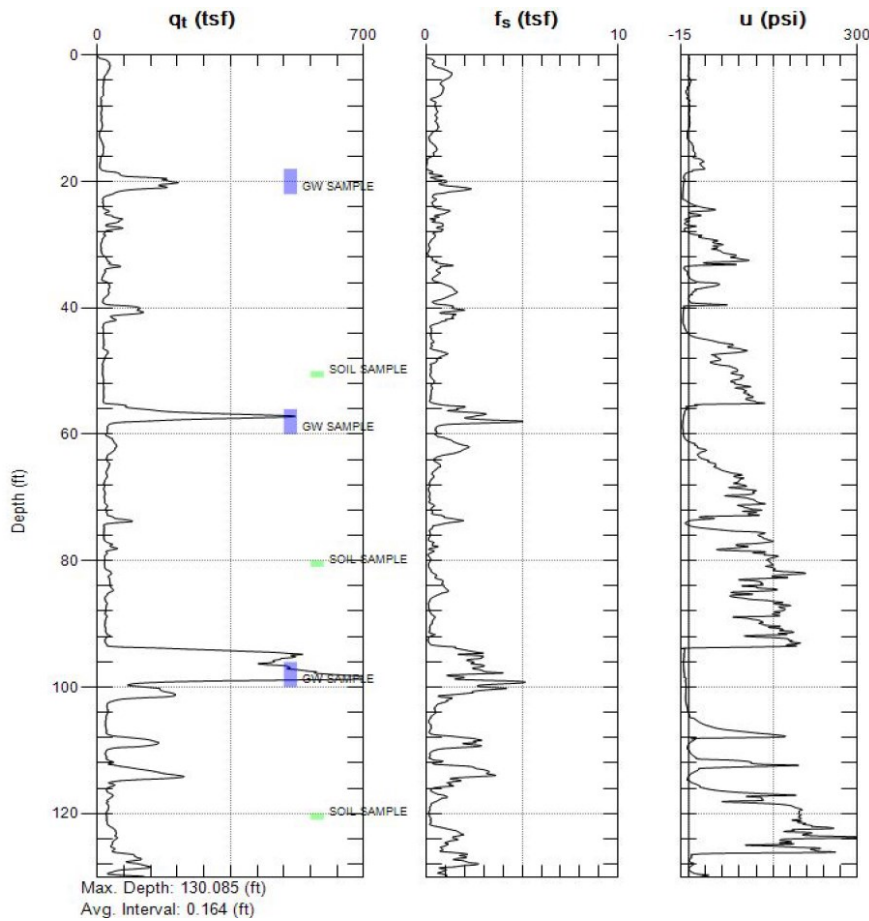


Fig. 1.7: Example of CPTu data. ( $q_t$  = corrected total cone resistance;  $f_s$  = sleeve friction;  $u$  = pore pressure; 1 tsf ~ 0.1 MPa; 14.5 psi = 100 kPa; 1 ft = 0.3048 m) (adapted from Robertson and Cabal, 2014)

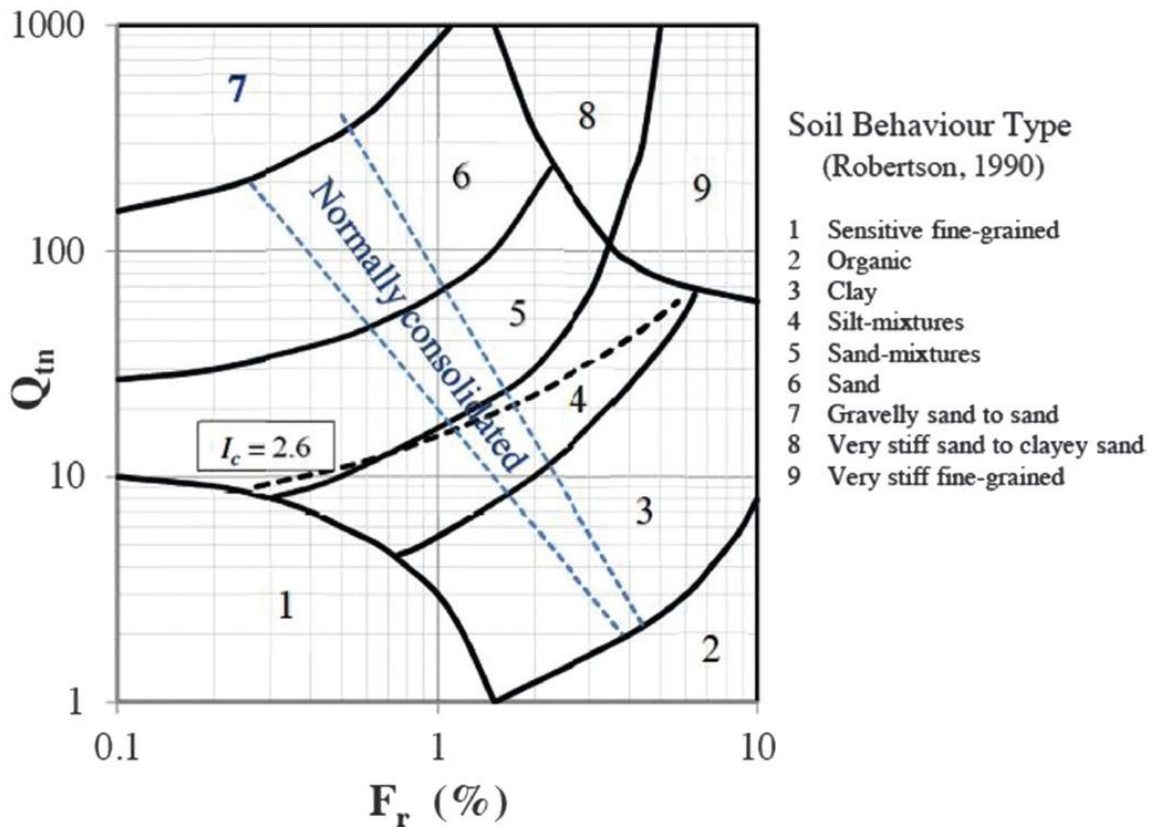
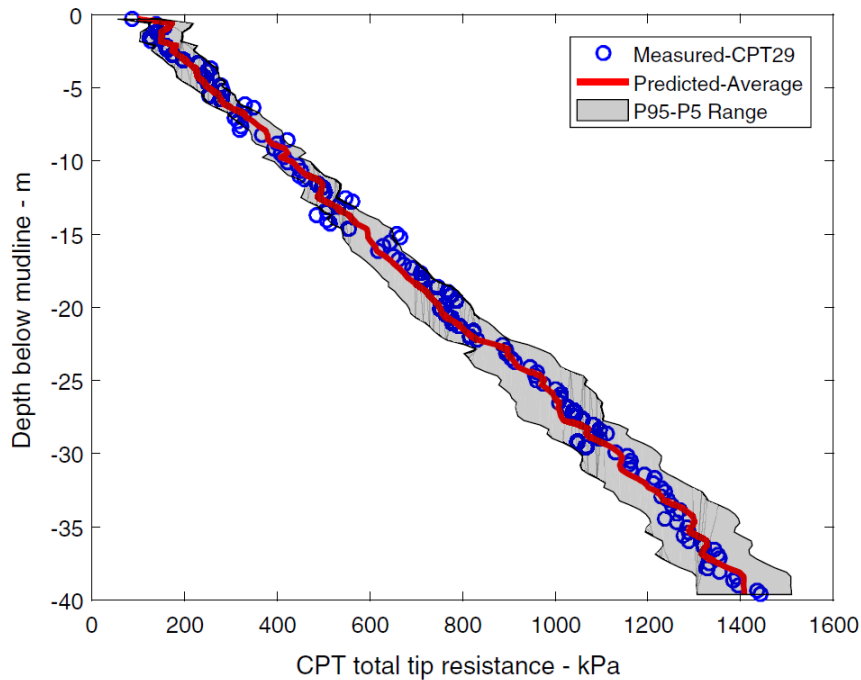


Fig. 1.8: SBTn chart proposed by Robertson (1990) and modified by Robertson (2009) for interpreting soil type from CPT data.  $Q_{tn}$  = normalized cone resistance;  $F_r$  = normalized friction ratio;  $I_c$  = soil behavior type index (adapted from Robertson, 2016)

of Robertson (1990) that was updated by Robertson (2009) (fig. 1.8). On the chart, soil type is interpreted based on the position of normalized data points. Determination of soil type helps to develop geotechnical stratigraphy which could be correlated with seismic stratigraphy to gain an understanding of the geotechnical behavior of seismic units.



**Fig. 1.9: Comparing blindly predicted and measured total tip resistance at location CPT29 in a deep-water site. The predicted tip resistance was derived from acoustic impedance (adapted from Chen et al., 2021)**

Furthermore, research about linking CPT data with acoustic impedance is gaining momentum across the globe. Chen et al. (2021) predicted CPT tip resistance using acoustic impedance derived from sub-bottom profiler data (ultrahigh-frequency >2000 Hz) in a deep-water setting. Their results showed a good correlation between predicted and measured tip resistance values during blind tests (e.g. fig. 1.9).

### 1.3 Regional geological setting

The Arkona Basin, the deepest point of which lies 48 meters below sea level, developed in the Pleistocene as a significant part of the Baltic Basin. Its boundary is delineated by the southern Swedish coast in the north, Krieger's Flak and Plantagenetgrund in the west, Pomeranian Bight in the south, and Bornholm Island in the east. The study area of this research lies in the southern section of the Arkona Basin (fig. 1.10).

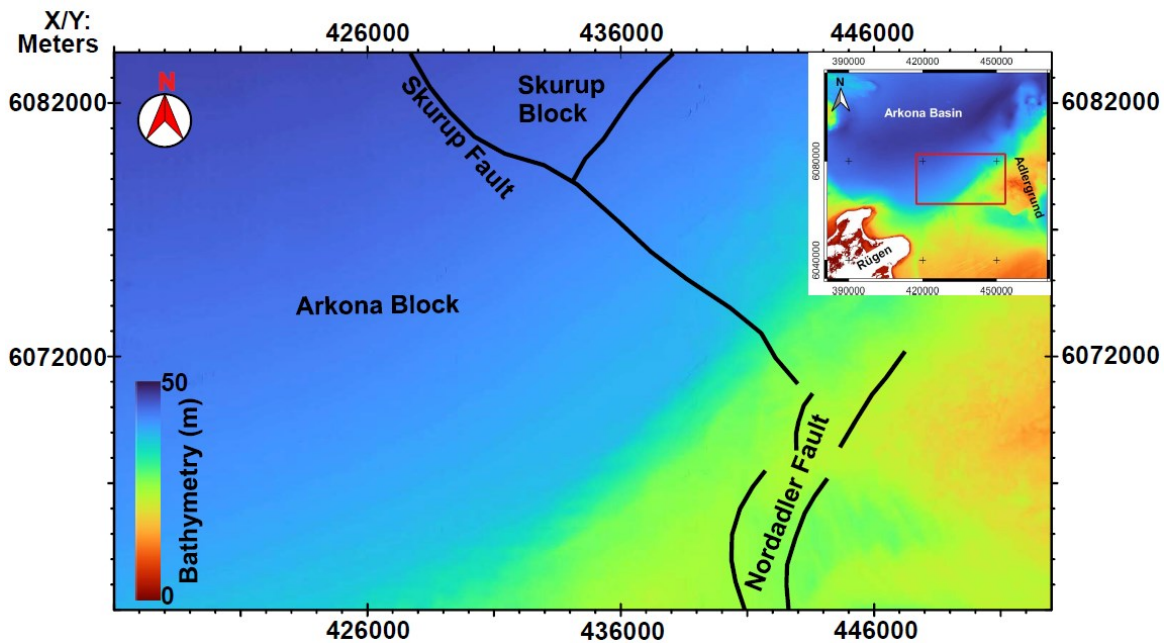


Fig. 1.10: Overview map of the study area (red outline in inset) in the southern Arkona Basin displaying the bathymetry and main pre-Quaternary faults of the Tornquist Zone (fault lines were adapted from Obst et al., 2017). EMODnet Bathymetry Consortium (2020) is the source of the water depth shown. Map coordinates are based on UTM 33N.

Faults in the Tornquist Zone dissect the basement rocks of the Arkona basin (fig. 1.10; Schlüter et al., 1997; Hübscher et al., 2019). In the region, Adler-Kamień Fault Zone (AKFZ) began evolving in the Permian. Deformation within AKFZ took place in multiple phases such that associated faults extended from the basement and cut into the Cretaceous succession (Seidel, 2019). Paleogeography of northwest Europe in Late Cretaceous showed the occurrence of marine deposits, mainly carbonates (table 1.3), in the area currently known as the Arkona Basin, with a contourite system developed in the southern section of the area. At this time, a submarine topographic high associated with Teisseyre-Tornquist Zone was contiguous to this contourite system (Hübscher et al., 2019). West of Tornquist Zone, a Late Cretaceous inversion affected the seafloor of an epeiric Chalk Sea in the Arkona Basin area. Tertiary extension faulted previously deposited strata in the southern Baltic Sea (Al Hseinat and Hübscher, 2017).

In the Arkona Basin, pre-Quaternary bedrock largely consists of Cretaceous successions of chalk and limestone (e.g. Winterhalter et al., 1981). Overlying this bedrock are glacially deposited Pleistocene sediments. In the southern Baltic Sea, the base of Quaternary interval was formed by the Scandinavian Ice Sheet during a Late Saalian advance in which the glacier eroded into the Upper Cretaceous strata,

**Table 1.3: Regional seismo-stratigraphic scheme for the study area as presented by Hübscher et al. (2019). BCU, base Cretaceous unconformity; BCG, base Chalk Group; BCA, base Campanian; BLM, base lower Maastrichtian; ILM, internal lower Maastrichtian; IUM, base internal upper Maastrichtian; BPU, base Pliocene unconformity.**

Time [Ma]	Chronostratigraphy		Seismic Units <small>(after Lykke-Andersen &amp; Surlyk, 2004)</small>		Lithostratigraphy <small>(Höllviken Well)</small>
			Sea floor		
2.58	Cenozoic	Quaternary	Unit 7		Glacial deposits
		H i a t u s			
61.6	Cenozoic	Danian	Unit 6		White chalk with interbedded clay and flint at top
66.0		Late Cretaceous	Maastrichtian	Late	
	Early			ILM	
72.1	Late Cretaceous	Campanian	BLM	Unit 3/4	White and grey limestone with marl
83.6			BCA	Unit 2	
86.3		Santonian	Unit 1	BCG	Limestone with interbedded clay
89.8		Coniacian			Grey limestone with interbedded clay
93.9		Turonian			White limestone with flint
100.5	Early Creta.	Cenomanian	BCG	Conglomerate and phosphoritic sandstone	Chalk Group
		Albian	BCU	Sandy shales	

removing the Tertiary cover. In the southeastern margin of the Arkona Basin, Saalian glacial tills have been preserved only in incised valleys (Obst et al., 2017). Late

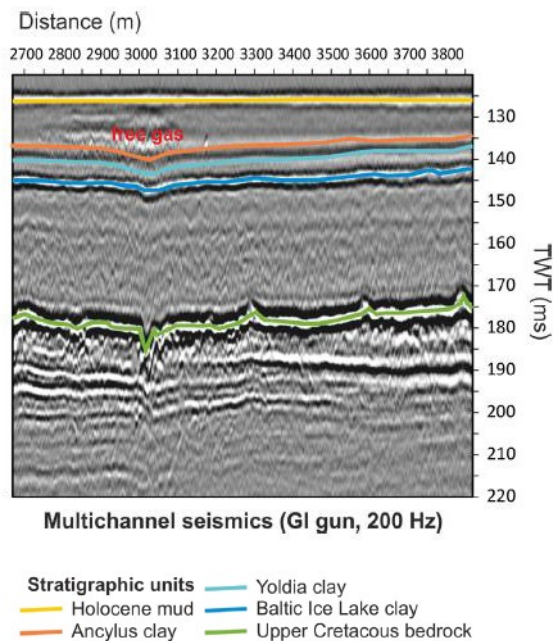


**Fig. 1.11: Seismo-stratigraphic units in the Bornholm Basin (modified from Tóth et al., 2014)**

Pleistocene ice masses in the southern Baltic depression (i.e. last Weichselian glacier advance) moved westwards and passed through an area between the islands of Bornholm and Rügen. They fanned out toward the southwest, west, northwest and north in the western Baltic region (Stephan, 2001). Weichselian glacial tills succeed the Upper Cretaceous carbonate interval in the central Arkona Basin (Mathys et al., 2005). Mid-Weichselian, Warnow, Pomeranian and Mecklenburg tills have been deposited in the southeastern margin of Arkona Basin (Obst et al., 2017). Although

Brandenburg/Frankfurt glacial till has been preserved onshore on the Jasmund Peninsula (Kenzler et al., 2010; Gehrman et al., 2017), Obst et al. (2017) did not observe its equivalent along the southeastern margin of the Arkona Basin. Furthermore, on the Jasmund Peninsula, Gehrman et al. (2017) and Gehrman and Harding (2018) studied and reported evidences of glaciotectonic deformation of Cretaceous chalk and glaciogenic sediments.

After the last deglaciation of the Baltic Sea basin in Quaternary, there was an interplay of glacio-isostatic uplift and eustatic sea-level changes which led to a series of stages with differing levels of water salinity as evident in the Baltic Sea sedimentary record (Kortekaas et al., 2007). In the Arkona Basin, Baltic Ice Lake sediments, consisting predominantly of late-glacial varved clay with silty to sandy layers at the top, form the oldest post-glaciation unit (Moros et al., 2002; Mathys et al., 2005). Following this, entry of marine water in Holocene led to the deposition of Yoldia Sea stage sediments which comprised of light silty 'Rosa' clay and fine sands in the central Arkona Basin (Mathys et al., 2005; Kortekaas et al., 2007). After the Yoldia regression, Ancylus Lake sediments (10.6-6.45ka±50) were deposited in a freshwater setting as silty grey clay (Moros et al., 2002; Mathys et al., 2005; Trimonis et al., 2008). Higher in the stratigraphic sequence, silty green mud and Gyttya unlaminated clay (Holocene mud rich in organic content) succeed the lacustrine clay, as they were deposited during the Littorina/Post-Littorina Sea phase from 6.45 ka ±50 to present (Moros et al., 2002; Mogollón et al., 2012). Past authors (e.g. Tóth et al., 2014; fig. 1.11) have identified and studied lateral equivalents of the Arkona Basin's lithostratigraphic units in the Bornholm Basin.

#### **1.4 Thesis outline and declaration of co-author contributions**

This is a cumulative thesis consisting of 6 chapters. Chapter 1 introduces the research by showing the motivation and objectives of the study within the context of the parent project (SynCore) and work of past researchers. It summarizes the research questions and state-of-the-art scientific background of this thesis, and reveals the geological setting of the study area. Chapter 2 describes the dataset and method of seismic data acquisition and processing used in this work. Chapters 3 to 5 present the primary components of the thesis as standalone research manuscripts which would be submitted for publication in peer-reviewed journals. These 3 main chapters are outlined in detail below with additional information provided about co-author

contributions in each manuscript. Finally, chapter 6 shows the conclusions reached in this research and an outlook for future work.

### **Chapter 3**

*Seismic stratigraphy and structural analysis of shallow seabed in the southern Arkona Basin, Baltic Sea*

**Authors:** Opeyemi Ogunleye, Hanno Keil and Volkhard Spiess

**Status:** To be submitted to *Geosciences*

Chapter 3 integrates ultra-high-resolution 3D and 2D multi-channel seismic reflection data with sediment descriptions and velocity logs in the southern Arkona Basin. It focuses on the lithologic characterization of near-surface seismic units in the area, and the stratigraphic and structural frameworks of the shallow seabed. The chapter investigates the effects of Late Cretaceous structural inversion, Tertiary extension and Quaternary glaciotectonic deformation on Cretaceous bedrock. Furthermore, it examines the deposition, erosion and deformation of glaciogenic sediments during Pleistocene, and the buried landforms left as glacial imprints in the southern Arkona Basin. Moreover, the chapter shows a local Weichselian ice flow direction and presents a model for the Late Cretaceous to Holocene evolution in the southcentral part of the study area. It discusses the significance of seismic stratigraphy and deduction of geological history in subsurface studies. Its conclusions reveal the importance of 3D seismic data for geological modeling.

#### **Co-author contributions:**

***Opeyemi Ogunleye (overall contribution: 85%):***

I largely formulated the concepts of the research. Not only did I organize seismic and borehole geological data used for this manuscript, I also processed the 2D and 3D seismic data in GLOBEClaritas and Schlumberger's VISTA software packages to increase the signal-to-noise ratio of the data and make the data interpretable in geological and geophysical domains. Beside analyzing the seismic and borehole geological data, I carried out the main scientific investigations that led to our findings. The methods used were designed by me. I exclusively performed interpretation of the seismic and borehole geological data in IHS Kingdom software, and validated the results. Furthermore, I prepared the data and results for visualization in the

manuscript. I wrote the original draft of the manuscript, and equally reviewed and edited it in the process.

***Hanno Keil (overall contribution: 5%):***

Hanno carried out geometry set-up of the 3D seismic data before the commencement of my PhD program and handed over the raw seismic data and geometry file to me. He wrote and executed a computer program for smoothing the 3D seismic horizon of the seafloor which I had picked during the seismic data processing stage. The smoothing was done in inline and crossline directions within the 3D seismic cube.

***Volkhard Spiess (overall contribution: 10%):***

Volkhard acquired the funding needed for this research as part of the SynCore project, and supported me in refining my research concepts as a supervisor. As the investigation was progressing, we held several meetings to evaluate my progress and presentation of ideas. He was in charge of project administration, and ensured the provision of data and computing resources by the University of Bremen.

**Chapter 4**

*Statistical boundary conditions of subsoil physical properties in the Arkona Basin - delineating potential seismic attributes for predicting near-surface geotechnical parameters*

**Authors:** Opeyemi Ogunleye, Natasha Morales, Taisiya Pein and Volkhard Spiess

**Status:** To be submitted to *Journal of Environmental and Engineering Geophysics*

The content of this chapter is based on an integration of 3D and 2D multi-channel seismic reflection data with sediment descriptions and velocity logs in boreholes as well as CPT data. The chapter relates changes in interface-related seismic attributes with variations in CPT parameters. It examines variations in acoustic impedance in relation to changes in lithology and CPT measurements. Based on these relationships, the chapter shows seismic attributes that can serve as a predictor and guide for CPT data prediction from seismic data, and equally reveals a geotechnical factor that should be considered in such predictions. Furthermore, it shows relatively precise values of physical property for each near-surface stratigraphic unit in the study area, relating the values with structural deformation and geotechnical parameters. The chapter discusses the usefulness of those physical property values in a seismic inversion procedure.

**Co-author contributions:*****Opeyemi Ogunleye (overall contribution: 80%):***

The research concepts were largely developed by me. In addition to the seismic and borehole geological data that were already loaded into IHS Kingdom software by me, I organized and integrated the geotechnical and geophysical data into the database. I utilized already-processed seismic data generated for the research shown in chapter 3. Beside analyzing the seismic, geotechnical, and borehole geological and geophysical data, I was the main scientific investigator for our research. The methodology was principally designed by me, although I received tutorials on the statistical approach to use during my research stay at the Norwegian Geotechnical Institute (NGI) in Oslo. I single-handedly interpreted the seismic and borehole geological and geophysical data using IHS Kingdom and Microsoft Excel, although the CPT data interpretation was a joint effort carried out with two other co-authors using GeoLogismiki CPeT-IT software package. I integrated and validated our various results. In addition, I prepared the dataset and results for visualization. I wrote the original draft of the manuscript. I critically reviewed and edited this draft until its current status was achieved.

***Natasha Morales (overall contribution: 5%):***

Natasha loaded the geotechnical data into the CPeT-IT software at Fraunhofer Institute for Wind Energy Systems (IWES) and participated in the joint-interpretation of the CPT data in this study.

***Taisiya Pein (overall contribution: 5%):***

Taisiya contributed to the joint-interpretation of the CPT data at Fraunhofer Institute for Wind Energy Systems (IWES).

***Volkhard Spiess (overall contribution: 10%):***

On the side of the University of Bremen, Volkhard sourced for the funding needed for the research project, and assisted with refining my research concepts while he played a supervisory role. Meetings were organized by him to assess my progress and the way I presented my findings. He contributed to the methodological approach to be used, and was in charge of project administration. He made sure that the required data and computing resources were made available.

## **Chapter 5**

*Post-Stack acoustic impedance as a reliable indicator of variation in lithologic and geotechnical properties in the southern Arkona Basin - Assessment of two near-surface impedance inversion approaches using stationary wavelets*

**Authors:** Opeyemi Ogunleye, Guillaume Sauvin, Nikolas Römer-Stange, Maarten Vanneste and Volkhard Spiess

**Status:** To be submitted to *Near Surface Geophysics*

Chapter 5 presents two 2D seismic profiles (total length 35 km, central frequency ~350 Hz, vertical resolution ~1.1 m), sediment descriptions from 4 boreholes, and CPT data from 1 site. The chapter shows the results of near-surface post-stack seismic inversion of the representative seismic profiles. It reveals how absolute acoustic impedance correlates with geological ground truths at borehole locations, and helps to resolve stratigraphic and structural complexity in the study area. Moreover, it shows explicitly that intra-unit property variation and boundary that are not clearly observable on seismic amplitude sections are captured on absolute acoustic impedance sections. In qualitative terms, it discusses how acoustic impedance values vary with measured cone resistance and sleeve friction. It equally shows the statistical correlation between the acoustic impedance of seismic units and their corresponding cone resistance and sleeve friction. The chapter ends with an assessment of two approaches of acoustic impedance inversion using stationary wavelets, and proposes improvements and factors to be considered for future work.

### **Co-author contributions:**

#### ***Opeyemi Ogunleye (overall contribution: 40%):***

Formulation of research concept was done by me. I organized seismic, geotechnical and borehole geological data for usage at the University of Bremen and NGI in Norway. I employed five 2D seismic lines that have been processed for the work done in chapter 3. After submitting a proposal to MARUM graduate school GLOMAR, I was granted funds for my research stay at NGI in Oslo. I provided not only the processed seismic and CPT data to NGI, but also the interval velocity field for each seismic profile and the summary statistical estimates of physical properties for each seismic unit which I already generated during the research detailed in chapter 4. I analyzed the data employed in this research and interpreted the acoustic impedance sections produced by NGI and the University of Bremen by integrating the impedance sections

with CPT and borehole geological data in IHS Kingdom. I investigated the use of acoustic impedance as a tool for resolving geological complexity and predicting CPT data, and evaluated the seismic inversion methods used by NGI and the University of Bremen. The interpretation methodology was developed and implemented by me. I jointly validated the impedance sections with other co-authors, and also prepared the results for visualization in the manuscript. I and two of the co-authors wrote the original draft of the manuscript, and equally reviewed and edited it in the process.

***Guillaume Sauvin (overall contribution: 20%):***

Guillaume, who works for NGI, inverted the processed seismic data I provided to him along five profiles. He used the computing facilities of NGI to perform the seismic impedance inversion during and after my research stay with them. Guillaume and I validated the inversion products. He also contributed to the writing of the original draft.

***Nikolas Römer-Stange (overall contribution: 20%):***

Nikolas inverted the processed seismic data I provided to him for one seismic line. He used the computer program, which was written by him during his PhD program at our research group, to perform the seismic inversion. Nikolas and I validated his inversion product. He equally contributed to the writing of the original draft of this manuscript and its editing.

***Maarten Vanneste (overall contribution: 5%):***

During my research stay, Maarten performed data curation and ensured online exchange of data between NGI and the University of Bremen using OneDrive. He approved my research stay at NGI, he being the head of the unit with which I was affiliated at the institute. He also managed the aspect of the research carried out at NGI, and made sure Guillaume and I had the necessary computing resources for the seismic inversion done in this research at NGI.

***Volkhard Spiess (overall contribution: 15%):***

Volkhard acquired the funding needed for the research project. Through meetings organized by us, he refined my concepts and methodological approach. He was my supervisor for the study. He performed the role of the major project administrator, and ensured that I had the computing facilities and license for IHS Kingdom to carry out the interpretation of absolute impedance sections.

## Chapter 2

### Data and methods

#### 2.1 Data

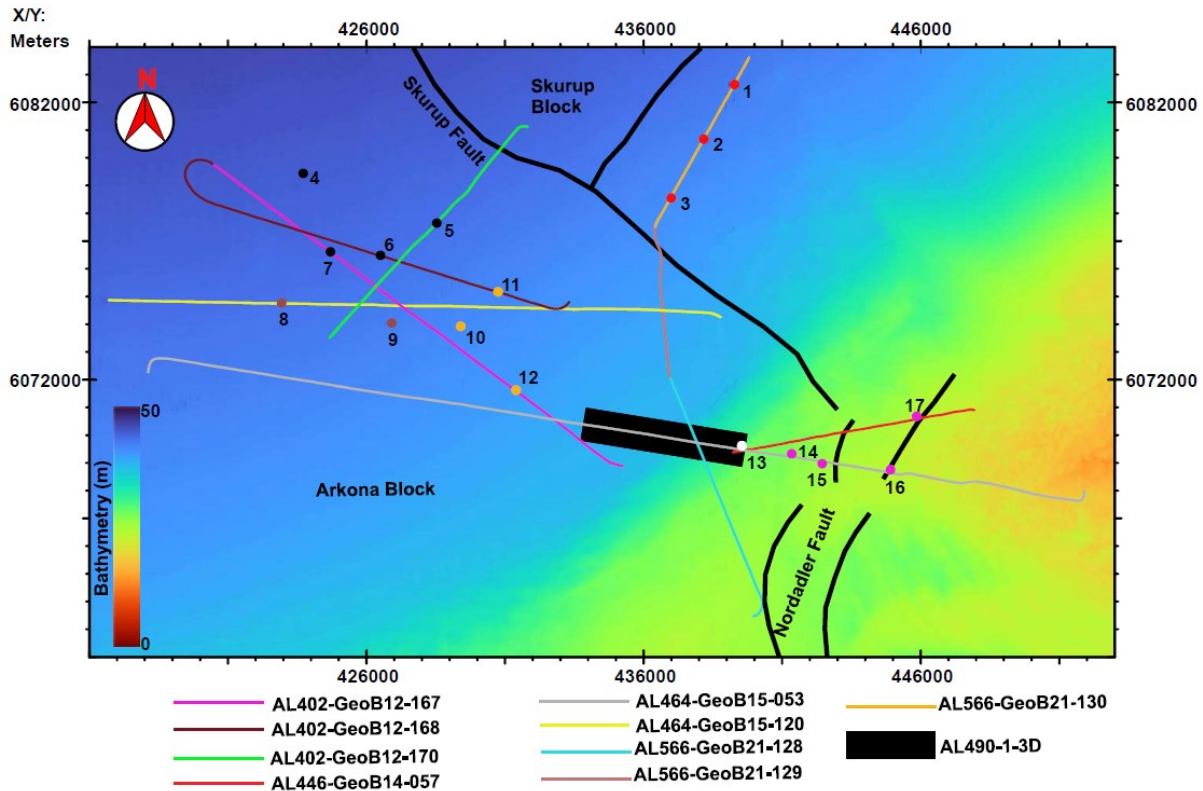


**Fig. 2.1:** An overview map of the southern Arkona Basin showing the coverage of 3D and 2D seismic reflection data and the sites with sediment descriptions, velocity logs and Cone Penetration Test (CPT) data used in this research. 17 sites in the central, northern, northwestern, western, southcentral and southeastern areas are represented with orange, red, black, brown, white and lilac points, respectively. The sites are named as follows: the number shown in the figure followed by BH/CPT (where CPT data are available); 16 of the sites have sediment descriptions; only Sites 1, 14 and 16 BH have no CPT data (i.e. their names are 1, 14 and 16 BH, without CPT). Velocity logs are available only at Sites 1 BH and 2, 3, 4, 6 and 11 BH/CPT. The faults shown belong to the Tornquist Zone (Obst et al., 2017). EMODnet Bathymetry Consortium (2020) is the source of the water depth; geographic coordinates are based on UTM 33N.

7 km<sup>2</sup> ultra-high-resolution 3D Multi-Channel Seismic (MCS) reflection data (central signal frequency ~250 Hz) were acquired along the marginal zone of the southern Arkona Basin by the Department of Geosciences (University of Bremen) and Fraunhofer Institute for Wind Energy Systems (Germany) in 2017 during the R/V ALKOR Device Test Cruise AL490-1. These available MCS data, hereinafter referred to as AL490-1-3D (fig. 2.1), were unprocessed, although their geometry has already been prepared in advance for this research.

Raw ultra-high-resolution 2D MCS data for nine profiles (total length of 133 km) were

**Table 2.1: Summary of sites with sediment descriptions, primary and shear wave velocity (P-S) logs, and CPT data in this study. Green- and orange-filled fields indicate that sediment descriptions or measurement types are available and unavailable, respectively.**

Area	Site name	Water depth (m)	Total depth of borehole (mbsf)	Sediment descriptions	Measurements	
					P-S logs	CPT data
North	1 BH	42.16	65.90			
	2 BH/CPT	41.50	86.30			
	3 BH/CPT	41.32	66.40			
North-west	4 BH/CPT	45.40	22.86			
	5 BH/CPT	44.20	50.50			
	6 BH/CPT	44.00	70.05			
	7 BH/CPT	44.50	50.15			
West	8 BH/CPT	44.00	51.05			
	9 BH/CPT	42.30	50.65			
Central	10 BH/CPT	42.30	15.89			
	11 BH/CPT	42.30	70.50			
	12 BH/CPT	39.00	50.10			
South-central	13 BH/CPT	30.60	59.60			
South-east	14 BH	25.75	55.10			
	15 BH/CPT	20.75	59.90			
	16 BH	22.75	54.00			
	17 BH/CPT	27.00	50.80			

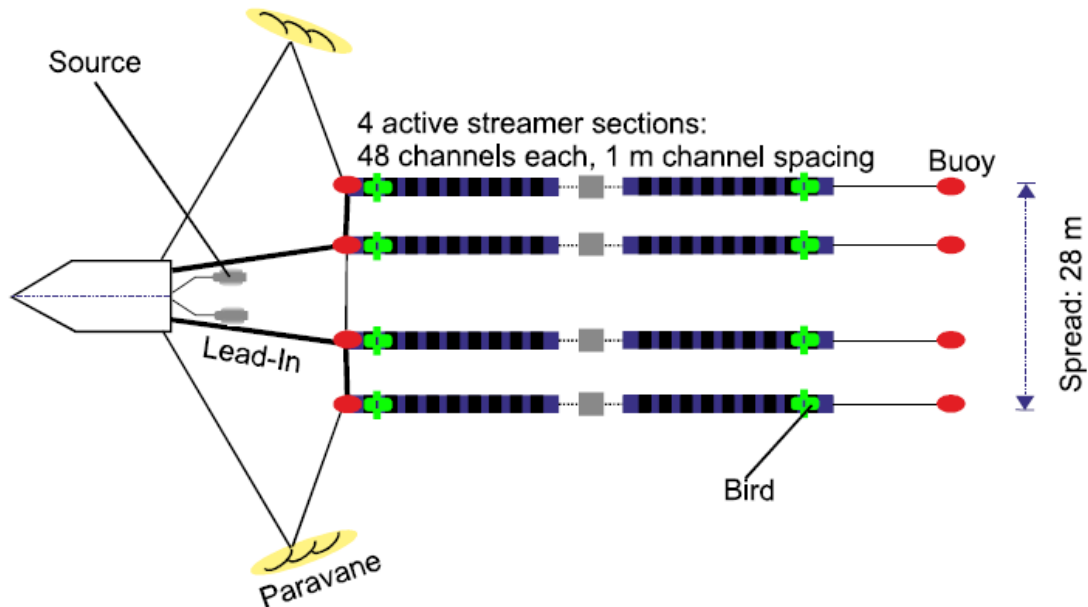
provided (fig. 2.1). These were acquired by the Department of Geosciences (University of Bremen) during the R/V ALKOR Cruises 402, 446, 464 and 566 in 2012 (AL402-GeoB12), 2014 (AL446-GeoB14), 2015 (AL464-GeoB15) and 2021 (AL566-GeoB21), respectively.

Furthermore, sediment descriptions from 16 out of 17 borehole sites used in this research were made available in subsoil investigation reports (table 2.1). 6 of these sites have associated primary and shear wave velocity (P-S) logs (see caption to fig. 2.1). Cone Penetration Test (CPT) data associated with 14 out of the 17 borehole sites were also utilized (see caption to fig. 2.1). A summary of sites with P-S logs and CPT data are shown in table 2.1.

## 2.2 Methods

In this section, details of the 2D and 3D seismic data acquisition and processing steps employed in this study are discussed. An explanation of the interpretation methodology used in this research for integrating seismic, lithologic, downhole

geophysical and CPT data is provided in each of the relevant chapters (i.e. chapters 3, 4 and 5).



Receiver cable:	Seamap High Resolution 3D for shallow water
Receiving Parts:	Lead-In
Sources:	4 active sections, 48 channels each, 1 m channel spacing
Geometry Parts:	4 x 2 birds 4 x 2 buoys 2 x paravane
Deck Equipment:	Winch with cable

Fig. 2.2: 3D MCS data acquisition configuration. Active streamer sections are represented as jointed horizontal bars with alternating purple and black segments. Offset ranges from 31 to 89 m.

## 2.2.1 Data acquisition

### 2.2.1.1 3D MCS data acquisition

During the 3D MCS data acquisition, two Sercel Mini-GI guns were shot flip-flop in True GI mode for adequate subsurface fold coverage. Seamap High-Resolution 3D receiver cables designed for shallow water were deployed. The cables consisted of four 48-m long streamers with 1-m spaced single-hydrophone channels, with the streamers supported by buoys (fig. 2.2). The spread of the streamers was 28 m. Streamer depth was controlled by birds. The digital data were transmitted from the streamers to the NTRS system and saved in SEG-D format. The record length was 1 s. The vertical resolution of the MCS data is 1.5 m (quarter of wavelength).

### 2.2.1.2 2D MCS data acquisition

The ultra-high-resolution 2D MCS reflection data along nine profiles were acquired with Sercel GI (Generator and Injector) guns. The seismic signals had a central frequency of ~350 Hz. Record length was 0.5-1 s. Vertical resolution of 1.1 m (calculated as a quarter of wavelength) was achieved.

For Profiles AL402-GeoB12-167, AL402-GeoB12-168 and AL402-GeoB12-170 (fig. 2.1), the GI gun was positioned on the starboard side of a Global Positioning System (GPS) sensor, with its along-track distance being 40.63 m behind the sensor and an across-track distance of 8.77 m. The profiles were acquired with a 48-channel streamer whose single-hydrophone channels were spaced at 1 m apart. The first channel was situated at an along-track distance of 59.55 m behind the GPS sensor; its across-track distance on the port side relative to the GPS sensor was 3.96 m.

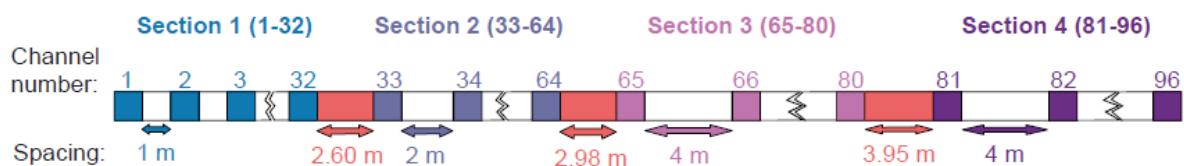


**Fig. 2.3: Geometry of the 96-channel streamer used for acquiring 2D MCS data along AL446-GeoB14, AL464-GeoB15 and AL566-GeoB21 profiles in this study. The spacing in red represents the length of connectors between active sections of the streamer.**

Furthermore, AL446-GeoB14, AL464-GeoB15 and AL566-GeoB21 profiles were acquired with a 224 m long 96-channel streamer which had four active sections of single-hydrophone channels. This streamer has varying channel spacing as shown in fig. 2.3.

Profile AL446-GeoB14-057 (fig. 2.1) was acquired with a GI gun positioned on the port side of a GPS sensor at an across-track distance of 1.90 m; the along-track distance being 53 m behind the sensor. The first channel was situated at an along-track distance of 59.55 m behind the GPS sensor; its across-track distance on the port side relative to the GPS sensor was 3.96 m.

Profiles AL464-GeoB15-053 and AL464-GeoB15-120 (fig. 2.1) were acquired with a GI gun situated on the port side of a GPS sensor such that the gun's along-track distance behind the sensor was 40.46 m; the across-track distance from the sensor was 1.7 m. During the survey, the first streamer channel was positioned at an along-track distance of 55.24 m behind the GPS sensor; its across-track distance on the starboard side relative to the GPS sensor was 0.35 m.

Data along the three AL566-GeoB21 profiles (fig. 2.1) were collected with the Sercel GI gun located on the starboard side of a GPS sensor. The gun's along-track distance behind the sensor was 55.76 m; its across-track distance from the sensor was 5.59 m. The first channel on the receiver cable was situated at an along-track distance of 59.26 m behind the GPS sensor; its across-track distance on the port side relative to the GPS sensor was 1.45 m.

In all of these 2D seismic surveys, digital birds were used to maintain streamer depth. Raw 2D seismic data were transmitted from the streamers and saved in SEG-Y format by the University of Bremen's custom digital seismograph, the Marine Multi-Channel Seismics (MaMuCS).

### **2.2.2 MCS data processing**

In addition to reflections of P-waves which are recorded as shot gathers during a conventional MCS survey, unwanted signals (noise) such as head waves might be received. Besides, in some seismic data processing steps, assumptions are made which do not always hold for points of reflections in the subsurface - for example, the assumption that the point of reflection in the subsurface is directly below the midpoint between the source and the receiver at the surface is untrue for inclined interfaces. Thus, seismic data processing generally targets preservation and enhancement of primary signals and suppression of noise to increase the signal-to-noise ratio of seismic data. In addition, it involves moving seismic events to their true subsurface locations to yield seismic images that can be reliably interpreted in geophysical and geological domains.

Coherent and/or incoherent noise might be encountered in seismic data. The former consists of linear events that correlate in phase from trace to trace such as head waves, guided waves, ground roll, diffractions, multiples and water column reverberations (Yilmaz, 2001). The latter category of noise is random and not phase-correlated between adjacent traces. Trace editing, frequency-wavenumber filtering, predictive deconvolution and Surface-Related Multiple Elimination (SRME) are among the ways to suppress coherent noise. Filtering of seismic data in the frequency domain of an amplitude spectrum also helps to reduce random noise. Stacking of traces in a common depth point (CDP) gather suppresses both incoherent and coherent noise by cancellation and enhances primary signals by summation. Adverse conditions of weather such as extreme wave heights, and bad condition of seismic equipment could

introduce some noise into the raw seismic data. Besides, petrophysical properties of geological formations - for instance, fluid content, saturation and flow as well as porosity - contribute to signal attenuation, thereby affecting the seismic images.

In this research, GLOBEClaritas seismic processing software by Petrosys (hereinafter referred to as Claritas) was used for processing the 3D MCS data and 2D seismic profiles, with the exception of Profile AL464-GeoB15-120 which was processed in

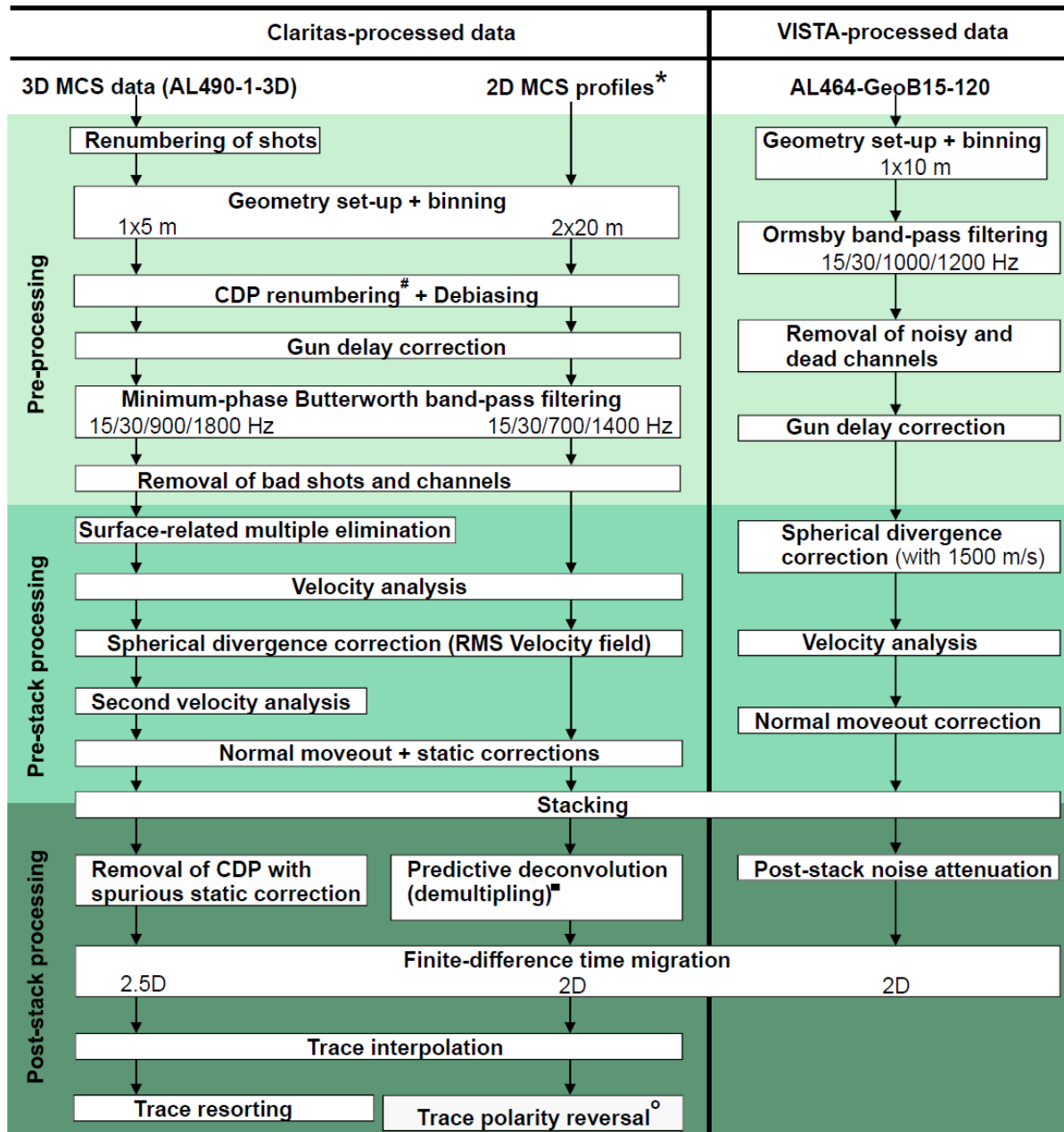


**Fig. 2.4:** 2D and 3D MCS data processing sequence used in this study (static correction was not applied to Profile AL464-GeoB15-053).

\* All 2D MCS profiles excluding AL464-GeoB15-120

# Applied to only 3D MCS data

■ Not applied to AL402-GeoB12-170

° Applied to MCS Profiles AL402-GeoB12-168 and AL402-GeoB12-170 only

Schlumberger's VISTA 2014 Desktop Seismic Data Processing software (herein referred to as VISTA). WinGeoApp (© Hanno Keil), a custom software package developed at the Marine Technology and Environmental Research Group of the Department of Geosciences (University of Bremen), was utilized for setting up geometry. The processing sequence for Claritas-processed data was designed to include amplitude preservation, although this was not a target during the processing of AL464-GeoB15-120 in VISTA. The entire sequence used to process every data in this study is summarized in fig. 2.4 and discussed in detail below.

### **2.2.2.1 3D MCS data processing in Claritas**

#### **2.2.2.1.1 3D seismic pre-processing**

As with all MCS data, AL490-1-3D was acquired in shot-receiver coordinates as shot gathers. However, by convention, most of the pre-stack and post-stack processing steps were performed in the midpoint-offset coordinates within common midpoint (CMP) gathers (CMP is a term commonly used interchangeably with common depth point (CDP)). Thus, coordinate transformation was done by sorting the data and assigning traces to their CDP.

The unprocessed data of all profiles which make up AL490-1-3D have been combined to generate a cube prior to the commencement of this research. However, during the acquisition of the raw 3D MCS data, shot identification number (SHOTID) generated by the NTRS system restarted from 1 after shot 105899 was reached and the seismograph recorded seismic traces for additional 7777 shots. These additional shot gathers were renumbered for consistency and seamless continuation of the original sequence of shot number.

Besides, the geometry of the 3D MCS data has already been set up in WinGeoApp before this study commenced by using the shot time, acquisition configuration and navigation data. For each source-receiver pair, traces in the seismic cube were assigned CDP, inline and crossline numbers, and geographic coordinates of shot, receiver and midpoint positions as well as shot-receiver offset and course. CDP bins with a regular dimension of 1 by 5 m in the inline and crossline directions, respectively, were created during the geometry set-up and multiple seismic traces were assigned to each bin based on the midpoint positions that fall within the bin, thereby forming CDP gathers. The bin size fostered a high lateral resolution balanced by a high signal-

to-noise ratio. The already-prepared geometry set-up was written into the header of the 3D MCS data. In the seismic data processing with Claritas, a specific numerical relationship ( $CDP = (INLINE \times INLINE\_CDP) + CROSSLINE$ ) must exist between header key values (CDP, INLINE, INLINE\_CDP and CROSSLINE) for the data to be treated as 3D seismic data. Thus, INLINE\_CDP was set as 10000 for easy readability of CDP numbers, and the CDP was renumbered accordingly in the 3D dataset.

The MCS data were debiased to remove DC bias from traces. Gun delay correction was applied; for the 3D seismic data, this correction involved a 13.74 ms upward bulk shift. A minimum-phase Butterworth band-pass filter (15/30/900/1800 Hz) was designed based on the amplitude spectrum and used to cut off unwanted frequencies. Bad shots and channels were removed during trace editing.

### 2.2.2.1.2 3D pre-stack seismic processing

#### 2.2.2.1.2.1 Surface-related multiple elimination (SRME)

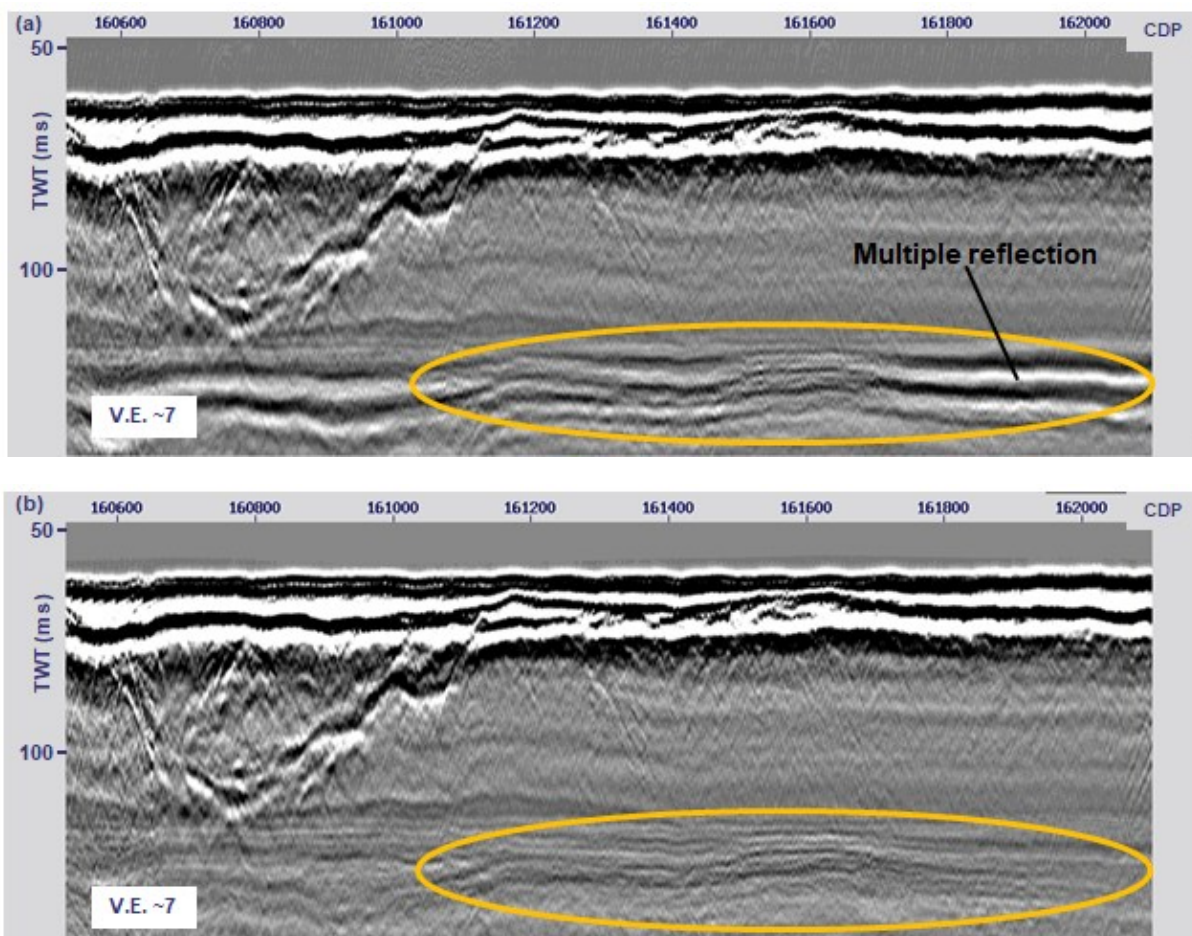


Fig. 2.5: Constant velocity stacks (1480 m/s) along Inline 16 in the 3D MCS data before (a) and after (b) SRME. Notice the suppression of multiples in the circled region. TWT = Two-Way Travel-time (vertical exaggeration was calculated based on a velocity of 2000 m/s)

SRME was applied to the 3D MCS data in the shot-domain to suppress multiples, particularly the first order ones. The process began with muting of the water column's wave field and all events above the seafloor in the pre-processed data. SRME3D module was used to model the first order surface-related multiples that have undergone a single reflection from the water surface. Seawater velocity of 1480 m/s was used for this purpose. The model was resorted using SHOTID as the primary key and CHANNEL as the secondary key, and empty channels were removed. Trace oscillations above the modeled multiples were muted, and the multiple model was bulk shifted by 4.25 ms to match corresponding events in the pre-processed data that have been muted above the seafloor. Then, a three-gate adaptive subtraction of the bulk-shifted multiple model from the muted pre-processed data (which contain both primary signals and multiples) was carried out by constrained cross-equalization using the MONKSUBT module in Claritas (Monk, 1993), and this generated the demultiplied data. The gates of the adaptive filter for the subtraction were set at 0, 25 and 50 ms. The demultiplied data (output of the SRME procedure) were resorted using SHOTID and CHANNEL keys, and the polarity of the seismic traces was flipped to create a seafloor reflector showing positive amplitudes. Fig. 2.5 shows the effectiveness of SRME in this study.

#### **2.2.2.1.2.2 Velocity analysis and spherical divergence correction**

Root mean square (RMS) velocity was picked at closely-spaced CDP locations along inlines in the seismic cube. To properly model the velocity field within a valley, a minimum of three CDP points were used to pick velocity at the flanks and center of the valley. In order to compensate for the attenuation in seismic wave amplitude due to geometrical spreading of the wave front through different velocity layers, the RMS velocity field in the seismic cube was employed for spherical divergence correction. The scalar used for the correction was the product of average velocity squared (velocity as a function of time) and time.

#### **2.2.2.1.2.3 Second velocity analysis - normal move-out and static corrections**

In an uncorrected CDP gather, reflection arrival times as a function of source-receiver offset follow a hyperbolic path. For any particular reflection in the gather, normal move-out (NMO) is the difference between the two-way travel-time at zero offset and the two-way travel-time at a given offset. NMO correction done with a correct RMS velocity field is expected to generate zero-offset traces that align horizontally in a CDP gather,

provided there is no residual statics in the data, thereby facilitating proper stacking of CDP traces. Even in the absence of statics, too low and high velocity field would lead to over- and under-correction, respectively, which would cause cancellation of primary signals during stacking.

Thus, after spherical divergence correction, a second velocity analysis was done across the seismic cube to generate an improved RMS velocity field, which was used for NMO correction. However, a detailed correction of residual statics in each NMO-corrected CDP gather was necessary, and we achieved this with a Python script by correcting NMO-corrected CDP gathers with smoothed seafloor picks. This static correction method involved the following sequential steps: (1) stacking of the NMO-corrected data that have residual statics; (2) picking of the seafloor along inlines in the stacked data; (3) interpolation and smoothening of the seafloor picks from the stacked data in both inline and crossline directions using a Python script; (4) writing of the two-way travel-time of the interpolated and smoothed seafloor picks into a dedicated header in the pre-stack NMO-corrected data; (5) automatic picking of the first break (seafloor event) of traces in each NMO-corrected CDP gather using an *Envthresh* method in Claritas which involves balancing of traces and then applying a simple threshold amplitude to the Hilbert transform; (6) subtraction of the first break time of

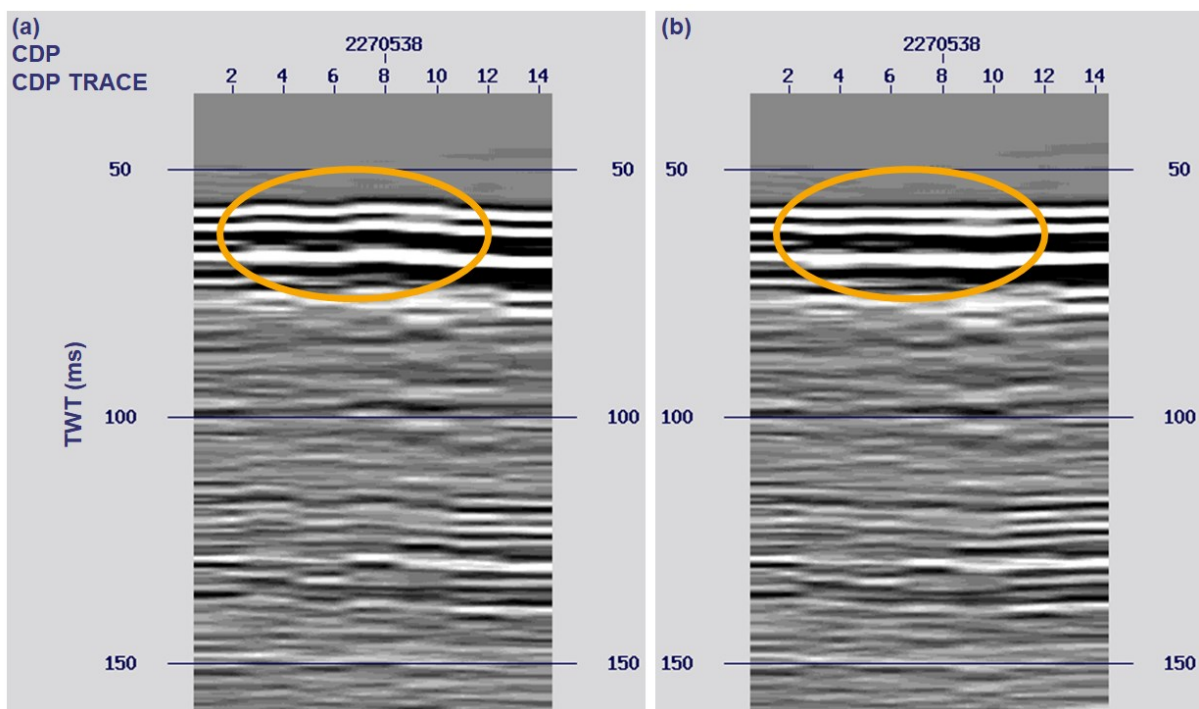


**Fig. 2.6:** Gather of CDP 2270538 in the 3D MCS cube before (a) and after (b) static correction using smoothed seafloor picks. The gather in '2.6a' has been corrected for NMO. Notice the improvement in event flattening within the circled region after static correction. TWT = Two-Way Travel-time.

each trace in an NMO-corrected CDP gather from the smoothed seafloor time generated for the CDP based on the stacked data; and (7) applying the difference derived in 'step 6' as a static time shift for every trace in an NMO-corrected CDP gather. The positive effect of this approach of static correction is shown in fig. 2.6.

### 2.2.2.1.3 3D stacking and post-stack processing

The traces in the 3D seismic cube were stacked per CDP. This reduced the number of traces in the data volume to one stacked trace per CDP and also improved the signal-to-noise ratio of the data. CDP traces with spurious static correction were removed from the data. This was followed by a 2.5D finite-difference post-stack time

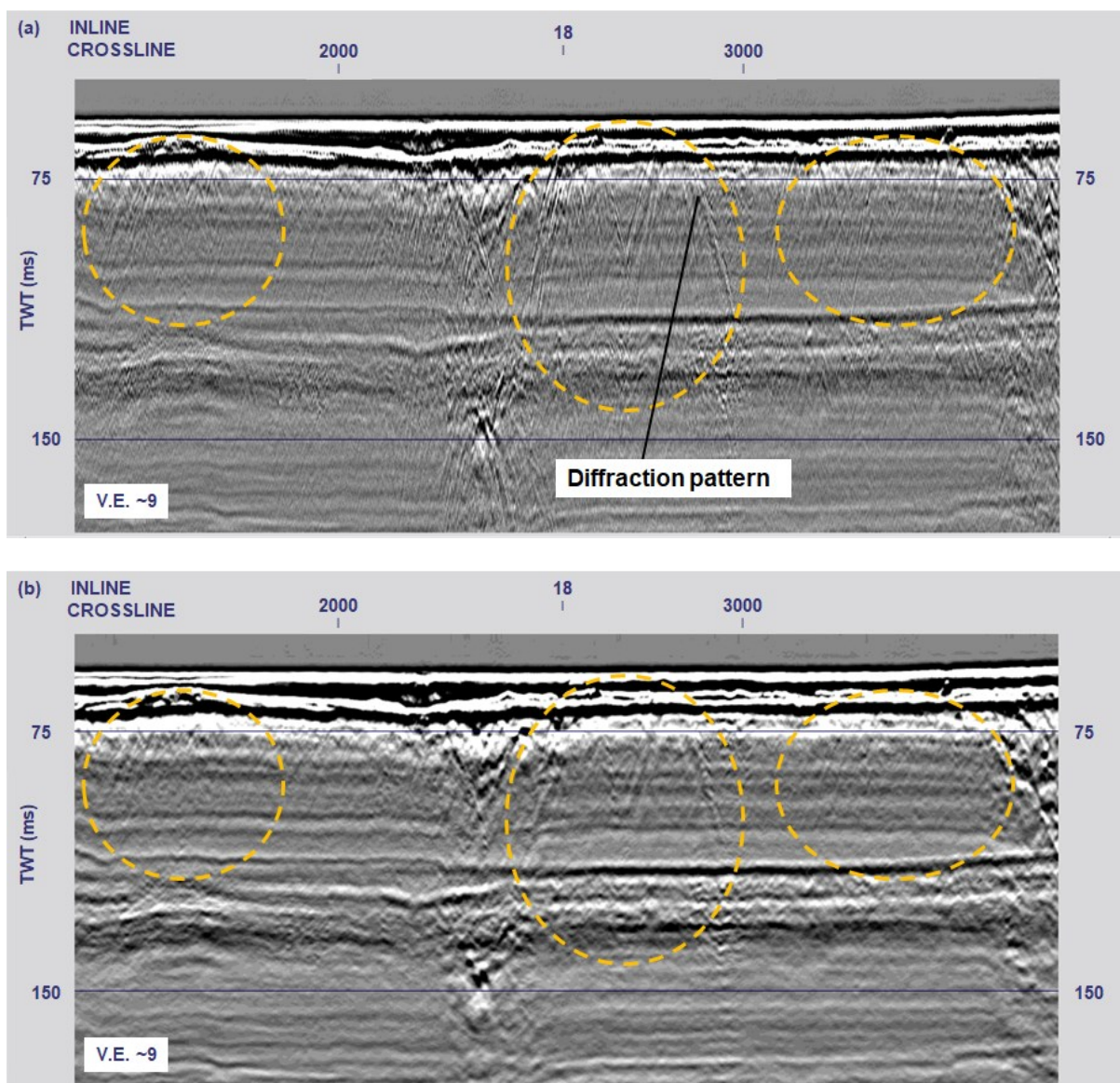


Fig. 2.7: Stacked MCS data along Inline 18 within the 3D seismic cube before (a) and after (b) 2.5D finite-difference time migration. In the circled regions, notice the significant reduction in the diffracted energy after migration. TWT = Two-Way Travel-time (vertical exaggeration was calculated based on a velocity of 2000 m/s)

migration carried out with an interval velocity cube derived from the improved (second) RMS velocity field. Migrating the data this way collapsed diffractions and moved subsurface seismic events to their true positions (fig. 2.7). Since there were gaps in the data partly due to deleted CDPs with spurious static correction, trace interpolation was done to fill the gaps using CROSSLINE as the primary key and INLINE as the secondary key. Finally, the processed data were resorted to make INLINE the primary key and CROSSLINE the secondary key.

### 2.2.2.2 2D MCS data processing in Claritas

The 2D seismic profiles used in this research, with the exception of AL464-GeoB15-120, were processed with the Claritas software. The processing sequence applied to

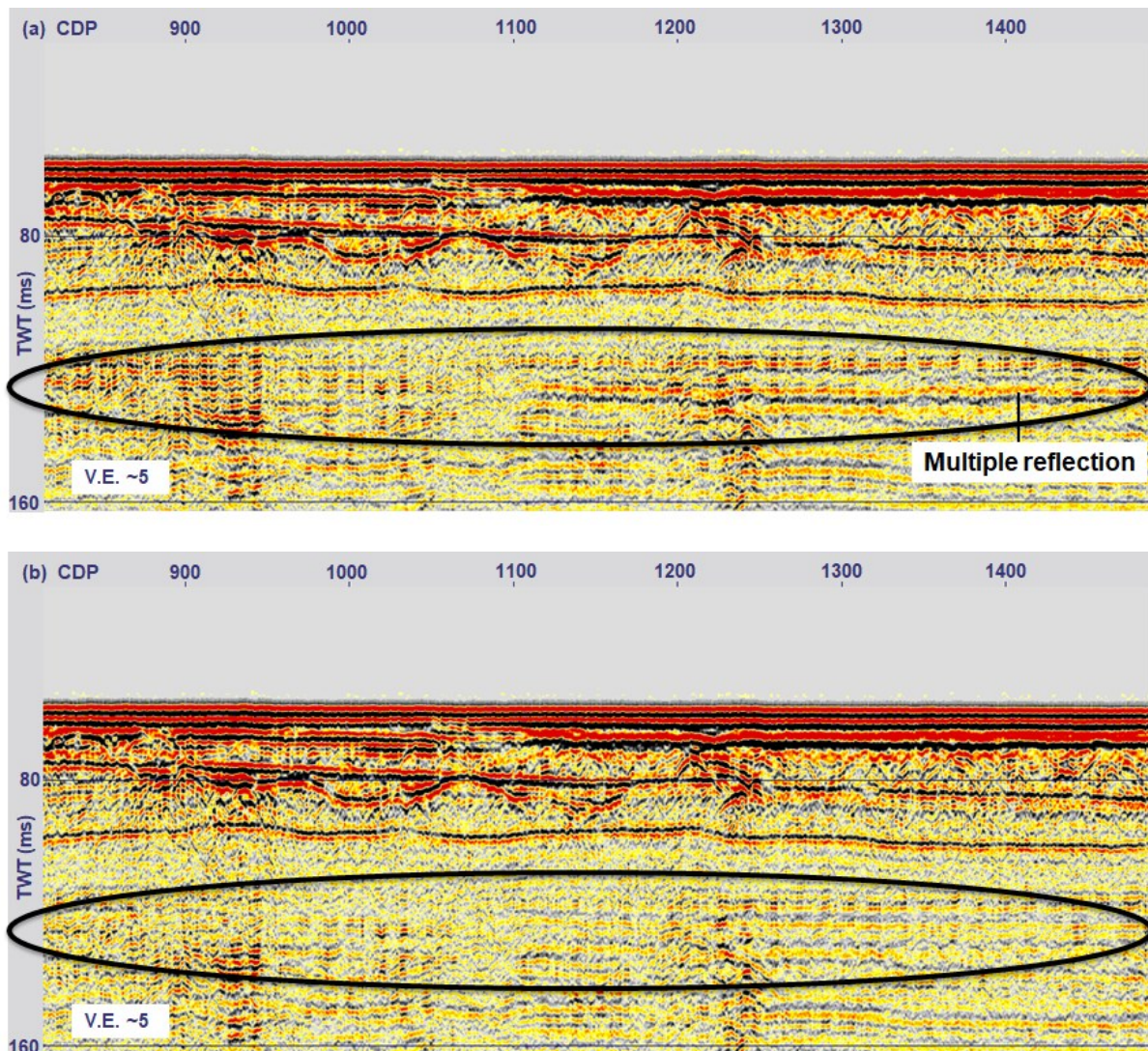


Fig. 2.8: Full stack of 2D seismic Profile AL402-GeoB12-167 before (a) and after (b) multiple suppression by predictive deconvolution method. Notice the reduction of multiple energy in the circled region. TWT = Two-Way Travel-time (vertical exaggeration was calculated based on a velocity of 2000 m/s)

the Claritas-processed profiles was similar to that of the 3D seismic data, although there were minor differences (fig. 2.4). The CDP bin size used for processing these profiles was 2 m in inline by 20 m in crossline directions. Velocity analysis was carried out once (i.e. before spherical divergence correction).

Since SRME was not performed before velocity analysis for the 2D seismic profiles processed with Claritas, gapped post-stack predictive deconvolution was used for multiple suppression along 7 out of the 8 seismic profiles (fig. 2.8) – multiple suppression was not applied to Profile AL402-GeoB12-170. The method of multiple suppression used for the 7 profiles involved defining the filter length based on autocorrelation of traces and also specifying a gap length estimated as the time difference between the seafloor and its first order multiple.

Besides, 2D finite-difference post-stack time migration was employed to move subsurface seismic events to their true positions. Because the seafloor was expressed as a negative amplitude seismic reflector along Profiles AL402-GeoB12-168 and AL402-GeoB12-170, the polarity of the seismic traces along the 2 profiles was reversed.

### **2.2.2.3 2D MCS data processing in VISTA**

Only seismic Line AL464-GeoB15-120 was processed in VISTA. Its processing sequence was different from that of the other 2D seismic profiles processed in Claritas. The bin size of this VISTA-processed line was 1 m in inline by 10 m in crossline directions. Ormsby band-pass filtering was applied (see fig. 2.4 for the low and high truncation and cut frequencies used). After trace editing, a spherical divergence correction was carried out with a constant velocity of 1500 m/s. An interactive velocity analysis was performed along the seismic profile within super-gather zones using constant velocity stack panels, semblance plots and offset gathers at a velocity increment of 10 m/s. Zero-offset seismic traces in each CDP were generated by using the resultant RMS velocity field for NMO correction. Due to NMO stretching which distorted the frequency in the far offset, a stretch mute of 30% was applied. Since the zero-offset traces in each CDP aligned horizontally without a relative time shift after NMO correction and stretch muting, there was no need for a residual static correction. CMP stacking was then performed, after which white noise was suppressed with the aid of the 4D-DEC tool in VISTA. The stacked seismic data, in which the white noise

has been suppressed, were then migrated using 2D finite-difference technique in the time domain.

## Chapter 3

# Seismic stratigraphy and structural analysis of shallow seabed in the southern Arkona Basin

Opeyemi Ogunleye<sup>1</sup>, Hanno Keil<sup>1</sup>, Volkhard Spiess<sup>1</sup>

<sup>1</sup>Department of Geosciences, University of Bremen, Klagenfurter Str., 28359 Bremen, Germany

## Abstract

Pre-Quaternary bedrock in the southern Arkona Basin mainly consists of Cretaceous chalk. Pleistocene deposits derived from glaciers succeed this interval, and the whole stratigraphic succession is capped by post-glacial sediments. Not much has been done to unravel the tectonic and glacial deformation of shallow bedrock in the area. Besides, spatial variation of glaciogenic sediments in relation to erosional, depositional and glaciotectonic processes, and the occurrence of buried glacial landforms have not been intensively studied in the area. In this current research, we integrate ultra-high-resolution 3D and 2D multi-channel seismic reflection data with borehole geological data and velocity logs. We present not only the seismic units and their lithologic characterization in the area, but also detailed stratigraphic and structural framework of the shallow sub-seafloor. We show that in addition to Late Cretaceous inversion which folded the Cretaceous interval and two-regime Tertiary extensional event which formed normal faults in the chalk, Quaternary glaciotectonic processes have deformed the bedrock. We equally demonstrate that heterogeneous glaciogenic units deposited in Pleistocene have been variably eroded and deformed by glacial activities which also left tunnel valleys, sculptured s-forms, ridges, permafrost structures and late-stage glaciofluvial channel(s) as buried landforms in the southern Arkona Basin. An erosional s-form present in the geological record indicates a northeast to southwest local Weichselian ice flow direction. We show that seismic stratigraphy and geological history aid facies prediction and sediment correlation.

**Keywords:** Cretaceous chalk; Pleistocene tunnel valleys; glaciogenic deposits; deformation; glacial landforms

### 3.1 Introduction

In the western, central and southeastern sections of the Arkona Basin (southern Baltic Sea), past research about near-surface sub-seafloor primarily focused on characterization of Quaternary intervals in relation to sedimentary processes, biostratigraphy, and gas presence using sediment cores and 2D seismo-acoustic data (Jensen et al., 1997; Mathys et al., 2005; Kortekaas et al., 2007; Mogollón et al., 2012; Endler et al., 2015; Obst et al., 2017). However, in the shallow seabed of the southern Arkona Basin, relatively little has been done on the application of ultra-high-resolution 2D and 3D seismic images to investigate the effects of Tertiary tectonic and Pleistocene glacial deformation on Cretaceous bedrock and younger strata. Besides, spatial variation of lithologic properties within tunnel valley infills has not been inferred and documented from geophysical attributes. In addition to subglacial valleys, buried glacial landforms such as ridges and permafrost structures have not been intensively

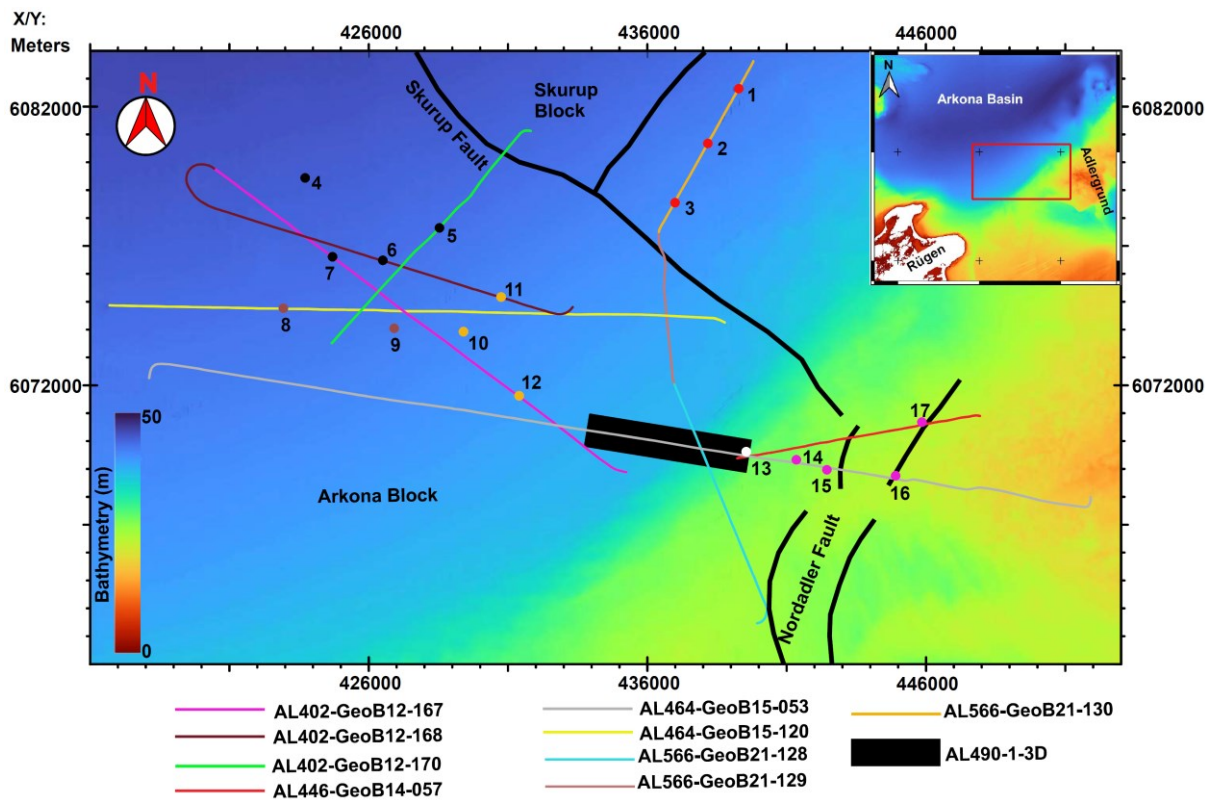


**Fig. 3.1:** Bathymetric map of the study area (red outline in inset) in the southern Arkona Basin showing the coverage of 3D and 2D seismic reflection data as well as boreholes available in this research. Boreholes in the central, northern, northwestern, western, southcentral and southeastern areas are displayed, and their locations are shown as orange, red, black, brown, white and lilac dots, respectively. The format of borehole names is the number of the borehole shown in the figure followed by BH/CPT (where borehole and Cone Penetration Test (CPT) data are available), except for Holes 1, 14 and 16 which have no CPT data (i.e. 1, 14 and 16 BH). Velocity logs are available at Sites 1 BH and 2, 3, 4, 6 and 11 BH/CPT alone. Main pre-Quaternary faults of the Tornquist Zone are indicated (e.g. Schluter et al., 1997). Water depth is based on the EMODnet Digital Bathymetry (DTM 2020) provided online by EMODnet Bathymetry Consortium (2020). Map coordinates are based on UTM 33N in this study.

studied and described in the shallow sub-seafloor interval of the Arkona Basin.

Thus, herein we carry out near-surface geophysical characterization of subsoil units and geological interpretation of the shallow seabed by integrating ultra-high-resolution 3D seismic reflection data and 2D seismic profiles with borehole lithologic and velocity logs acquired in our study area (fig. 3.1) in the southern Arkona Basin. The objectives are to: (1) reveal very-high-resolution stratigraphic and structural architecture of shallow Cretaceous to Holocene succession; (2) elucidate the erosional, sedimentation and post-depositional processes recorded in the geological interval; and (3) provide an integrated conceptual model for the Late Cretaceous to Holocene evolution. The outcomes will serve as a geological framework for establishing the relationship between seismic reflection attributes and Cone Penetration Test (CPT) data in the study area.

### 3.2 Geological setting

The Arkona Basin was formed in the Pleistocene as part of the Baltic Basin. Its maximum water depth is 48 m. It is bordered to the north by the southern Swedish coast, to the west by Krieger's Flak and Plantagenetgrund, to the south by Pomeranian Bight, and to the east by Bornholm Island. Faults belonging to the Tornquist Zone dissect the basement of the Arkona Basin (Schlüter et al., 1997; Hübscher et al., 2019; fig. 3.1). In the region, multiphase evolution of Adler-Kamień Fault Zone (AKFZ) began in the Permian, with associated faults extending from the basement to Cretaceous unit (Seidel, 2019). West of the Tornquist Zone, Late Cretaceous inversion affected the seafloor of an epeiric Chalk Sea within the study area (Hübscher et al., 2019). In the southern Baltic Sea, Tertiary extension faulted pre-existing strata (Al Hseinat and Hübscher, 2017).

Pre-Quaternary bedrock in the Arkona Basin largely consists of Cretaceous chalk and limestone (Winterhalter et al., 1981), and is overlain by Pleistocene glaciogenic sediments. In the basin, the Quaternary base was formed by Late Saalian advance of the Scandinavian Ice Sheet which removed the Tertiary cover and eroded into the Upper Cretaceous interval. Saalian glacial tills have been preserved in incised valleys in the southeastern margin of the Arkona Basin (Obst et al., 2017). Late Pleistocene ice masses in the southern Baltic depression (those of the last Weichselian glacier advance) flowed westwards and passed through the opening between the islands of Bornholm and Rügen, fanning out toward the southwest, west, northwest and north in

the western Baltic region (Stephan, 2001). In the central Arkona Basin, Weichselian glacial tills overlie Upper Cretaceous carbonate interval (Mathys et al., 2005). Mid-Weichselian, Warnow, Pomeranian and Mecklenburg tills were deposited along the southeastern margin of the basin (Obst et al., 2017).

After the last deglaciation of the Baltic Sea basin in the Quaternary, interplay of glacio-isostatic uplift and eustatic sea-level changes led to a series of stages with different water salinity during the Baltic Sea sedimentation (Kortekaas et al., 2007). In the Arkona Basin, Baltic Ice Lake sediments, the oldest post-glaciation unit, consists predominantly of late-glacial varved clay with silty to sandy layers at the top (Moros et al., 2002; Mathys et al., 2005). In the Holocene, subsequent entry of marine water led to the deposition of Yoldia Sea stage sediments consisting of light silty 'Rosa' clay (Mathys et al., 2005) and fine sands (Kortekaas et al., 2007) in the central Arkona Basin. Following the Yoldia regression, freshwater Ancylus Lake sediments (10.6-6.45ka±50) were deposited as silty grey clay (Moros et al., 2002; Mathys et al., 2005; Trimonis et al., 2008). Succeeding this lacustrine clay are silty green mud and Gytja unlaminated clay (Holocene organic-rich mud) deposited during the Littorina/Post-Littorina Sea phase from 6.45 ka ±50 to present (Moros et al., 2002; Mogollón et al., 2012).

### **3.3 Material and methods**

#### **3.3.1 Material**

3D Multi-Channel Seismic (MCS) reflection data (AL490-1-3D) covering 7 km<sup>2</sup> in the southern Arkona Basin (fig. 3.1) were acquired by the Department of Geosciences (FB5), University of Bremen and Fraunhofer Institute for Wind Energy Systems (Germany) during R/V ALKOR Device Test Cruise AL490-1 in 2017. With two Sercel Mini-GI (Generator and Injector) guns being fired flip-flop in True GI mode for adequate subsurface fold coverage, the seismic signals generated had a central frequency of ~250 Hz. Record length was 1 s. A vertical resolution of ~1.5 m was achieved. Vertical and horizontal sections of the seismic cube are shown in this chapter.

Herein, ultra-high-resolution 2D MCS reflection data along four profiles (i.e. AL402-GeoB12-167, AL402-GeoB12-168, AL464-GeoB15-053 and AL566-GeoB21-130; fig. 3.1) are presented and/or specifically referred to. These four seismic profiles have a total length of 77 km. They were acquired with Sercel GI guns by FB5 during R/V

ALKOR Cruises 402, 464 and 566 in 2012 (AL402-GeoB12), 2015 (AL464-GeoB15) and 2021 (AL566-GeoB21), respectively. The seismic signals generated had a central frequency of ~350 Hz. Signals down to 0.5-1 s were recorded. While the two AL402-GeoB12 profiles were acquired with a 48-channel streamer, the other two profiles were collected with a 96-channel receiver cable. A vertical resolution of ~1.1 m was achieved. Streamer depth was maintained by birds. The 2D and 3D seismic data used in this research were transmitted from the streamers as raw data and saved in SEG-Y and SEG-D formats, respectively.

Sediment descriptions in 12 out of 17 available boreholes are specifically presented and/or referred to in this chapter. 6 primary and shear wave velocity logs in the study area have been used to guide time-depth conversion (see fig. 3.1 for location). In the northern section of our working area, a 2021 geotechnical report based on a preliminary site investigation carried out by Ramboll (client: Bundesamt für Seeschifffahrt und Hydrographie, Hamburg) and associated sediment descriptions from 3 boreholes were used. Besides, in the western through northwestern to central sub-areas, the 2012 geotechnical report prepared by IGB Berlin Brandenburg GmbH for Financial Insurance GmbH was utilized and lithologic descriptions for 5 borehole locations in the sub-areas are shown in this study. Furthermore, sediment descriptions from 4 boreholes in the southcentral and southeastern parts of the study area (fig. 3.1) are presented in the current research based on the 2012 geotechnical report prepared by Geo- und Umwelttechnik Ingenieur-Gesellschaft mbH for Arkona-Windpark Entwicklungsgesellschaft mbH.

### **3.3.2 Methods**

#### **3.3.2.1 2D and 3D MCS data processing**

The 2D and 3D MCS data were processed to improve imaging of geological units and structures. For reliable interpretation, the processing was tailored to increase signal-to-noise ratio and resolution of the data, suppress multiples, and also migrate seismic events to their true subsurface positions. For a very good lateral resolution, the bin size for the 3D MCS cube was 1 m (inline) by 5 m (crossline); inline bin sizes of 1-2 m were used for the 2D profiles. To contribute to the preservation of relative amplitude in both the 2D and 3D data, the picked root mean square (RMS) velocity field was used for spherical divergence correction. Besides, Surface Related Multiple Elimination technique (SRME) with adaptive subtraction was applied for multiple

suppression in the 3D cube, whereas post-stack predictive deconvolution was employed to demultiple the 2D data. Although similar processing steps were applied to the 3D and 2D MCS data, velocity was only picked once before spherical divergence correction (i.e. no second velocity analysis) and 2D finite difference migration was applied in the case of the latter data type.

During the processing of the 3D seismic volume, gun delay correction was applied. The data were filtered with a Butterworth bandpass minimum phase filter (15-30-900-1800 Hz) and traces were edited to remove the data from bad and dead channels. A first-stage RMS velocity field was picked and used for spherical divergence correction, and this was followed by re-picking of the RMS velocity for a subsequent normal moveout (NMO) correction. Due to inherent static errors in the 3D cube, smoothed seafloor horizon times were used for static correction, and full stack data were generated. Post-stack time-migration with 2.5D finite difference technique was employed using an interval velocity field.

Two major processing software packages were employed: (1) *WinGeoApp*, a custom geometry-setup package developed at the Marine Technology and Environmental Research Group of FB5; and (2) *GLOBEClaritas*, a software product of Petrosys, which was used for the main seismic data processing steps (although Profile AL464-GeoB15-120 was processed with Schlumberger's VISTA software).

### **3.3.2.2 Seismic data interpretation**

The IHS Kingdom software package (2019 version) was used for seismic interpretation. In the study area, mappable seismic units were described and analyzed based on seismic characteristics. Boreholes were tied to seismic data using average velocity of intervals based on available primary wave velocity logs; where these logs were not available, the velocity profile at nearby locations, seismic velocity picked during processing stage, or interval velocity associated with expected lithologic units was used. Lithologic interpretation of seismic facies was corroborated with sediment descriptions at borehole locations and published stratigraphy in the southern Baltic Sea and its coastal regions.

Horizons were mapped across the study area to show their configuration in time domain and also correlate the seismo-stratigraphic units. Faults were picked based on sudden termination, abrupt change in dip and displacement of reflectors across

lineaments. The dip angle of a fault was estimated by correlating a seismic reflector across the fault line, determining the ratio of the reflector's vertical displacement to

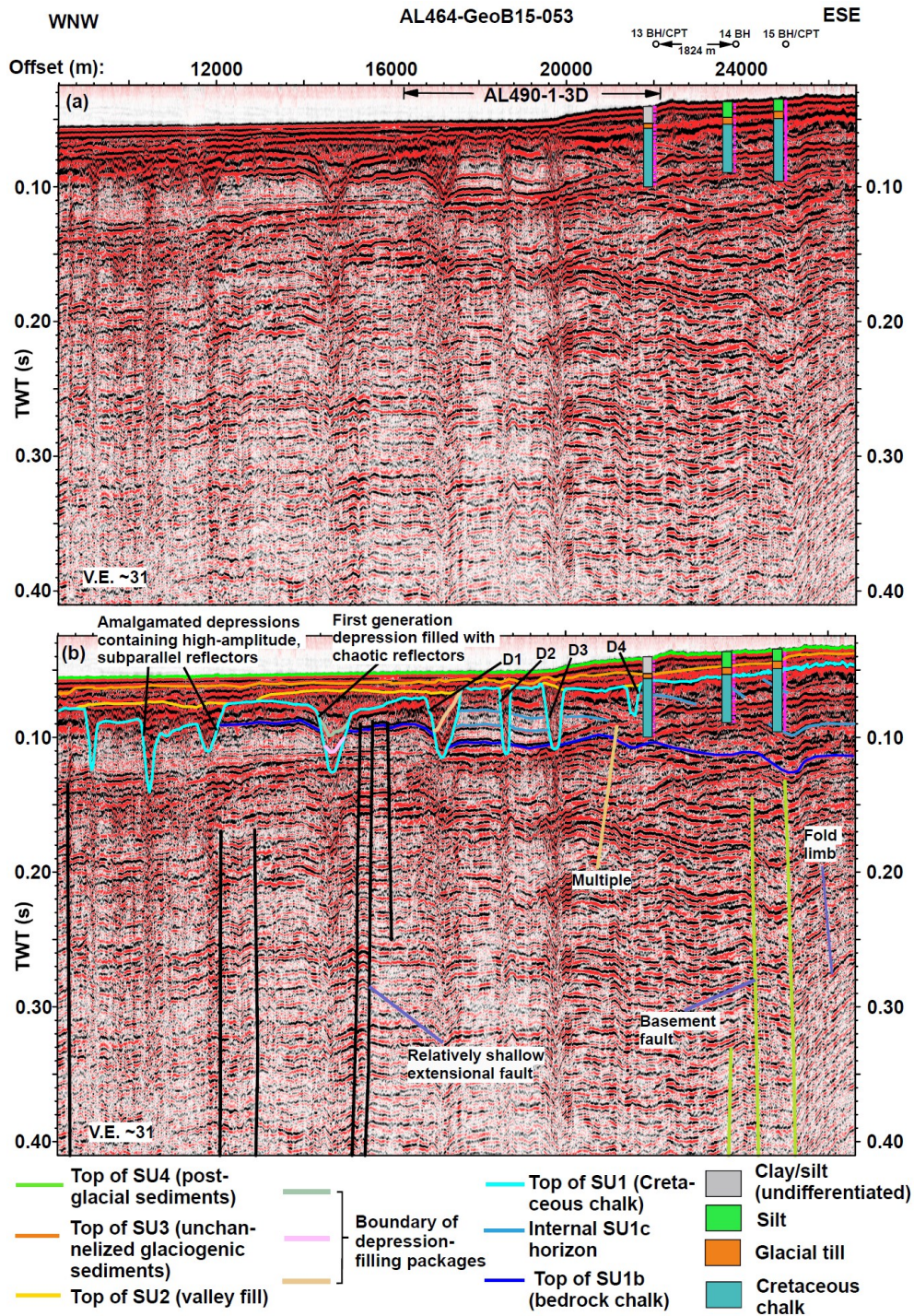


Fig. 3.2: 2D seismic Profile AL464-GeoB15-053 (see fig. 3.1 for location): (a) un-interpreted seismic section of the profile tied with lithologic logs from 13 BH/CPT, 14 BH and 15 BH/CPT; (b) regional stratigraphy and structure interpreted on the seismic section shown in '3.2a'. SU1 reflectors (Cretaceous bedrock) have been displaced along lineaments (faults) and bent (folded). Notice the major lineaments interpreted as relatively shallow and basement faults, the latter category being the Nordadler faults (see text for details). D1-4 are Depressions 1 to 4 in fig. 3.3. These and other channels shown in '3.2b' contain either subparallel or chaotic seismic reflectors (glaciogenic sediments) which are different in character from the surrounding SU1. TWT = Two-Way Travel-time; SU = Seismic Unit (vertical exaggeration was calculated based on a velocity of 2000 m/s)

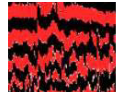
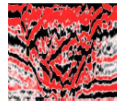
horizontal displacement, and finally calculating the arc tangent ( $\tan^{-1}$ ) of this ratio. RMS amplitude maps were generated for units using a time window.

### 3.4 Results

#### 3.4.1 Regional seismic units

The 35 km long AL464-GeoB15-053 seismic profile extends from the southeastern to western parts of the study area (fig. 3.1), showing the regional stratigraphic framework in detail. Four main seismic units have been observed, which represent the principal sedimentary facies in the region (fig. 3.2).

**Table 3.1: Representative seismic units and their geological interpretation corroborated with sediment descriptions in boreholes, published stratigraphy of the southern Baltic Sea and its coastal region, and glaciotectonic concepts (e.g. Mathys et al., 2005; Kenzler et al., 2010; Gehrmann et al., 2017).**

Seismic unit	Subunit	Description	Interpretation
SU4		It consists of medium- to very-high-amplitude reflectors that are fairly continuous to discontinuous; internal reflectors partly onlap the lower boundary of the unit	Post-glacial sediments (clay, silt and sand)
SU3		High-amplitude, subparallel reflectors that are fairly continuous to discontinuous and bent in places; sometimes with localised discontinuous, medium-amplitude reflectors at the base of the unit	Unchannelized till-dominated Pleistocene glacial sediments with local glaciotectonic structures and glaciolacustrine clay; glaciofluvial coarse-grained sediments may occur at the base
SU2		Predominantly low- to high-amplitude, discontinuous and chaotic internal reflectors filling a trough-shaped structure; locally intercalated reflectors exhibiting amplitude burst may occur within the unit; high-amplitude, subparallel reflectors exist in some amalgamated troughs	Incised valley fill dominated by Pleistocene till (chaotic seismic events); sometimes with other glaciogenic sediments; glaciofluvial to glaciolacustrine sediments fill some valleys
SU1	c	Irregular external morphology due to incisions; low- to high-amplitude, parallel reflectors which are partly discontinuous and bent in places	Youngest (uppermost) Cretaceous chalk subunit tectonically and glacially deformed in places
	b	Medium- to high-amplitude, largely continuous, subparallel reflectors which are bent in places and displaced along lineaments	Folded and faulted middle Cretaceous chalk subunit
	a	Internal reflectors are subparallel and fairly continuous; they exhibit low to medium amplitude; reflectors are displaced along lineaments and partly bent	Oldest (lowermost) Cretaceous chalk subunit observed (it is deformed)

##### 3.4.1.1 Seismic Unit 1 (SU1)

The deepest seismic unit, SU1, consists of three subunits (table 3.1). SU1a, the lowermost subunit in this study, was observed in the northwestern to southcentral parts. In the southcentral region, SU1b succeeds SU1a and is characterized by subparallel reflectors that are largely continuous, bent in places and display medium to high amplitude. This subunit in the central, western and northwestern area exhibits

reflectors that are only fairly continuous. In the northern region, SU1b shows high-amplitude, fairly discontinuous, subparallel reflectors which terminate by erosional truncation along the top of SU1.

SU1c is the uppermost seismic subunit of SU1. In the southcentral, SU1c reflectors exhibit low to high amplitude and are not only parallel but also partly discontinuous. Besides, in the southeastern, western and northwestern regions, this subunit shows

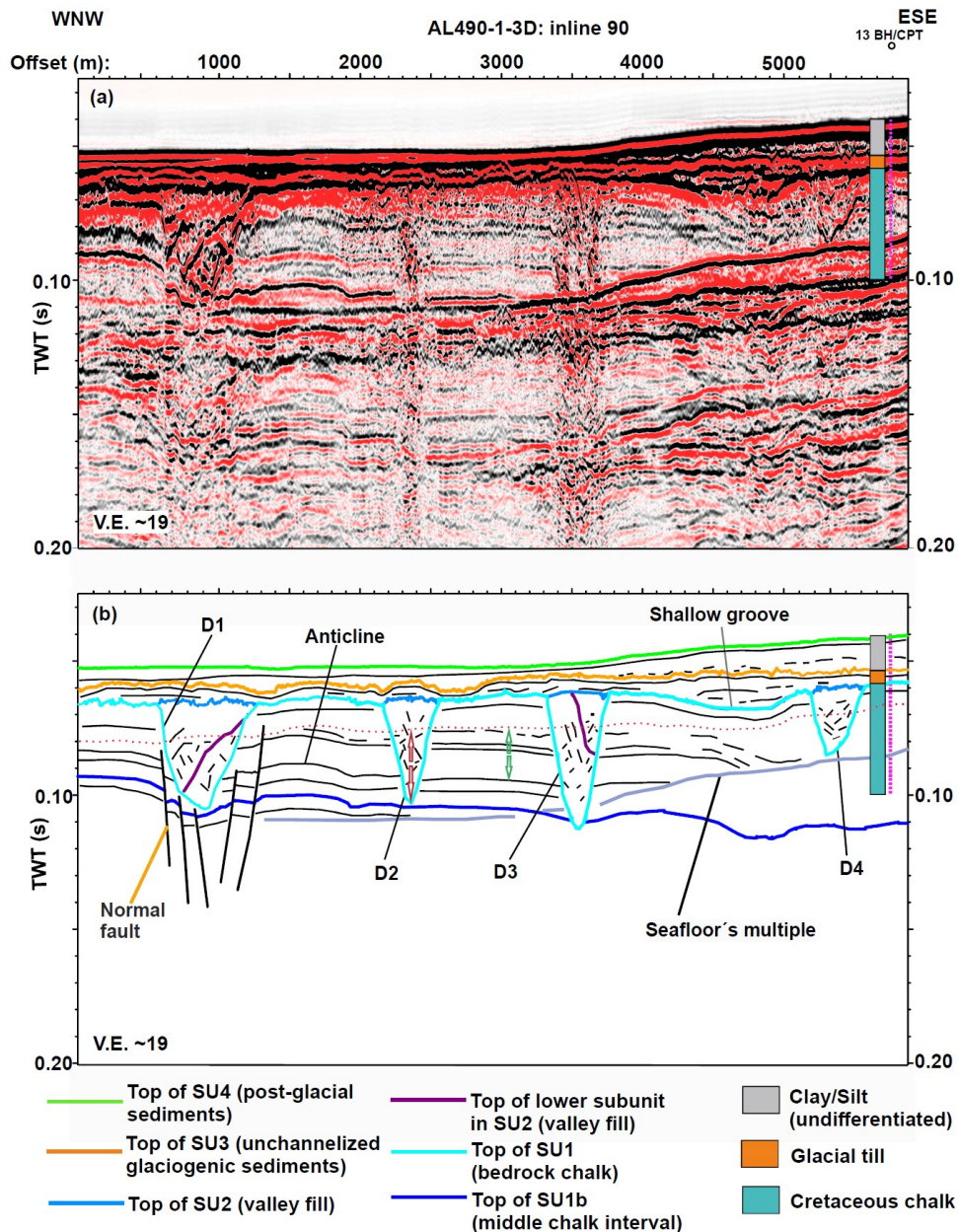


Fig. 3.3: In-line 90 in the 3D MCS cube acquired in the southcentral part of the study area (see fig. 3.4b for location): (a) un-interpreted seismic section of the inline tied with lithologic log from Hole 13 BH/CPT; (b) sketch of seismo-stratigraphic and structural framework interpreted along '3.3a'. Notice the lineaments of fault and bending of reflectors in SU1 (bedrock chalk). Four depressions (D1-4) have been incised into SU1. The double-ended red and green arrows together with the dotted red line delineate the interval within which the RMS amplitude map in fig. 3.8a was extracted. TWT = Two-Way Travel-time; SU = Seismic Unit (vertical exaggeration was calculated based on a velocity of 2000 m/s)

high-amplitude, parallel reflectors that are largely continuous. The northern part of the study area is characterized by low- to medium-amplitude, subparallel SU1c reflectors that are discontinuous and equally terminate by erosional truncation along the base of an overlying seismic unit (Seismic Unit 2).

#### **3.4.1.2 Seismic Unit 2 (SU2)**

Seismic Unit SU2 consists of reflectors that fill deep depressions (channels) incised into SU1 (table 3.1; figs. 3.2 and 3.3). It shows spatially varying seismic attributes. In the southcentral parts, the infill of Depression 1 consists of two successive packages of high-amplitude, chaotic seismic reflectors (fig. 3.3). Within Depressions 2, 3 and 4 in the area, infills are characterized by low- to high-amplitude, chaotic and discontinuous reflectors. Traversing along AL464-GeoB15-053 from ESE to WNW, three successive packages of chaotic seismic events exist within a channel adjacent to Depression 1 in the southcentral part of the study area (fig. 3.2). Moving further WNW along the profile, seismic facies filling amalgamated depressions consists of subparallel, high-amplitude reflectors.

In the central part of the study area, fills of deep depressions display two successive packages of chaotic reflectors which differ from each other in seismic amplitude. The top of the lower package is a channel-like erosional surface. Each depression in the south contains a package of high-amplitude, chaotic reflectors. Within the major channel observed in the north, a lens of anomalously high-amplitude reflectors is interbedded within the predominantly low- to medium-amplitude, discontinuous internal reflectors of SU2.

#### **3.4.1.3 Seismic Unit 3 (SU3)**

SU3 comprises of subparallel, medium- to high-amplitude reflectors that are fairly continuous to discontinuous and bent in places. It overlies not only SU1, but also SU2 as revealed by a strong seismic reflector which simultaneously forms the top of SU1 and SU2 and the base of SU3. SU3 is unchannelized and laterally extensive throughout the study area (figs. 3.2 and 3.3). Its seismic attributes are remarkably different from those of the underlying SU2 as it is not filling a depression, and its internal reflectors are not chaotic at any place. Thus, the sedimentary facies of SU3 is different from that of SU2.

### **3.4.1.4 Seismic Unit 4 (SU4)**

The shallowest seismic unit is SU4 (table 3.1). It caps the whole succession of the shallow seabed (figs. 3.2 and 3.3) and largely consists of high-amplitude reflectors that are continuous in the southcentral and northern parts of the study area. Its internal reflectors partly onlap the top of SU3 in the north. In the northwestern area, high-amplitude internal reflectors in the lower part of SU4 are fairly continuous. However, the upper part of the unit is seismically transparent in this area.

## **3.4.2 South central area: detailed 3D stratigraphic and structural description**

### **3.4.2.1 Vertical stacking pattern and lineaments**

In the 3D seismic cube which covers the southcentral area, the uppermost 55 to 80 meters below the seafloor were imaged without interference from multiples. Within SU1b and SU1c, lineaments trending in the NW-SE and NNW-SSE directions form a mini-graben structure and cross-cut an anticline in the western half of the 3D MCS coverage (fig. 3.3). The dip angle of these lineaments is  $\sim 24^\circ$  to the NE and WSW, respectively, and their hanging wall blocks are downthrown relative to the footwall blocks (fig. 3.3).

Deep V-shaped Depressions 1-4 (D1-4) have been incised into SU1. Depression 1 truncates the top of some of the aforementioned lineaments (fig. 3.3). Depressions 1 and 3 host two subunits of SU2 each, whereas 2 and 4 contain one. In the eastern half of the area, a shallow groove has been carved out along the top of SU1 between the location of Depressions 3 and 4. The top of SU1 and infills of all deep depressions are overlain by the laterally extensive SU3. This is succeeded by a thin veneer of SU4 reflectors.

### **3.4.2.2 Time structure and thickness maps**

The time structure map of an internal SU1 horizon reveals the NW-SE and NNW-SSE strike directions of lineaments which lie adjacent to Depression 1. This further shows a NW-SE curvilinear hinge line of the anticline observed on the vertical section (figs. 3.3b and 3.4a). Depressions 1, 2 and 3 are oriented in the NW-SE, NNE-SSW and NE-SW directions, respectively, on the map. These depressions have undulating thalwegs.

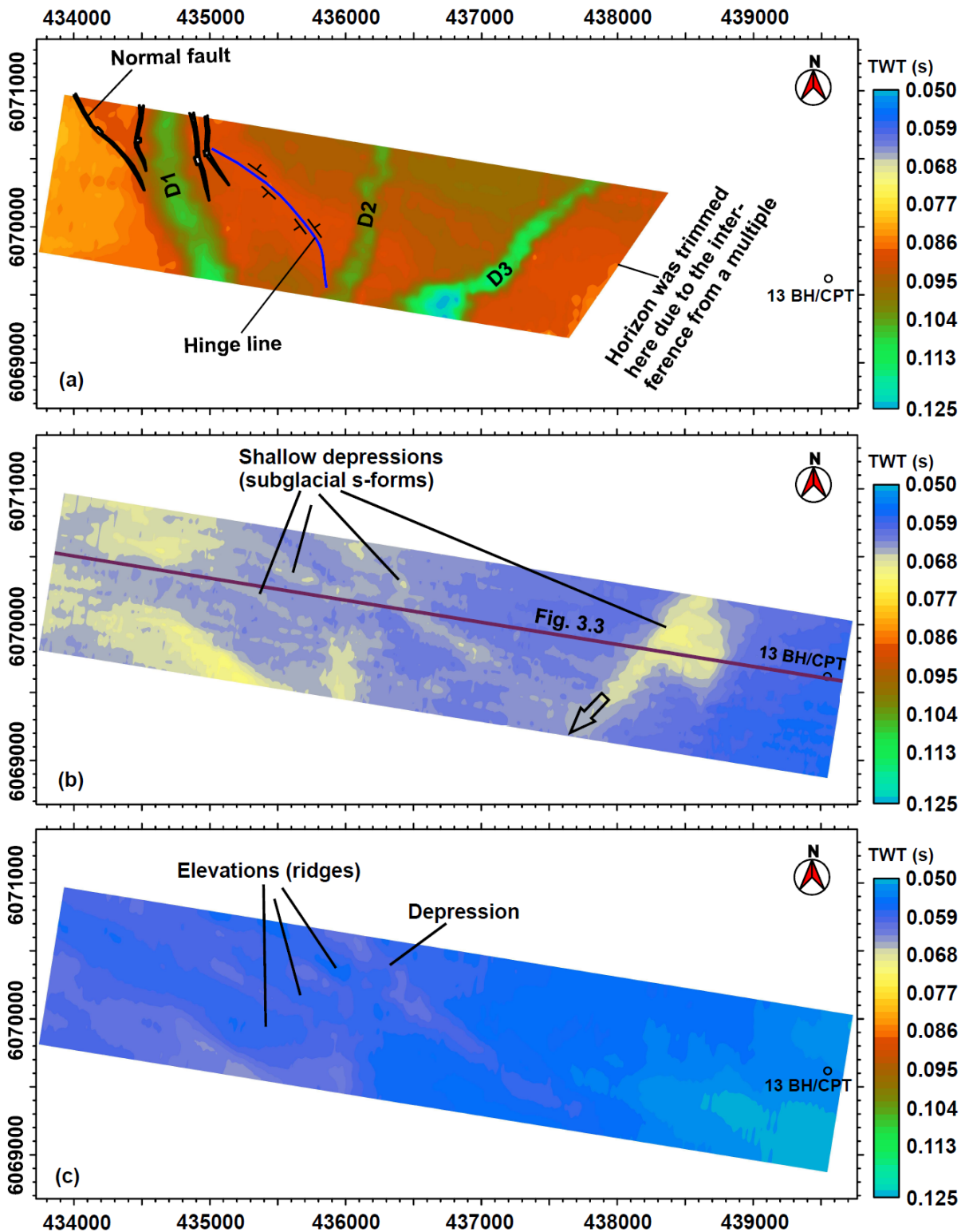


Fig. 3.4: Time structure maps derived from the 3D seismic cube (see fig. 3.1 for location): (a) an internal Cretaceous horizon dissected by normal faults in the vicinity of D1 and deformed into an anticline. Notice the converging orientations of Depressions 1-3; (b) the base of the laterally extensive SU3 (unchannelized till-dominated glaciogenic sediments). The black arrow indicates the local ice flow direction of a Weichselian glacier in the study area; (c) the top of SU3. D = Depression; TWT = Two-Way Travel-time; SU = Seismic Unit.

The time structure map of the base of SU3 (fig. 3.4b) shows a surface that generally dips to the NW. On this map, NW-SE trending shallow depressions (~3 m deep) alternate with elevations (~2 m high). Besides, a shallow groove in the eastern half of

the map is imaged as an ~7 m deep depression oriented in the NE-SW direction. These shallow depressions cut across the tops of SU1 and SU2. Moreover, the time structure map of the top of SU3 reveals alternating depressions (~3 m deep) and elevations (~2 m high) oriented in the NW-SE direction (fig. 3.4c), with their locations respectively coinciding with those of similarly-sized NW-SE trending depressions and elevations observed along the base of the unit.

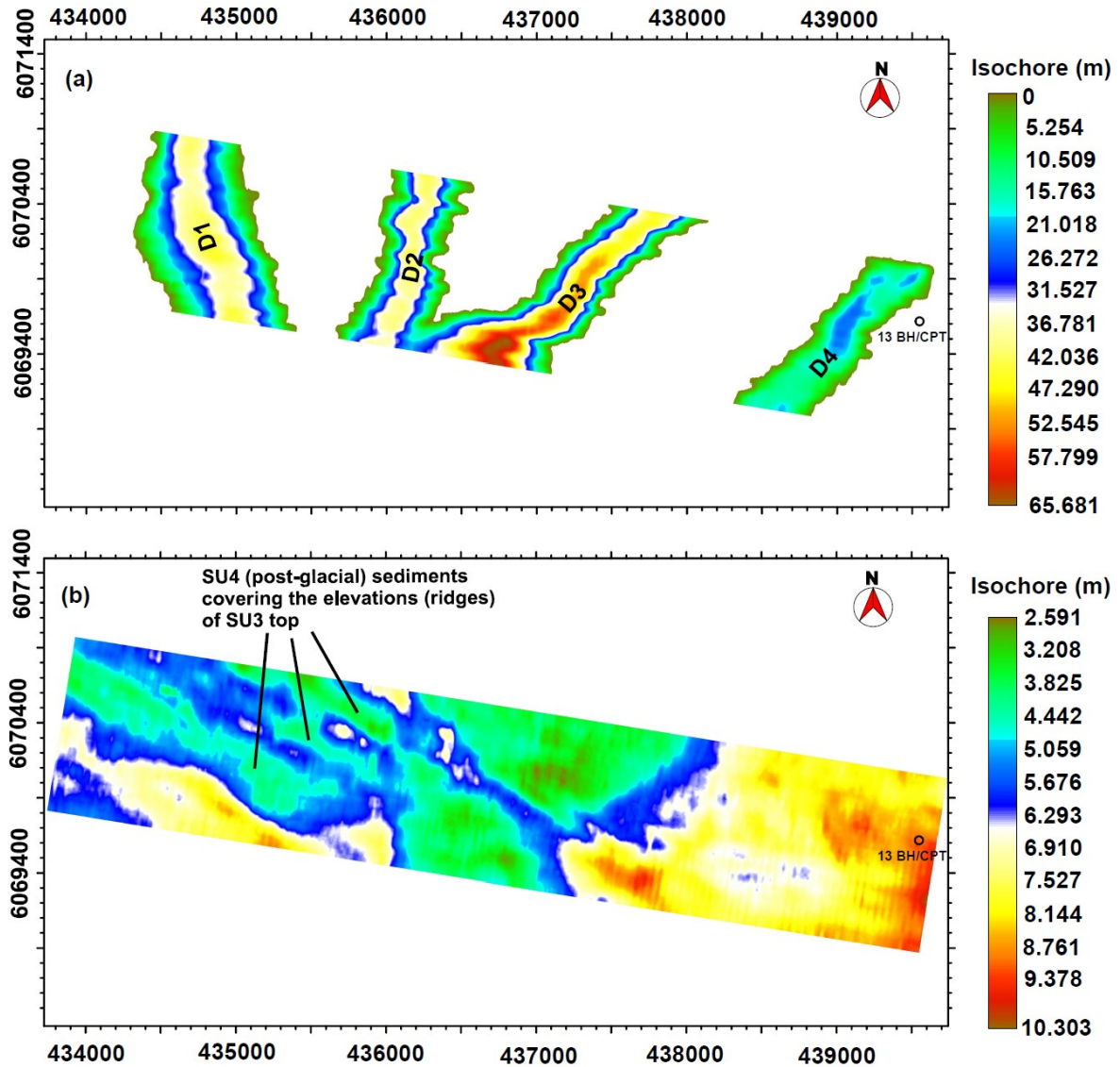


Fig. 3.5: Isochore maps based on the 3D MCS data: (a) the true vertical thickness of SU2 sediments filling D1-4 (Quaternary glacial valleys; see fig. 3.3 for a vertical section cutting across the depressions). These depressions appear to interconnect in the southern part of the area and beyond; (b) the true vertical thickness map of SU4 (post-glacial) sediments. D = Depression (time-depth conversion was carried out with stacking velocity values of 2100 and 1475 m/s for SU2 and SU4, respectively, which were deduced during seismic data processing).

The true vertical thickness map generated for the channel fills (SU2) indicates that the 340-900 m wide depressions (D1-4) have a maximum depth of ~66 m, with their flanks being very jagged (fig. 3.5a). Besides, thickness variation of SU4 shows that its sediments are relatively thin above the underlying NW-SE trending elevations and

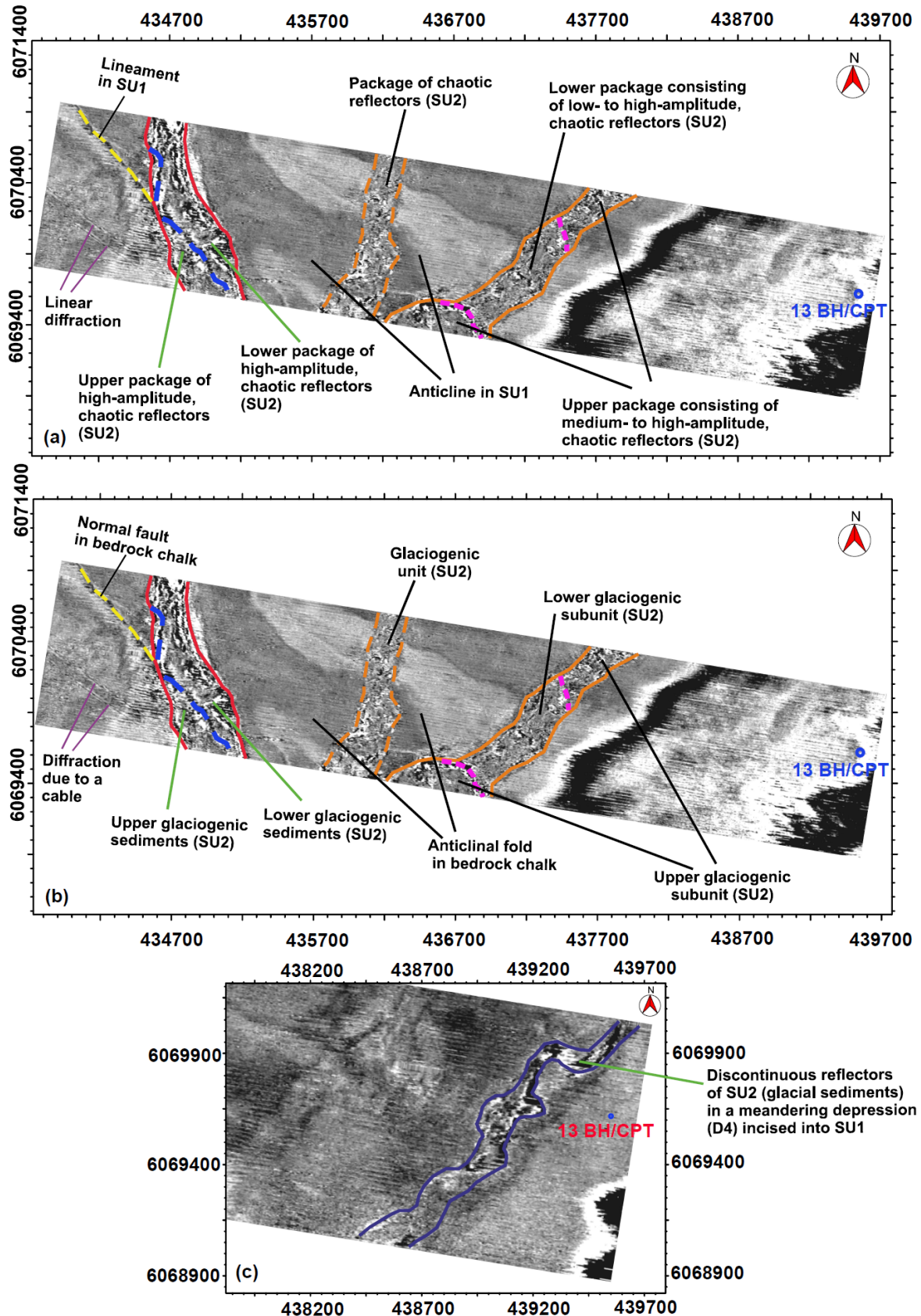


Fig. 3.6: Time slices through SU1 and SU2 in the 3D MCS data: (a) time slice at 0.097 s TWT and its description. Red outline delineates NW-SE trending Depression 1 (valley) filled with high-amplitude packages (SU2). Stippled and bold orange outlines are the respective spatial limits of Depressions 2 and 3. Facies boundaries of valley fills are shown as stippled blue and lilac lines; (b) interpreted version of '3.6a' showing the spatial distribution of sedimentary facies and structures; (c) section of the time slice at 0.080 s TWT displaying a meandering section of Depression 4 (purple outline) oriented NE-SW. TWT = Two-Way Travel-time; SU= Seismic Unit.

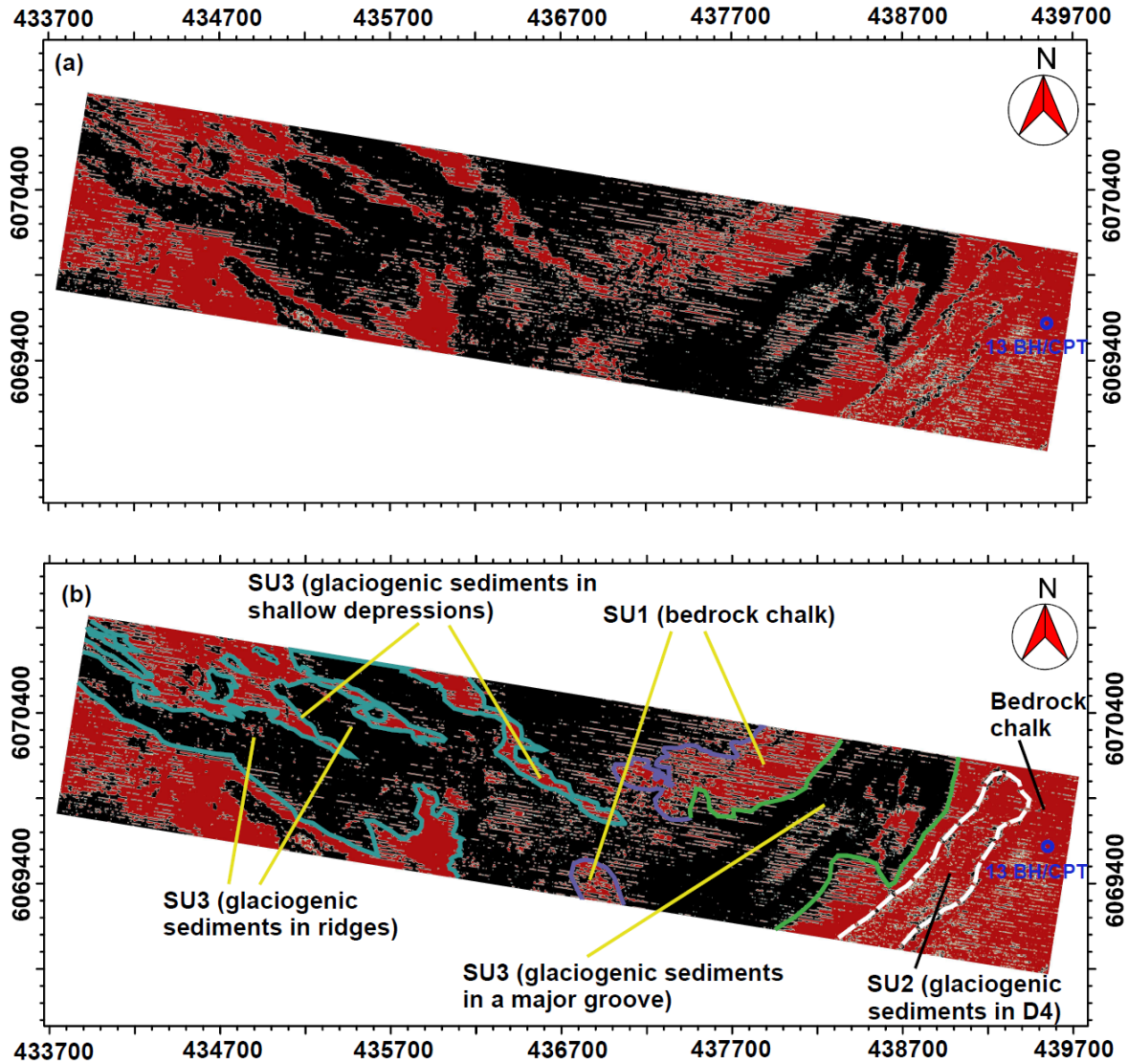


Fig. 3.7: Time slice at 0.064 s TWT in the 3D seismic cube: (a) un-interpreted version of the time slice; (b) distribution of sedimentary facies of SU1, SU2 and SU3 as interpreted on the time slice. Notice the NW-SE and NE-SW trending amplitude structures defined by seismic events in SU3. TWT = Two-Way Travel-time; SU = Seismic Unit.

gradually thicken towards the alternating depressions along the top of SU3 (figs. 3.4c and 3.5b).

### 3.4.2.3 Facies and structures observed on horizontal seismic sections

In the southcentral part of the study area, the time slice at 0.097 s two-way travel-time (TWT) reveals the structural framework of SU1 (figs. 3.6a-b). A NW-SE trending lineament is seen within SU1 in the western half of this time slice (fig. 3.6a).

On the time slices at 0.097 and 0.080 s TWT, Depressions 1-4 cut through SU1 and are variably oriented, probably interconnecting outside the 3D seismic cube area toward the south (figs. 3.6a-c). The NE-SW trending Depression 4 is sinuous (fig. 3.6c). Seismic facies within these depressions differ from those of SU1 (fig. 3.6a).

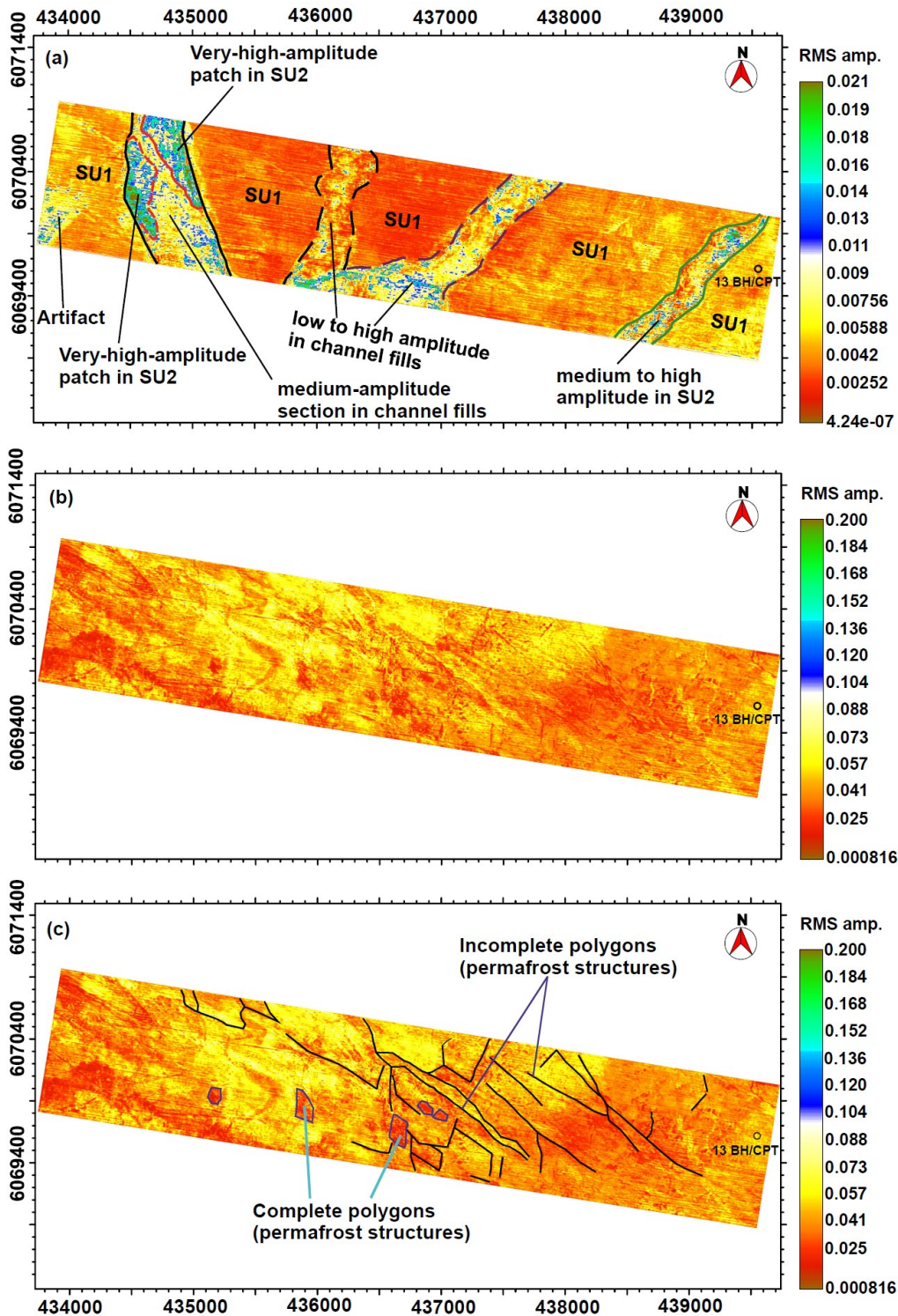


Fig. 3.8: RMS amplitude maps generated for SU1 to SU3 in the southcentral part of the study area: (a) an integrated map showing the amplitude characteristics of SU1 (Cretaceous chalk) and depression-filling SU2. Bold black and green lines delineate the flanks of Depressions 1 and 4, respectively; stippled black and purple lines are the respective limits of Depressions 2 and 3. The depressions are surrounded by SU1. The time windows within which RMS amplitudes of SU1 and SU2 were calculated are shown in fig. 3.3b; (b) un-interpreted RMS amplitude map generated from the top to base of SU3 (unchannelized glaciogenic unit) in the area; (c) interpreted RMS amplitude map of '3.8b'. Notice the polygonal features of a patterned ground in an ancient permafrost terrain. SU =Seismic Unit; amp. = amplitude

Facies boundaries between the lower and upper sedimentary subunits in Depressions 1 and 3 are represented as lineaments on the time slice at 0.097 s TWT (figs. 3.6a-b).

Traversing from WNW to ESE on the time slice at 0.064 s TWT, seismic events delineate NW-SE trending linear amplitude structures of SU3 which pass into a broader NE-SW oriented amplitude structure of the same seismic unit (figs. 3.7a-b). The location of these amplitude structures correspond to that of similarly oriented elevations and depressions observed on the time structure map of SU3 base (fig. 3.4b).

#### **3.4.2.4 RMS amplitude maps**

SU1 exhibits RMS amplitude which is relatively lower than that of SU2 and gradually changes laterally (fig. 3.8a). The amplitude characteristics of SU2 vary from depression to depression. Among the fills of Depressions 1-4, the lowest RMS amplitude was observed in Depression 2. In Depression 1, the RMS amplitude map shows two distinct patches of very high amplitude, one of which is associated with the depression's eastern flank, while the other is associated with its western flank (fig. 3.8a).

Moreover, on a map of RMS amplitude extracted from the top of SU3 to its base, there are networking lineaments that form polygonal features (figs. 3.8b-c). While the sides of only a few of the polygons are complete, most polygons in the network are incomplete.

### **3.4.3 2D stratigraphic and structural description in adjoining areas**

#### **3.4.3.1 Southeastern to western profile**

Within SU1, two main categories of lineaments exist (fig. 3.2), namely: (1) basement-reaching linear structures dissecting SU1a and SU1b and having an easterly dip of  $\sim 49^\circ$  in the southeastern part of the study area (across one of these lineaments, a thick package of reflectors is continuously bent from the hanging wall to the foot wall blocks without displacement of the folded structure); and (2) several relatively shallow lineaments (not reaching the basement) dipping at  $\sim 70^\circ$  easterly and westerly, cutting through the sequence from SU1a through SU1b to SU1c in the southcentral to western region, with this group of lineaments cross-cutting and displacing the bent reflectors (folded structure) observed in the shallowest part of SU1. The degree of folding of SU1 reflectors decreases further away from the basement-reaching lineaments (fig. 3.2).

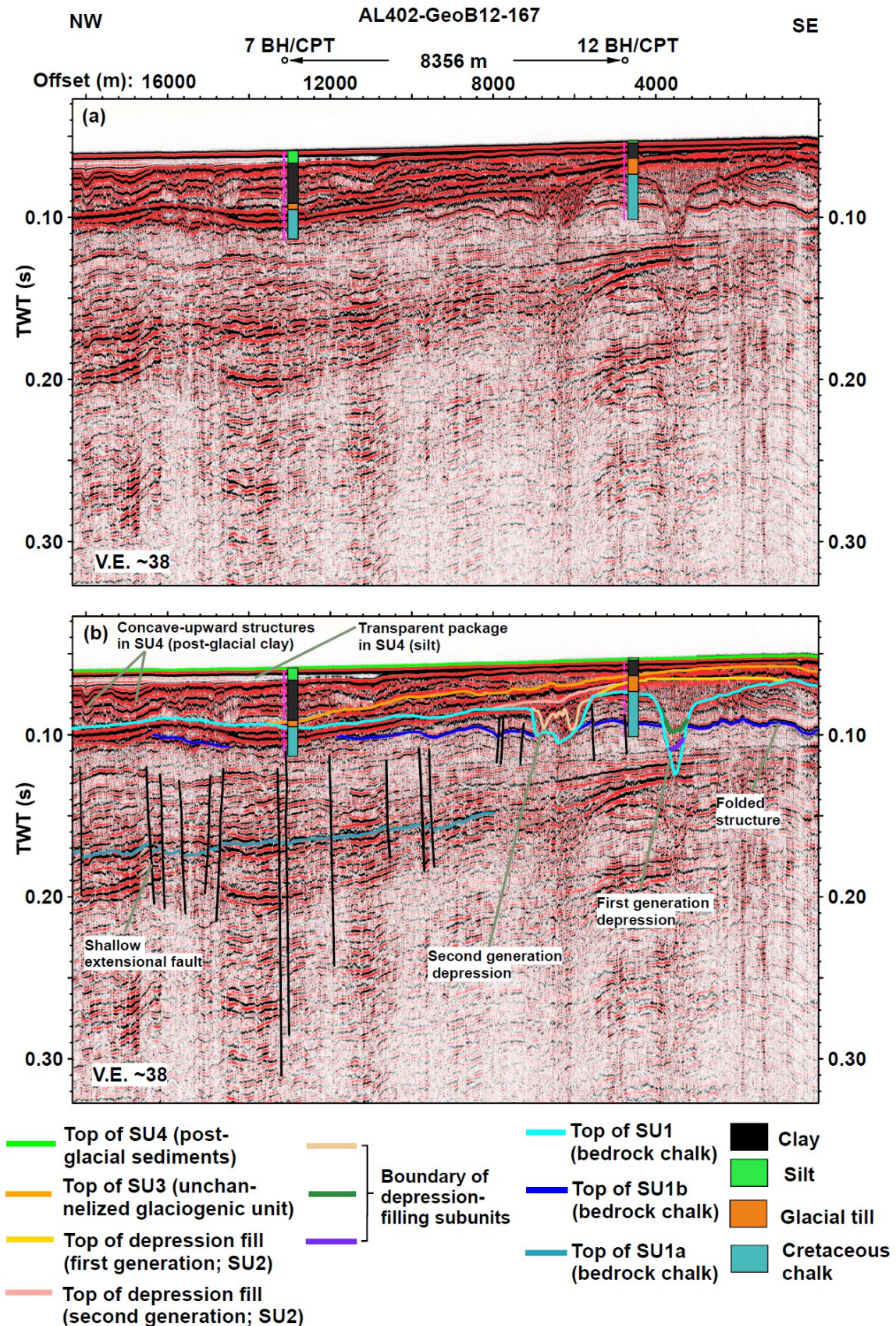


Fig. 3.9: 2D seismic Profile AL402-GeoB12-167 (see fig. 3.1 for location): (a) un-interpreted of the seismic section tied with lithologic logs from boreholes 7 and 12 BH/CPT; (b) seismo-stratigraphic succession and structural features interpreted on '3.9a'. SU1a-c represent three subunits of the bedrock chalk. Two generations of depressions (Pleistocene tunnel valleys) which cut into SU1 are shown. TWT = Two-Way Travel-time; SU = Seismic Unit (vertical exaggeration was calculated with a velocity of 2000 m/s)

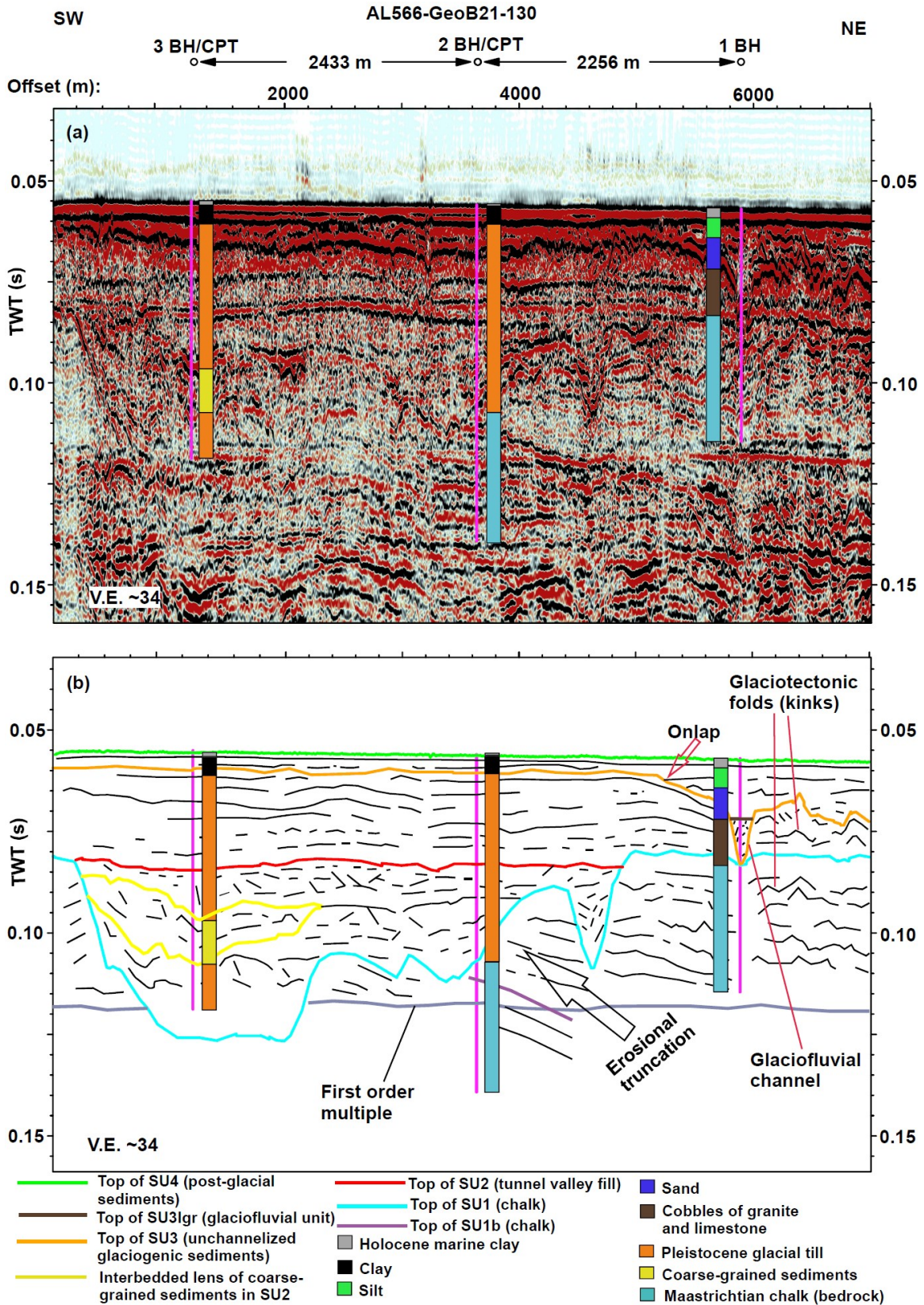


Fig. 3.10: 2D MCS Profile AL566-GeoB21-130 (see fig. 3.1 for location): (a) un-interpreted version of the seismic section tied with lithologic logs from boreholes 1 BH, 2 BH/CPT and 3 BH/CPT in the northern part of the study area; (b) sketch of the stratigraphic framework interpreted from '3.10a'. Notice a major depression belonging to an undifferentiated generation of tunnel valley, which contains an interbedded lens of coarse-grained sediments as part of its infill. A relatively minor depression interpreted as a glaciofluvial channel was incised into SU3. TWT = Two-Way Travel-time; SU = Seismic Unit (vertical exaggeration was calculated based on a velocity of 2000 m/s)

In the southeast, depression-filling packages of low-amplitude, discontinuous reflectors (SU2) exist. Deep channels incised into SU1 in the southcentral region contain one to three package(s) of discontinuous seismic reflectors within each depression, with V-shaped surfaces separating the multiple packages (fig. 3.2). Further west of these depressions along the seismic profile shown in fig. 3.2, amalgamated deep depressions are filled with stratified sediments represented as subparallel, strong seismic reflectors that are discontinuous and bent.

#### **3.4.3.2 Northwestern to southcentral profile**

Along seismic Profile AL402-GeoB12-167, SU1a-c are dissected by shallow lineaments dipping easterly and westerly at  $\sim 24^\circ$  (fig. 3.9). These linear features also cross-cut the folded reflectors in SU1b and SU1c in the southcentral area. In this area, first and second generations of deep depressions are filled with older and younger sediments of SU2, respectively (fig. 3.9). In the first generation depression, three distinct packages of low-amplitude, chaotic seismic reflectors exist, and these are separated by continuous, high-amplitude seismic events. The two reflector packages occurring in the younger valley exhibit high amplitudes. In the northwestern to southcentral region, SU3 shows high-amplitude, fairly continuous reflectors that are subparallel. SU4 thickens in the northwestern direction.

#### **3.4.3.3 Central to northern profile**

In the central and northern parts of the study area, the degree to which SU1 reflectors are folded west of the basement-reaching lineaments reduces as one traverses away from the lineaments. In the northern part, SU1c reflectors are bent into kinks below the top of SU1 (fig. 3.10). Besides, close to the top of SU1 in the central area, a localized zone with a maximum width of  $\sim 940$  m exists in which lineaments separate blocks of SU1c reflectors.

The major deep channel structure observed in the northern region contains medium-amplitude, discontinuous and predominantly chaotic SU2 reflectors (fig. 3.10). Unchannelized and laterally extensive SU3 has an irregular top and develops kinks in the extreme northern section. Here, a minor concave-upward V-shaped depression filled with low-amplitude, chaotic reflectors forms along the top of SU3 (fig. 3.10). The overlying seismic reflectors of SU4 partly onlap the top of SU3 in the area.

## 3.5 Discussion

### 3.5.1 Architecture of the shallow Cretaceous to Holocene succession

SU1 consists of Cretaceous bedrock chalk with three subunits (fig. 3.9). 14 boreholes drilled into intervals below the top of SU1 in the northern, northwestern, western, central, southcentral and southeastern parts of the study area (e.g. 2, 6 and 12 BH/CPT) have confirmed this lithologic interpretation. In the southeastern through central to northern areas, bent seismic reflectors in the Cretaceous chalk sections exhibit convex-upward structures (e.g. fig. 3.2) associated with the Tornquist Zone (Schluter et al., 1997). One of these convex-upward structures crosses the basement-reaching Nordadler faults without any linear displacements of the structure (a limb of this structure associated with the Nordadler faults is shown in fig. 3.2). Thus, the convex-upward structures in the study area post-date the Nordadler faults which began forming in the Permian (cf. Seidel, 2019). The set of relatively shallow lineaments cutting through and displacing the anticlinal (convex-upward) structures in southcentral to western regions (figs. 3.2, 3.3, 3.4a and 3.9) are interpreted as normal faults (cf. Tearpock and Bischke, 1991). This category of normal faults dissects the three subunits of chalk and is subdivided into two based on dip angles, namely: (1) high-angle normal faults dipping at  $\sim 70^\circ$ ; and (2) low-angle normal faults with a dip angle of  $\sim 24^\circ$ .

In the central part of the study area, the Cretaceous bedrock chalk has been fractured directly below the Top of Cretaceous (TC) within a localized section which has a width  $< 950$  m as observed on our seismic data. This particular zone was confirmed as fissured chalk in Hole 11 BH/CPT.

Although it might be thought that the chaotic reflectors of SU2 constitute glaciodynamic mélanges formed by the mixing of bedrock chalk in a subglacial setting, this argument is not supported by our observations. Lateral boundaries of SU2 have a V-shaped structure in places (e.g. first generation deep depression shown in fig. 3.2). Even in the southcentral area where these V-shaped boundaries are obscured on inlines in the 3D seismic cube due to their jaggedness (figs. 3.3 and 3.5a), they are clearly observable on arbitrary seismic lines passing perpendicularly through smooth sections of the boundaries. This probably implies that the distinct lateral boundaries of SU2 represent interfaces between two sedimentary units that are acoustically different from each other, as in the case of a depression carved into a bedrock and filled with a

different material. Furthermore, the V-shape of the distinct interfaces between SU1 and SU2 (figs. 3.2, 3.3 and 3.9) and the interconnectivity of some zones delineated by these interfaces as evidenced in planar view (figs. 3.5a and 3.6) as well as the meandering nature of the interface between SU1 and SU2 along Depression 4 (fig. 3.6c) apparently show that these interfaces delineate depressions or channels whose origin is related to bedrock-cutting by a system of flowing water. In the Arkona Basin, the TC is the base of Quaternary glacial deposits (Obst et al., 2017). Consequently, the channels containing SU2, part of which are 340-900 m wide with a maximum depth of ~66 m and an undulating thalweg in the southcentral area, are herein interpreted as subglacial tunnel valleys formed by meltwater erosion of the Cretaceous chalk (bedrock) during a 'steady state' drainage of meltwater and/or by catastrophic discharge (Huuse and Lykke-Andersen, 2000; Jørgensen and Sandersen, 2006; van der Vegt et al., 2012). Similar V-shaped tunnel valleys have been incised in Cretaceous chalk in East Anglia (Woodland, 1970). In our study area, the occurrence of distinct facies boundaries representing erosional surfaces between successive packages of SU2 within the deep depressions partly supports the interpretation that SU2 sediments are valley fills (figs. 3.2, 3.3 and 3.6a). The aforementioned internal and external characteristics of SU2 which fills the tunnel valleys in our study area indicate that the unit consists of glaciogenic sediments deposited within the channels. Glacially derived diamictons are generally poorly sorted and could be massive in appearance. Thus, their preponderance in the valleys could be the reason for the predominantly chaotic and discontinuous nature of the seismic reflectors of SU2. Boreholes drilled into the valleys in the northern and southeastern parts of the study area (2, 3 and 17 BH/CPT) confirm that these valley fills associated with low- to medium-amplitude, chaotic and discontinuous reflectors are mainly Pleistocene glacial tills. The discontinuous, chaotic, high-amplitude events present in SU2 in some valleys (e.g. Depression 1 in fig. 3.3) could be due to the coarser particles in the glacial till. However, where subparallel to parallel configuration of seismic reflectors indicate apparent stratification in the valley fills, it could be that there are other types of glaciogenic sediments present.

On one hand, three generations of glacially incised valleys have been recognized in the North Sea and around England, namely: Elsterian, Saalian and Weichselian (Wingfield, 1990). Although Flodén et al. (1997) reported two and three generations of valleys in the Hanö Bay and Arkona Basin, respectively, only two generations of glacial

valleys could be unequivocally distinguished in the southcentral part of our study area (fig. 3.9). In this area, horizon interpretation reveals that both Depression 1 in the 3D MCS cube area and other valleys with infills connected to those of Depression 1 belong to the first generation valley system. Depression 1 which bears two subunits of Pleistocene glaciogenic sediments truncates the aforementioned low-angle normal faults formed in the Cretaceous bedrock (fig. 3.3).

Valley fills in the study area are highly heterogeneous. In the north and southeast, seismic attributes and evidences from Holes 2, 3 and 17 BH/CPT drilled into valleys show that Pleistocene tills in the valleys might be interbedded with sand units and/or lenses of subangular to subrounded gravel-to-cobble sized particles (fig. 3.10). In the southcentral area, valleys clearly distinguished as belonging to the first generation are filled with multiple (two to three) packages of till-dominated Pleistocene glaciogenic sediments (figs. 3.2, 3.3 and 3.9). Besides, several valleys belonging to an unidentified generation contain one to two package(s) of till-dominated sediments in the southern, southcentral and central parts of our research area. In this study, however, valleys which partly or wholly contain apparently stratified sediments are of the second and undifferentiated generation(s) (e.g. the second generation valley in fig. 3.9 which shows bent and discontinuous stratifications of infills, and the major valley in fig. 3.10 which contains a lens of interbedded coarse-grained sediments and thin beds of sand within the valley fill). These also include the amalgamated depressions filled with high-amplitude, subparallel reflectors in fig. 3.2 which indicate parallel stratification of sediments typical of glaciofluvial to glaciolacustrine depositional settings. These parallel stratified sediments are evidently not glacial tills as tills are usually massive. This degree of heterogeneity of valley fills has been recognized by past authors who showed that although several till units are unstratified, massive and unstructured (e.g. Menzies et al., 2018), within subglacial depressions and channels a variety of stratified sediments including laminated clays might be present (e.g., Menzies and Woodward, 1993; Goldschmidt, 1994; Roberts and Hart, 2005).

The regionally extensive and areally unrestricted SU3 in our study area is interpreted as a Pleistocene interval dominated by unchannelized tills (cf. Menzies et al., 2018). This interpretation is supported by sediment descriptions at 15 borehole locations, which indicates that the dominant lithofacies of this unit is Pleistocene glacial till, but as discussed in section 3.4.1.3, this sedimentary unit is obviously different from SU2 tills. In a localized place in the central part of the study area, sediment descriptions in

Hole 11 BH/CPT reveals that SU3 partly consists of a basal layer of cobble-sized fragments of granite, flint and chalk directly overlying the Cretaceous chalk and tapering to the NW along seismic Profile AL402-GeoB12-168. This basal sedimentary interval is succeeded by two till units separated by a clay horizon in SU3. Based on the dominance of the till facies in SU3, the entire seismic unit is hereinafter referred to as 'unchannelized till.'

In the southcentral area covered by the 3D MCS data, the NW-SE trending set of parallel shallow depressions and the NE-SW oriented major groove at the base of the unchannelized till have dimensional characteristics typical of subglacially sculptured s-forms (fig. 3.4b). Such s-forms are generally either longer than they are wide (longitudinal variants) or wider than they are long (transverse types) (Kor et al., 1991; Munro-Stasiuk et al., 2013). On one hand, it might be thought that the elongated depressions which partly alternate with elevated sections at the base of the unchannelized till (fig. 3.4b) are due to pre-existing undulating morphology associated with bending of Cretaceous chalk strata prior to deposition of the till. However, this is unlikely because only one major anticlinal structure in the Cretaceous chalk was observed beneath the multiple NW-SE oriented depressions and elevations at the base of the till, and the hinge line of this anticline is curvilinear, which differs from the linear structure of the s-forms (figs. 3.4a-b).

The ~2 m high NW-SE trending elevations which alternate with depressions along the top of the unchannelized till in the southcentral area are glacial ridges (fig. 3.4c), probably structurally similar to the moraine ridges mentioned by Menzies et al. (2018) and the submarine De Geer moraines observed in the Kvarken Archipelago between Sweden and Finland in the Baltic Sea (Kotilainen et al., 2012). The locations of these ridges in our study area coincide with those of similarly trending elevations (protrusions in a glacial substratum) observed at the base of SU3 (fig. 3.4b).

In the northern area, since a concave-upward depression filled with cobbles of granite and limestone (no finer grains) has been carved into the top of the unchannelized till (shallowest till unit) in the stratigraphic record and the infill of the depression has been reported to be the shallowest glaciogenic unit as observed in Hole 1 BH, the trough itself is herein interpreted as a Quaternary glaciofluvial channel in the area (fig. 3.10). The textural description of its sedimentary infill shows that the infill is probably not till.

In the northern area, SU4 sediments partly onlap the top of the unchanneled till unit (fig. 3.10). In the southcentral area, SU4 sediments draping over the underlying NW-SE trending glacial ridges formed by SU3 deposits are thinner than those filling structural depressions associated with these ridges (fig. 3.5b). Lithologic description at 15 borehole locations (e.g. 1 BH, 8 BH/CPT and 13 BH/CPT) shows that SU4 represents post-glacial clay, silt and sand (table 3.1).

### **3.5.2 Pleistocene ice flow during tunnel valley formation in the Arkona Basin - sedimentation and reworking of glaciogenic valley fills**

Flodén et al. (1997) mentioned that valleys in the North Sea and around England were filled with sediments of the same age as the incisions. Obst et al. (2017) showed that the oldest sediments within valleys incised into the Cretaceous chalk in the southeastern part of our study area are of the Late Saalian Warthe glacier advance, with the top of Cretaceous being the base of Pleistocene glacial deposits. Besides, the valley-filling glacial till observed in the north were dated to be Pleistocene. Thus, we posit that the V-shaped tunnel valleys in our study area (e.g. figs. 3.2 and 3.9; including Depression 1 in figs. 3.3 and 3.6) were incised by meltwater into the Cretaceous bedrock chalk (see section 3.5.1) and filled during Pleistocene. Although two distinct generations of these Pleistocene valleys were obvious in the southcentral part of our study area, it is possible that the valleys were incised during one or more glaciation(s). Patterns of tunnel valleys in northern Europe within the Pleistocene reveal that several valley generations can be eroded and filled during one glaciation (e.g. Baker 1977).

Tunnel valleys occur within past ice margins and their general orientation is parallel to ice flow (Huuse and Lykke-Andersen, 2000; van der Vegt et al., 2012). However, since the path of the tunnel valleys was not mapped regionally across the entire study area in this research, the overall ice flow direction of the valley-forming glacier is not very obvious. Following the opening of the valleys, the Pleistocene glacier must have moved into most valleys and deposited its loads in the channels mainly as tills in our study area. Relatively minor meltwater deposition might have also taken place in these valleys as indicated by interlayered sand encountered in some of the channels. In valleys where there are two or three main packages of till-dominated valley fill (figs. 3.2, 3.3 and 3.9), multiple depositional episodes by glacier(s) have taken place. These major episodes were separated by erosion of underlying sediments at valley locations probably due to periodic discharge of significant meltwater and/or direct glacier-

sediment interaction (cf. van der Vegt et al., 2012) as indicated by V-shaped and rugged surfaces separating the major valley fill packages. Removal of pre-existing sediments might be due to intermittent resumption of erosional activities by the same glacier that deposited those sediments or it might be associated with advancement of a different Pleistocene glacier. It is noteworthy that tills of two different advances (Saalian and Middle Weichselian) were reported in tunnel valleys in the southeastern part of our study area (Obst et al., 2017). Furthermore, valley fills characterized by high-amplitude, subparallel seismic reflectors are interpreted as glaciofluvial to glaciolacustrine sediments (e.g. the fills of the amalgamated depressions in the southcentral area in fig. 3.2). Similarly, on Jasmund peninsula, layers of glaciofluvial to glaciolacustrine clay, sand and gravel are interbedded with four Pleistocene subglacial diamictons (M0, M1, M2 and M3), with M0 and M1 representing the Saalian ice advance, and M2 and M3 tills belonging to the Weichselian (Kenzler et al., 2017; Plonka et al., 2022).

Menzies et al. (2018) pointed out that variability in sedimentary facies and internal structures as well as grain size distributions within subglacial tunnels are evidences of changing subglacial meltwater stream competency. Thus, the intercalation of sand layers and lenses of gravel-to-cobble sized sediments within tunnel valley fills in the southern Arkona Basin might indicate fluctuations in meltwater discharge and velocity within those valleys which probably led to meltwater deposition of the sand units and coarser-grained intervals. Although in the northern part of the study area the lens of gravel-to-cobble sized sediments corresponds to anomalously high-amplitude seismic events and has been sandwiched within a valley fill dominated by till (fig. 3.10), the cohesive nature of glacial tills observed along the Baltic Sea coastline of Schleswig-Holstein in Germany (Averes et al., 2021) indicates that it might be unlikely that the lens is a product of winnowing of finer particles away from a pre-existing till unit.

As a Pleistocene glacier responsible for the deposition advanced, underlying glaciogenic sediments deposited and eroded within the valleys, including previously deposited tills, formed part of the newer substratum and as such might have been deformed (cf. Evans et al., 2006). Besides, it has been reported that when a glaciogenic deposit is re-activated in a deforming bed due to renewal of glacier activity, primary structures of the deposits are at least partly lost (cf. Paul and Eyles, 1990; Möller, 2010; Menzies, 2012). In the southcentral area, glaciotectonic deformation beneath an advancing Pleistocene glacier was probably responsible for the folding

and discontinuity of stratification not only in the glaciofluvial to glaciolacustrine sediments filling the amalgamated depressions (fig. 3.2), but also in the younger glaciogenic package in the second generation valley (fig. 3.9). It is to be noted that above-mentioned interpretations of valley fills are subject to refinement when more boreholes are drilled through the fills and additional information is available.

### **3.5.3 Weichselian glaciation - local ice flow direction, sediment deposition and buried glacial landforms**

The last major advancement of Pleistocene glacier is documented in the topmost regionally extensive and unchannelized glacial till interval consisting of two till units, and which overlies valley fills and Cretaceous bedrock across the entire study area. In the southern Arkona Basin, the youngest glacier advance recorded was the Mecklenburg advance. Obst et al. (2017) reported a regionally extensive youngest till interval which was ubiquitously deposited during this advance in the southeastern part of our study area. Besides, they showed that some Pomeranian tills were deposited outside the valleys, on top of the Cretaceous bedrock and beneath the Mecklenburg tills in some places in the southeast. Thus, in this current research we herein interpret the unchannelized till interval consisting of two till subunits and corresponding to an extension of the Mecklenburg-Pomeranian interval of aforementioned authors as being deposited in the Weichselian.

During the Mecklenburg advance, a westward flowing ice mass passed through the depression between South Skane and North Germany, and the main stream moved through the opening between Bornholm and Rügen islands, fanning out in diverse directions including SW-wards toward Rügen Island and Pomeranian Bight (Stephan, 2001). Thus, in the southcentral area in our study, the major groove with a longer axis trending in the NE-SW direction at the base of the unchannelized till most probably represents a longitudinal s-form sculptured into the Cretaceous chalk by erosional activities beneath Weichselian glacier(s) that locally flowed in the NE to SW direction (fig. 3.4b; Munro-Stasiuk et al., 2013; see section 3.5.1 for the basis of this interpretation). Similarly, the NW-SE oriented shallow depressions cutting across the top of the Cretaceous chalk and Pleistocene valley fills have a relatively short dimension in the perpendicular direction, and are also likely to be s-forms formed through subglacial erosion (fig. 3.4b; Munro-Stasiuk et al., 2013; Menzies et al., 2018)

during Weichselian, but the timing of their formation relative to the NE-SW trending s-forms could not be clearly ascertained.

The interval of cobble-sized rock fragments observed in the lowermost part of SU3 directly overlies the Cretaceous chalk in the central part of the study area. The cobbly interval was not reported as a glacial till, which possibly meant that it was not deposited directly by a glacier. Besides, its coarse grain size appears to depict a high-energy depositional setting which would make a glaciolacustrine setting unlikely. Thus, owing to its stratigraphic position on the TC, it is probable that the cobbly interval represents glaciofluvial sediments associated with the retreat of a previous valley-filling Pleistocene glacier. Gravel-sized sediments deposited in ice-free conditions have been documented on the Jasmund Peninsula (Plonka et al., 2022).

The two till subunits occurring in SU3 record two glacial depositional episodes in the Weichselian as they are separated by a clay unit in the central part of the study area. This clay unit itself is not till and its fine grain size indicates a low-energy depositional environment. Thus, we posit that the clay unit was deposited probably in a glaciolacustrine setting during a retreat of the Weichselian glacier. It is noteworthy that Plonka et al. (2022) similarly reported glaciofluvial, glaciolacustrine and alluvial sediments between the two subglacial M2 and M3 Weichselian tills along a Dwasieden cliff section exposed on the Jasmund peninsula. The sediments of alluvial and glaciofluvial origin along the cliff section were of sand to gravel size. This probably implies that the clay unit mentioned above in the central part of our study area is not alluvial or glaciofluvial in origin.

Furthermore, NW-SE trending ridges have been observed as positive structures alternating with depressions along the top of the Weichselian till unit in the southcentral area (fig. 3.4c). The ridge-forming process could be associated with the accumulation of glacially deposited sediments around some nuclei of similarly oriented protrusions in the bedrock of the depositing glacier which we observed at the same geographic locations along the top of Cretaceous chalk and valley fills (i.e. base of the unchannelized Weichselian till-dominated unit) in the area (figs. 3.4b-c).

Moreover, the networking lineaments that form geometric patterns on the RMS amplitude map of the unchannelized till unit are relict permafrost structures on an ancient patterned ground associated with the Weichselian glacier (figs. 3.8b-c). This feature has not been recognized by previous authors in the Weichselian till unit in the

Arkona Basin. The mega-scale geometric patterns of the original patterned ground might have formed by thermal contraction cracking in a permafrost associated with networks of intersecting vertically oriented ice wedges (Pollard, 2018). However, the permafrost itself probably melted away considering that the last glacier advance took place in Weichselian after which global temperature rose significantly and the local setting in the Arkona Basin changed from a glacial environment through different water-dominated stages of varying salinity to present-day Baltic Sea conditions (cf. Kortekaas et al., 2007).

Furthermore, based on its stratigraphic position as presented in section 3.5.1, the cobble-filled Quaternary channel incised through the top of the unchanneled Weichselian till unit in the northern part of the study area (fig. 3.10) was probably formed during the last glacier retreat in which a glaciofluvial stream cut into the underlying till unit through erosional activities and deposited its load within its channel. We do not interpret the channel fill as a glacial till since there is no evidence of poor sorting in the sediment. Above-mentioned interpretations of Weichselian deposition are subject to further investigation and improvement through the drilling of additional boreholes and detailed sediment descriptions in the study area.

#### **3.5.4 Post-glacial sedimentation**

In the northern part of the study area, the onlap of SU4 reflectors along the top of SU3 signifies the end of Quaternary glacial deposition and the onset of late-glacial to Holocene sedimentation in lacustrine and marine to brackish-water settings in the study area (fig. 3.10; cf. Xu and Haq, 2022). Post-glacial sediments in this research include sand, silt and clay (fig. 3.10) deposited sequel to the retreat of the Scandinavian Ice Sheet (cf. Obst et al., 2017). In the southcentral part of the study area, undifferentiated clay and/or silt cap(s) the entire lithostratigraphic succession. In the northwestern area, the thick clay interval in the basal section of post-glacial sediments is characterized by concave-upward structures (fig. 3.9), with this interval being overlain by a seismically transparent zone of silt in the shallowest sub-seafloor. The bent structures within the clay section might be morphological features that existed prior to sedimentation of overlying silt.

### **3.5.5 Late Cretaceous to Pleistocene structural deformation of bedrock chalk and unchanneled Pleistocene till unit – the influence of varying tectonic and glacial processes**

Although it could be said that the convex-upward structures in the Cretaceous chalk were probably inherited from pre-existing morphology on the seafloor of the Chalk Sea during sedimentation, this appears not to be the case because we did not observe divergent reflectors in the bent section of the chalk (figs. 3.2, 3.3, and 3.9). Thus, it appears that the bending of Cretaceous chalk strata to form the convex-upward structures was post-depositional. The undisplaced anticlinal structure of Cretaceous chalk that crosses Nordadler faults in the southeastern area and other similarly bent structures within the bedrock in the study area could be formed during the Late Cretaceous structural inversion that occurred in the vicinity of the Tornquist Zone and adjoining faults (Hübscher et al., 2019). This structural inversion was associated with compressional stress that must have caused crustal shortening and in turn folding of Cretaceous strata.

Although it could be thought that the relatively shallow extensional faults in the bedrock chalk (figs. 3.2, 3.3, 3.4a and 3.9) were formed in the Quaternary, probably through glaciotectonic deformation, our observations show that this is not plausible. Foremost, the major glaciotectonic faults in the Cretaceous chalk on Jasmund Peninsula are thrust faults. Besides, the relatively shallow normal faults do not reach the top of Cretaceous, which might exclude the possibility of an advancing Quaternary glacier moving along the top of Cretaceous as the source of deformation. However, it is noteworthy that if a glacier freezes to the bedrock and is mechanically coupled to the ground, it can deform deeply, but with melting, the surface layers may be affected and modified. This explanation would need field evidence to argue for it. Furthermore, these relatively shallow extensional faults do not cut into any valley fills, which probably implies that they were not formed during glacio-isostatic rebound in the Quaternary. Since a first generation valley (Depression 1 in fig. 3.3) in the southcentral area partly forms the Quaternary base and the valley truncates some of the relatively shallow normal faults that cut across the folds formed in the Late Cretaceous (figs. 3.2, 3.3, 3.4a and 3.9), it follows that these relatively shallow normal faults were formed before Pleistocene, but most likely during a crustal extension in Tertiary after the Late Cretaceous inversion. Al Hseinat and Hübscher (2017) showed that a Tertiary extensional event faulted existing strata in the southern Baltic Sea. Furthermore,

based on the variation in dip angles of these Tertiary normal faults in our study area, it appears that the causal tectonic crustal extension that affected the area was in two regimes, namely: (1) a regime which formed relatively shallow normal faults steeply dipping at  $\sim 70^\circ$  and extending to intermediate levels in the bedrock chalk (fig. 3.2); and (2) another regime that led to low-angle ( $\sim 24^\circ$ ) normal faulting which predominantly affected the shallowest sections of the bedrock chalk (fig. 3.3). However, the exact order of these regimes is not evident.

In the Quaternary, glaciotectonic deformation of the bedrock by advancing glaciers has also left imprints in the Cretaceous chalk. In the central part of the study area, a localized zone (maximum width of  $\sim 940$  m) exists in which lineaments interpreted as fractures separate blocks of bedrock chalk directly beneath the TC. This fissured zone of chalk was observed in Hole 11 BH/CPT. Due to its location directly beneath the TC, it must have formed during non-penetrative brittle deformation of the shallowest part of the bedrock by a Pleistocene glacier (Phillips, 2018), probably in a subglacial setting.

Also, in the northern part of the study area, an  $\sim 40$  m thick interval of kink folds vertically extends from the shallowest section of the Cretaceous chalk into an overlying section of the unchannelized Weichselian till up to the top of the till unit (fig. 3.10). In view of the sections affected in the stratigraphic record, a possible source of the kink structures could be stress-induced deformation in the Quaternary. However, this would not be an active neotectonic process because the post-glacial sediments are completely unaffected. Thus, considering the closeness of this interval of kink folds to the top of unchannelized till unit and TC, these kinks are likely evidences of subglacial shearing in the bedrock chalk and till sediments when the last Pleistocene glacier(s) advanced in the area (Aber, 1982). This deformed interval would consist of glaciodynamic *mélange* formed when the affected materials were partly or largely frozen (Berthelsen, 1979; Aber, 1980). Menzies et al. (2018) explained that glaciogenic sediments are sometimes further re-activated and deformed by an advancing glacier, and the deformation obliterates many or all of previous sedimentary structures.

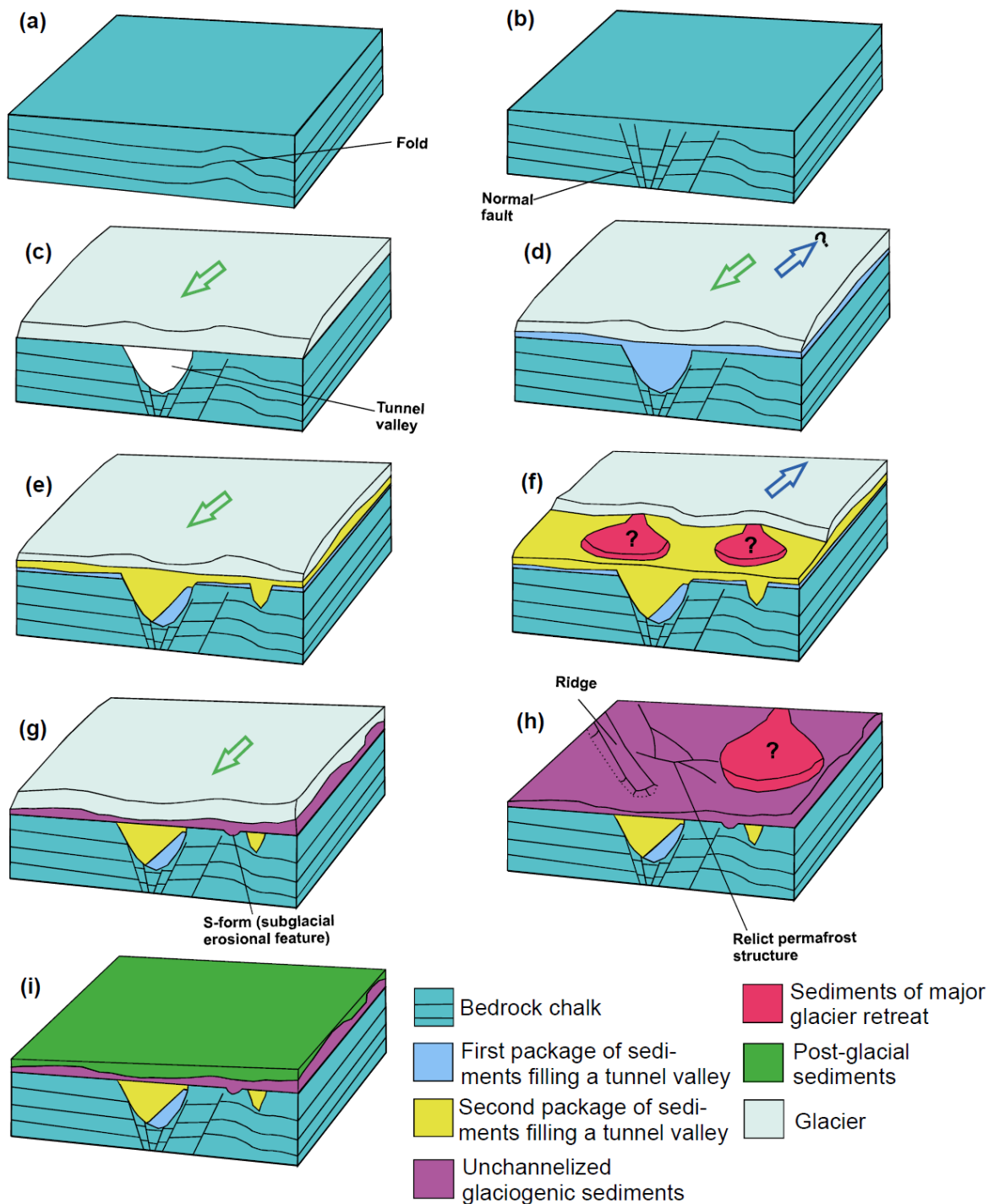


Fig. 3.11: Model of the Late Cretaceous to Holocene geological evolution in the 3D MCS coverage area. Green and blue arrows indicate ice advance and retreat, respectively, in Pleistocene. (a) folding of the bedrock chalk during a Late Cretaceous inversion; (b) Tertiary crustal extension formed normal faults in the chalk; (c) subglacial meltwater erosion of the bedrock during Pleistocene glacier advancement(s) formed tunnel valleys in the area. (d-e) one to two episode(s) of till-dominated sedimentation filled the valleys, with multiple events of deposition being separated by a period of erosion of pre-existing valley fills; (f) retreat of valley-filling glacier was probably associated with deposition of sediments; (g) advancing Weichselian glacier(s) removed part of the pre-existing glaciogenic sediments and produced subglacial s-forms across the top of Cretaceous chalk and Pleistocene valley fills. Subsequent deposition of glacial debris led to formation of the laterally extensive Weichselian till unit; (h) after the last glacial retreat, NW-SE trending ridges and relict permafrost structures have been left on and within the Weichselian till unit, respectively; (i) sedimentation in the area culminated in the deposition of post-glacial silt and/or clay.

### **3.5.6 Conceptual model for the Late Cretaceous to Holocene evolution of shallow seabed in the 3D MCS area**

The Late Cretaceous to Holocene geological evolution in the 3D MCS coverage area commenced with structural folding of the bedrock chalk (fig. 3.11a) during a Late Cretaceous inversion which affected the seafloor of the epeiric Chalk Sea west of the Tornquist Zone (Hübscher et al., 2019). This was followed by a Tertiary crustal extension that led to normal faulting of the chalk (fig. 3.11b). Subsequent evolution of the area from Pleistocene to Holocene is summarized in figs. 3.11c-i. The sequence of events recorded in the sub-seafloor across the study area indicates that sediments of major glacier retreats might have been or are still present in the geological record (figs. 3.11f and h).

### **3.5.7 Significance of seismic stratigraphy for facies prediction and sediment correlation**

In the 2021 geotechnical report prepared by Ramboll for the northern part of the study area during a preliminary site investigation, the shallowest glaciogenic unit consisting of cobble-sized sediments lying on top of the Cretaceous chalk in Hole 1 BH (fig. 3.10) was correlated to be an extension of the Pleistocene tills of SU3 encountered in Hole 2 BH/CPT using only borehole data. However, integration of the borehole data with 2D seismic data along Profile AL566-GeoB21-130 shows that the structural configuration of SU3 top is characterized by a concave-upward structure (interpreted as a glaciofluvial channel in this study) and 1 BH was drilled into this channel (fig. 3.10). Besides, the seismic profile indicates that internal reflectors of SU3 display erosional truncation at the channel's flank (fig. 3.10). Therefore, it follows that the cobble-sized sediments encountered above the Cretaceous chalk in 1 BH are different from the tills of SU3 encountered in 2 BH/CPT (fig. 3.10). In this study, seismic facies analysis (see sections 3.4.1.3 and 3.4.3.3 for the respective descriptions of seismic facies seen in SU3 and glaciofluvial channel) shows spatial and temporal extent not only of the unchannelized Pleistocene till unit but also of the sediments filling the glaciofluvial channel (fig. 3.10). Moreover, distribution of sediments in an area is always evident on time slices that cut through a 3D seismic cube (for example, fig. 3.7). Thus, in comparison to using only borehole data, integrating both seismic stratigraphy and borehole sediment descriptions ensures better facies predictions regarding spatial continuity and correlation of geological formations in inter-borehole areas and beyond borehole locations (Hart, 2013; Catuneanu, 2019).

Besides, understanding geological evolution of an area including relative timing of events provides insight into the prediction of sediment property variations. In this study, vertical stacking of seismo-stratigraphic units and the resultant geological history of the area indicate marked differences in transportation history, depositional episode and erosional event between the tunnel valley fills (SU2), which were at least partly deposited in Saalian, and the unchannelized till unit (SU3) deposited in Weichselian. Thus, on the basis of the geological history of the area, it is expected that the sedimentary and geotechnical properties of these two glaciogenic units would differ, for example, in terms of mineralogical fractions and textural properties. Obst et al. (2017) recognized such differences between Saalian and Weichselian tills in terms of their Paleozoic limestone and shale fractions and sandstone content.

### **3.6 Conclusions**

Ultra-high-resolution 3D and 2D multi-channel seismic reflection data acquired in the southern Arkona Basin have been integrated with sediment descriptions and velocity logs. This revealed three subunits of Cretaceous bedrock chalk (oldest geological unit observed). The lower section of the pre-Quaternary bedrock has been dissected by basement-reaching Nordadler faults of the Tornquist Zone in the southeastern, central and northern regions. A Late Cretaceous inversion event folded the Cretaceous chalk in the study area. Relatively shallow normal faults produced during two regimes of crustal extension in the Tertiary are major structural features in the bedrock's framework.

At least two generations of V-shaped tunnel valleys have been incised into the Cretaceous bedrock by subglacial meltwater erosion during glacier advancement(s) in the Pleistocene. In the southcentral region covered by our 3D seismic data, these evidently interconnected valleys are 340-900 m wide, with a maximum depth of ~66 m. The responsible glacier deposited its loads in most subglacial channels as till-dominated units. Deposition of sediments other than tills took place during depositional episodes in these valleys. In valleys filled with several packages of till-dominated sediments, major depositional episodes were separated from each other by meltwater and/or glacial erosion as indicated by the occurrence of erosional surfaces between main sedimentary packages in the valleys. Glaciofluvial to glaciolacustrine stratified sediments fill some amalgamated depressions in the southcentral area. Sands and

coarser-grained sediments have been deposited probably from meltwater in subglacial tunnel valleys in the southeastern and northern parts of the study area.

Deposition of a unit of cobbles on top of the Cretaceous chalk in the central part of the study area probably took place in a glaciofluvial setting and could point to the retreat of a valley-filling Pleistocene glacier. Subsequently, Weichselian glaciation led to the sedimentation of a laterally extensive, unchannelized interval dominated by two tills across the entire study area, with the base of this interval being characterized by s-forms sculptured by subglacial erosion across the top of Cretaceous chalk and valley fills in the southcentral part of the study area. A NE-SW oriented s-form probably documents NE to SW local ice flow pathway for a Weichselian glacier in the southcentral area. However, the timing of NW-SE trending s-forms relative to the afore-mentioned NE-SW oriented one could not be unequivocally defined in the area. A localized clay interval probably of a glaciolacustrine origin occurs within the composite unchannelized Weichselian till unit in the central part of the study area as an evidence of a glacial retreat phase. Three dimensional structural configuration of the top of the gross Weichselian till unit exhibits NW-SE trending glacial ridges buried in the southcentral part of the study area. The origin of these ridges is likely related to protrusions in the bedrock of the responsible Weichselian glacier. In the northern area, a sediment-filled Quaternary channel probably cut into a till-dominated interval in a glaciofluvial setting during a final glacial retreat has been preserved in the geological record.

Glaciotectonic stress induced by overriding glaciers likely deformed the pre-existing till units in their substratum including the valley fills. This led to the folded and discontinuous character of stratified valley fills in places, for example, in the southcentral part of the study area. Subglacial shearing of substratum during Pleistocene glacier movement led to the formation of glaciotectionic kinks in the bedrock chalk and unchannelized Weichselian till unit in the northern part of the study area. Within a localized patch where the bedrock chalk is fractured directly beneath the top of Cretaceous in the central area, non-penetrative glaciotectionic processes have deformed the bedrock in a brittle manner. The Weichselian glacial episode left imprints of permafrost lineaments in an ancient patterned ground within the unchannelized till unit in the southcentral part of the study area. The onlap of post-glacial sediments on the Weichselian till unit signifies the onset of clay, silt and sand

sedimentation that caps the entire stratigraphic succession in the southern Arkona Basin.

A conceptual model for the Late Cretaceous to Holocene evolution in the southcentral part of the study area has been developed. Our study has revealed that seismic stratigraphic analysis and deduction of geological history aid accurate sediment correlation and facies prediction in an area. However, it is noteworthy to point out that the above-mentioned conclusions are subject to refinement when more borehole data are available.

Moreover, this study has shown that the Tertiary extensional event recorded in the region of the southern Baltic Sea occurred in multiple regimes, which could be differentiated based on the dip angle of the normal faults produced. Besides, the subsurface image recorded in our 3D seismic data fostered an accurate mapping of sediment distribution, tectonic structures and buried glacial features in the working area at a level of detail that is not possible with 2D seismic profiles. Although 2D seismic lines might be good for preliminary imaging of regional structures, resolving the detailed complexity and interconnectivity of geological features in an area requires 3D seismic data and their time slices (horizontal slices are not available in 2D seismic data).

Based on our relatively small seismic cube, we have shown that the formation mechanism of the interconnected and partly meandering Pleistocene subglacial channels in the southern Baltic Sea region was driven by meltwater erosion. From the seismic cube, a local ice flow direction of a Weichselian glacier has been known in the southcentral part of our study area, thereby contributing to the regional understanding of ice movement during the Quaternary. Furthermore, the relict permafrost structures that were left after the retreat of the Weichselian glacier(s) were revealed, for the first time, in the Arkona Basin by extracting RMS amplitude across our 3D seismic cube in the southcentral part of our working area. This amplitude extraction would be practically impossible with 2D seismic profiles.

Thus, acquiring 3D seismic data and combining them with borehole geological descriptions would ensure the generation of reliable ground models which accurately capture detailed stratigraphic and structural features, for instance, in a glacially influenced terrain. In addition, integrating 2D and 3D seismic reflection data with borehole geological data within the near-surface geological formations in the southern

Arkona Basin has improved our regional understanding of glacial dynamics and erosion in the southern Baltic Sea.

### **3.7 Acknowledgements**

The seismic data and computer facilities used in this research were provided by the University of Bremen. Non-commercial licenses granted by IHS Markit and Petrosys ensured the respective use of the Kingdom and GLOBEClaritas software packages. The parent project, SynCore, is funded by the Federal Ministry for Economic Affairs and Climate Action, Germany. We appreciate the support from other members of SynCore's consortium: Fraunhofer Institute for Wind Energy Systems (IWES), Fraunhofer Institute for Industrial Mathematics (ITWM), Geotechnik und Dynamik Consult GmbH, and RWE Renewables. Noteworthy is our discussion with Drs. Karsten Obst and Michael Kenzler of the University of Greifswald, Germany.

## Chapter 4

# Statistical boundary conditions of subsoil physical properties in the Arkona Basin - delineating potential seismic attributes for predicting near-surface geotechnical parameters

Opeyemi Ogunleye<sup>1</sup>, Natasha Morales<sup>2</sup>, Taisiya Pein<sup>2</sup>, Volkhard Spiess<sup>1</sup>

<sup>1</sup>Department of Geosciences, University of Bremen, Klagenfurter Str., 28359 Bremen, Germany

<sup>2</sup>Fraunhofer-Institut für Windenergiesysteme, Am Fallturm 1, 28359 Bremen, Germany

## Abstract

Since the German Baltic Sea became a target for windfarm development, more studies on combining high-quality seismic data with soil properties are required. However, the geological setting of the Baltic Sea/Arkona Basin is complex, it being characterized by Cretaceous bedrock consisting of chalk successions, which were subsequently glacially overprinted and covered by glacial till, sands and clay followed by fine-grained brackish to marine organic-rich deposits.

Therefore, we (1) investigated the relationship between seismic attribute and Cone Penetration Test (CPT) parameter changes; (2) delineated interface- and layer-related seismic attributes as indicators of geotechnical and lithologic properties in geological formations; and (3) established constraints of initial models for acoustic impedance inversion of seismic data. Herein, we present results from 3D multi-channel seismic data covering 7 km<sup>2</sup>, 87 km of 2D seismic lines, sediment descriptions from 14 out of 17 available boreholes, 6 velocity logs, and CPT data from 14 locations. The 2D and 3D seismic data have a central frequency of ~350 and 250 Hz and vertical resolution of ~1.1 and 1.5 m, respectively.

In this research, we show that composite spatial changes in interface-related seismic attributes correlate with variations in normalized Soil Behavior Type (SBT<sub>n</sub>), and the variations in acoustic impedance correspond to lithologic and CPT changes. Impedance-based CPT data prediction can be guided with trace envelope, instantaneous frequency and lateral continuity of seismic events. From ground truths, relatively precise physical property values were derived for the Cretaceous chalk, till-dominated valley fill and unchannelized till as well as the soft post-glacial sediment cover, which could be well-correlated to the seismic facies, structural deformation and geotechnical parameters. These property values would help to derive low-frequency trends for seismic inversion.

**Keywords:** Seismic attributes; Cone Penetration Test; acoustic impedance; low-frequency trend; lithology

#### **4.1 Introduction**

Acoustic impedance of a geological formation is a product of its density and acoustic wave velocity. During seismic reflection data acquisition, elastic waves are sent into the subsurface, and the wave field reflected from interfaces with acoustic impedance contrast is recorded. The wave field is closely sampled in multiple directions and subsequently processed such that the subsurface structure and stratigraphy in any grid cell can be interpreted along a profile (in the case of 2D seismic data) or in a 3D cube. Basic interface-related attributes in stacked and migrated seismic data include time, amplitude and frequency of reflectors. Generally, time-derived attributes yield information about structure of formations, whereas amplitude-related attributes indicate stratigraphy, lithologic properties and fluid content. Anomalously high instantaneous frequency has been correlated with high sand content in some depositional settings (Brown, 2004). Furthermore, Mitchum et al. (1977) showed that reflector configuration in a seismic unit is related to bedding patterns and allows an interpretation of depositional processes, erosion and paleo-topography. Continuity of reflectors indicate the lateral extension of strata.

On one hand, acoustic impedance - a quantitative physical property of geological layers - could be derived from 1D downhole velocity logs of primary (P) and shear (S) waves, provided density is known. On the other hand, closely sampled trace-by-trace acoustic impedance along a seismic profile could be derived by inverting post-stack seismic reflection data, which in the simplest form entails convolving seismic wavelet

with reflectivity series in a forward modeling approach and minimizing the residuals between field and synthetic seismic trace to generate a final model of acoustic impedance (Vardy, 2015; Gutowski et al., 2002). It has been proposed that post-stack impedance inversion of high-resolution seismic data could start with random generation of initial acoustic impedance models for calculating reflectivity series (Vardy, 2015). However, it is important to examine the use of summary statistics of the physical properties of seismic units to constrain starting models in seismic inversion.

Besides, a common ground modeling approach in the wind energy industry is to create a geometric model in which only seismic horizons are used to guide the prediction of geotechnical soil properties. In other cases, seismically derived structural configuration and P-wave velocity are employed as constraints in a geostatistical co-kriging approach to predict these geotechnical properties. As predicting geotechnical data from seismic reflection data is gaining momentum in the wind energy industry, it

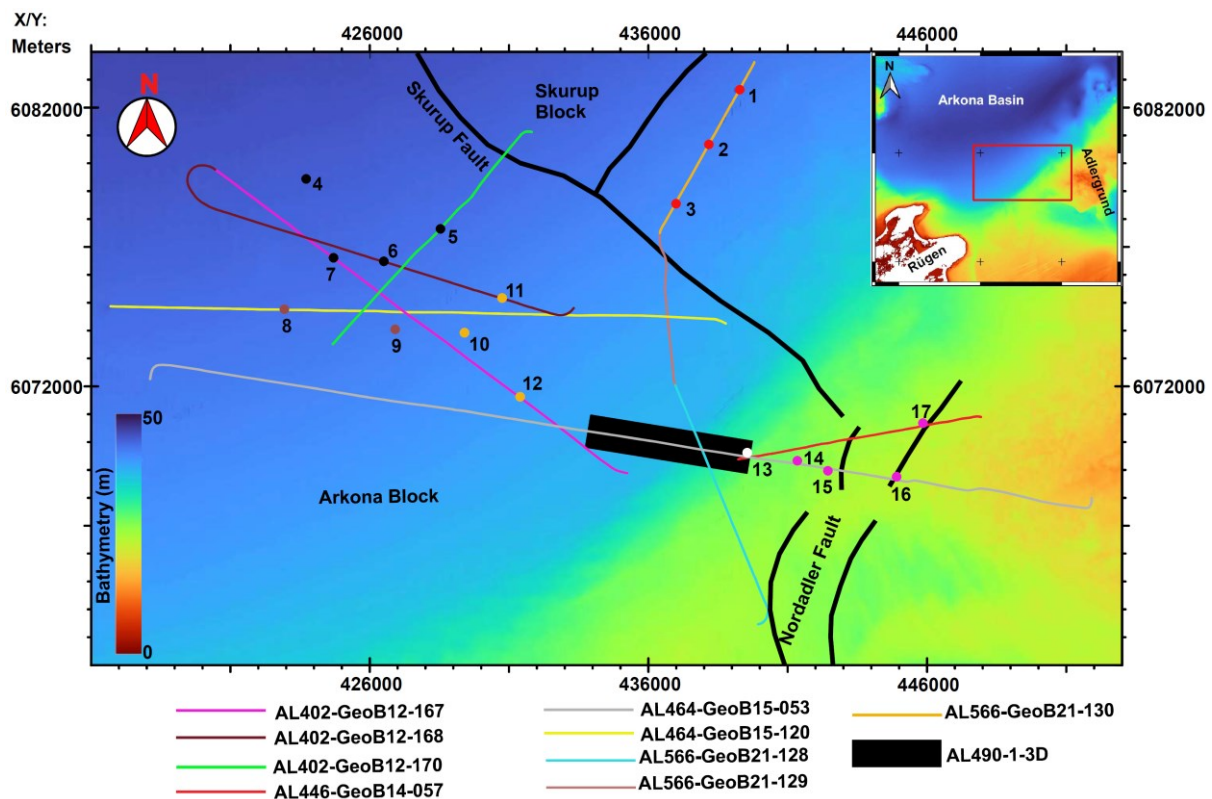


Fig. 4.1: Map of the Arkona Basin showing the study area (red outline in inset), coverage of 3D and 2D seismic reflection data, and sites with sediment descriptions, velocity logs and CPT data. The sites in the central, northern, northwestern, western, southcentral and southeastern areas are shown as orange, red, black, brown, white and lilac dots, respectively. The format of site names is the number shown in the figure followed by BH/CPT (where CPT data are available); only Sites 1, 14 and 16 have no CPT data (i.e. their names are 1, 14 and 16 BH). Only 10 BH/CPT has no sediment description. Velocity logs are available only at 6 sites, namely: 1 BH and 2, 3, 4, 6 and 11 BH/CPT. The pre-Quaternary faults shown belong to the Tornquist Zone (Obst et al., 2017). The bathymetry is based on EMODnet Bathymetry Consortium (2020). Map coordinates are based on UTM 33N (adapted from chapter 3).

becomes all the more important to investigate whether such predictions could be guided with multiple seismic attributes to exploit the full potential of seismic data.

In our current study, we build on the seismo-stratigraphic and structural framework interpreted in chapter 3, and present 2D and 3D seismic data, sediment descriptions, downhole logs of Primary and Shear wave velocity (P-S logs), and CPT data acquired in the southern Arkona Basin (fig. 4.1). Our objectives are to: (1) investigate the possible relationship between seismic attribute and CPT changes; (2) evaluate CPT data prediction from ultra-high-resolution seismic data, and propose seismic attributes that can be used as guides for such predictions; and (3) define physical boundary conditions for initial models of seismic inversion in the southern Arkona Basin, and correlate seismic units' median small strain physical properties with their corresponding large strain parameters within the study area. This research will improve seismic inversion in the Arkona Basin by showing statistical estimates of physical properties, the trend of which is useful for acoustic impedance inversion. It further shows the factor and seismic attributes that should be considered when carrying out an impedance-based CPT data prediction.

## **4.2 Geological setting**

The Arkona Basin is located south of the southern Swedish coast, east of Krieger's Flak and Plantagenetgrund, north of Pomeranian Bight, and west of Bornholm Island. The pre-Quaternary bedrock in the basin mainly consists of Cretaceous chalk and limestone (Winterhalter et al., 1981), which is overlain by sediments deposited by Pleistocene glaciers and related glaciofluvial and glaciolacustrine systems. In the southern Baltic Sea, the Late Saalian advance of the Scandinavian Ice Sheet eroded into the Upper Cretaceous interval, removing the Tertiary cover, thereby creating the top of Cretaceous (TC) as the Quaternary base. Saalian glacial tills have been preserved only in incised valleys in the southeastern margin of the Arkona Basin (Obst et al., 2017). Deposits of the Mid-Weichselian, Warnow, Pomeranian and Mecklenburg glacier advances have been reported in the area. Furthermore, Mathys et al. (2005) reported that Weichselian glacial tills overlie Upper Cretaceous chalk in the central Arkona Basin. Glaciofluvial to glaciolacustrine sediments occur as part of the valley fills and in the overlying unchannelized Weichselian till unit. There are evidences of glaciotectonic deformation in the bedrock, valley fills and unchannelized till unit (chapter 3).

After the last deglaciation in the Arkona Basin, Baltic Ice Lake sediments, the oldest post-glaciation unit, were deposited as late-glacial varved clay with silty to sandy layers at the top (Moros et al., 2002; Mathys et al., 2005). During the Yoldia Sea stage in Holocene, light silty 'Rosa' clay (Mathys et al., 2005) and fine sands (Kortekaas et al., 2007) were laid down in the central Arkona Basin. After the regression of the Yoldia Sea, Ancylus Lake sediments (10.6-6.45ka±50) were deposited as silty grey clay (Moros et al., 2002; Mathys et al., 2005; Trimonis et al., 2008). The period of 6.45 ka ±50 to present (Littorina/Post-Littorina Sea phase) has been characterized by deposition of silty green mud and Gyttja unlaminated clay (Holocene organic-rich mud; Moros et al., 2002; Mogollón et al., 2012).

### **4.3 Material and methods**

#### **4.3.1 Material**

7 km<sup>2</sup> 3D Multi-Channel Seismic (MCS) reflection data (AL490-1-3D) and five 2D seismic profiles (AL402-GeoB12-167, AL402-GeoB12-168, AL402-GeoB12-170, AL464-GeoB15-053 and AL566-GeoB21-130) covering 87 km are presented in this chapter (see fig. 4.1 for location). These 2D seismic data were acquired in 2012 (AL402-GeoB12), 2015 (AL464-GeoB15) and 2021 (AL566-GeoB21), while the 3D data were collected in 2017. The central frequency was ~250 and 350 Hz for the 3D and 2D seismic data, respectively, with vertical resolution of ~1.5 and 1.1 m, respectively. Sediment descriptions from 14 out of 17 available sites (i.e. only lithologic information at Sites 10, 14 and 15 BH/CPT were not used in this study), CPT data from 14 locations, and downhole velocity logs from 6 sites are included in the data used to generate the results presented in this chapter (compare text with fig. 4.1 for location). The geotechnical data consist of cone resistance, sleeve friction and pore pressure measurements. The velocity logs comprise of P- and S-wave readings.

#### **4.3.2 Methods**

##### **4.3.2.1 CPT data interpretation integrated with seismic facies**

The CPeT-IT v.3.9.1.3 (copyright © 2017) by GeoLogismiki was used for CPT data interpretation. CPT data from every location were loaded into the software, and layers were defined based on the tops of seismic units, which have been correlated with borehole-derived lithologic tops. Normalized cone resistance and friction ratio were computed. These were cross-plotted for each seismic unit (or sometimes subunits)

and displayed on the normalized Soil Behavior Type (SBTn) chart of Robertson (1990) to show the spatial variation of CPT behavior within each unit across different sections of the study area. The average SBTn of seismic units was used to construct typical geotechnical sections at each borehole location.

True amplitude was preserved during seismic processing. Seismic attributes of each geological unit penetrated at CPT locations were described in detail, and the resultant seismic facies variations were correlated with changes in SBTn.

#### **4.3.2.2 Derivation of physical properties from downhole velocity logs**

Logs of P- and S-wave velocities were used to generate the Poisson's ratio of stratigraphic units based on equation 4.1 as presented by Yang et al. (2011). Density of those geological formations was derived from P-wave velocity using the empirical relationship proposed by Gardner et al. (1974; see equation 4.2). However, it is known that both Gardner et al. (1974) and Raymer et al. (1980) relationships are not very accurate for slow rocks. Besides, the latter relationship requires knowing matrix density. In our study area, since Pleistocene glacial tills (our focus in addition to the Cretaceous bedrock chalk) partly consist of fragments of Paleozoic limestone and shale as well as Nordic crystalline rocks (Obst et al., 2017), we employed Gardner et al. (1974) relationship for velocity-to-density transformation because of its simplicity, without having to specify matrix density. Thus, P-impedance was derived as a product of density and P-wave velocity, while density was multiplied by S-wave velocity to generate S-impedance. Furthermore, small strain shear modulus was calculated from density and S-wave velocity (equation 4.3; Dutta and Saride, 2016; Robertson, 2009). Small strain Young's modulus was estimated with equation 4.4 (Robertson and Cabal, 2014; Gu et al., 2013).

$$\sigma = \frac{0.5\left[\left(\frac{V_p}{V_s}\right)^2 - 2\right]}{\left[\left(\frac{V_p}{V_s}\right)^2 - 1\right]} \quad \text{equation 4.1}$$

where  $\sigma$  = Poisson's ratio;  $V_p$  = P-wave velocity (m/s); and  $V_s$  = S-wave velocity (m/s).

$$\rho = 0.23V_p^{0.25} \quad \text{equation 4.2}$$

where  $\rho$  = density (g/cc); and  $V_p$  = P-wave velocity (ft/s).

$$G_0 = \rho V_s^2 \quad \text{equation 4.3}$$

where  $G_0$  = small strain shear modulus (Pa);  $\rho$  = density ( $\text{kg/m}^3$ ); and  $V_s$  = S-wave velocity (m/s).

$$E_0 = 2(1 + \sigma)G_0 \quad \text{equation 4.4}$$

where  $E_0$  = small strain Young's modulus (MPa);  $\sigma$  = Poisson's ratio; and  $G_0$  = small strain shear modulus (MPa).

### **4.3.2.3 Statistical analysis of small strain physical properties of geological units and their comparison with measured cone resistance**

Derived physical property values at all locations having velocity measurements and the values of measured CPT parameters were pooled together per seismic unit (and subunit in certain cases) to form a composite sample of the population for each unit, and their statistical distribution was examined using histograms. Microsoft Excel was used to compute minimum, maximum, grand mean, standard deviation, median, skewness and 95% confidence interval of mean for the derived physical and measured geotechnical properties of each unit. Herein, we use median values in the summary statistics to set quantitative boundary conditions of physical properties for seismic inversion in the Arkona Basin, with step plots of acoustic impedance and small strain shear modulus being correlated with that of measured cone resistance.

## **4.4 Results**

Based on the seismo-stratigraphic and structural analyses carried out in chapter 3, four main seismic units (SU) were recognized within the interval covered by our ultra-high-resolution seismic data in the southern Arkona Basin. An 18.4 km long AL402-GeoB12-167 seismic profile, which extends from northwestern to southcentral parts of the study area, summarizes the stratigraphic framework (figs. 4.1 and 4.2a). As discussed in chapter 3, bedrock chalk (SU1) in the area was deposited in the Cretaceous. During Pleistocene, V-shaped tunnel valleys were incised into this bedrock and filled with sediments (SU2; fig. 4.2a), which were dominated by till, but sometimes consisted of coarse-grained meltwater unit, sand, and glaciofluvial to glaciolacustrine deposits. On the top of the valley fills and Cretaceous chalk, the Weichselian glacier deposited a widespread unchannelized till unit (SU3), which consisted mainly of two till subunits separated by a glaciolacustrine clay, with the lower till subunit being underlain by a localized glaciofluvial cobbly interval in the central part of our study area. In the northern part of our working area, a depression incised into

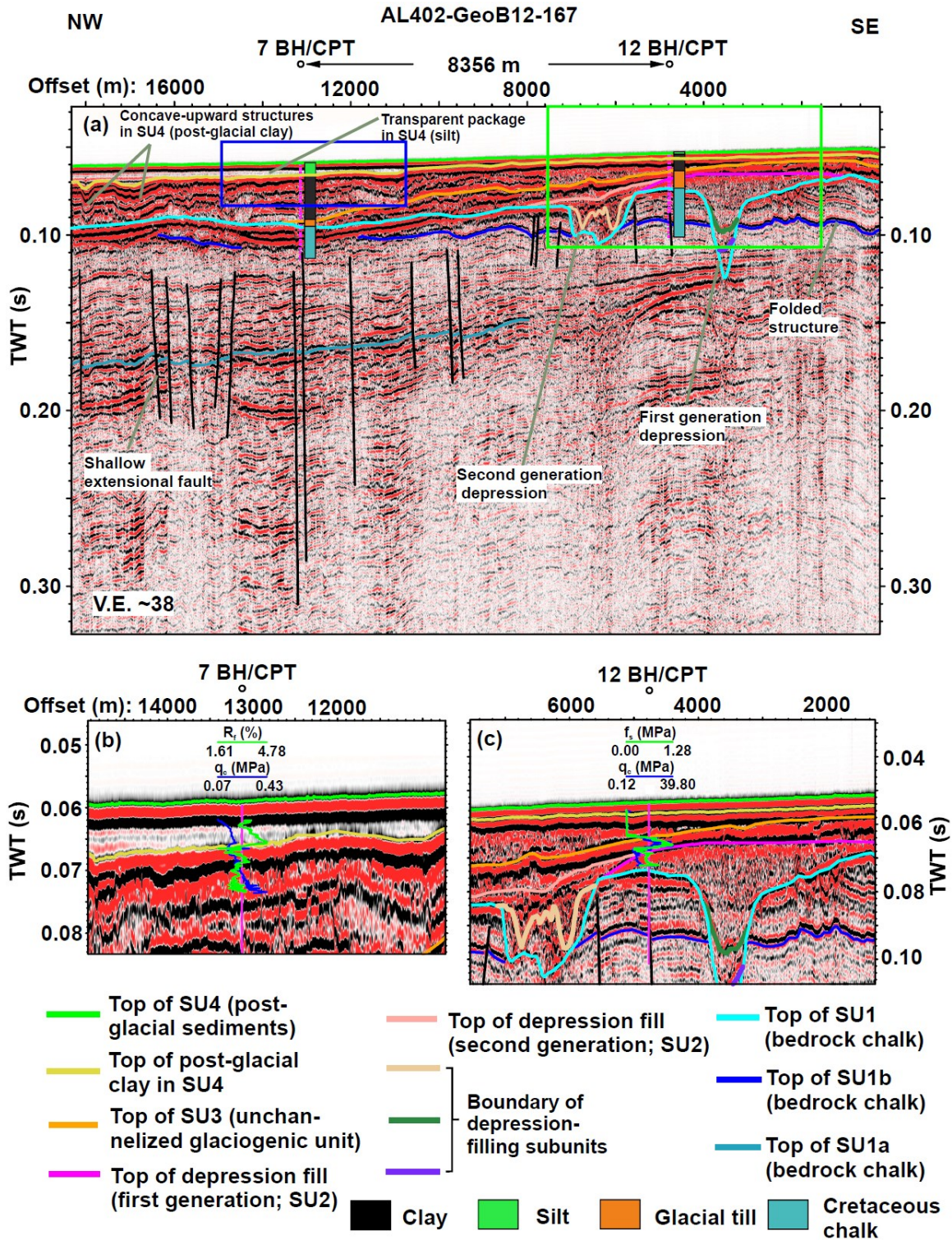


Fig. 4.2: Correlation of 2D seismic Profile AL402-GeoB12-167 with lithologic logs and CPT profiles: (a) interpreted seismic section of the profile showing the stratigraphic and structural framework of the shallow Cretaceous to Holocene succession in the study area (see fig. 4.1 for location; modified from chapter 3). The profile is tied with lithologic logs from two sites, namely: 7 and 12 BH/CPT; (b) zoomed seismic section (blue outline in '4.2a') showing the correlation of variations in measured cone resistance ( $q_c$ ) and friction ratio ( $R_f$ ) at 7 BH/CPT with changes in seismic subsurfaces within the post-glacial interval; (c) close-up section (green rectangle in '4.2a') showing the correlation of changes in measured cone resistance and sleeve friction ( $f_s$ ) at 12 BH/CPT with variations in seismic facies from the post-glacial interval through the unchanneled till to the depression (valley) fill. TWT = Two-Way Travel-time; SU = Seismic Unit; CPT = Cone Penetration Test (vertical exaggeration was calculated based on a velocity of 2000 m/s)

SU3 during the glaciofluvial stage associated with the last glacial episode was filled with cobbles of granite and limestone. Post-glacial sediments (SU4), which vary mainly from clay to silt, sometimes with sandy intervals, cap the stratigraphic succession.

#### **4.4.1 Correlation of a vertical seismic section with borehole sediment descriptions and CPT profiles**

A layer of silt, the top of which was encountered on the seafloor at Site 7 BH/CPT, is expressed as a transparent low-amplitude package of seismic reflectors (figs. 4.2a-b). The base of the silt is situated at 4.65 mbsf (meters below the seafloor) at the site. As one transits across this basal boundary into an underlying clay within the post-glacial interval, the clay shows high-amplitude seismic reflectors. Correspondingly, across the basal boundary of the silt, the measured cone resistance ( $q_c$ ) decreased from  $\sim 0.1953$  MPa in the silt to  $\sim 0.1611$  MPa in the clay, while the friction ratio ( $R_f$ ) simultaneously decreased from  $\sim 4.78$  to  $1.61\%$  (fig. 4.2b). Similarly, along 12 BH/CPT, drastic variations in the  $q_c$  and sleeve friction ( $f_s$ ) occur across boundaries where there are both lithologic and seismic property changes, particularly at the interfaces between: (1) post-glacial clay of SU4 and underlying unchannelized till of SU3; and (2) SU3 and underlying tunnel valley fill constituting SU2 (figs. 4.2a and c).

#### **4.4.2 Spatial variation of seismic facies in relation to the CPT behavior of subsoil units**

Across the study area, every seismic unit penetrated by a borehole has been investigated in terms of the relationship between its seismic attributes and CPT behavior, which was interpreted on the Robertson (1990) chart. The seismic reflectors of the Cretaceous chalk around CPT Sites 13 and 15 BH/CPT, which are located in the southcentral and southeastern parts of the study area, respectively, differ in terms of amplitude and continuity, but are similar in configuration (fig. 4.3). On the Robertson (1990) chart, the plots of normalized cone resistance versus normalized friction ratio in the chalk (fig. 4.3) also display corresponding differences as point-clouds at the two CPT locations do not fit perfectly together, but partly overlap. Besides, in typical geotechnical sections along 13 and 2 BH/CPT (the latter site is located in the north), the Cretaceous chalk shows an average SBT<sub>n</sub> of 5, which falls in the category of silty sand and sandy silt, whereas at 15 BH/CPT it exhibits the behavior of sand and silty sand. Similar to the observation within the bedrock interval at 13 BH/CPT, the

Normalized soil behaviour type (SBTn) plot for the chalk (SU1)

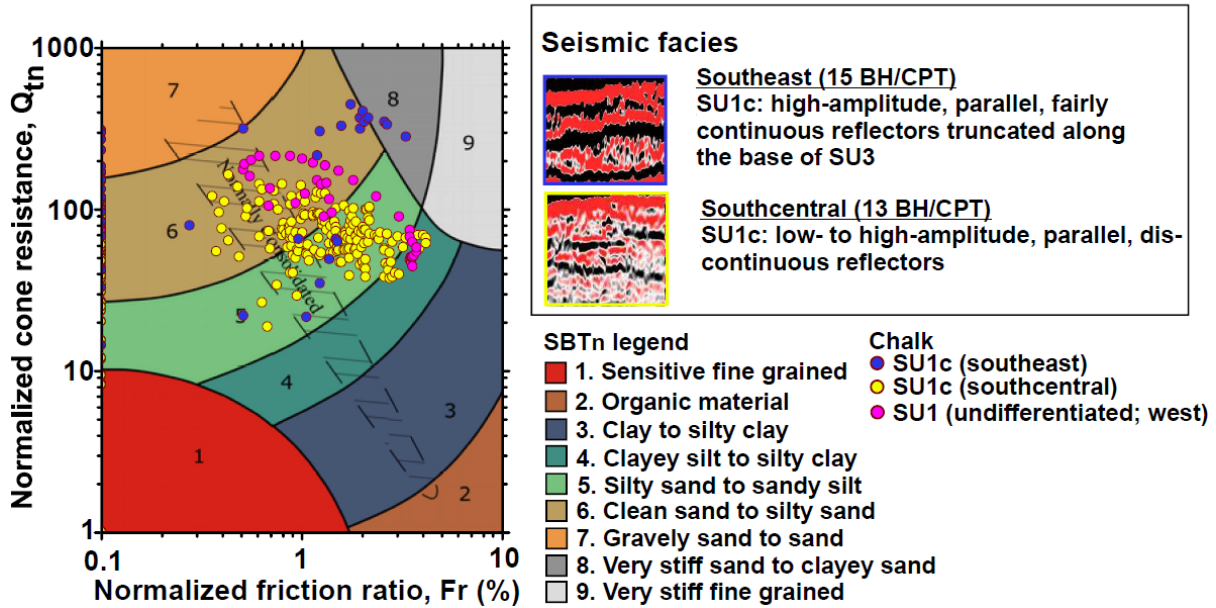


Fig. 4.3: Normalized soil behavior type plots for Seismic Unit 1 (SU1) at different parts of the study area using the Robertson (1990) chart. The geotechnical plots for SU1 in the southeastern, southcentral and western areas are color-coded on the chart. Corresponding seismic facies of the uppermost chalk subunit (SU1c) penetrated at Sites 13 and 15 BH/CPT are shown, described and bounded with corresponding colored outlines.

Normalized soil behaviour type (SBTn) plot for the unchannelized till unit (SU3)

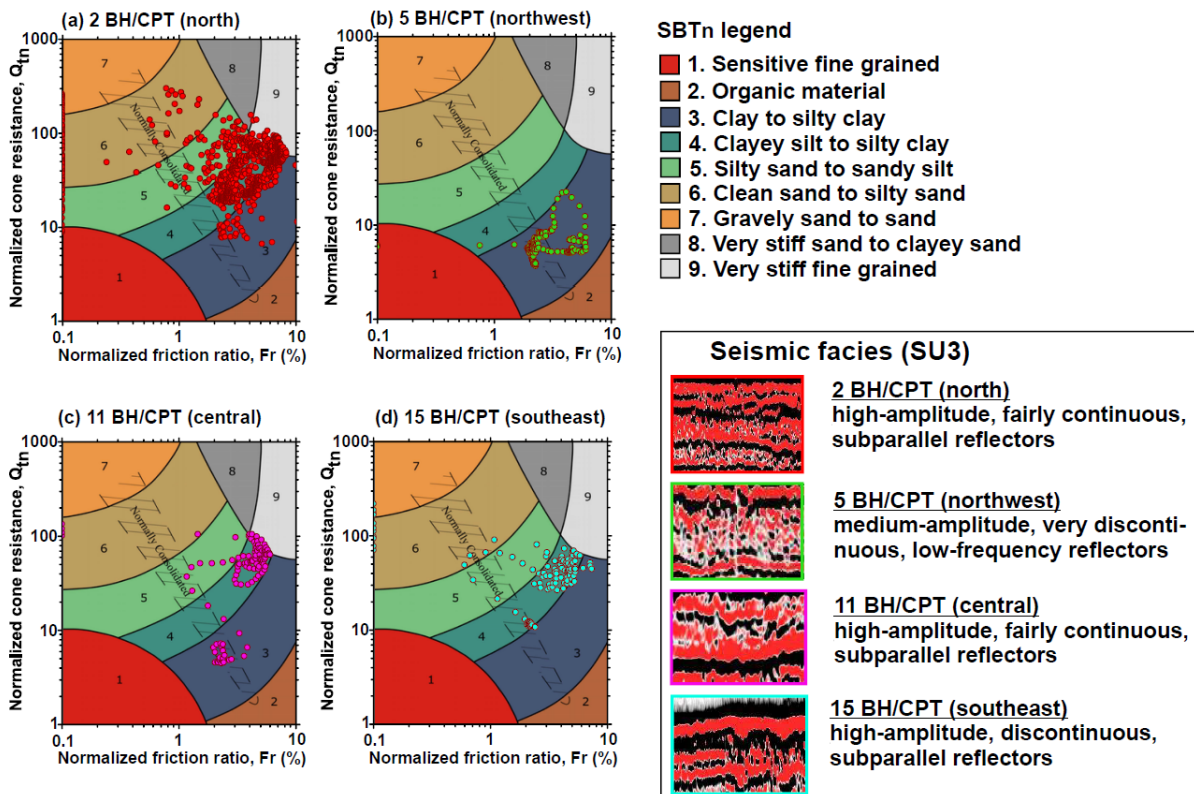
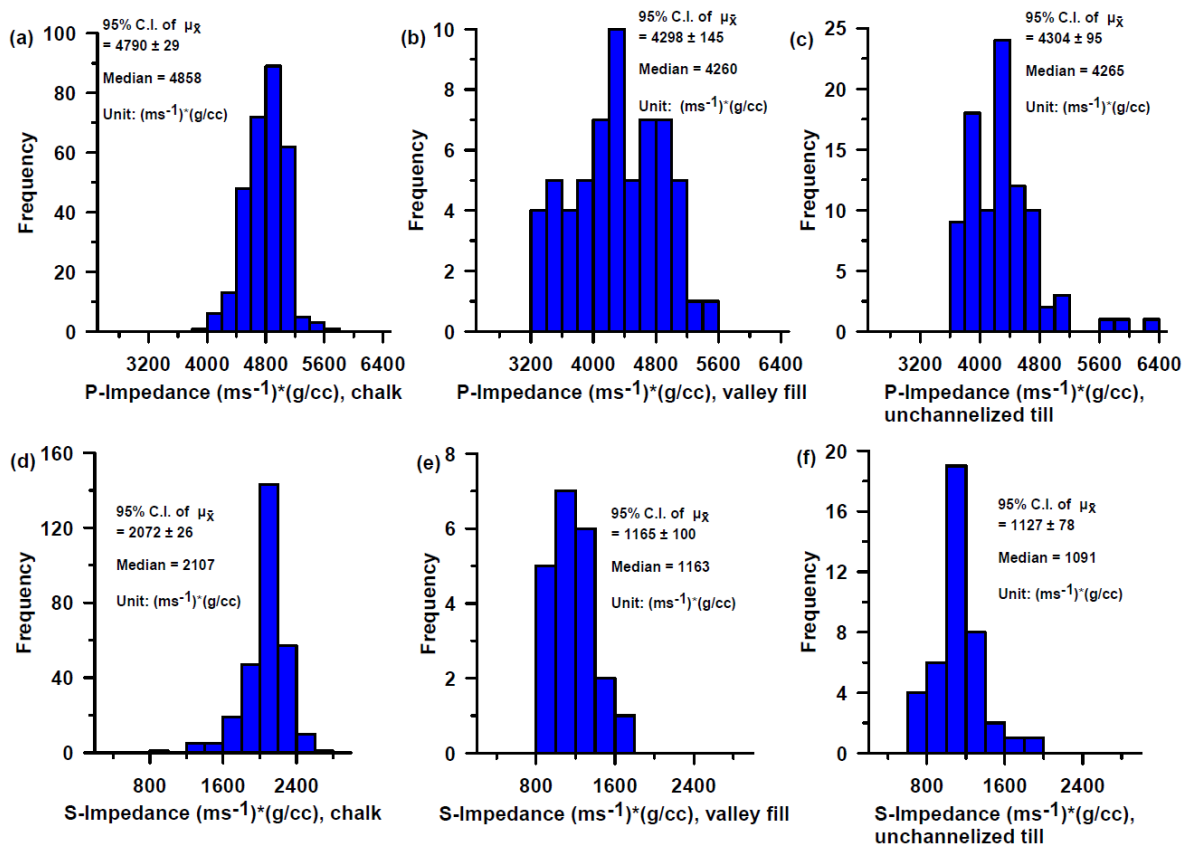


Fig. 4.4: Normalized soil behavior type plots for Seismic Unit 3 (SU3) at Sites 2, 5, 11 and 15 BH/CPT on the Robertson (1990) chart. Corresponding seismic facies of the unchannelized till unit (SU3) penetrated at these sites are shown, described and bounded with corresponding colored outlines.

Cretaceous chalk penetrated at Site 2 BH/CPT shows high-amplitude, subparallel, fairly discontinuous reflectors displaying erosional truncation along the base of SU2.

The seismic facies observed in the unchannelized till (SU3) at Sites 2, 11 and 15 BH/CPT are similar and characterized by high-amplitude, subparallel, fairly continuous to discontinuous reflectors. At these three CPT locations, the unit exhibits an average SBTn of 4, which indicates the CPT behavior of clayey silt and silty clay (fig. 4.4). However, the seismic attributes of unchannelized till at these locations differ from those at 5 BH/CPT (fig. 4.4) and so does its average SBTn; SU3 behaves as clay (average SBTn of 3) at 5 BH/CPT. Traversing to 12 BH/CPT in the central part of the study area, the CPT behavior of the unchannelized till unit changes to very dense/stiff soil (average SBTn of 8), thereby depicting spatial variability of the till's geotechnical properties.



**Fig. 4.5: Histograms of Primary (P) and Shear (S) impedances of geological formations showing the range, 95% confidence interval of grand mean (C.I. of  $\mu_x$ ) and median value. (a) and (d) are for the chalk, (b) and (e) for the valley fill, and (c) and (f) for the unchannelized till in our study.**

Table 4.1: Summary statistics of the small strain physical properties of each seismo-stratigraphic unit and its subunits (the error in estimated density relative to the measured value at Site 2 BH/CPT: -9.4% in SU3 and SU2; +0.5% in SU1)

(a)	Seismo-stratigraphic Unit												Density (kg/m <sup>3</sup> )						P-impedance (m/s) <sup>2</sup> (g/cc)						S-impedance (m/s) <sup>2</sup> (g/cc)											
	Count			Grand Mean			Stdev.			Median			Skew* [X]			95% C.I.			Max.			Mean			Stdev.			Median			Skew* [X]			95% C.I.		
	Min.	Max.		Min.	Max.		Min.	Max.		Min.	Max.		Min.	Max.		Min.	Max.		Min.	Max.		Min.	Max.		Min.	Max.		Min.	Max.		Min.	Max.				
SU4 (post-glacial sediments)	85	1896	2132	2007	93	2040	0.16	20	85	2670	4794	3622	840	3850	0.27	181	72	214.7	1145	566	359	281	0.34	84												
SU3lgr (last episode's glaciofluvial channel fill)	16	2105	2201	2149	27	2145	0.31	15	16	4498	5629	4998	321	4947	0.41	171	16	1015	2125	1624	414	1765	-0.59	221												
SU3 (unchannelized till unit)	91	2018	2247	2085	42	2082	1.16	9	91	3647	6243	4304	457	4265	1.54	95	41	681	1872	1127	248	1091	0.65	78												
SU2 (tunnel valley fill)	19	2060	2189	2120	27	2114	0.42	13	20	4039	5472	4674	299	4595	0.67	140	20	703.9	1921	1254	400	1075	0.69	187												
SU1 (Cretaceous chalk)	61	1967	2185	2083	55	2082	-0.21	14	61	3204	5430	4298	565	4260	-0.03	145	21	835.9	1660	1165	220	1163	0.37	100												
	300	2050	2203	2131	23	2137	-0.42	3	300	3942	5648	4790	251	4858	-0.23	29	288	953.2	2687	2072	223	2107	-1.28	26												

(b)	Seismo-stratigraphic Unit												Poisson's Ratio						Small Strain Shear Modulus (MPa)						Small Strain Young's Modulus (MPa)											
	Count			Grand Mean			Stdev.			Median			Skew* [X]			95% C.I.			Max.			Mean			Stdev.			Median			Skew* [X]			95% C.I.		
	Min.	Max.		Min.	Max.		Min.	Max.		Min.	Max.		Min.	Max.		Min.	Max.		Min.	Max.		Min.	Max.		Min.	Max.		Min.	Max.		Min.	Max.				
SU4 (post-glacial sediments)	72	0.46	0.50	0.49	0.01	0.49	-0.62	0.002	72	24	637	214	212	41	0.45	50	72	72	1855	632	624	123	0.44	147												
SU3lgr (last episode's glaciofluvial channel fill)	16	0.40	0.48	0.44	0.03	0.43	0.26	0.015	16	483	2087	1299	580	1424	-0.36	309	16	1426	5835	3703	1606	4105	-0.40	856												
SU3 (unchannelized till unit)	41	0.43	0.48	0.47	0.01	0.47	-0.73	0.004	41	227	1559	628	272	560	1.29	86	41	673	4524	1836	782	1648	1.30	247												
SU2 (tunnel valley fill)	20	0.36	0.49	0.45	0.04	0.47	-1.27	0.017	20	234	1747	815	528	537	0.91	247	20	698	4870	2332	1444	1586	0.87	676												
SU1 (Cretaceous chalk)	21	0.43	0.47	0.46	0.01	0.46	-1.39	0.006	21	355	1297	671	247	653	0.93	112	21	1040	3707	1953	699	1902	0.86	318												
	288	0.32	0.47	0.38	0.02	0.38	0.62	0.002	288	443	3279	2035	393	2073	-0.73	46	288	1302	8876	5619	1026	5748	-0.82	119												

Min. = minimum; Max. = maximum; Stdev. = standard deviation; C.I. = confidence interval of mean; SU = Seismic Unit

Table 4.2: Summary statistics of the measured large strain geotechnical properties of each seismo-stratigraphic unit and its subunits

Seismo-stratigraphic Unit	Cone Resistance, qc (MPa)						Sleeve Friction, fs (kPa)											
	Count			Grand Mean			Stdev.			Median			Skew* [X]			95% C.I.		
	Min.	Max.		Min.	Max.		Min.	Max.		Min.	Max.		Min.	Max.		Min.	Max.	
SU4 (post-glacial sediments)	7237	0.00	31.58	0.72	1.49	0.51	8.03	0.03	7089	0	449	17	22	13	7.33	1		
SU3 (unchannelized till)	3804	0.04	50.13	7.41	6.43	5.65	1.76	0.20	3605	2	1492	321	347	191	1.32	11		
SU2 (tunnel valley fill)	42	2.79	62.71	34.64	17.32	36.15	-0.22	5.40	20	53	525	231	132	208	0.70	62		
SU1 (Cretaceous chalk)	2099	0.06	69.44	16.15	11.74	12.67	1.75	0.50	1432	11	1874	610	340	555	0.76	18		
	1817	0.06	77.55	22.31	11.34	19.77	1.16	0.52	1135	29	1359	424	200	383	0.93	12		

Min. = minimum; Max. = maximum; Stdev. = standard deviation; C.I. = confidence interval of mean; SU = Seismic Unit

### **4.4.3 Summary statistics and vertical profiles of the small strain physical properties of near-surface geological formations**

#### **4.4.3.1 Histograms and quantitative measures of the derived physical parameters**

The distribution of Cretaceous chalk's physical properties (fig. 4.5a) shows that the grand mean of P-impedance in the unit has a 95% confidence interval of  $4790 \pm 29$  (m/s)\*(g/cc), with the median P-impedance value being 4858 (m/s)\*(g/cc). This median value is remarkably higher than those of the till-dominated valley fill and unchannelized till unit (figs. 4.5b-c). These glacially deposited geological units display very similar median values of P-impedance (difference of only +0.12% in the former relative to the latter) and Poisson's ratio (table 4.1). The post-glacial sediments (SU4) exhibit the highest Poisson's ratio and the least values of impedance and small strain shear and Young's moduli (table 4.1). Cobbles of granite and limestone filling a glaciofluvial channel incised into SU3 during the last glacial episode in the northern part of the study area (chapter 3) is characterized by median Poisson's ratio and small strain shear modulus of 0.43 and 1424 MPa, respectively. Among the four major seismic units, the SU1 has the highest median small strain shear modulus of 2073 MPa, which reduces to 653 and 560 MPa in the till-dominated valley fill and unchannelized till, respectively.

#### **4.4.3.2 Vertical profiles of Poisson's ratio and small strain shear modulus across seismo-stratigraphic units**

In the northern, northwestern and central parts of the study area, as depth and overall confining pressure increase along boreholes from the shallowest sediments of SU4 through the till-bearing units (SU2 and SU3) to the deepest interval of chalk (SU1), the Poisson's ratio and small strain shear modulus generally decreases and increases, respectively (fig. 4.6). Deviation from the trend happens where glaciofluvial channel sediments occur in the stratigraphic sequence as it could be seen in Hole 1 BH. Within the Cretaceous chalk at each of Sites 2, 6 and 11 BH/CPT, the Poisson's ratio and small strain shear modulus fluctuate around a relatively constant value from the top of the chalk unit to its deeper parts. However, in the chalk section along 1 BH, the Poisson's ratio and small strain shear modulus reduces and increases, respectively, with depth.

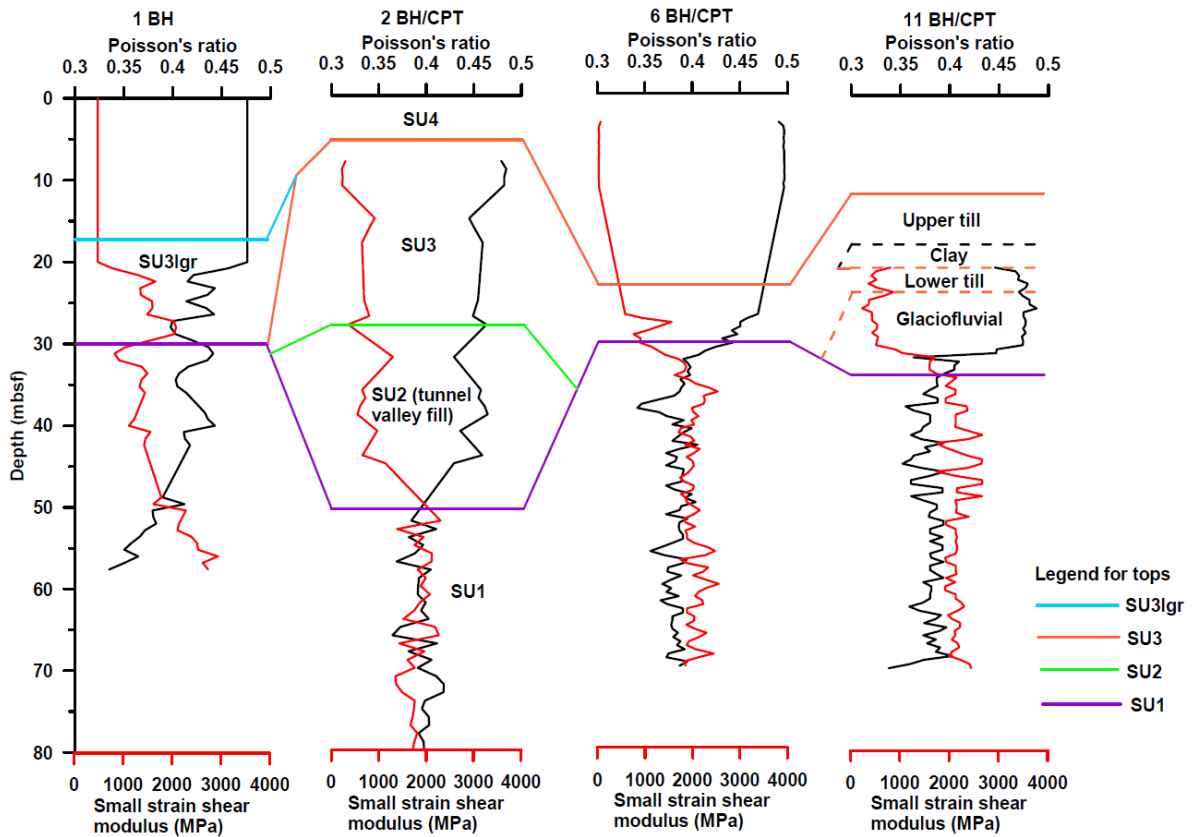


Fig. 4.6: Vertical profiles of Poisson's ratio (black) and small strain shear modulus (red) correlated per seismic unit across Sites 1 BH (north) and 2, 6 and 11 BH/CPT (located in the northern, northwestern and central parts of the study area, respectively). SU = Seismic Unit; SU1 = Cretaceous chalk; SU2 = valley fill; SU3 = unchannelized till; SU3lgr = sediments in glaciofluvial channel; SU4 = post-glacial sediments.

#### 4.4.4 Plots of the median physical and CPT properties of subsoil units

The median value of  $q_c$  progressively increases from 0.51 MPa in the post-glacial sediments through 5.65 and 12.67 MPa in the unchannelized till unit and till-dominated valley fill, respectively, to 19.77 MPa in the bedrock chalk (table 4.2). This increase in the  $q_c$  is accompanied by a general increase in the median P-impedance across those geological formations (fig. 4.7a). However, a cross plot of the measured median  $q_c$  versus median P-impedance across all seismic units shows that although a very slight decrease in the median acoustic impedance was observed from SU3 to SU2, this small change in the small strain physical property occurs simultaneously with a significant increase in the median  $q_c$  across these seismic units. Thus, the regression line of the cross plot has a coefficient of determination (R-squared value) of only ~0.88 (fig. 4.7b). As a test of the reliability of the regression line, its equation was used to predict the median cone resistance for each of the seismic unit, and this was cross-plotted with the measured median cone resistance (fig. 4.7c). In the seismic units, median  $f_s$  consistently increases downward from SU4 through SU3 to SU2, followed by a drop to 383 MPa in SU1.

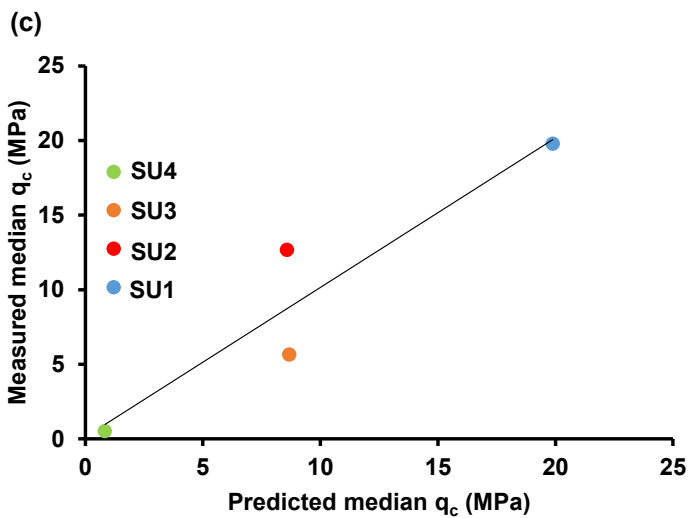
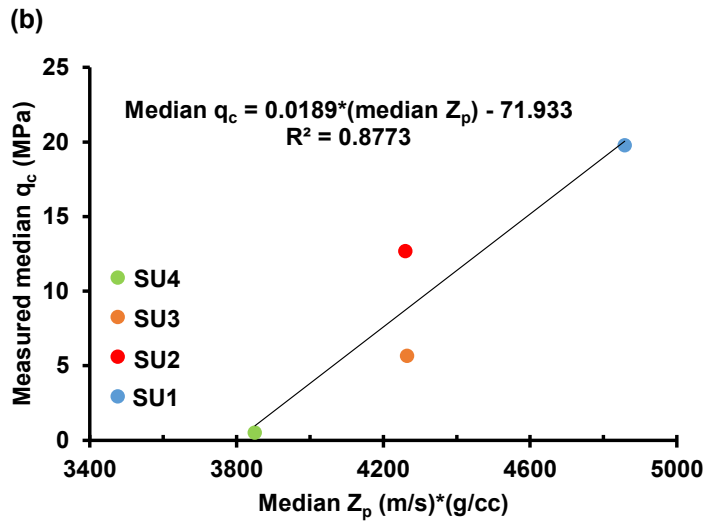
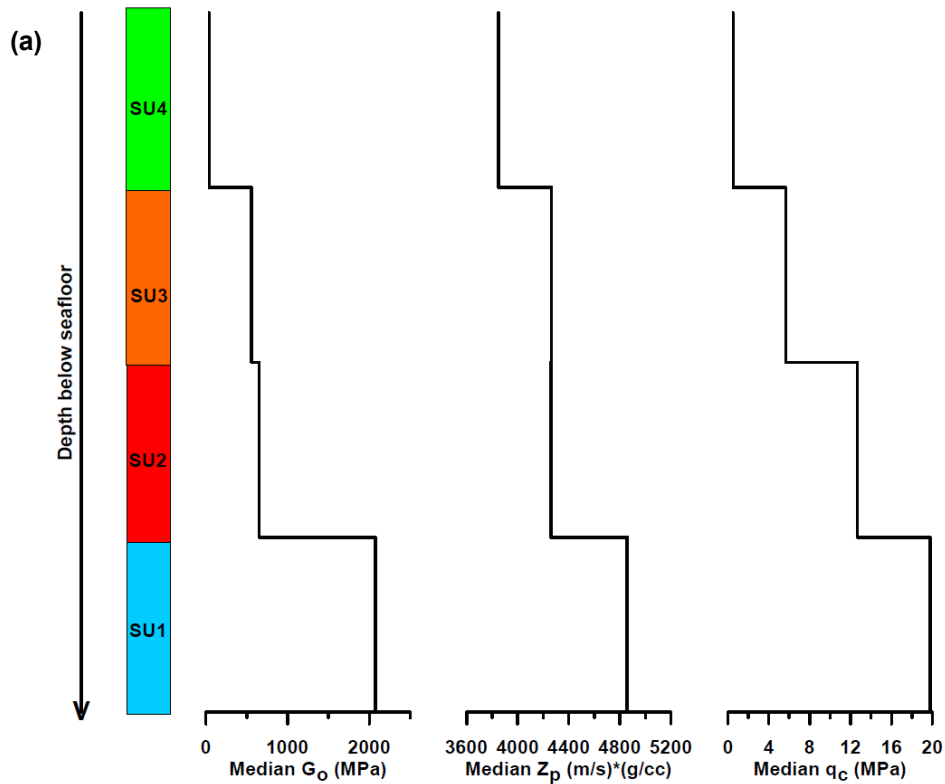


Fig. 4.7: Plots of the physical properties and measured cone resistance across Seismic Units 1 to 4 (SU1-4) based on their median values: (a) step plots of the median  $G_o$  and  $Z_p$  as well as the measured median  $q_c$ ; (b) cross plot of the measured median  $q_c$  versus the median  $Z_p$ ; (c) cross plot of the measured versus predicted median  $q_c$ .  $G_o$  = small strain shear modulus;  $Z_p$  = primary impedance;  $q_c$  = cone resistance; SU1 = Cretaceous chalk; SU2 = till-dominated valley fill; SU3 = unchannelized till; SU4 = post-glacial sediments

## **4.5 Discussion**

### **4.5.1 Relationship between seismic and CPT data - its implication for CPT data prediction**

Research has been conducted in the past to study the effect of grain size on seismic signals in marine sediments (McCann and McCann, 1969). In unconsolidated sediments, grain size affects pore size distribution and porosity. Seismic velocity, bulk density and attenuation of seismic waves in sediments vary with coarseness of grains (Mavko et al., 2009; Gardner et al., 1974; Hamilton, 1972). As grain size influences reflectivity across interfaces, dispersion and wave spreading (Yilmaz, 1987), it contributes significantly to the amplitude of reflected seismic signals. In the northwestern part of our study area, the lithologic change in grain size from a silt layer at the seafloor to an underlying clay unit - the boundary being at 4.65 mbsf in Hole 7 BH/CPT - is associated with a corresponding change in seismic amplitude and transparency of reflectors within the post-glacial interval (figs. 4.2a-b). In our ultra-high-resolution seismic data, the seismic amplitude's relationship with grain size might be partly due to the application of amplitude-preserving seismic processing steps, which included a spherical divergence correction implemented with accurately picked velocity field (chapter 2). Besides, in the central part of the study area, the lithologic change across the boundary between the unchannelized till unit and underlying valley fill at 12 mbsf along Hole 12 BH/CPT correlates with changes in seismic facies from high-amplitude and fairly continuous reflectors in the former unit to low- to medium-amplitude discontinuous seismic events in the latter (figs. 4.2a and c). These two sedimentary units belong to different glacial episodes, thereby making their transportation history and mineralogical composition different (chapter 3; Obst et al., 2017). Thus, the interface-related seismic amplitude and continuity of reflectors in our study are controlled by the lithologic properties of the sediments (compare Khan et al., 2000).

Furthermore, CPT measurements relate to grain sizes on the Robertson (1990) chart. Soil behavior type varies with coarseness of sediment grains. Besides, in our research, changes in lithology from one gross lithologic unit or subunit to the other show corresponding drastic changes not only in the seismic attributes, but also in the CPT measurements of cone resistance and sleeve friction (figs. 4.2a-c). Thus, there exists at least an indirect relationship between the seismic reflector attributes and CPT parameters, and it might be possible to predict or synthesize the latter from the former.

However, since reflector attributes observed on seismic amplitude sections are controlled by acoustic impedance contrast across interfaces, it is important to invert such seismic sections to derive layer-based geophysical attributes such as absolute acoustic impedance along each seismic trace during CPT data prediction from seismic data. On the step plots of median acoustic impedance and cone resistance (fig. 4.7a; tables 4.1 and 4.2), it is evident that both parameters generally decrease from the deeper to shallower seismic units. It therefore follows that closely sampled acoustic impedance along each trace in a seismic profile or a 3D seismic cube might be employed as the main predictor for generating synthetic CPT data, although this prediction would need to be guided by other seismic attributes. When such predictions are made with a machine learning approach (e.g. Sauvin et al., 2019), an artificial neural network (ANN) could be trained to establish a regression between seismic attribute(s) and CPT data at known locations where actual CPT measurements have been carried along a seismic profile.

#### **4.5.2 Interface-related seismic attributes: guides for CPT data prediction**

Interpretation of the average SBT<sub>n</sub> of SU1 interval in relation to its seismic facies (section 4.4.2; fig. 4.3) indicates that the seismic amplitude and discontinuity of reflectors, which are interface-related attributes, vary spatially as the average SBT<sub>n</sub> changes across the study area. This implies that for the bedrock chalk, trace envelope (a measure of instantaneous amplitude or reflection strength (Brown, 2004; Taner et al., 1979)) and numerical measure of lateral continuity of reflectors might be used as guides in CPT prediction. Since both the seismic amplitude and discontinuity of reflectors simultaneously change with the average SBT<sub>n</sub>, it implies that both trace envelope and lateral continuity are best used together, not independently, as a composite guide to support acoustic impedance for CPT data prediction in the Cretaceous chalk interval.

In the SU3, not only are multiple interface-related seismic attributes similar at Locations 2, 11 and 15 BH/CPT, the CPT behavior (average SBT<sub>n</sub>) of the seismic unit at those locations are the same (section 4.4.2; fig. 4.4). The seismic attributes which are similar in the unchannelized till unit at those locations are the reflector amplitude and configuration. On the other hand, at Locations 5 and 15 BH/CPT, the seismic attributes of SU3 - namely amplitude, continuity, reflector configuration and frequency - are different and so is the average SBT<sub>n</sub>. While SU3 behaves as clay at the former

CPT location, it exhibits the behavior of clayey silt and silty clay at the latter location. It follows that trace envelope, instantaneous frequency (rate of change of time-dependent phase as defined by Taner et al., 1979) and numerical quantification of lateral continuity would be related to CPT behavior. Thus, they have the potential to serve as guides for predicting CPT parameters in the unchannelized till unit. However, they are best used together as a composite guide for CPT data prediction, since multiple seismic attributes either remain similar or vary in relation to average SBTn within SU3 across all the aforementioned CPT locations. Besides, a graphical display of lateral continuity of reflectors also accounts for the configuration of reflectors.

### **4.5.3 Statistical boundary conditions of small strain physical properties of geological units - their evaluation and usefulness for seismic inversion**

A stress-strain curve of soils consists of two stages: (1) the initial small strain linear range in which the soil is elastic; and (2) the latter nonlinear elastic range ending at the peak state (Lee et al., 2009; Lee and Salgado, 2000). Softening after the peak might be observed as well. In the small strain range, shear strain is less than  $10^{-4}\%$  (Robertson and Cabal, 2014).

In our study, the deepest subsoil unit observed in the near-surface range consists of chalk deposited in Cretaceous, which is characterized by the lowest Poisson's ratio and highest impedance and small strain shear and Young's moduli. This subsoil unit is remarkably different from the overlying glacially deposited Pleistocene valley fill and unchannelized till units. The till-dominated valley fill and unchannelized tills have intermediate values for those small strain physical properties (table 4.1). The sediments deposited after the glacial episodes cap the sedimentary succession in the study area and exhibit the lowest P- and S-impedance values and least resistance to shear and tensile stress. This observed trend in physical properties shows that within the near-surface interval, resistance to stress in the small strain domain generally increases as one moves into the deeper sections of the stratigraphic column from the post-glacial sediments through the unchannelized tills and till-dominated valley fill to the chalk. A similar and parallel trend is seen in the values of  $q_c$  (a large strain parameter) for these main sedimentary units. Every subsoil unit differs in its large strain properties as evident in their geotechnical parameters and soil behavior type (figs. 4.3 and 4.4; table 4.2).

#### Chapter 4: Boundary conditions of physical properties - potential seismic attributes

The Cretaceous chalk appears to be largely uniform in physical properties, particularly in terms of its Poisson's ratio and small strain shear modulus, across different locations in the northern, northwestern and central parts of our working area (fig. 4.6). Although the Cretaceous chalk interval penetrated at Hole 11 BH/CPT in the central part of the study area has been glaciotectonically fissured (chapter 3), the signatures of its small strain shear modulus and Poisson's ratio along a vertical profile are similar to those of un-fissured chalk sections in other areas. This probably implies that fissuring of the Cretaceous chalk by the Pleistocene glacier did not significantly affect its physical properties. However, as evident along seismic Profile AL566-GeoB21-130, 1 BH was drilled into a glaciotectonic kink zone in the Cretaceous chalk (chapter 3), and while the Poisson's ratio decreases with depth, the small strain shear modulus increases. Although the cause(s) of this vertical trend of chalk's physical property in 1 BH might not be unequivocally apparent, the trend might be explained in terms of the geological process of deformation that led to the development of the kinky zone. Chapter 3 showed that the kinky zone was formed when a Weichselian glacier deformed its substratum, part of which was the Cretaceous chalk. Since that source of glacial deformation must have acted downward from the top of and/or above the chalk, it follows that the downward decrease and increase of Poisson's ratio and small strain shear modulus, respectively, might be expected as one moves deeper through the deformed chalk section towards the unaffected chalk interval. On the whole, the physical property trend observed in this chalk unit along Hole 1 BH seemingly agrees with the geological interpretation presented in the above-mentioned chapter.

It therefore follows that the summary statistical estimates of small strain physical properties presented in table 4.1 are reliable. On one hand, Vardy et al. (2015) suggested an acoustic impedance inversion algorithm that begins with random generation of initial impedance model. Since quantifiable physical properties characterize geological formations in our study, the minimum and maximum values of those physical parameters for each subsoil unit as well as the corresponding 95% confidence intervals of their grand mean could be used to constrain the search radius of physical property values in initial models during seismic inversion. Although both the mean and median values of physical properties might serve as measures of central tendency, we suggest assigning the median values as initial model parameters through which a low-frequency trend would be determined during seismic inversion

because the histogram and statistical summary of those physical properties indicate that their distribution is mostly skewed (fig. 4.5; table 4.1).

Thus, we propose a seismic inversion approach in which the top and base of geological units in the stratigraphic framework of an initial impedance model are defined with interpreted seismic horizons. Thereafter, the median values of physical parameters (table 4.1) should be specified for each geological unit for the purpose of creating the low-frequency trend of physical properties across the formations. At least, the low-frequency trend generated by using the median acoustic impedance values would be useful for predicting absolute acoustic impedance along seismic profiles during seismic inversion.

#### **4.5.4 Predicting cone resistance from acoustic impedance**

It has been observed that there is a positive correlation between the measured median  $q_c$  and median P-impedance of geological formations in this study (figs. 4.7a-b). Consequently, our study shows that it is possible to predict cone resistance from acoustic impedance, for example, as shown by Sauvin et al. (2019). However, since the data points on the cross plot of measured versus predicted median cone resistance do not align on a straight line (fig. 4.7c), it means that a single regression line across multiple seismic units would not be suitable for the prediction of median  $q_c$  from median acoustic impedance. It might be possible to reliably predict the median  $q_c$  and invariably other  $q_c$  values within each seismic unit by using a unique regression line deduced specifically for the seismic unit only. Vardy et al. (2018) mentioned that the relationship between cone resistance and acoustic impedance in the subsurface probably varies between facies.

#### **4.6 Conclusions**

We have presented information from ultra-high-resolution multi-channel seismic reflection data, sediment descriptions from boreholes, velocity logs, and CPT data in the southern Arkona Basin. This integrated study revealed that the changes in CPT measurements correspond to variations in physical property and seismic attributes of subsoil units. Since multiple attributes of seismic reflectors - amplitude, continuity, configuration and frequency – either simultaneously vary with average SBTn or remain similar when average SBTn does not change in each seismic unit at different CPT locations, it follows that trace envelope, instantaneous frequency and lateral continuity

of reflectors are interface-related seismic attributes that can serve as composite guides for CPT data prediction from ultra-high-resolution seismic data.

Vertical profiles of the Poisson's ratio and small strain shear modulus show trends that agree with geological interpretation in the study area. Thus, the corresponding statistical estimates of small strain physical parameters, particularly P-impedance, which have been derived and shown in this study, have the potential to serve as reliable boundary conditions for constraining initial models during acoustic impedance inversion in the southern Arkona Basin. By using seismic horizons to establish a stratigraphic framework and flooding each seismic unit with the median value of physical properties, especially P-impedance, a low-frequency trend could be derived for an initial model during impedance inversion.

Correlation of the small strain physical properties of seismic units with their large strain geotechnical property based on summary statistical estimates indicates that the measured median cone resistance and median acoustic impedance are positively correlated across multiple seismic units. Thus, cone resistance can be predicted from acoustic impedance, a layer attribute. However, to predict the uncorrected cone resistance ( $q_c$ ) including its median value from acoustic impedance, it might be necessary to define a unique regression line for each seismic unit, with the regression line of the seismic unit being different from that of other units. Furthermore, we suggest that additional borehole geophysical and CPT data including bulk density profiles should be compiled and integrated into our database in the future so as to improve the statistical estimates of subsoil physical and geotechnical properties in the southern Arkona Basin.

#### **4.7 Acknowledgements**

The geoscientific and geotechnical data, computing facilities, and non-commercial license of IHS Kingdom used in this research were provided by the University of Bremen. The license for the GeoLogismiki CPeT-IT v.3.9.1.3 (copyright © 2017) was made available by the Fraunhofer Institute for Wind Energy Systems (IWES). SynCore is the parent project of this research, and it is fully funded by the Federal Ministry for Economic Affairs and Climate Action, Germany. We appreciate the immense support of SynCore's syndicate consisting of the University of Bremen, Fraunhofer IWES, Fraunhofer Institute for Industrial Mathematics, Geotechnik und Dynamik Consult GmbH, and RWE Renewables. We acknowledge the research placement opportunity

#### Chapter 4: Boundary conditions of physical properties - potential seismic attributes

offered to the first author at the Norwegian Geotechnical Institute in Oslo, which led to fruitful discussions about CPT data interpretation. The research placement was funded by the MARUM graduate school GLOMAR.

## Chapter 5

# Post-stack acoustic impedance as a reliable indicator of variation in lithologic and geotechnical properties in the southern Arkona Basin - assessment of two near-surface impedance inversion approaches using stationary wavelets

Opeyemi Ogunleye<sup>1</sup>, Guillaume Sauvin<sup>2</sup>, Nikolas Römer-Stange<sup>1</sup>, Maarten Vanneste<sup>2</sup>, Volkhard Spiess<sup>1</sup>

<sup>1</sup>Department of Geosciences, University of Bremen, Klagenfurter Str., 28359 Bremen, Germany

<sup>2</sup>Norwegian Geotechnical Institute, Sandakerveien 140, 0484 Oslo, Norway

## Abstract

Subsurface investigations in structurally and lithologically complex areas could be incomplete and biased, if seismic data was insufficiently incorporated and not used to the full capacity. However, seismic inversion is not yet routinely applied for wind farm development, although impedance has been identified as a predictor of spatial changes in lithology and geotechnical parameters. To facilitate a more wide spread application, there is the need for more case studies especially in the Baltic Sea, the evaluation of the predictive potential of acoustic impedance, and the evaluation of different inversion approaches.

We performed near-surface post-stack seismic inversion on seismic data sets collected in the Arkona Basin in the southern Baltic Sea and (1) correlated the absolute acoustic impedance with geological ground truths at borehole locations; (2) showed how acoustic impedance vary with the measured cone resistance and sleeve friction; and (3) assessed two approaches of acoustic impedance inversion. The dataset presented comprises of 2D seismic lines (total length 35 km, central frequency ~350

Hz, vertical resolution ~1.1 m), sediment descriptions from four boreholes, and Cone Penetration Test (CPT) data from one location.

This study reveals the absolute acoustic impedance as a significant seismic tool to resolve stratigraphic and structural complexity in a geological succession. The simultaneous variation of acoustic impedance with measured cone resistance and sleeve friction across lithologic boundaries and the statistical correlation of the predicted impedance and measured CPT parameters indicate that acoustic impedance derived from UHR seismic reflection data has the potential to serve as a predictor of cone resistance and sleeve friction in the southern Arkona Basin. The two seismic inversion approaches used are based on stationary wavelets, and they produce absolute acoustic impedance anomalies which correlate well with ground truths.

**Keywords:** Near-surface; seismic; inversion; cone-penetration-test; site characterization

## 5.1 Introduction

The acoustic impedance is a key seismic unit property which can also be estimated from laboratory measurements, core logging, or borehole geophysical logs of Primary and Shear wave velocity (P-S logs), where density is known or could be estimated by empirical relationships (e.g., Gardner et al., 1974; Raymer et al., 1980). Seismic inversion techniques have been developed for analyzing elastic properties of formations by transforming seismic records related to reflection coefficients at interfaces to unit-based quantitative geophysical properties such as acoustic impedance (Avseth et al., 2005). Full and partial stacks of seismic reflection data can be inverted to generate an impedance estimate. Simultaneous inversion of partial stacks or pre-stack data can yield multiple layer properties including P- and S-impedance, ratio of Primary to Shear wave velocity, and density. This sort of inversion is based on the Amplitude Versus Angle effect (Zoeppritz, 1919), which can be approximated by, e.g., the Fatti et al. (1994) or Aki-Richards (2002) equation. In our study, however, we carried out seismic inversion of full stacks. In this case, only post-stack acoustic impedance has been generated, which is expected to show formation heterogeneities (Filippova et al., 2011).

Using ultra-high-resolution (UHR, International Organisation for Standardization [ISO], 2021) seismic reflection data acquired in northern Norway, Vardy (2015) showed that empirical relationships exist between post-stack acoustic impedance and sediment properties including P-wave velocity, density, mean grain size and porosity. Moreover, through impedance inversion and modeling coupled with geological and geotechnical data, Vanneste et al. (2015) developed a method to derive geotechnical properties from seismic data in a coastal area affected by shallow landslides in northern Norway. Thus, it is imperative for geologic characterization and windfarm development in the Baltic Sea to evaluate the use of post-stack acoustic impedance as a tool for (1) distinguishing and mapping near-surface lithologic units and their internal property boundaries in the southern Arkona Basin; and (2) predicting geotechnical data in the area.

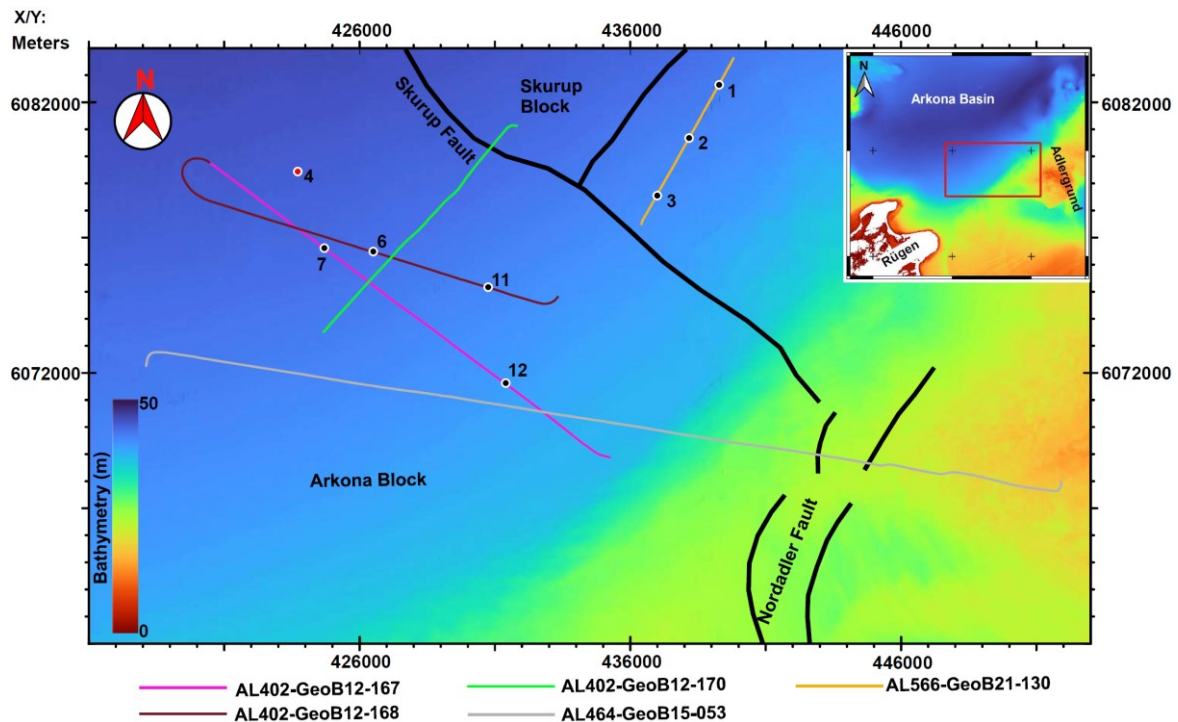


Fig. 5.1: Map of the study area (red outline in inset) in the southern Arkona Basin showing the 2D seismic reflection profiles that were inverted in this study and sites with sediment descriptions, velocity logs and Cone Penetration Test (CPT) data. The sites are shown as dots (black dots represent sites located on the inverted seismic profiles; red dot indicates an additional site utilized in both chapters 3 and 4). The name of each site is the number shown in the figure (numbers follow the order introduced in chapter 3) followed by BH/CPT at the locations with CPT data; Site 1 has no CPT data, so its name is 1 BH. 1 BH and 2, 3, 4, 6 and 11 BH/CPT have velocity logs which were utilized in chapter 4 for estimating median physical properties of geological units. Pre-Quaternary faults of the Tornquist Zone are depicted (Obst et al., 2016). EMODnet Bathymetry Consortium (2020) is the basis of the water depth values. Map coordinates are in UTM 33N (modified from chapter 3).

In this current study, we employ and improve on the seismo-stratigraphic and structural framework interpreted in chapter 3 in our study area. We present UHR 2D seismic reflection profiles, sediment descriptions, and CPT profiles in the southern

Arkona Basin. In the study area (fig. 5.1), our objectives are to: (1) demonstrate the applicability of acoustic impedance as an attribute for resolving geological complexity; (2) qualitatively and quantitatively correlate acoustic impedance with measured cone resistance and sleeve friction; and (3) assess the acoustic impedance sections generated by two near-surface post-stack inversion methods, and suggest improvements that could be made in the inversion approaches. This research shows that acoustic impedance is a viable tool for detailed stratigraphic and structural interpretation of geological formations in the southern Arkona Basin. It further points to the usefulness of this quantitative physical property as an attribute for CPT data prediction.

## **5.2 Geological setting**

The Arkona Basin in the southern Baltic Sea is characterized by a maximum water depth of 48 m and is bordered to the north by the Swedish coast, west by the Krieger's Flak and Plantagenetgrund, south by the Pomeranian Bight, and east by the Bornholm Island (Obst et al., 2016). Pre-Quaternary bedrock chalk in the basin was deposited in the Cretaceous (Winterhalter et al., 1981). During Pleistocene glaciations, subglacial valleys were incised into this bedrock in the southern Arkona Basin (Obst et al., 2016). On the top of the till-dominated valley fills and Cretaceous chalk in the study area, Weichselian glaciers deposited a widespread unchannelized till unit within which a layer of glaciolacustrine clay is sandwiched and the basal section of which is characterized by a localized glaciofluvial cobbly interval in the central part of our study area (chapter 3). Similarly, Weichselian glacial tills have been reported as overlying Cretaceous chalk in the central Arkona Basin (Mathys et al., 2005). Post-glacial sediments, which vary from clay through silt to sand (Moros et al., 2002; Kortekaas et al., 2007), cap the stratigraphic succession.

## **5.3 Material and methods**

### **5.3.1 Dataset**

The five 2D Multi-Channel Seismic (MCS) reflection profiles inverted for acoustic impedance in this study (see fig. 5.1 for location) were acquired in 2012 (AL402-GeoB12), 2015 (AL464-GeoB15) and 2021 (AL566-GeoB21). Only Profiles AL402-GeoB12-167 and AL402-GeoB12-168 (combined length of 35 km) are presented. Other profiles were used to ensure that picked horizons were consistent with already-

established seismo-stratigraphic framework (chapter 3) in the study area. The central frequency of the seismic data is ~350 Hz with a vertical resolution of ~1.1 m (calculated as a quarter of a wavelength with a velocity of 1500 m/s). The MCS data were processed, tied to lithologic logs, and qualitatively interpreted during the work documented in chapter 3. Lithologic descriptions and CPT data were provided for our study (see fig. 5.1). The CPT data consist of cone resistance, sleeve friction and pore pressure measurements. In this paper, sediment descriptions from 4 sites (i.e. 6, 7, 11 and 12 BH/CPT) and CPT data from Site 12 BH/CPT are presented as representatives. Lithologic logs at 6 and 11 BH/CPT were tied to the seismic data by using the average velocity of intervals deduced from primary wave velocity logs at the respective locations. Sites 7 and 12 BH/CPT were tied to the seismic data by using the velocity profiles of 6 and 11 BH/CPT, respectively.

### **5.3.2 Post-stack impedance inversion**

The 2D full stacks of seismic data processed for the near-surface intervals were inverted for absolute acoustic impedance using stationary wavelets in two approaches. The inversion products were then correlated with sediment descriptions and CPT data at various sites. Geological boundaries, which were initially interpreted as horizons from seismic amplitude sections, were refined using absolute acoustic impedance sections, and intra-unit boundaries that became newly apparent on the impedance sections were picked. The two near-surface impedance inversion procedures are described below.

#### **5.3.2.1 Impedance inversion with velocity-guided background trend (velocity-guided approach)**

For the purpose of UHR seismic reflection data inversion, we developed a post-stack acoustic impedance inversion algorithm based on the methodology proposed by Vardy (2015). This algorithm integrates a convolutional forward model with a genetic optimization approach to derive estimated acoustic impedance at each trace location.

In this inversion scheme, which is termed velocity-guided approach in this study, the algorithm initiates an initially random set of impedance models within a user-defined impedance range. This range is based on the minimum and maximum impedance values for each seismic unit as calculated from P-S logs in chapter 4. The range is varying with depth and guided by the velocity model. Subsequently, the algorithm

calculates a corresponding set of synthetic traces by convolving the models with a theoretical source waveform (zero phase wavelet). The fitness of each impedance model within the family is evaluated by quantifying the residual between the synthetic traces and the actual field seismic traces. The generation of new models employs the Stochastic Remainder technique, wherein models with superior fitness are retained along with a random selection of those with lower fitness. These new models are then paired to facilitate crossovers and mutations, simulating the principles of natural selection. A new set of associated synthetic traces is generated. The process of natural selection is controlled by user-specified cross-over and mutation probabilities, which govern the likelihood of paired samples undergoing exchange (crossing over) or a specific sample being substituted with another randomly determined value (mutation). This iterative procedure continues until one of the specified termination conditions is met: reaching the maximum number of generations, achieving a field trace data residual below a user-defined threshold, or attaining a stable gradient in the residual evolution from generation to generation.

### **5.3.2.2 Impedance inversion with layer cake low-frequency model (band-limited approach)**

A band-limited acoustic impedance section has been generated based on post-stack seismic data and merged with a low-frequency model to generate an absolute impedance estimate (see fig. 5.2 for the work flow), which is termed band-limited approach in the following. As a first step for the low-frequency model generation, unit boundaries were identified in a joint interpretation of the seismic and geotechnical data, as well as the available core descriptions. Those boundaries were used to develop a layer cake model, which was flooded with median impedance values estimated from P-S logs (chapter 4; see fig. 5.1 for sites with the velocity logs).

Secondly, band-limited impedance was determined based on the post-stack seismic image with a genetic algorithm as described in Vardy (2015). In this global search and stochastic algorithm (Sen and Stoffa, 1992), forward modelling was performed with a convolution of randomly initialized reflectivity models with a wavelet. The band-limited impedance is consecutively determined from the reflectivity. For this approach, the wavelet was extracted from the post-stack seismic image by stacking the tapered seafloor reflection along the profile. Further details of the reproducible implementation

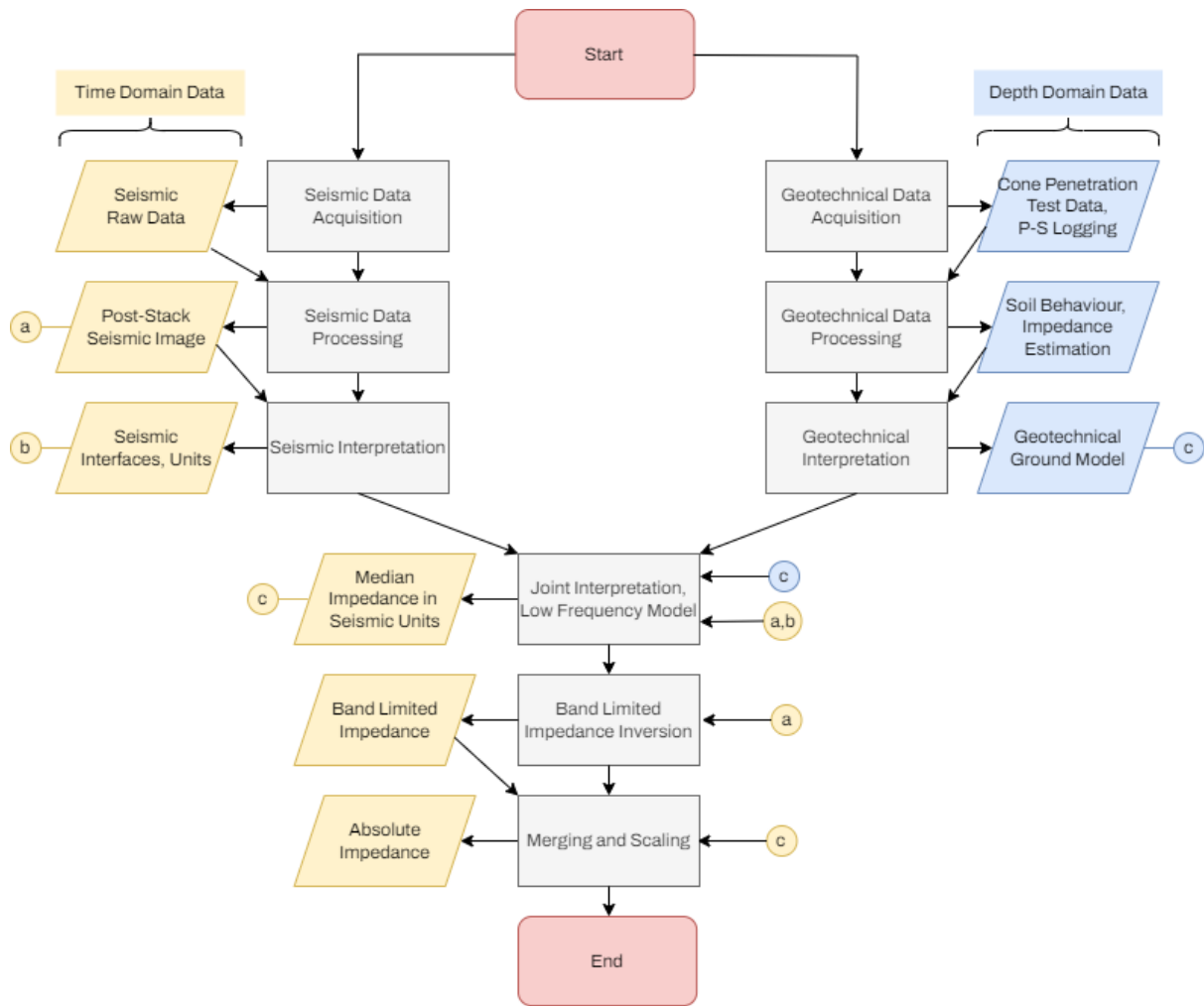


Fig. 5.2: Work flow of the band-limited acoustic impedance inversion approach in which a band-limited impedance result is merged with a layer cake low-frequency model

Table 5.1: Impedance inversion parameters for the genetic algorithm and merging of band-limited impedance with a low-frequency model

<b>Band-Limited Impedance Inversion Parameters for the Genetic Algorithm</b>	
Number of individual in each generation	1000
Number of generations for optimization	500
Cross-over probability	60%
Mutation probability	0.15%
Probability of a time sample to be a reflector for initialization	2%
Number of individuals to determine final result	100
<b>Low-Frequency Model Merging Parameters</b>	
Low pass frequency for scaling	180 Hz
High pass frequency for scaling	60 Hz
Characteristic frequency for merging	25 Hz

are described in Römer-Stange et al. (in prep. 2023) and the parameters are given in table 5.1.

Finally, and to merge the band-limited impedance inversion results with the low-frequency model and thus generate an absolute impedance estimate, the BLIMP algorithm described in Ferguson and Margrave (1996) was extended and applied. In this method, the band-limited impedance was merged with the low-frequency model in the frequency domain with a Linkwitz-Riley crossover filter (Linkwitz, 1978), after scaling the band-limited impedance. Using this procedure, the wavelet and post-stack seismic image did not need calibration.

## **5.4 Results**

Four main near-surface seismic units (SU1-4) occur in our study area (fig. 5.3a). In parts of our current research, the horizons produced from seismic amplitude data during the work presented in chapter 3 were overlaid on the absolute acoustic impedance sections generated with the velocity-guided approach. Besides, in the band-limited approach, new horizons, which were used to build the stratigraphic framework of the low-frequency model, were superimposed on the inversion product. In both approaches, these horizons were re-picked on the impedance sections by following the configuration of corresponding geophysical interfaces across which there was an acoustic impedance contrast, and picking intra-unit boundaries where there were distinct zones of anomalous impedance values within a unit. The succession of geophysical anomalies bounded by these refined horizons is presented in sections 5.4.1 and 5.4.2 below.

### **5.4.1 Lithology-related anomalies on the absolute acoustic impedance sections derived from an inversion of full stacks using the velocity-guided approach**

Post-stack inversion of the seismic Profile AL402-GeoB12-168 using the velocity-guided approach yielded the highest values of absolute acoustic impedance in the Cretaceous chalk interval. Lineaments occur on the impedance section within a zone of bedrock described as fissured chalk at Site 11 BH/CPT (fig. 5.4). Within the tunnel valleys incised into the bedrock chalk in places, multiple valley-filling subunits exist and are separated by curved surfaces across which there is an acoustic impedance contrast (figs. 5.3b-c). In the uppermost subunit of Valley 1 shown in figs. 5.3b-c, a lenticular low-impedance anomaly is defined.

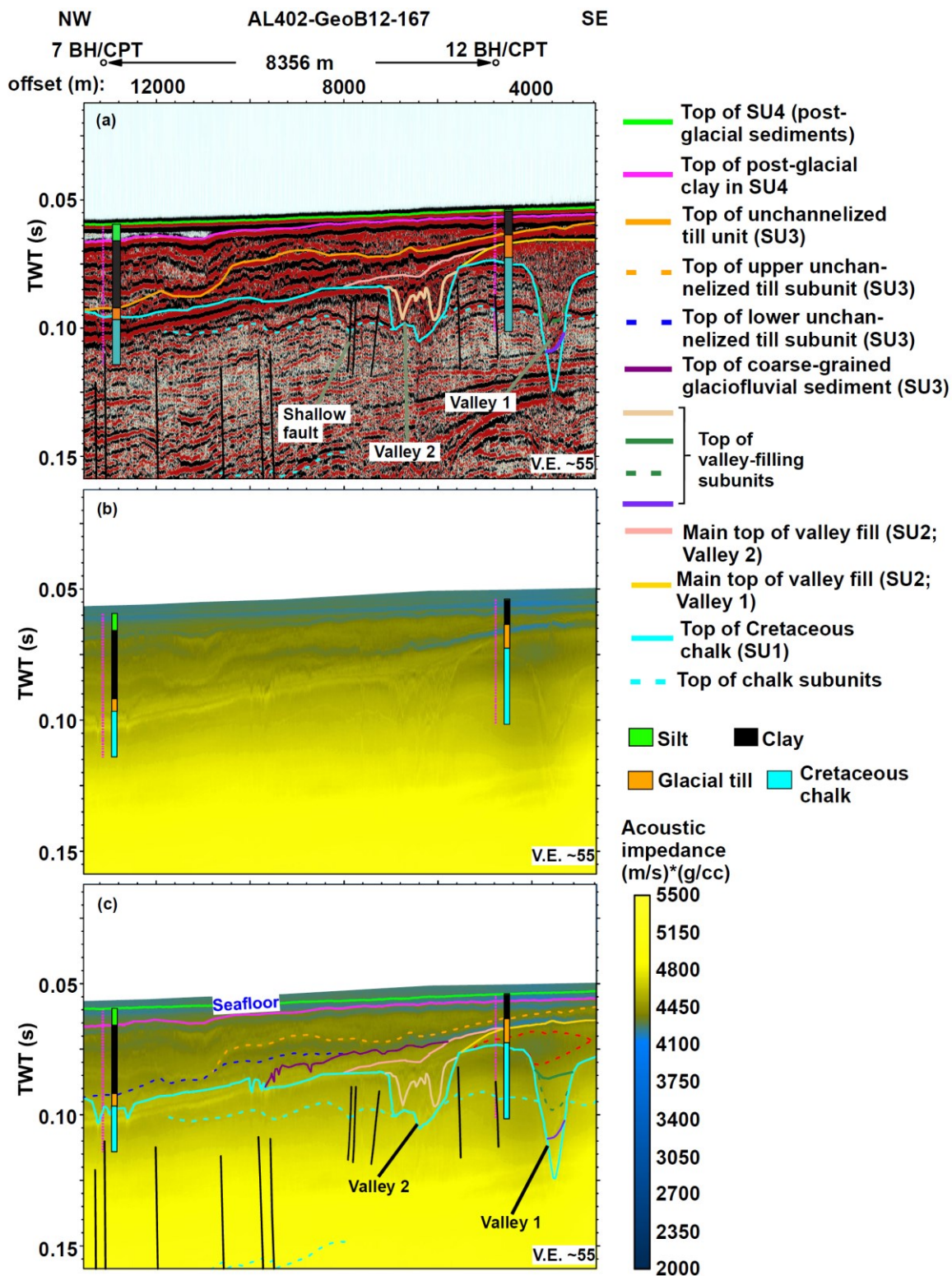


Fig. 5.3: 2D seismic Profile AL402-GeoB12-167 tied to the lithologic logs at Sites 7 and 12 BH/CPT (see fig. 5.1 for location): (a) interpreted seismic amplitude section showing the major near-surface seismic units and their lithologic characterization in our study area based on the work presented in chapter 3; (b) un-interpreted absolute acoustic impedance section of the profile generated with the velocity-guided inversion approach; (c) interpreted version of the impedance section in '5.3b' which has been correlated with sediment descriptions. Notice how impedance anomalies indicate the lateral extent and vertical stacking of stratigraphic units. Two Pleistocene valleys are depicted as cutting into the Cretaceous chalk. Stippled red lines delineate a lenticular zone with relatively low impedance values in a valley fill. TWT = Two-Way Travel-time; SU = Seismic Unit (vertical exaggeration was calculated based on a velocity of 2000 m/s)

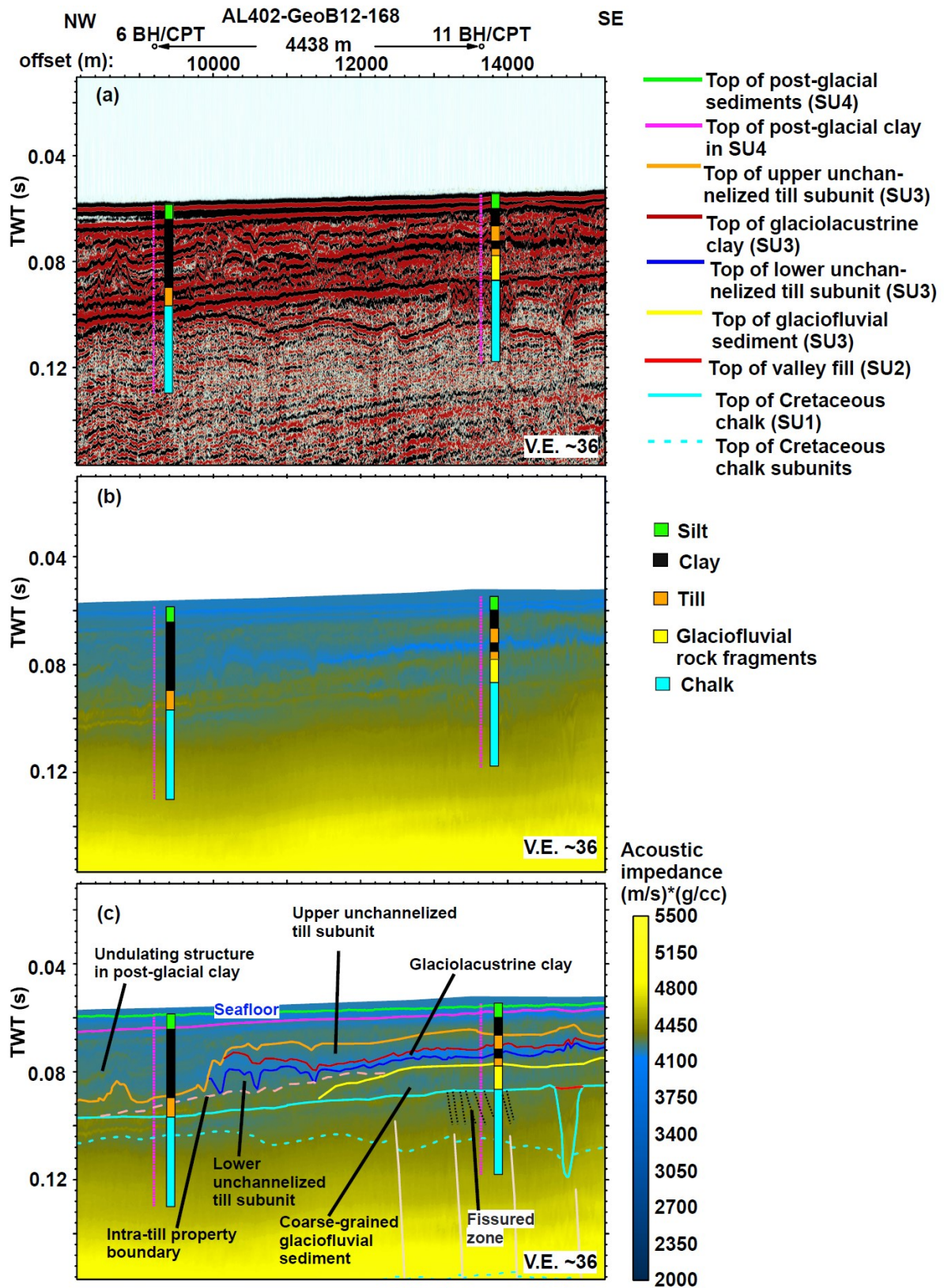


Fig. 5.4: 2D seismic Profile AL402-GeoB12-168 tied to the lithologic logs at Sites 6 and 11 BH/CPT (see fig. 5.1 for location): (a) un-interpreted seismic amplitude section along the profile; (b) un-interpreted absolute acoustic impedance section generated from '5.4a' with the velocity-guided inversion approach; (c) interpreted version of the impedance section in '5.4b' showing the spatial distribution of lithologic units, an intra-till property boundary, and the structural features of geological intervals. TWT = Two-Way Travel-time; SU = Seismic Unit (vertical exaggeration was calculated based on a velocity of 2000 m/s)

A layer of glaciofluvial rock fragments overlying the Cretaceous chalk at Site 11 BH/CPT ties with anomalously low impedance values (fig. 5.4). The anomaly extends laterally and tapers to the NW and SE, lying on top of the valley fill in places (figs. 5.3b-c and 5.4b-c). Higher up in the stratigraphic sequence, variations in the geophysical attribute show an impedance anomaly associated with the lower till subunit in SU3 at 11 BH/CPT, and this anomaly extends to and beyond Site 6 BH/CPT, a location where it correlates with the only till unit observed in the borehole (fig. 5.4). Based on the distribution of impedance values, a subtle boundary could be delineated within the lower till subunit, further separating the till subunit into lower and upper compartments. This boundary terminates on the top of the glaciofluvial rock fragments in the inter-borehole area (fig. 5.4). Furthermore, the top of the lower till subunit shows an undulating and irregular interface across which there is a marked acoustic impedance contrast with the overlying lithologic unit. Along Profile AL402-GeoB12-168, this top is draped by a blanket of distinctively low values of impedance which corresponds to the glaciolacustrine clay at 11 BH/CPT (fig. 5.4) and thickens in the northwestern direction, only to taper out abruptly without being penetrated at 6 BH/CPT. Succeeding the clay unit is the upper subunit of unchannelized till encountered at 11 BH/CPT, which not only exhibits relatively higher acoustic impedance values than the clay, but also defines an anomaly that morphologically thins out to the NW without extending to Site 6 BH/CPT (fig. 5.4). Impedance section along Profile AL402-GeoB12-167 reveals that the anomalies of the lower and upper unchannelized till subunits are vertically stacked directly on top of each other where the glaciolacustrine clay does not exist, with the interface between them exhibiting a distinct impedance contrast (figs. 5.3b-c). Horizon interpretation along the interfaces of acoustic impedance contrast indicates that in SU3 the tills encountered at 7 and 12 BH/CPT coincide with the impedance anomalies of the lower and upper till subunits, respectively (figs. 5.3b-c).

Within the post-glacial sediments at Sites 6 and 7 BH/CPT, a thick layer of clay underlying a silt unit was penetrated (figs. 5.3 and 5.4). The lithologic boundary between these units corresponds to a distinct interface between two successive intervals with different acoustic impedance on the velocity-guided impedance sections; the relatively higher impedance values characteristically occur in the underlying layer of clay (figs. 5.3b-c). The undulating structures in the post-glacial clay unit are also preserved on the impedance sections (figs. 5.3 and 5.4).

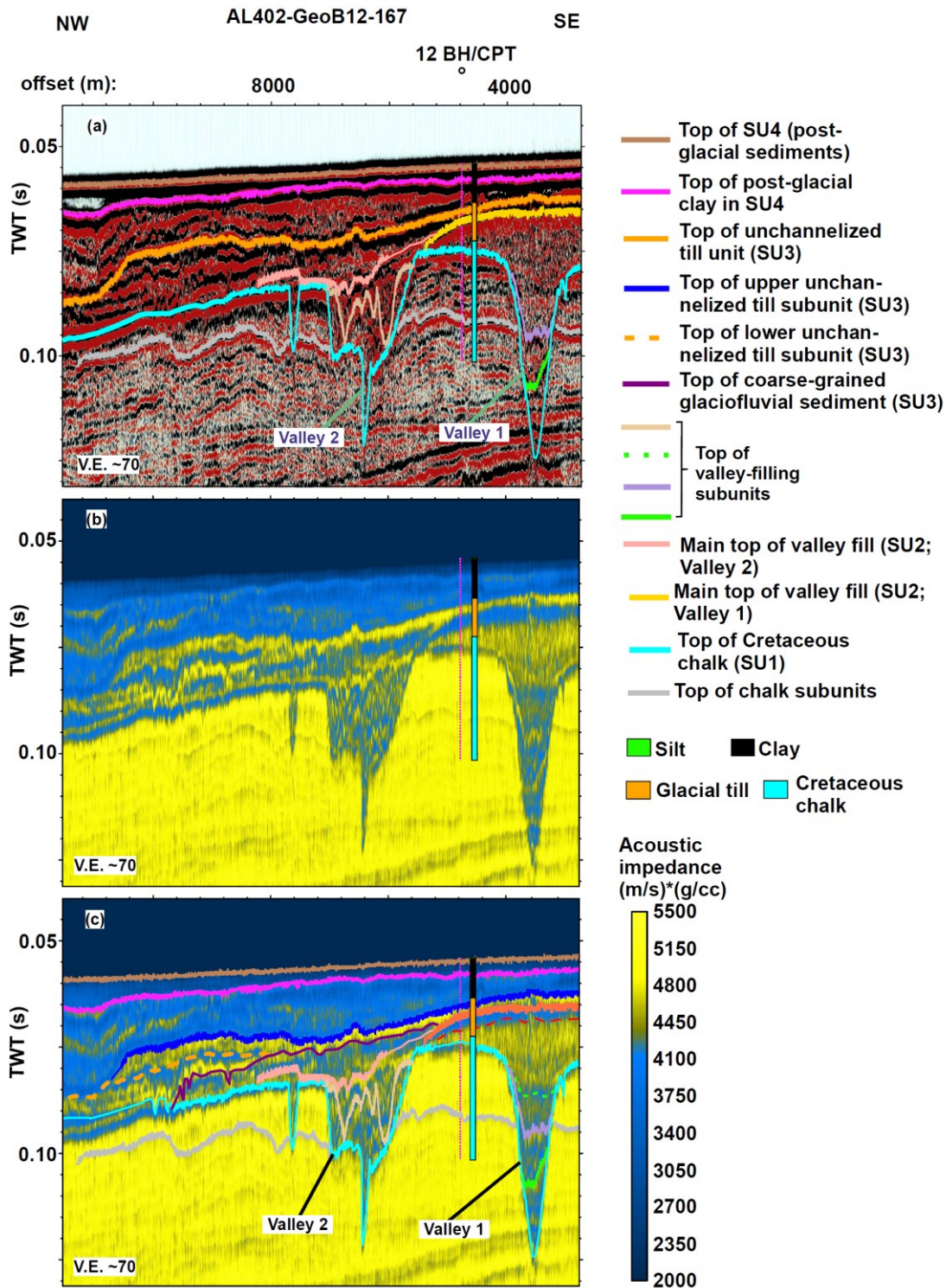


Fig. 5.5: 2D seismic Profile AL402-GeoB12-167 tied to the lithologic log at Site 12 BH/CPT: (a) seismic amplitude section of the profile showing the horizons independently picked along the same unit boundaries that were interpreted in chapter 3. These horizons formed the stratigraphic framework of an initial low-frequency impedance model employed in the band-limited approach; (b) un-interpreted absolute impedance section of the profile generated with the band-limited inversion approach. It corresponds to a part of fig. 5.3; (c) interpreted version of '5.5b' correlated with sediment descriptions. The stippled red line is the top of the high-impedance interval within the uppermost subunit filling Valley 1. This high-impedance zone is characterized by anomalous lithologic and geotechnical properties within the valley. Notice how impedance anomalies show the detailed spatial distribution of lithologic units, thereby allowing improvements on the initial horizon interpretation shown in '5.5a'. Artifacts occur as vertical stripes on this impedance section. TWT = Two-Way Travel-time; SU = Seismic Unit (vertical exaggeration was calculated based on a velocity of 2000 m/s)

### 5.4.2 Post-stack absolute acoustic impedance predicted with the band-limited approach - its comparison with the product of velocity-guided inversion

On the band-limited impedance section of Profile AL402-GeoB12-167, the Cretaceous chalk and post-glacial sediments have the highest and lowest mean impedance values, respectively, in the near-surface geological interval (table 5.2). The spatial position and geometry of geophysical boundaries are markedly similar in both the band-limited and velocity-guided impedance sections along the profile (compare figs. 5.3c and 5.5c). However, the range of impedance values predicted with the two approaches for most seismic units and subunits differs (table 5.2). For each seismic unit and subunit along the seismic profile, the range of predicted impedance values is wider in the band-limited inversion product than the velocity-guided impedance section (figs. 5.3 and 5.5; table 5.2). Using the statistical estimates derived for each seismic unit from velocity logs as the ground truth in our study area, the range of impedance predicted with the band-limited approach is more comparable to the ground truth than that of the velocity-guided approach does (table 5.2).

**Table 5.2: Measured and predicted statistical estimates of acoustic impedance for each seismic unit. The ground truth (measured) values are based on a compilation of velocity logs as shown in chapter 4, while the velocity-guided and band-limited values are based on the impedance predicted in each seismic unit along the entire section of Profile AL402-GeoB12-167. The velocity-guided and band-limited values for each seismic unit are calculated by summing the products of mean impedance and sample size at each trace location and dividing this sum by the total number of samples for all the locations. The unit of the statistical measures is (m/s)\*(g/cc). The estimated mean values are grand means. Min. = Minimum Value; Max. = Maximum Value; SU = Seismic Unit**

Source of estimate	Measure of statistics	Seismo-stratigraphic unit				
		SU4 (post-glacial sediment)	SU3		SU2 (valley fill)	SU1 (chalk)
			Till	Glaciofluvial sediment		
Ground truth	Min.	2670	3647	4039	3204	3942
	Max.	4794	6243	5472	5430	5648
	Mean	3622	4304	4674	4298	4790
Velocity-Guided inversion	Min.	4162	4146	4318	4220	4288
	Max.	4581	4690	4683	4830	5227
	Mean	4362	4413	4492	4484	4758
Band-Limited inversion	Min.	874	2609	2843	2989	2505
	Max.	5771	5974	5782	6006	6483
	Mean	3711	4411	4338	4374	4855

Within the Cretaceous chalk interval, the velocity-guided inversion approach applied to the Profile AL402-GeoB12-167 predicted a grand mean that was very close to the ground truth (table 5.2). Along the profile, the band-limited approach produced reliable

impedance values in both the chalk and post-glacial sediments on the basis of the grand means estimated for the lithologic units. Furthermore, it is evident that the impedance values predicted for the post-glacial sediments with the velocity-guided approach are too low in comparison to the ground truth (table 5.2). On one hand, along the Profile AL402-GeoB12-167, the band-limited seismic inversion approach produced a lesser grand mean impedance value than the velocity-guided approach within the Seismic Unit SU2, glaciofluvial section of SU3 and post-glacial interval (table 5.2). On the other hand, a comparison of the band-limited impedance section with its velocity-guided counterpart along the seismic profile appears to indicate that there is no significant difference in the mean impedance values predicted for the till sections of Seismic Unit SU3 (table 5.2). While the Seismic Unit SU2 on the band-limited impedance section exhibits a lesser grand mean impedance value relative to the SU3 till, the reverse is the case in the velocity-guided impedance section (table 5.2).

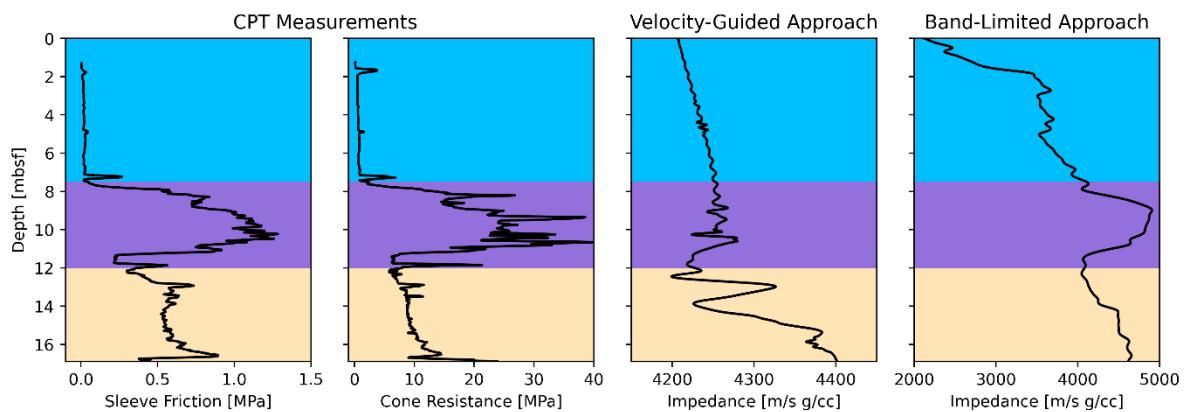


**Fig. 5.6: Raw data plot of the CPT measurements of sleeve friction and cone resistance and the impedance inversion results at Site 12 BH/CPT. Seismic Units SU4, SU3 and SU2 are shown with blue, purple and light brown backgrounds, respectively. Please note that the band-limited impedance is shifted upward by 1.07 m (the rationale for this decision is given in fig. 5.9).**

### 5.4.3 Correlation of the measured cone resistance and sleeve friction with the predicted absolute acoustic impedance - velocity-guided and band-limited inversion approaches

At Site 12 BH/CPT, the CPT profiles of measured cone resistance and sleeve friction were correlated with the acoustic impedance traces predicted by the velocity-guided and band-limited approaches (figs. 5.6 to 5.8). The measured sleeve friction and cone resistance in Seismic Unit SU4 show basically no variations (fig. 5.6). In addition, the resolution of the CPT data and acoustic impedance is at a different level. While the CPT data show very fine variations in the sub-meter scale, the seismic resolution is more at 0.5-1 m (fig. 5.6). This difference in resolution generally impacts CPT-to-

impedance correlation. Traversing from the shallower to deeper sections of the subsurface at Site 12 BH/CPT, it would be observed that the measured cone resistance and sleeve friction are relatively high in the unchannelized glacial till of SU3, and these CPT parameters decrease significantly into the Seismic Unit SU2, within which they progressively vary with depth.

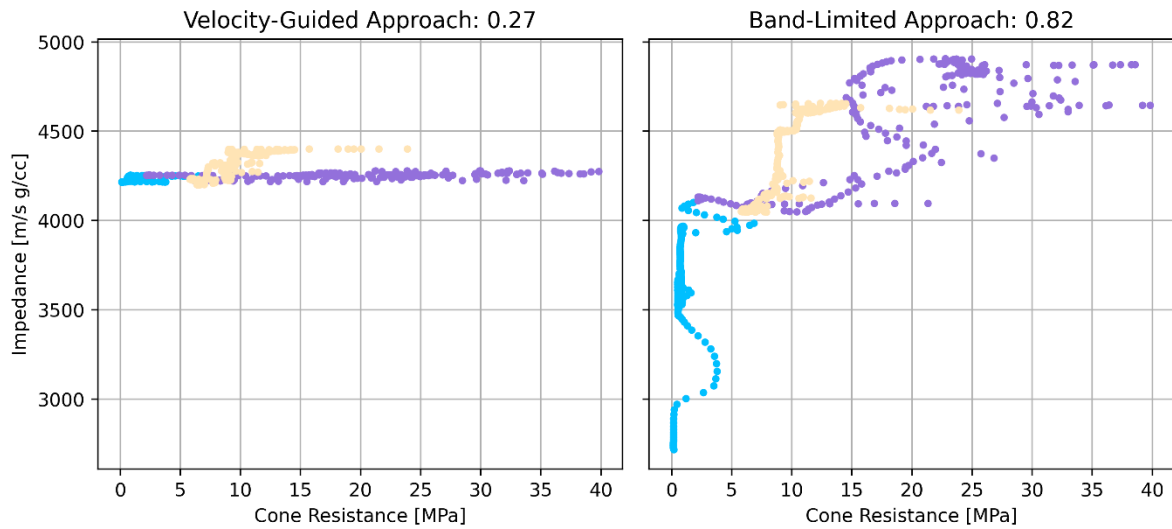


**Fig. 5.7:** Cross plots of measured cone resistance and predicted impedance at Site 12 BH/CPT with a correlation coefficient of 0.27 for the velocity-guided results and 0.82 for the band-limited results. The color code of the seismic units follows the code in fig. 5.6.

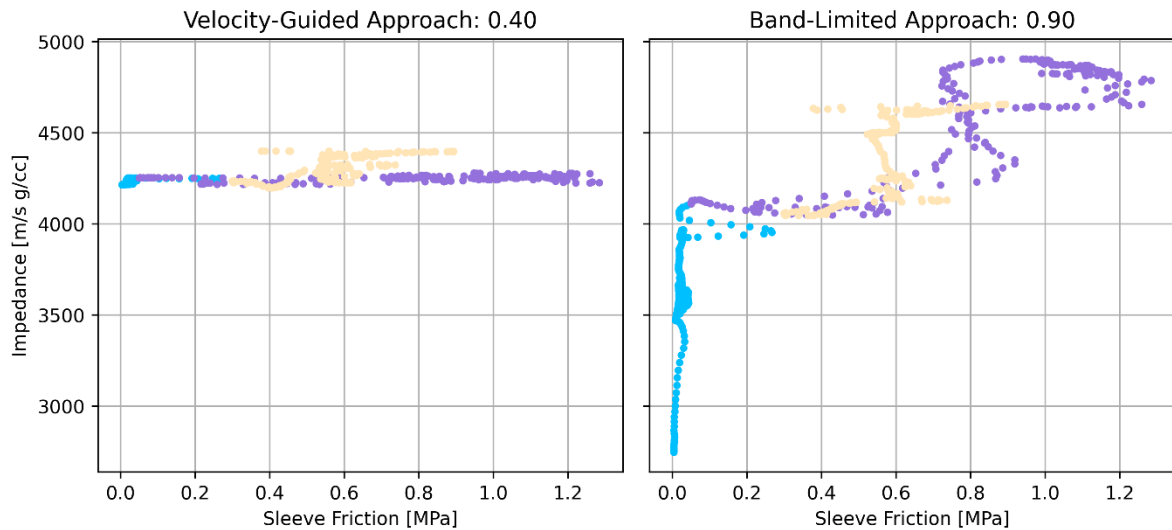


**Fig. 5.8:** Cross plots of measured sleeve friction and predicted impedance at Site 12 BH/CPT with a correlation coefficient of 0.40 for the velocity-guided results and 0.90 for the band-limited results. The color code of the seismic units follows the code in fig. 5.6.

The cross plots between cone resistance measurements and predicted acoustic impedance at Site 12 BH/CPT indicate correlation coefficients of 0.27 and 0.82 for the velocity-guided and band-limited inversion approaches, respectively (fig. 5.7). In addition, the cross plots between sleeve friction and predicted impedance at the same

site exhibit correlation coefficients of 0.40 and 0.90 for the velocity-guided and band-limited impedance inversions, respectively (fig. 5.8).

Depth conversion in a strict sense requires some form of calibration and possibly some shifting. To test whether a potential vertical shift is affecting the correlation of impedance and CPT data, a constant shift was applied and the correlation coefficient was calculated. The result is given in fig. 5.9. While no clear indication for a potential up- or downward shift is visible for the velocity-guided result, it seems to be rather clear that the band-limited should be shifted by about 1 m to achieve a fit with the CPT data (figs. 5.6 and 5.9).

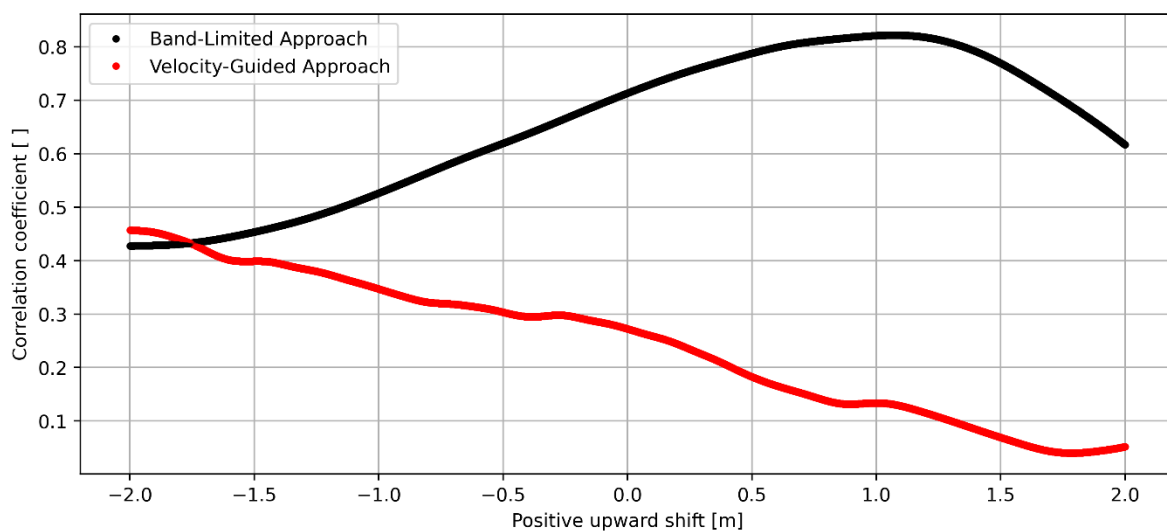


**Fig. 5.9:** Correlation coefficient of measured cone resistance and predicted impedance as a function of constant depth shift at Site 12 BH/CPT.

## 5.5 Discussion

### 5.5.1 Resolving stratigraphic and structural complexity in the near-surface sedimentary record of the southern Arkona Basin - significance of the correlation between absolute acoustic impedance and lithologic ground truth

Foremost, the four major seismic units and their subunits, which were correlated with borehole sediment descriptions in the study area in chapter 3, have been delineated on the absolute acoustic impedance sections in our current research (figs. 5.3 to 5.5). This finding agrees with Veeken and Da Silva (2004), who mentioned that interpretation of seismic inversion results helps to recognize significant geological boundaries in the subsurface. Besides, the succession of imaged geological units on the velocity-guided and band-limited impedance sections ties well with the lithologic succession described at Sites 7 and 12 BH/CPT (figs. 5.3b-c and 5.5b-c).

The difference of the statistical values between the ground truth and impedance inversion results in table 5.2 can partly be explained by the spatial restriction of the boreholes. While the unit statistics have been calculated for the entire profile for the impedance inversion results, those statistics are restricted to the borehole sites for the ground truthing. Thus a larger sample size and changing geologic settings are encountered for the impedance inversion results. The occurrence of the highest values of absolute acoustic impedance in the Cretaceous chalk on the impedance sections (e.g. figs. 5.3c and 5.5c, table 5.2) is supported by the trend observed in the median values of acoustic impedance derived for the seismic units on the basis of a compilation of P-S logs in the area (cf. chapter 4). Based on the report of fissures in the Cretaceous chalk at Site 11 B/CPT, it is evident that the lineaments seen in the chalk zone around the borehole on the acoustic impedance section of Profile AL402-GeoB12-168 (fig. 5.4) correspond to the surfaces of weakness which were interpreted as evidences of glaciotectonic brittle deformation within the bedrock chalk in chapter 3.

On the seismic amplitude section of Profile AL402-GeoB12-167, three subunits of SU2 have been interpreted within Valley 1 (fig. 5.5a). On the corresponding band-limited impedance profile, the shallowest of those three subunits could be further differentiated into a lower interval showing relatively low impedance values and an upper section with predominantly high impedance values, thereby indicating that four subunits of SU2 actually occur within Valley 1 (figs. 5.5b-c). Multiple units of impedance anomaly separated by curved interfaces within the tunnel valleys constitute the sedimentary packages of SU2 produced during multiple depositional episodes in the valleys (figs. 5.3 and 5.5). On the band-limited impedance section of Profile AL402-GeoB12-167, the uppermost subunit of SU2 occurring in Valley 1 has impedance values that are predominantly higher than those of the three underlying valley-filling subunits (figs. 5.5b-c). Since the primary acoustic impedance of a formation is dependent on P-wave velocity and its density, and in turn on its fluid content, mean grain size, porosity and mineralogical composition (Veeken and Da Silva, 2004; Vardy, 2015), the predominantly higher impedance values observed in the uppermost subunit of SU2 in Valley 1 might have a multi-factorial cause which might include relative preponderance of coarser material, low porosity and/or high proportion of crystalline rock fragments. However, sufficient core data are not available for a more specific explanation.

On the impedance sections, an interpretation of the areal coverage and morphology of the coarse-grained glaciofluvial interval at the base of SU3 is facilitated (figs. 5.4 and 5.5). This cobbly sedimentary interval would evidently have a relatively large mean grain size and low porosity (Gupta and Ramanathan, 2019), which might be expected to produce high acoustic impedance. Therefore, the relatively low values of absolute acoustic impedance associated with this coarse-grained glaciofluvial unit (e.g. figs 5.4c and 5.5c) might be due to the effect of a relatively low fraction of crystalline material. An alternative explanation such as high gas contents is unlikely, as the presence of gas was not reported in this glaciofluvial unit. Moreover, the mapping of the top and base of impedance anomalies not only indicates the lateral extent of the lower unchannelized till subunit in SU3, but it also shows that the Pleistocene glacial till penetrated at 6 BH/CPT is the lateral equivalent of the lower unchannelized till subunit encountered at 11 BH/CPT (fig. 5.4). It is noteworthy that this lower till subunit is not uniform in lithologic properties. Variation in impedance from its lower to upper parts indicates the occurrence of an intra-till boundary that compartmentalizes the subunit itself into two different sections vertically stacked on each other, with probable changes in lithologic properties occurring across the boundary (fig. 5.4). Thus, it was the upper compartment of this lower till subunit that was penetrated at 11 BH/CPT. This level of internal details in SU3 was not very evident on the corresponding seismic amplitude section (fig. 5.4).

Although there is limited ground truth for some units and subunits, the impedance inversion results can still depict the unit property changes and thus allow a more comprehensive interpretation. The surface of the lower till subunit of SU3 is undulating and irregular as evidenced from the configuration of impedance anomaly associated with it along the Profile AL402-GeoB12-168 (figs. 5.4b-c). Deposition in a Pleistocene glacial lake blanketed the rugged top of the lower till subunit with the glaciolacustrine clay encountered at 11 BH/CPT in the central part of the study area. Thickness variation of the low-impedance anomaly corresponding to this clay on the impedance section of Profile AL402-GeoB12-168 indicates that the clay unit gradually thickens in the northwestern direction, only to taper out abruptly (figs. 5.4b-c). This explains why the glaciolacustrine clay was not observed at 6 BH/CPT. Similarly, due to the tapering out of the upper unchannelized till subunit in the northwestern direction along the Profile AL402-GeoB12-168, as revealed by the morphology of its impedance anomaly, the upper till subunit was not penetrated at 6 BH/CPT (figs. 5.4b-c). Besides, the

spatial mapping of the top and base of the lower and upper unchannelized till subunits as defined by impedance anomalies showed that 7 BH/CPT penetrated the former till subunit, while the section of SU3 drilled at 12 BH/CPT was the latter till subunit (figs. 5.3b-c).

Furthermore, the lithologic variation in the post-glacial sediments particularly at Sites 6 and 7 BH/CPT can be correlated with significant impedance changes (e.g. figs. 5.3b-c). On the absolute impedance sections, this correlation allows the discrimination of the silt unit, which extends to the seafloor, from the underlying post-glacial clay in areas not penetrated by boreholes. Along the Profile AL402-GeoB12-167, the internal structures of geological units, which can be seen on the seismic amplitude section, are equally evident on the corresponding impedance sections. The velocity-guided and band-limited impedance sections preserve and reveal the undulating structural features in the post-glacial clay unit along the profile (figs. 5.3 and 5.5).

### **5.5.2 Qualitative consideration of the potential of acoustic impedance as an attribute for predicting CPT data**

According to Stoll (1989), the properties affecting the acoustic response of marine sediments include sediment structure, dynamic strain amplitude, overburden stress, lithification and grain size. These parameters also determine the cone resistance and sleeve friction during CPT measurements (Vardy et al., 2018). However, P-wave seismic data and geotechnical measurements are acquired under different strain regimes (Sauvin et al., 2019). While seismic data are collected under small strain conditions, conventional CPT measures large strain parameters. Besides, conventional seismic data have much lower resolution than geotechnical measurements (e.g. fig. 5.6), with the former and latter data types being recorded in time and depth domains, respectively. Noteworthy is that although events on seismic amplitude sections are interface-related, acoustic impedance and CPT measurements are both quantitative unit-based properties of formations. On the other hand, the difference in resolution between seismic and geotechnical measurements generally impacts the correlation between predicted acoustic impedance and CPT data.

In our study, the absolute acoustic impedance was derived from UHR seismic reflection data (central frequency ~350 Hz). The impedance values predicted by the band-limited and velocity-guided approaches show variations across unit boundaries from the Cretaceous chalk through valley fill and unchannelized till interval to post-

glacial sediments (figs. 5.3 to 5.5). Starting from 7.5 mbsf at Site 12 BH/CPT, measured cone resistance and sleeve friction increase drastically from SU4 to SU3, and their values decrease from SU3 to SU2 (fig. 5.6). At this site, the acoustic impedance predicted with the band-limited approach shows similar simultaneous changes across the boundaries of the seismic units (fig. 5.6). On the basis of the concurrent variations in predicted acoustic impedance, measured cone resistance and sleeve friction across the seismic units as observed at Site 12 BH/CPT (fig. 5.6), we posit from a qualitative point of view that the absolute acoustic impedance produced with the band-limited approach has the potential to serve as a predictor of cone resistance and sleeve friction during CPT data synthesis from UHR seismic data. This observation indicates that a risk for the generation of subsurface model can be mitigated. In general, there is a risk of missing potentially relevant units when a subsurface characterization was only based on boreholes (compare e.g. Henson and Sexton, 1991). In the case of the generation of integrated ground models incorporating inversion results, this risk is reduced as the lateral homogeneity and changes are revealed by the seismic data.

### **5.5.3 Assessment of the approaches for post-stack acoustic impedance prediction – quantitative relationship between the predicted impedance and CPT data**

Genetic algorithms have been employed for the two seismic inversion approaches in this study. The genetic algorithms used in the velocity-guided and band-limited approaches incur significantly higher computational costs compared to conventional deterministic optimization methods, but the benefits are threefold. First, the algorithms' randomized initial generation of models results in a final impedance model that is derived from field seismic data. Consequently, the ultimate impedance model is more independent of interpreter bias, and the inversion algorithm autonomously determines an optimal model that offers the best global fitness solution from a statistical standpoint. Second, as the inversion explores a substantial portion of impedance space, it permits the calculation of statistically meaningful Probability Density Functions for each sample at every trace location. This enables the determination of confidence limits in addition to the statistically optimal solution. Third, stochastic optimization algorithms like genetic algorithms deliver robust optimization solutions, even in the presence of significant noise contamination. For genetic algorithms, the mutation operator allows the algorithm to continuously explore a wide region of the

parameter space, enabling it to overcome local minima in the optimization space and converge toward the global minimum.

In the two post-stack inversion approaches carried out in this study, a stationary wavelet was used and attenuation was not compensated. Due to the significant occurrence of fine grained sediments and chalk in the working area, Quality Factors  $Q > 100$  are to be expected (Pinson et al., 2008). Considering the source signal of the air gun used in acquiring the seismic data, the source signal change due to attenuation is thought to be negligible for those high  $Q$  values. With relatively high  $Q$  values, the level of uncertainty introduced by attenuation is negligible as exemplified by Römer-Stange et al. (in prep. 2023).

The impedance sections produced by the band-limited and velocity-guided inversion approaches exhibit meaningful impedance values that differentiate seismic units from one another along the same seismic line (figs. 5.3 and 5.5). The numerical difference between the two inversion approaches (section 5.4.2) could be due to: (1) difference in the wavelet used for convolution; (2) difference in the cost function for minimization; and (3) smoothing of a-priori impedance model in the velocity-guided approach only. In the band-limited technique, a statistical wavelet extraction was performed on the post-stack seismic image by stacking the tapered seafloor reflection along the seismic line and this yielded a true, mixed phase wavelet that was used for the inversion. Although the velocity-guided approach equally employed a statistical wavelet derived from the seismic data, the phase of the wavelet used in the approach was imposed to be 0. The zero phase wavelet used in the velocity-guided inversion scheme is therefore different from the mixed phase wavelet present in the actual seismic amplitude data. Thus, the lenticular low-impedance anomaly, which occurs within the uppermost subunit filling Valley 1 at the southeastern end of Profile AL402-GeoB12-167 (figs. 5.3b-c), might be an artifact partly or wholly caused by the difference between the phase of the wavelet used for inversion and that of the true wavelet.

Comparing the band-limited impedance section to its velocity-guided counterpart along the seismic Profile AL402-GeoB12-167, it appears that there is no significant difference in the mean impedance values predicted for the till subunits of Seismic Unit SU3 (table 5.2). However, at Site 12 BH/CPT and nearby areas, the impedance values of the SU3 till are generally higher in the band-limited product than in the velocity-guided section (figs. 5.3, 5.5 and 5.6). Thus, the similarity in the mean impedance

values of the SU3 till in both inversion products could be due to the presence of significantly lower values of impedance within the till subunits in other parts of the band-limited product than in the velocity-guided section, which leads to a much lower minimum value and broader range of impedance in the band-limited impedance section than in its velocity-guided counterpart within the SU3 till (table 5.2).

At Site 12 BH/CPT, based on the correlation coefficients, both velocity-guided and band-limited approaches yielded a better correlation between the sleeve friction and predicted acoustic impedance than between the measured cone resistance and predicted acoustic impedance (figs. 5.7 and 5.8). While the impedance predicted by the band-limited approach highly correlates with the measured cone resistance and sleeve friction (correlation coefficients of 0.82 and 0.90, respectively), the velocity-guided approach yielded acoustic impedance values that have little to low correlation with the measured CPT parameters (figs. 5.7 and 5.8). Therefore, the band-limited approach yielded absolute acoustic impedance values that would better predict CPT data than the product of the velocity-guided inversion approach. This difference might be partly or wholly due to the difference between the phases of wavelets used in the inversion approaches. Consequently, the velocity-guided approach might be improved by utilizing the true wavelet of the seismic data in the inversion scheme.

The high level of correlation between the band-limited impedance values and measured cone resistance and sleeve friction in our current study means that impedance values generated with the band-limited approach can be used to reliably predict CPT parameters in the southern Arkona Basin. Sauvin et al. (2019) also reported a good correlation between measured and predicted tip resistance values when they used an artificial neural network in multi-attribute regression for tip resistance prediction. The regression was performed between acoustic impedance and other seismic property on one hand and measured tip resistance on the other hand by training at multiple calibration sites. Besides, Chen et al. (2021) showed that acoustic impedance generated by inverting ultrahigh-frequency (>2000 Hz) geophysical data can serve as a predictor of tip resistance for site characterizations.

Furthermore, in our study, horizons initially picked on seismic amplitude sections have been refined by re-picking them on the impedance sections. Along Profile AL402-GeoB12-167, the impedance sections produced with the two inversion approaches reveal remarkably similar stratigraphic and structural framework (compare figs. 5.3

and 5.5). The interpreted geological features from both impedance sections also correlate with lithologic ground truths at the associated borehole sites (figs. 5.3 to 5.5). However, while the impedance section generated with the velocity-guided approach is smooth, the product of the band-limited approach has vertical stripes that occur as artifacts (compare figs. 5.3 and 5.5). This difference could be due to the smooth acoustic impedance a-priori information which was applied in the former approach only and the abstaining of all kinds of smoothing in the latter approach.

## **5.6 Conclusions**

Conventional seismic amplitude sections allow qualitative interpretation of stratigraphic and structural features based on interface-related seismic attributes. Our study has shown that such qualitative analysis of ultra-high-resolution seismic data should be checked and improved with seismic inversion results such as the post-stack absolute acoustic impedance.

In this research, post-stack absolute acoustic impedance of formations has been predicted using two different seismic inversion approaches based on stationary wavelets. Those approaches have been used to resolve subsoil geological complexity in the southern Arkona Basin. Impedance variation along seismic profiles has revealed anomalies that depicted not only the spatial extent and structure of stratigraphic intervals, but also the intra-unit boundary caused by internal lithologic variations which were not obvious on seismic amplitude sections. In our study, absolute acoustic impedance anomaly of formations accurately tied with lithologic ground truths at borehole locations in the southern Arkona Basin. This fostered the lateral correlation of lithologic units between boreholes and provided a detailed understanding of stratigraphic compartments, particularly within an unchannelized till unit. It also aided delineation of glaciofluvial rock fragments and glaciolacustrine clay. In the Cretaceous bedrock, fissures were depicted as lineaments on an absolute acoustic impedance section. The multiple sedimentary packages making up valley fills were represented as stacked units of impedance anomaly separated by curved interfaces across which there was a major acoustic impedance contrast. The internal geomorphologic features seen on seismic amplitude sections within the post-glacial clay interval were equally preserved on absolute acoustic impedance profiles. Consequently, post-stack absolute acoustic impedance should be predicted through inversion of UHR seismic data and tied to lithologic logs to resolve near-surface stratigraphic and structural

complexity, for example, in glaciated terrains consisting of Cretaceous bedrock chalk covered by glaciogenic sediments, which have in turn been succeeded by post-glacial clay and silt. Absolute acoustic impedance might have the potential to be used for predicting lithologic properties in the southern Arkona Basin.

Besides, we have shown that, in the southern Arkona Basin, qualitative changes in the measured cone resistance and sleeve friction across major unit boundaries within the post-glacial to glaciogenic interval occur concurrently with variations in the predicted absolute acoustic impedance. At a CPT site, the predicted absolute acoustic impedance from the band-limited inversion approach (described in this study) highly correlates with the measured cone resistance and sleeve friction values. We therefore conclude that when properly utilized, post-stack absolute acoustic impedance from UHR seismic reflection data has the potential to serve as an attribute for predicting geotechnical parameters - at least cone resistance and sleeve friction values - of subsoil units in the southern Arkona Basin.

The impedance inversion approaches used in this study - velocity-guided and band-limited approaches - were based on stationary wavelets, and they yielded meaningful results that variably tied with ground truths. However, it appears that an improved result might be realized with the velocity-guided approach, if the true wavelet and its actual phase are used for the inversion. It is equally apparent that attention should be given to improving the smoothness of predicted impedance sections in the band-limited approach. In the implementation of a genetic algorithm for impedance inversion using stationary wavelets, the phase of the applied wavelet in relation to that of the true wavelet, cost function for minimization, and smoothing of acoustic impedance a-priori information are factors that might have an impact on predicted impedance values.

## **5.7 Acknowledgements**

This study was funded through the project 'SynCore' (project number 03EE3020C) by the German Federal Ministry for Economic Affairs and Climate Action on the basis of a parliamentary resolution passed by the German Bundestag. The authors thank the partners in the project (Fraunhofer ITWM, GuD Geotechnik und Dynamik Consult GmbH, RWE Renewables GmbH) for their cooperation.

We also thank the captains and the crews of R/V Alkor for the successful conduction of the seismic data acquisition campaign during the research expeditions.

The geological, geophysical and geotechnical data as well as computers and IHS Kingdom license were made available by the University of Bremen for this study. The Norwegian Geotechnical Institute equally used its computing facility to carry out seismic inversion during and after a research placement of the first author at the institute. This research stay was funded by the MARUM graduate school GLOMAR. Our study benefited from fruitful discussions with Dr. Jean-Rémi Dujardin.

## Chapter 6

### Conclusions and outlook

In the last three decades, the offshore wind energy sector has received increased attention in Europe. Therefore, site investigations are being carried out in the Arkona Basin more than ever before, and these involve integrating geological, geophysical and geotechnical data for building ground models. However, the limitation of Cone Penetration Test (CPT) data and sediment cores to 1D domain and upper few 10s of meters below the seafloor and the unavoidable disturbance of seabed during drilling operations indicate that there is a need to cost-effectively use already-existing geophysical and geotechnical data for predicting CPT parameters between and beyond drilled points during site characterization. Following the use of acoustic impedance for lithologic predictions in the oil and gas industry, recent studies have shown that when impedance is derived from ultra-high-frequency and high-resolution seismic data, it has the potential to serve as a predictor of CPT profiles away from drilled locations (e.g. Sauvin et al., 2019; Chen et al., 2021). Thus, the objectives of this current research were to: (1) establish the stratigraphic and structural framework of near-surface geological formations in the southern Arkona Basin using qualitative and quantitative seismic attributes; (2) assess CPT data prediction from ultra-high-resolution seismic reflection data in the study area, and reveal the interface-related and layer-based seismic attributes that can be used for the prediction; (3) estimate statistical boundary conditions of small strain physical properties of geological formations, and show their usefulness in seismic inversion; and (4) evaluate two near-surface impedance inversion approaches carried out with stationary wavelets.

Using 2D and 3D multi-channel seismic (MCS) reflection data and sediment descriptions at borehole sites, the current study has revealed not only the detailed geological framework of the shallow sedimentary succession in the southern Arkona Basin, but also the geological processes that have shaped the area from Late Cretaceous to Holocene. These would be useful for ground modeling purposes during site investigations in the area. Furthermore, with the aid of the MCS and CPT data integrated with sediment descriptions and velocity logs, the research has not only shown a statistical summary of subsoil physical and geotechnical properties within principal geological formations in the area, but it has also revealed the possibility of

using physical property estimates for building initial low-frequency models during seismic inversion. In the body of the work, potential seismic attributes for predicting near-surface geotechnical parameters have been delineated. In addition, by combining seismic and CPT data with lithologic descriptions, the role of post-stack acoustic impedance as a reliable indicator of lithologic and geotechnical changes in glacially influenced terrains has been established using the southern Arkona Basin as an example. Finally, two impedance inversion approaches carried out with velocity-guided background trend (velocity-guided approach) and layer cake low-frequency model (band-limited approach) have been assessed for the improvement of those approaches. The principal conclusions reached in the three standalone research manuscripts of this thesis (chapters 3 to 5) are shown in the succeeding sections.

### **6.1 Seismic stratigraphy and structural analysis of shallow seabed in the southern Arkona Basin**

In the research covered in chapter 3, 2D and 3D ultra-high-resolution MCS reflection data, sediment descriptions in boreholes, and velocity logs were integrated to: (1) reveal the stratigraphic and structural architecture of shallow seabed in the southern Arkona Basin; (2) elucidate depositional and post-depositional processes that affected the terrain; and (3) provide a conceptual model for the Late Cretaceous to Holocene geological evolution in the area. In the chapter, three subunits of Cretaceous chalk have been imaged within the bedrock section of the seismic data. In the southeastern, central and northern parts of the study area, basement-reaching Nordadler faults of the Tornquist Zone dissect the lower section of the imaged pre-Quaternary bedrock. During a Late Cretaceous inversion, the Cretaceous chalk was folded in the study area. Two regimes of crustal extension in Tertiary were revealed in the southern Arkona Basin; they produced relatively shallow normal faults as major structural features in the bedrock.

Pleistocene glaciation(s) incised a minimum of two generations of V-shaped tunnel valleys into the Cretaceous bedrock by subglacial meltwater erosion during glacier advancement(s). Within the 3D seismic coverage in the southcentral part of the study area, some of these valleys evidently connect with each other and are 340-900 m wide, the maximum depth being ~66 m. In most subglacial channels encountered in our study, the loads deposited by glacier(s) are till-dominated. In valleys filled with multiple packages of the till-dominated sediments, erosional surfaces between the

main sedimentary packages indicate that major depositional episodes were interrupted by meltwater and/or glacial erosion. The episodic deposition in these valleys included sedimentation of materials other than tills. Stratified sediments of glaciofluvial to glaciolacustrine origin fill some amalgamated depressions in the southcentral area. The sands and coarser-grained sediments deposited in subglacial tunnel valleys in the southeastern and northern parts of the study area were probably laid down from meltwater.

Glaciofluvial processes probably associated with the retreat of a valley-filling Pleistocene glacier deposited a unit of cobbles on top of the Cretaceous chalk in the central part of the study area. Subsequently, during Weichselian glaciation, sedimentation of a laterally extensive, unchannelized interval dominated by two tills occurred across the entire study area. At the base of this interval, s-forms sculptured by subglacial erosion across the top of the Cretaceous chalk and valley fills have been preserved in the 3D MCS coverage. The NE-SW oriented s-form probably documents NE to SW local ice flow for a Weichselian glacier in the southcentral area. However, the timing of the NW-SE trending s-forms relative to the afore-mentioned NE-SW oriented one could not be clearly defined. A glacial retreat phase is documented by a localized clay interval - probably of a glaciolacustrine origin - which occurs within the composite unchannelized Weichselian till unit in the central part of the study area. In the southcentral part of our working area, the top of the gross unchannelized till unit exhibits buried NW-SE trending glacial ridges, the origin of which might be related to protrusions in the bedrock of the responsible Weichselian glacier(s). During the last glacial retreat documented in the northern area, glaciofluvial processes probably cut a sediment-filled Quaternary channel into the unchannelized till-dominated unit.

Glaciotectonic deformation of the pre-existing till units and valley fills in the substratum of overriding glaciers occurred in the Pleistocene. This is partly evident in the folded and discontinuous character of the stratified valley fills in places (e.g. in the southcentral part of the study area). The glaciotectonic kinks in the Cretaceous chalk and unchannelized Weichselian till were formed by subglacial shearing of the substratum during Pleistocene glacier movement in the northern part of our working area. Brittle non-penetrative glacial deformation of the bedrock chalk occurred in the central part of the study area where a localized patch of chalk is fissured directly beneath the top of Cretaceous. Permafrost lineaments in an ancient patterned ground have been preserved within the unchannelized till unit as evidences of the Weichselian

glacial episode in the southcentral part of the working area. Post-glacial lacustrine to marine/brackish water processes deposited clay, silt and sand that partly onlap the unchannelized Weichselian till unit and cap the entire stratigraphic succession in the southern Arkona Basin.

A conceptual model has been developed for the Late Cretaceous to Holocene geological evolution of the shallow seabed in the southcentral part of our study area (fig. 3.11). We showed that seismic stratigraphy and deduction of geological history allow accurate sediment correlation and facies prediction in an area. However, it is noteworthy to point out that the above-mentioned interpretations might be refined when more borehole and seismic data are available.

Furthermore, it has been shown that the Tertiary crustal extension in the southern Baltic Sea occurred in multiple regimes, which could be differentiated based on the dip angle of the normal faults produced. In addition, our data have revealed that although 2D seismic lines might be good for preliminary imaging of regional structures, 3D seismic data and their time slices (horizontal slices are not available in 2D seismic data) are necessary to resolve the complexity and interconnectivity of geological units, structures and buried landforms, particularly in a glacially affected terrain.

Our relatively small seismic cube has shown that the interconnected and partly meandering Pleistocene subglacial channels in the southern Baltic Sea region were formed by meltwater erosion. From the seismic cube, the current knowledge of local ice flow direction of a Weichselian glacier deduced in the southcentral part of our study area has contributed to the regional understanding of ice movement during the Quaternary. Furthermore, RMS amplitudes extracted in the 3D seismic cube unraveled, for the first time, evidences of buried relict permafrost structures left behind in the Arkona Basin after the retreat of the Weichselian glacier(s). Extraction of such amplitudes would not be possible with 2D seismic profiles.

Consequently, acquiring 3D seismic data and integrating them with geological data from boreholes are required for building accurate ground models of stratigraphic units and structural features, for instance, in a glacially influenced terrain. Furthermore, in our study, integrating 2D and 3D seismic reflection data with borehole geological descriptions has added to our regional understanding of past glacial dynamics and erosional activities in the southern Baltic Sea.

## 6.2 Statistical boundary conditions of subsoil physical properties and the potential seismic attributes for predicting near-surface geotechnical parameters

Chapter 4 presented information based on ultra-high-resolution 3D and 2D MCS reflection data (which were processed during the study covered in chapter 3), sediment descriptions from boreholes, downhole Primary and Shear wave velocity (P-S) logs, and CPT measurements in the southern Arkona Basin. Therein, we built on the seismo-stratigraphic and structural framework revealed in chapter 3, and investigated the relationship between seismic attribute and CPT parameter changes within each seismic unit. We did not only assess the prediction of CPT data from ultra-high-resolution seismic data, but also delineated the interface-related and layer-based seismic attributes that can be used for such predictions. We further established boundary conditions of subsoil physical properties that characterize geological formations in the southern Arkona Basin. Finally, we correlated seismic units' median small strain physical properties with their corresponding median large strain parameter - measured cone resistance - within the study area.

The study in chapter 4 revealed that, in the near-surface interval, the variations in CPT measurements across major unit and subunit boundaries correspond to changes in physical property and seismic attributes. At various locations, multiple seismic reflector attributes - amplitude, continuity, configuration and frequency - either vary concurrently with average normalized Soil Behavior Type (SBT<sub>n</sub>) or remain similar when the average SBT<sub>n</sub> does not change within each seismic unit from one CPT location to another. Thus, trace envelope, instantaneous frequency and lateral continuity of reflectors are derived interface-related seismic attributes that can be used as composite guides for CPT data prediction from seismic data.

In this study, trends in the summary statistical estimates of Poisson's ratio and small strain shear modulus agree with geological interpretation. Consequently, statistical estimates of the small strain physical parameters, particularly P-impedance, which have been generated and itemized in chapter 4 for each geological unit, could potentially function as boundary conditions for initial model building during acoustic impedance inversion in the southern Arkona basin. In a stratigraphic framework built with seismic horizons, assigning the median value of a physical property to corresponding geological units would help to deduce a low-frequency trend in an initial model for seismic impedance inversion where there are no boreholes on the seismic line of interest. Furthermore, based on the positive correlation between the measured

median cone resistance and median acoustic impedance across multiple seismic units, we concluded that cone resistance could be predicted from acoustic impedance, a layer attribute. Nonetheless, prediction of uncorrected cone resistance including its median value from acoustic impedance might require defining a unique regression line for each seismic unit, as the relationship between cone resistance and acoustic impedance appears to vary from one seismic unit to another.

### **6.3 Post-stack acoustic impedance as a reliable indicator of variation in lithologic and geotechnical properties - assessment of two near-surface impedance inversion approaches using stationary wavelets**

Since conventional seismic amplitude sections only allow qualitative interpretation of stratigraphic and structural features based on interface-related seismic attributes (the interpretation approach adopted in chapter 3), in chapter 5 we presented two 2D seismic lines (central frequency ~350 Hz, vertical resolution ~1.1 m), sediment descriptions from 4 boreholes, and CPT data from 1 location to demonstrate the use of acoustic impedance as a quantitative layer-based seismic tool for resolving geological complexity within the Cretaceous to Holocene succession in the southern Arkona Basin. Furthermore, acoustic impedance was qualitatively and quantitatively correlated with variation in measured cone resistance and sleeve friction within the post-glacial to glaciogenic interval. Finally, we evaluated the acoustic impedance sections generated with two post-stack inversion approaches.

Using stationary wavelets and not accounting for attenuation, 2D post-stack absolute acoustic impedance sections along seismic profiles were derived with the velocity-guided and band-limited inversion approaches, which were described in chapter 5. Anomalous changes in impedance values along the profiles revealed the vertical stacking, spatial extent and structure of geological units. For instance, in our study, the spatial extent of glaciofluvial rock fragments and glaciolacustrine clay was clearly evident on the impedance sections. Within a glacial till interval, variations of impedance values revealed an intra-unit property boundary caused by internal lithologic variations, though this boundary was not clearly evident on the seismic amplitude section. The accurate tie between absolute acoustic impedance anomaly and lithologic ground truths at borehole locations in the southern Arkona Basin enabled lateral correlation of lithologic units. Changes in the acoustic impedance of formations provided an understanding of compartmentalization in the stratigraphic units, particularly within the unchannelized till unit. Besides, on an absolute acoustic

impedance section, the lineaments observed within a localized chalk zone directly below the top of Cretaceous corresponded to fissures reported in the Cretaceous chalk samples retrieved from the zone during borehole drilling. The multiple sedimentary packages deposited within the tunnel valleys in our working area were depicted as stacked units of impedance anomaly separated by curved interfaces across which there was an acoustic impedance contrast. Moreover, internal seismic-scale geomorphologic features seen on the seismic amplitude sections within the post-glacial clay interval could be observed on the absolute acoustic impedance profiles as well. Therefore, we concluded that post-stack absolute acoustic impedance sections should be generated by inverting ultra-high-resolution seismic reflection data, and the impedance sections should be tied to geological descriptions of sediments along boreholes. This would establish an impedance-to-lithology relationship that could be used to resolve near-surface stratigraphic and structural complexity, for instance, in glaciated terrains consisting of Cretaceous chalk bedrock overlain by glaciogenic sediments, which are in turn succeeded by post-glacial clay and silt.

Furthermore, our qualitative analysis revealed that, in the southern Arkona Basin, variations in the measured cone resistance and sleeve friction across major unit boundaries within the post-glacial to glaciogenic stratigraphic interval occurred concurrently with changes in the absolute acoustic impedance. As shown in chapter 5, the absolute acoustic impedance predicted with the band-limited approach highly correlated with the measured cone resistance and sleeve friction at an investigated CPT site. Thus, we concluded that when properly applied, absolute acoustic impedance from full stacks of ultra-high-resolution seismic reflection data has the potential to be a predictor of geotechnical parameters - at least cone resistance and sleeve friction - of subsoil units in the southern Arkona Basin.

The velocity-guided and band-limited acoustic impedance inversion approaches employed in this study yielded meaningful results that tied with ground truths. However, we posited that more accurate impedance values might be predicted with the former approach, if the true wavelet in the seismic data and its actual phase could be utilized for the inversion. In the band-limited inversion approach, improving the smoothness of predicted impedance sections should be considered. Finally, when implementing a genetic algorithm for impedance inversion using stationary wavelets, the factors that might have an impact on predicted impedance values include cost function for minimization, smoothing of a-priori impedance models, and the phase of

the wavelet used for the inversion in comparison to that of the true wavelet contained in the actual seismic amplitude data. These factors should be given attention.

#### **6.4 Outlook**

In the Arkona Basin, future research would benefit greatly from an extensive 3D seismic coverage in the region. Given that a relatively small 3D seismic cube and sparsely distributed 2D seismic profiles were used in this current research, additional 3D seismic reflection data should be acquired, processed and interpreted, or perhaps integrated with closely-spaced 2D seismic profiles in the basin. Besides, new boreholes in which sediments have been cored and dated should be provided and combined with this larger seismic dataset. The objectives of this integrated study should be to: (1) establish the linkage of the Tertiary fault system that has been recognized in the region in this current study; (2) reveal the regional extent, orientation and interconnectivity of the tunnel valleys across a much larger area; (3) unravel the regional distribution of glacially derived erosional and depositional features/landforms recorded in the near-surface sedimentary succession; and (4) determine the micro-scale lithologic characteristics of glaciogenic sediments and Cretaceous chalk in the Arkona Basin.

Extensively mapping the Tertiary normal fault system and its linkage on a regional scale would provide more insights into the pre-Quaternary extensional tectonics that caused brittle deformation of the Cretaceous chalk interval in the Arkona Basin. The further research would clarify the relative timing of the two regimes of Tertiary crustal extension deduced in this current work. Perhaps, the future study might reveal additional stages in the multi-phased faulting event that took place in the Arkona Basin during the Tertiary.

Since we know that tunnel valleys tend to develop parallel to ice flow, deciphering the coverage, orientation and interconnectivity of the tunnel valleys across a large area of the Arkona Basin, and integrating these with the age and lithologic characteristics of associated valley fills, would allow large-scale reconstruction of past ice flow directions during the valley-forming stage(s). Furthermore, these integrated approach would foster a regional understanding of erosional and depositional events associated with the glacier(s) that formed and filled the valleys. In addition, within and along the base of the unchannelized Weichselian till interval, integrating the 3D regional structure and distribution of glacial landforms with the exact age of sediments constituting the unit

would unravel not only the regional flow directions of the Weichselian glaciers, but also the temporal and spatial changes in those directions. Moreover, while seismic amplitude data in the region would provide only the macro-features of geological units, sediment cores from boreholes would provide micro-scale properties of the sediments. Thus, carrying out detailed micro-structural analyses of sediment cores in the context of seismic data in our study area and in the Arkona Basin as a whole would provide insights into the mechanism of glaciotectonic deformation of the valley fills, unchannelized till unit and Cretaceous chalk in the region. The above-mentioned information would ensure an accurate modeling of Quaternary glacial dynamics in the region of the Arkona Basin.

Since post-stack acoustic impedance has been established as an indicator of lithologic properties in our study area, current and/or future 3D seismic cube and additional 2D profiles should be inverted for acoustic impedance as this would help to further resolve geological complexity that might exist in the stratigraphic and structural framework across the study area. Besides, extra borehole geophysical and geotechnical data should be compiled and integrated into our database in the future. These would generate more representative statistical estimates of subsoil physical properties in the southern Arkona basin. Moreover, the velocity-guided and band-limited impedance inversion approaches used in this current study might be further developed by paying attention to the factors that can have an impact on the impedance values predicted with genetic algorithms. As mentioned in the conclusions of this thesis, these factors include smoothing of a-priori impedance models, cost function for minimization, and the phase of the wavelet used for inversion in comparison to the true wavelet in the seismic data.

Finally, in the southern Arkona Basin, multi-attribute prediction of CPT data from ultra-high-resolution seismic data should be tested and carried out by using layer-based acoustic impedance as the main predictor and composite interface-related seismic attributes - trace envelope, instantaneous frequency and lateral continuity - as supporting guides.

## Acknowledgements

The pivotal role played by my supervisor, Volkhard Spiess, in the development of my doctoral thesis is truly invaluable. Your guidance significantly contributed to refining my research ideas. Additionally, I am grateful for the opportunity you opened up for me to engage in a meaningful discussion with Baltic Sea researchers. I extend my heartfelt appreciation for your encouragement regarding conference presentations and my research placement.

I express my gratitude to Katrine Andresen, who, despite primary obligations, graciously accepted the role of a second reviewer on my examining committee, even with short notice.

The constructive suggestions provided by members of my thesis committee led to my research stay at the Norwegian Geotechnical Institute (NGI). I would like to thank Hanno Keil, Karsten Obst, and Stefan Wenau for their involvement in this committee. Karsten Obst notably provided a valuable forum at the University of Greifswald (Germany) for scientific discussions pertaining to my findings.

During my research placement at NGI in Oslo, Maarten Vanneste, Guillaume Sauvin, and Jean-Rémi Dujardin significantly enriched my knowledge base and fostered a welcoming environment. This stay has resulted in a fruitful scientific collaboration and a meaningful friendship. My immense thanks go to Maarten, Guillaume, and Jean-Rémi for the enjoyable evenings we spent together. Special appreciation is extended to Maarten and his family for their unparalleled hospitality. The culinary experiences, particularly the sumptuous octopus and whale, were truly memorable. I am grateful to GLOMAR for funding my research stay at NGI.

I want to highlight the friendly atmosphere at the Marine Technology and Environmental Research Group, University of Bremen, and express my appreciation for the shared lunch and discussions.

In conclusion, my sincere appreciation goes to my family and friends who stood by me through challenges. Your unwavering support saw me through the difficulties of the Covid-19 period and significant life changes that could have disrupted my career. To my siblings - Gbenga Ogunleye, Shola Ogunleye, Folake Sagbale and Bimbo Ogunleye - I hold deep affection for you. Mayokun and Joy Fisayo, your timely support

is truly appreciated. Thanks to Abraham, Frank, Ruru, Uche, Stanley, and Helmut for your loyal friendship. Profound gratitude is reserved for the most beautiful woman on Earth - my lovely, elegant, and supportive wife, Lois. I will forever cherish the invaluable love you showed me during the period when my dedication to you and my passion for my Ph.D. seemed to collide. You know what I mean...my one and only fish. Last but definitely not the least, I deeply appreciate the greatest love shown to me by my Life-Giver, Jehovah God.

## References

- Aber, J.S., 1980. Kineto-stratigraphy at Hvideklint, Møn, Denmark and its regional significance. *Bull. geol. Soc. Denmark* 28: 81-93.
- Aber, J.S., 1982. Model for glaciotectionism. *Bull. geol. Soc. Denmark*, vol. 30, pp. 79-90.
- Aki, K., Richards, P.G., 2002. *Quantitative seismology*. Sausalito, Calif.: University Science Books. Retrieved from [http://katalog.suub.uni-bremen.de/DB=1/LNG=DU/CMD?ACT=SRCHA&IKT=8000&TRM=40206166\\*](http://katalog.suub.uni-bremen.de/DB=1/LNG=DU/CMD?ACT=SRCHA&IKT=8000&TRM=40206166*)
- Al Hseinat, M., Hübscher, C., 2014. Ice-load induced tectonics controlled tunnel valley evolution – instances from the southwestern Baltic Sea. *Quaternary Science Reviews*, 97, 121-135.
- Al Hseinat M., Hübscher, C., 2017. Late Cretaceous to recent tectonic evolution of the North German Basin and the transition zone to the Baltic Shield/southwest Baltic Sea. *Tectonophysics* 708, 28-55.
- Avseth, P., Mukerji, T., Mavko, G., 2005. *Quantitative seismic interpretation: Applying rock physics tools to reduce interpretation risk*. Cambridge: Cambridge University Press, doi:10.1017/CBO9780511600074
- Averes, T., Hofstede, J.L.A., Hinrichsen, A., Reimers, H-C., Winter, C., 2021. Cliff Retreat Contribution to the Littoral Sediment Budget along the Baltic Sea Coastline of Schleswig-Holstein, Germany. *J. Mar. Sci. Eng.*, 9, 870. <https://doi.org/10.3390/jmse9080870>
- Baker, C.A., 1977. *Quaternary stratigraphy and environments in the Upper Cam Valley, North Essex*. Unpublished PhD thesis, University of London.
- Berthelsen, A., 1979. Recumbent folds and boudinage structures formed by subglacial shear: An example of gravity tectonics. In: van der Linden, W.J.M. (Ed.), *Van Bemmelen and his search for harmony*. *Geol. en Mijnbouw* 58: 252-260.
- Bilgili, M., Yasar, M., Simsek, E., 2011. Offshore wind power development in Europe and its comparison with onshore counterpart. *Renewable and Sustainable Energy Reviews* 15, 905-915

- Brown, A.R., 2004. Interpretation of Three-Dimensional Seismic Data. Sixth Edition. AAPG Memoir 42, SEG Investigations in Geophysics, No. 9, 1-541.
- Catuneanu, O., 2019. Model-independent sequence stratigraphy. *Earth-Science Reviews*, Volume 188, Pages 312-388. <https://doi.org/10.1016/j.earscirev.2018.09.017>
- Chen, J., Vissinga, M., Shen, Y., Hu, S., Beal, E., Newlin J., 2021. Machine Learning-Based Digital Integration of Geotechnical and Ultrahigh-Frequency Geophysical Data for Offshore Site Characterizations. *J. Geotech. Geoenviron. Eng.*, 147(12): 04021160.
- Coughlan, M., Fleischer, M., Wheeler, A.J., Hepp, D.A., Hebbeln, D., Mörz, T., 2017. A revised stratigraphical framework for the Quaternary deposits of the German North Sea sector: a geological-geotechnical approach. *Boreas*, 1-26, 10.1111/bor.12253. ISSN 0300-9483.
- Dutta, T.T., Saride, S., 2016. Influence of Shear Strain on the Poisson's Ratio of Clean Sands. *Geotech Geol Eng* 34:1359-1373.
- Emery, A.R., Hodgson, D.M., Barlow, N.L.M., Carrivick, J.L., Cotterill, C.J., Phillips, E., 2019. Left High and Dry: Deglaciation of Dogger Bank, North Sea, Recorded in Proglacial Lake Evolution. *Front. Earth Sci.* 7:234. doi: 10.3389/feart.2019.00234
- EMODnet Bathymetry Consortium, 2020. EMODnet Digital Bathymetry (DTM 2020). <https://doi.org/10.12770/bb6a87dd-e579-4036-abe1-e649cea9881a>
- Endler, M., Endler, R., Bobertz, B., Leipe, T., Arz, H.W., 2015. Linkage between acoustic parameters and seabed sediment properties in the south-western Baltic Sea. *Geo-Mar Lett*, DOI 10.1007/s00367-015-0397-3.
- Evans, D.J.A., Phillips, E.R., Hiemstra, J.F., Auton, C.A., 2006. Subglacial till: formation, sedimentary characteristics and classification. *Earth Sci. Rev.* 78, 115–176.
- Fatti, J.L., Smith, G.C., Vail, P.J., Strauss, P.J., Levitt, P.R., 1994. Detection of gas in sandstone reservoirs using AVO analysis: A 3-D seismic case history using the Geostack technique. *Geophysics*, vol. 59, No. 9, p. 1362-1376.
- Ferguson, R.J., Margrave, G.F., 1996. A simple algorithm for band-limited impedance inversion. *CREWES Res. Rep.* 8(21):1–10

- Filippova, K., Kozhenkov, A., Alabushin, A., 2011. Seismic inversion techniques: choice and benefits. *First break*, volume 29, 103-114.
- Flodén, T., Bjerkéus, M., Sturkell, E., Gelumbaускаite, Ž., Grigelis, A., Ender, R., Lemke, W., 1997. Distribution and seismic stratigraphy of glacially incised valleys in the southern part of the Baltic, in: Cato, I., Klingberg, F. (Eds.), *Proceedings of the Fourth Marine Geological Conference – the Baltic*, Uppsala 1995. *Sveriges Geologiska Undersökning, Ser. Ca 86*, pp. 43-49. ISBN 91-7158-553-2.
- Gardner, G.H.F., Gardner, L.W., Gregory, A.R., 1974. Formation velocity and density—the diagnostic basics for stratigraphic traps. *Geophysics*, Vol. 39, No. 6, p. 770-780.
- Gehrmann, A., Harding, C., 2018. Geomorphological Mapping and Spatial Analyses of an Upper Weichselian Glacitectonic Complex Based on LiDAR Data, Jasmund Peninsula (NE Rügen), Germany. *Geosciences*, 8, 208, 1-24; doi:10.3390/geosciences8060208
- Gehrmann, A., Hüneke, H., Meschede, M., Phillips, E., 2017. 3D microstructural architecture of deformed glacial sediments associated with large-scale glacitectonism, Jasmund Peninsula (NE Rügen, Germany). *Journal of Quaternary Science*, 32(2), 213-230. DOI: 10.1002/jqs.2843.
- Goldschmidt, P.M., 1994. Armoured and unarmoured till balls from the Greenland Sea floor. *Mar. Geol.* 121, 121-128.
- Gu, X., Yang, J., Huang M., 2013. Laboratory measurements of small strain properties of dry sands by bender element. *Soils and Foundations*, 53(5): 735-745.
- Gupta, A., Ramanathan, A.L., 2019. Grain texture as a proxy to understand porosity, permeability and density in Chandra Basin, India. *SN Applied Sciences* 1:1, <https://doi.org/10.1007/s42452-018-0001-3>.
- Gutowski, M., Bull, J.M., Dix, J., Henstock, T., Hogarth, P., White, P., Leighton T., 2002. Chirp sub-bottom profiler source signature design and field testing. *Marine Geophysical Researches* 23, 481-492.
- Hamilton, E.L., 1972. Compressional-wave attenuation in marine sediments. *Geophysics*, 37(4): 620–646.

- Hart, B.S., 2013. Whither seismic stratigraphy? INTERPRETATION, Vol. 1, No. 1; p. SA3-SA20. <http://dx.doi.org/10.1190/INT-2013-0049.1>.
- Henry, S., 2004. Understanding seismic amplitudes. AAPG Search and Discovery Article #40135, pp. 1-7.
- Henson, H., Sexton, J.L., 1991. Preliminary study of shallow coal seams using high-resolution seismic reflection methods. *GEOPHYSICS*, 56(9), 1494–1503. <https://doi.org/10.1190/1.1443171>
- Hübscher, C., Al Hseinat, M., Schneider, M., Betzler, C., 2019. Evolution of contourite systems in the late Cretaceous Chalk Sea along the Tornquist Zone. *Sedimentology*, 1-20. doi:10.1111/sed.12564.
- Huuse, M., Lykke-Andersen, H., 2000. Overdeepened Quaternary valleys in the eastern Danish North Sea: morphology and origin. *Quaternary Science Reviews*, 19, 1233–1253.
- ISO 19901-10, 2021, March. Petroleum and natural gas industries — Specific requirements for offshore structures — Part 10: Marine geophysical investigations. ISO Standard, Geneva, Switzerland: International Organisation for Standardization. Retrieved from <https://www.iso.org/standard/77017.html>
- Jensen, J.B., Bennike, O., Witkowski, A., Lemke, W., Kuijpers, A., 1997. The Baltic Ice Lake in the southwestern Baltic: sequence-, chrono- and biostratigraphy. *Boreas*, Vol. 26, pp. 217-236. Oslo. ISSN 0300-9483.
- Jørgensen, F., Sandersen, P.B.E., 2006. Buried and open tunnel valleys in Denmark – erosion beneath multiple ice sheets. *Quaternary Science Reviews*, 25, 1339–1363.
- Kenzler, M., Obst, K., Hüneke, H., Schütze K., 2010. Glaciotectonic deformation of Cretaceous and Pleistocene sediments at the coastal cliff of Jasmund peninsula north of Königsstuhl (Rügen). *Brandenburgische Geowissenschaftliche Beiträge*, Cottbus, 17, 1/2, S. 107-122, 9 Abb., 67 Lit.
- Kenzler, M., Tsukamoto, S., Meng, S., Frechen, M., Hüneke, H., 2017. New age constraints from the SW Baltic Sea area – implications for Scandinavian Ice Sheet dynamics and palaeoenvironmental conditions during MIS 3 and early MIS 2. *Boreas* 46 (1), 34–52.

- Khan, A.A., Hamid, G., Hasany, S.I., 2000. Mineralogical Variations and Physical Properties of Deep Sea Sediments, Northwest Arabian Sea. *Pakistan Journal of Marine Sciences*, Vol. 9(1&2), 17-31.
- Kor, P.S.G., Shaw, J., Sharpe, D.R., 1991. Erosion of bedrock by subglacial meltwater, Georgian Bay, Ontario: a regional view. *Canadian Journal of Earth Sciences* 28, 623–642.
- Kortekaas, M., Murray, A.S., Sandgren, P., Björck, S., 2007. OSL chronology for a sediment core from the southern Baltic Sea: A continuous sedimentation record since deglaciation. *Quaternary Geochronology*, 2, 95-101.
- Kotilainen, A.T., Kaskela, A.M., Bäck, S., Leinikki, J., 2012. Submarine De Geer Moraines in the Kvarken Archipelago, the Baltic Sea. *Seafloor Geomorphology as Benthic Habitat*. DOI: 10.1016/B978-0-12-385140-6.00017-7, Elsevier Inc., pp. 289–298.
- Lee, J., Kyung, D., Kim, B., Prezzi, M., 2009. Estimation of the Small-strain Stiffness of Clean and Silty Sands Using Stress-strain Curves and CPT Cone Resistance. *Soils and Foundations*, Vol. 49, No. 4, 545-556.
- Lee, J., Salgado, R., 2000. Analysis of calibration chamber plate load tests. *Canadian Geotechnical Journal*, 37(1), 14-25.
- Linkwitz, S.H., 1978. Passive Crossover Networks for Noncoincident Drivers. *Journal of the Audio Engineering Society*, 26(3), 149–150.
- Lu, Y., Duan, Z., Zheng, J., Zhang, H., Liu, X., Luo, S., 2020. Offshore Cone Penetration Test and Its Application in Full Water-Depth Geological Surveys. *IOP Conf. Series: Earth and Environmental Science* 570, 042008, 1-9; doi:10.1088/1755-1315/570/4/042008
- Lykke-Andersen, H., Surlyk, F., 2004. The Cretaceous-Palaeogene boundary at Stevns Klint, Denmark: Inversion tectonics or sea-floor topography? *J. Geol. Soc.*, 47, 343–352.
- Mathys, M., Thießen, O., Theilen, F., Schmidt, M., 2005. Seismic characterisation of gas-rich near surface sediments in the Arkona Basin, Baltic Sea. *Marine Geophysical Researches*, 26: 207-224.

- Mavko, G., Mukerji, T., Dvorkin, J., 2009. *The Rock Physics Handbook* (2nd ed.), Cambridge University Press. 503 pp.
- McCann, C., McCann, D.M., 1969. The attenuation of compressional waves in marine sediments. *Geophysics*, 34(6): 882–892.
- Menzies, J., 2012. Strain pathways, till internal architecture and microstructures—perspectives on a general kinematic model—a ‘blueprint’ for till development. *Quat. Sci. Rev.* 50, 105-124.
- Menzies, J., van der Meer, J.J.M., Shilts, W.W., 2018. Subglacial Processes and Sediments, in: Menzies, J., van der Meer, J.J.M. (Eds.), *Past Glacial Environments* (Second Edition), Elsevier Ltd, pp. 105-158.
- Menzies, J., Woodward, J., 1993. Preliminary Study of Subglacial Diamicton Microstructures as Reflected in Drumlin Sediments at Chimney Bluffs, New York. *Glaciotectonics and Mapping Glacial Deposits*. INQUA Commission on Formation and Properties of Glacial Deposits, Proceedings, Canadian Plains Research Centre, University of Regina, Regina, pp. 36-45.
- Mitchum Jr., R.M., 1977. Seismic stratigraphy and global changes of sea level. Part 11: glossary of terms used in seismic stratigraphy, in: Payton, C.E. (Ed.), *Seismic Stratigraphy—Applications to Hydrocarbon Exploration*, vol. 26. A.A.P.G. Memoir, pp. 205–212.
- Mitchum Jr., R.M., Vail, P.R., Sangree, J.B., 1977. Seismic stratigraphy and global changes of sea level, part 6: stratigraphic interpretation of seismic reflection patterns in depositional sequences, in: Payton, C.E. (Ed.), *Seismic Stratigraphy—Applications to Hydrocarbon Exploration: AAPG Memoir 26*, pp. 117–133.
- Mogollón, J.M., Dale, A.W., Fossing, H., Regnier, P., 2012. Timescales for the development of methanogenesis and free gas layers in recently-deposited sediments of Arkona Basin (Baltic Sea). *Biogeosciences*, 9, 1915-1933. doi:10.5194/bg-9-1915-2012.
- Monk, D.J., 1993. Wave-Equation Multiple Suppression Using Constrained Gross-Equalization. *Geophysical Prospecting* 41, 725-736.

- Möller, P., 2010. Melt-out till and ribbed moraine formation, a case study from south Sweden. *Sediment. Geol.* 232, 161-180.
- Moros, M., Lemke, W., Kuijpers, A., Endler, R., Jensen, J.B., Bennike, O., Gingele, F., 2002. Regressions and transgressions of the Baltic basin reflected by a new high-resolution deglacial and postglacial lithostratigraphy for Arkona Basin sediments (western Baltic Sea). *Boreas*, Vol. 31, pp. 151-162. Oslo. ISSN 0300-9483.
- Munro-Stasiuk, M.J., Heyman, J., Harbor, J., 2013. Erosional features, in: Shroder, J. (Editor in Chief), Giardino, R., Harbor, J. (Eds.), *Treatise on Geomorphology*, Academic Press, San Diego, CA, Vol. 8, *Glacial and Periglacial Geomorphology*, pp. 83–99.
- Obst, K., Nachtweide, C., Müller, U., 2017. Late Saalian and Weichselian glaciations in the German Baltic Sea documented by Pleistocene successions at the southeastern margin of the Arkona Basin. *Boreas*, DOI 10.1111/bor. 12212, 1-16.
- Paul, M.A., Eyles, N., 1990. Constraints on the preservation of diamict facies (melt-out tills) at the margins of stagnant glaciers. *Quat. Sci. Rev.*, Vol. 9, Issue 1, 51-69.
- Phillips, E.R., 2018. Glacitectonics, in: Menzies, J., van der Meer, J.J.M. (Eds.), *Past Glacial Environments (Second Edition)*, Elsevier Ltd, pp. 467-502.
- Pinson, L.J.W., Henstock, T.J., Dix, J.K., Bull, J.M., 2008. Estimating quality factor and mean grain size of sediments from high-resolution marine seismic data. *GEOPHYSICS*, 73(4), G19–G28. <https://doi.org/10.1190/1.2937171>
- Plonka, N., Kenzler, M., Hüneke, H., 2022. Syn-kinematic sedimentation between ice margin-parallel thrust-bounded ridges of the Glacitectonic Complex of Jasmund (Rügen Island, SW Baltic Sea, Weichselian). *Quaternary International* 630, 48-64. <https://doi.org/10.1016/j.quaint.2021.02.040>
- Pollard W. 2018. Periglacial Processes in Glacial Environments, in: Menzies, J., van der Meer, J.J.M. (Eds.), *Past Glacial Environments (Second Edition)*, Elsevier Ltd, pp. 537-564.
- Prins, L.T., Andresen, K.J., 2021. A geotechnical stratigraphy for the shallow subsurface in the Southern Central Graben, North Sea. *Engineering Geology* 286, 106089; <https://doi.org/10.1016/j.enggeo.2021.106089>

- Raymer, L., Hunt, E., Gardner, J., 1980. An improved sonic transit time-to-porosity transform. In SPWLA 21st Annual Logging Symposium (pp. 1–13).
- Roberts, D.H., Hart, J.K., 2005. The deforming bed characteristics of a stratified till assemblage in north East Anglia, UK: investigating controls on sediment rheology and strain signatures. *Quat. Sci. Rev.* 24, 123-140.
- Robertson, P.K., 1990. Soil classification using the cone penetration test. *Canadian Geotechnical Journal*, **27**(1): 151–158. doi:10.1139/t90-014.
- Robertson, P.K., 2009. Interpretation of cone penetration tests—a unified approach. *Can. Geotech. J.* 46: 1337-1355, doi:10.1139/T09-065
- Robertson, P.K., 2016. Cone penetration test (CPT)-based soil behaviour type (SBT) classification system — an update. *Can. Geotech. J.* 00:1-18 (0000) dx.doi.org/10.1139/cgj-2016-0044
- Robertson, P.K., Cabal (Robertson), K.L., 2014. Cone penetration testing for geotechnical engineering. Gregg Drilling & Testing, Inc., California (Sixth Edition), 1-133.
- Römer-Stange, N., Morales, N., Keil, H., Ettrich, N., Wilhelm, S., Wenau, S., Oguro, A., Merl, M., Ramos Cordova, C., Siemann, L., Pein, T., Arnold, P., Spieß, V., 2023. From Interface to Unit Characterisation: Stochastic Near Surface Seismic Impedance Inversion in the German North Sea. Submitted to *Geophysical Journal International* on 23.08.2023.
- Sauvin, G., Vanneste, M., Madshus, C., 2018. High-Resolution Quantitative Ground-Model for Shallow Subsurface. EAGE, Near Surface Geoscience Conference and Exhibition 2018, 9-12 September 2018, Porto, Portugal, Mo 3ASM 03, 1-5
- Sauvin, G., Vanneste, M., Vardy, M.E., Klinkvort, R.T., Fredrik, F.C., 2019. Machine Learning and Quantitative Ground Models for Improving Offshore Wind Site Characterization, in *Proc., Offshore Technology Conference, USA*, OTC-29351-MS, pp. 1-17.
- Schlüter, H., Best, G., Jürgens, U., Binot, F., 1997. Interpretation reflexionseismischer Profile zwischen baltischer Kontinentalplatte und kaledonischem Becken in der

südlichen Ostsee – erste Ergebnisse. Zeitschrift der Deutschen Geologischen Gesellschaft 148, 1-32.

Seidel, E., 2019. The Tectonic Evolution of the German offshore area, as part of the Trans-European Suture Zone (North and East of Rügen Island. Preparation for a 3D-modelling of the southern Baltic Sea, USO project. Inauguraldissertation zur Erlangung des akademischen Grades eines Doktors der Naturwissenschaften (Dr. rer. nat.) der Mathematisch-Naturwissenschaftlichen Fakultät der Universität Greifswald, 1-170.

Sen, M.K., Stoffa, P.L., 1992. Rapid sampling of model space using genetic algorithms: Examples from seismic waveform inversion. Geophysical Journal International, 108, 281–292. <https://doi.org/10.1111/j.1365-246X.1992.tb00857.x>

Stephan, H.-J., 2001. The Young Baltic advance in the western Baltic depression. Geological Quarterly, 45 (4): 359-363.

Stoll, R., 1989. Sediments Acoustics, Lecture Notes in Earth Science, Springer-Verlag, Inc.

Sun, L., Ding, L., Wang, X., 2022. Research on Initial Model Construction of Seismic Inversion Based on Velocity Spectrum and Siamese Network. Appl. Sci., 12, 10593, pp. 1-13; <https://doi.org/10.3390/app122010593>

Taner, M.T., Koehler, F., Sheriff, R.E., 1979. Complex seismic trace analysis. Geophysics, vol. 44, No. 6; p. 1041-1063.

Tarantola, A., 1984. Inversion of seismic reflection data in the acoustic approximation. Geophysics, 49(8), 1259-1266.

Tearpock, D.J., Bischke, R.E., 1991. Applied Subsurface Geological Mapping. Prentice-Hall PTR, A Simon & Schuster Company, Upper Saddle River, NJ, 217-231.

Tóth, Zs., Spieß, V., Jensen, J., 2014. Seismo-acoustic signatures of shallow free gas in the Bornholm Basin, Baltic Sea. Continental Shelf Research, 88, 228-239.

Trimonis, E., Vaikutienė, G., Grigienė A., 2008. Sedimentation in the Western Baltic Sea as recorded in the sediment core from the Arkona Basin. GEOLOGIJA, T. 50. No. 2(62). P. 105-113.

van der Vegt, P., Janszen, A., Moscariello, A., 2012. Tunnel valleys: current knowledge and future perspectives. Geological Society, London, Special Publications v.368, doi 10.1144/SP368.13.

Vanneste, M., Forsberg, C.F., Knudsen, S., Kvalstad, T.J., L'Heureux, J-S., Lunne, T., Vardy, M.E., Chand, S., Longva, O., Morgan, E., Kopf, A., Mörz, T., Steiner, A., Brendryen, J., Hafliðason, H., 2015. Integration of very-high-resolution seismic and CPTU data from a coastal area affected by shallow landsliding—the Finneidfjord natural laboratory. *Frontiers in Offshore Geotechnics III—Meyer (Ed.)*. Taylor & Francis Group, London, ISBN: 978-1-138-02848-7, 1017-1022.

Vardy, M.E., 2015. Deriving shallow-water sediment properties using post-stack acoustic impedance inversion. *Near Surface Geophysics*, 13, 143-154: doi:10.3997/1873-0604.2014045

Vardy, M.E., Vanneste, M., Henstock, T.J., Morgan, E., Pinson, L.J.W., 2015. Can high-resolution marine geophysical data be inverted for soil properties? *Proceedings of the Institute of Acoustics*, Vol. 37, Pt. 1, pp. 149-156.

Vardy, M.E., Clare, M.A., Vanneste, M., Forsberg, C.F., Dix, J.K., 2018. Seismic Inversion For Site Characterization: When, Where and Why Should We Use It? Paper based on presentation abstract at Offshore Technology Conference, 2018, OTC-28730-MS, pp. 1-8

Veeken, P.C.H, Da Silva, M., 2004. Seismic inversion methods and some of their constraints. *First break*, volume 22, p. 15-38.

Waters, K.H., 1987. *Reflection seismology: a tool for energy resource exploration*. Wiley, New York

Wenau, S., Burmeister, T., Dodds, S., Morales, N., Haberkern, J., 2022. EAGE GET 2022, Nov 2022, Volume 2022, p.1-6; DOI: <https://doi.org/10.3997/2214-4609.202221080>

Wingfield, R., 1990. The origin of major incisions within the Pleistocene deposits of the North Sea. *Marine Geology*, Volume 91, Issues 1-2, 31-52.

Winterhalter, B., Flodén, T., Ignatius, H., Axberg, S., Niemistö L., 1981. *Geology of the Baltic Sea*. Elsevier Oceanography Series, vol. 30, p. 1-121.

Woodland, A.W., 1970. The buried tunnel-valleys of East Anglia. Proceedings of the Yorkshire Geological Society, 37, *Part 4, No. 22*, 521–578. York 1968.

Xu, G., Haq, B.U., 2022. Seismic facies analysis: Past, present and future. Earth-Science Reviews 224, 103876. <https://doi.org/10.1016/j.earscirev.2021.103876>

Yang, W., Qu, C., Yu, C., 2011. Crustal Poisson's ratio anomalies in the eastern part of North China and their origins. Geoscience Frontiers 2(3): 313-321.

Yilmaz, Ö., 1987. Seismic Data Processing. Society of Exploration Geophysics, Tulsa, 526 pp.

Yilmaz, Ö., 2001. Seismic Data Analysis - Processing, Inversion, and Interpretation of Seismic Data. Society of Exploration Geoph, Tulsa.

Zoeppritz, K., 1919. Erdbebenwellen VII. VIIb. Über Reflexion und Durchgang seismischer Wellen durch Unstetigkeitsflächen. Nachrichten von der Königlichen Gesellschaft der Wissenschaften zu Göttingen, Mathematisch-physikalische Klasse, 66-84.

## Appendix

### A1 DGG 2023 – 83 Jahrestagung der Deutschen Geophysikalischen Gesellschaft

**Abstract number:** A-227

**Abstract title:** *3D High Resolution Multichannel Seismic Data Acquired in Shallow Marine Waters of Southern Arkona Basin*

**Presentation type:** Poster; **Poster number:** S2-P.05; **Session:** Poster S2, GE, GD, GO, GF

**Session date:** 7 March 2023; **Session topic:** S2 - Renewable Energy—Contributions of geophysics on- and offshore

**Status:** Presented

**Authors:** O. Ogunleye<sup>1\*</sup>, H. Keil<sup>1</sup>, C. Ramos Cordova<sup>2</sup>, V. Spieß<sup>1</sup>

<sup>1</sup>University of Bremen, Department of Geosciences, Bremen, Deutschland

<sup>2</sup>Fraunhofer Institute for Wind Energy Systems, Bremen, Deutschland

\*Presenter

#### **Abstract:**

In Arkona Block (Baltic Sea), not much has been done to delineate: (1) Tertiary tectonic faults within Cretaceous chalk, and (2) glacially-derived erosional structures formed in the Weichselian. Thus, a 3D Multi-Channel Seismic (MCS) reflection data covering 7 km<sup>2</sup> was acquired along the southern margin of Arkona Basin by the Department of Geosciences (University of Bremen) in 2017 to reveal not only the regional seismic units and their lithologic characteristics, but also a detailed stratigraphic and structural framework of the shallow sub-seafloor. This MCS data was acquired during a RV ALKOR Device Test Cruise with the aid of two Sercel air guns fired in a flip-flop mode for adequate subsurface fold coverage. Seismic signals generated had a central frequency of ~250 Hz. A Seemap High Resolution 3D receiver cable designed for shallow waters was deployed. It consisted of four 48-m long streamers with 1-m spaced single-hydrophone channels. Acquisition geometry led to an offset distribution of 31-89 m. High vertical resolution in the order of 0.75 m (calculated as a quarter of a wavelength) was achieved. We ensured very good lateral resolution during data processing by using a bin size of 1 m (inline) by 5 m (crossline). Owing to shallow water depths, multiples occurred at relatively shallow depths in the shot gathers. Consequently, Surface Related Multiple Elimination technique with

adaptive subtraction was applied for multiple suppression. The short wavelength of seismic signals necessitated detailed correction of residual statics which we achieved with a Python script by correcting normal move-out corrected gathers with smoothed seafloor picks. Vertical sections and time slices of stacked MCS data showed that in addition to Tertiary extension which deformed bedrock chalk, glacial units have been deposited in the Pleistocene, with the glacial activities leaving tunnel valleys, s-forms and ridges as buried landforms in Arkona Basin.

## **A2 American Geophysical Union—AGU23 meeting, San Francisco, CA and Online Everywhere**

**Abstract ID:** 1336585

**Final paper number and abstract title:** *NS21A-0537: Statistical Boundary Conditions of Subsoil Physical Properties in the Arkona Basin – Delineating Interface-Related and Layer-Based Seismic Attributes for Predicting Near-Surface Geotechnical Parameters*

**Presentation type:** Poster; **Session date:** 12 December 2023

**Session number and title:** NS21A: Advances in Exploration Geophysics II Poster

**Status:** Accepted for presentation

**Authors:** Opeyemi Ogunleye<sup>1</sup>, Nikolas Römer-Stange<sup>1\*</sup>, Volkhard Spiess<sup>1</sup>, Hanno Keil<sup>1</sup>, Paola Natasha Morales Hernandez<sup>2</sup>, Jean-Rémi Dujardin<sup>3</sup>, Taisiya Pein<sup>2</sup>, Guillaume Sauvin<sup>3</sup> and Maarten Vanneste<sup>3</sup>

<sup>1</sup>University of Bremen, Faculty of Geosciences, Bremen, Germany

<sup>2</sup>Fraunhofer Institute for Wind Energy Systems, Bremen, Germany

<sup>3</sup>Norwegian Geotechnical Institute, Oslo, Norway

\*Presenting author

### **Abstract:**

Since the German Baltic Sea became a target for windfarm development, more studies on combining high-quality seismic data with soil properties are required. However, the geologic setting of the Baltic Sea/Arkona Basin is complex, it being characterized by Cretaceous bedrock consisting of chalk successions, which were subsequently glacially overprinted and covered by glacial till, sands and clays followed by fine-grained brackish to marine organic-rich deposits.

Therefore, as part of the SynCore project, we (1) established constraints of initial models for acoustic impedance inversion of seismic data; and (2) delineated interface- and layer-related seismic attributes as indicators of geotechnical and lithologic

properties in geologic formations. Our comprehensive database consists of 3D multichannel seismic data over 7 km<sup>2</sup> and 133 km of 2D lines (central frequency ~300Hz, vertical resolution ~0.8 m) as well as sediment descriptions from 17 boreholes, 6 velocity logs, and Cone Penetration Test (CPT) data from 14 locations.

After migration, the seismic cube images the 3D stratigraphic architecture and structural framework of the development area. Vertical sections and time slices through the cube show that – in addition to Tertiary extension which deformed the bedrock – glacial processes created subglacial tunnel valleys, s-forms and ridges as buried landforms. Root mean square amplitude maps within an un-channelized till unit also reveal the presence of polygonal features of an ancient permafrost terrain.

In this research, we show that composite spatial changes in interface-related seismic attributes correlate with variations in normalized Soil Behavior Type (SBT<sub>n</sub>), and anomalous variations in post-stack acoustic impedance correspond to lithologic and CPT changes. Guiding CPT data prediction with trace envelope, instantaneous frequency and lateral continuity of seismic events will reduce uncertainties. From ground truthing, relatively precise physical property values were derived for Cretaceous chalk, till-dominated valley fill and un-channelized till as well as the soft post-glacial sediment cover, which could be well correlated to seismic facies, acoustic impedance, and SBT<sub>n</sub>. These values provide low-frequency trends for seismic inversion.